



Computer aided surgery : Application to aortic dissection

Wenyang Pan

► To cite this version:

Wenyang Pan. Computer aided surgery : Application to aortic dissection. Biomechanics [physics.med-ph]. Université de Lyon, 2021. English. NNT : 2021LYSEI075 . tel-03547623

HAL Id: tel-03547623

<https://theses.hal.science/tel-03547623>

Submitted on 28 Jan 2022

HAL is a multi-disciplinary open access archive for the deposit and dissemination of scientific research documents, whether they are published or not. The documents may come from teaching and research institutions in France or abroad, or from public or private research centers.

L'archive ouverte pluridisciplinaire **HAL**, est destinée au dépôt et à la diffusion de documents scientifiques de niveau recherche, publiés ou non, émanant des établissements d'enseignement et de recherche français ou étrangers, des laboratoires publics ou privés.

N° d'ordre NNT : 2021LYSEI075

THÈSE DE DOCTORAT DE L'UNIVERSITÉ DE LYON
opérée au sein de
l'INSA Lyon

École Doctorale N°ED165
Mécanique, Énergétique, Génie Civil et Acoustique (MEGA)

Spécialité/discipline de doctorat :
Biomécanique

Soutenue publiquement le 26/11/2021, par :
Wenyang Pan

**Computer Aided Surgery : application to
aortic dissection**

Devant le jury composé de :

Corneliu BALAN	Professeur des Universités	Université Politehnica de Bucarest	Rapporteur
Francesco MASSI	Professeur des Universités	Université Sapienza de Roma	Rapporteur
Pascale KULISA	Chargée de Recherche	École Centrale de Lyon	Examinatrice
Loïc BOUSSEL	Professeur des Universités/PH	Hospices Civils de Lyon	Examineur
Michel FILLON	Directeur de Recherche	Université de Poitiers	Examineur
Benyebka BOU-SAÏD	Professeur des Universités	INSA Lyon	Directeur de thèse
Antoine MILLON	Professeur des Universités/PH	Hospices Civils de Lyon	Invité
Monica SIGOVAN	Chargée de Recherche	INSA Lyon	Invitée
Xavier ESCRIVA	Maître de Conférences	Université Lyon 1	Invité
Marine MENUT	CEO	CISTEN	Invitée
Patrick LERMUSIAUX	Professeur des Universités/PH	Hospices Civils de Lyon	Invité

Département FEDORA – INSA Lyon - Ecoles Doctorales

SIGLE	ECOLE DOCTORALE	NOM ET COORDONNEES DU RESPONSABLE
CHIMIE	<u>CHIMIE DE LYON</u> https://www.edchimie-lyon.fr Sec. : Renée EL MELHEM Bât. Blaise PASCAL, 3e étage secretariat@edchimie-lyon.fr	M. Stéphane DANIELE C2P2-CPE LYON-UMR 5265 Bâtiment F308, BP 2077 43 Boulevard du 11 novembre 1918 69616 Villeurbanne directeur@edchimie-lyon.fr
E.E.A.	<u>ÉLECTRONIQUE, ÉLECTROTECHNIQUE, AUTOMATIQUE</u> https://edeea.universite-lyon.fr Sec. : Stéphanie CAUVIN Bâtiment Direction INSA Lyon Tél : 04.72.43.71.70 secretariat.edeea@insa-lyon.fr	M. Philippe DELACHARTRE INSA LYON Laboratoire CREATIS Bâtiment Blaise Pascal, 7 avenue Jean Capelle 69621 Villeurbanne CEDEX Tél : 04.72.43.88.63 philippe.delachartre@insa-lyon.fr
E2M2	<u>ÉVOLUTION, ÉCOSYSTÈME, MICROBIOLOGIE, MODÉLISATION</u> http://e2m2.universite-lyon.fr Sec. : Sylvie ROBERJOT Bât. Atrium, UCB Lyon 1 Tél : 04.72.44.83.62 secretariat.e2m2@univ-lyon1.fr	M. Philippe NORMAND Université Claude Bernard Lyon 1 UMR 5557 Lab. d'Ecologie Microbienne Bâtiment Mendel 43, boulevard du 11 Novembre 1918 69 622 Villeurbanne CEDEX philippe.normand@univ-lyon1.fr
EDISS	<u>INTERDISCIPLINAIRE SCIENCES-SANTÉ</u> http://ediss.universite-lyon.fr Sec. : Sylvie ROBERJOT Bât. Atrium, UCB Lyon 1 Tél : 04.72.44.83.62 secretariat.ediss@univ-lyon1.fr	Mme Sylvie RICARD-BLUM Institut de Chimie et Biochimie Moléculaires et Supramoléculaires (ICBMS) - UMR 5246 CNRS - Université Lyon 1 Bâtiment Raulin - 2ème étage Nord 43 Boulevard du 11 novembre 1918 69622 Villeurbanne Cedex Tél : +33(0)4 72 44 82 32 sylvie.ricard-blum@univ-lyon1.fr
INFOMATHS	<u>INFORMATIQUE ET MATHÉMATIQUES</u> http://edinfomaths.universite-lyon.fr Sec. : Renée EL MELHEM Bât. Blaise PASCAL, 3e étage Tél : 04.72.43.80.46 infomaths@univ-lyon1.fr	M. Hamamache KHEDDOUCI Université Claude Bernard Lyon 1 Bât. Nautibus 43, Boulevard du 11 novembre 1918 69 622 Villeurbanne Cedex France Tél : 04.72.44.83.69 hamamache.kheddouci@univ-lyon1.fr
Matériaux	<u>MATÉRIAUX DE LYON</u> http://ed34.universite-lyon.fr Sec. : Yann DE ORDENANA Tél : 04.72.18.62.44 yann.de-ordenana@ec-lyon.fr	M. Stéphane BENAYOUN Ecole Centrale de Lyon Laboratoire LTDS 36 avenue Guy de Collongue 69134 Ecully CEDEX Tél : 04.72.18.64.37 stephane.benayoun@ec-lyon.fr
MEGA	<u>MÉCANIQUE, ÉNERGÉTIQUE, GÉNIE CIVIL, ACOUSTIQUE</u> http://edmega.universite-lyon.fr Sec. : Stéphanie CAUVIN Tél : 04.72.43.71.70 Bâtiment Direction INSA Lyon mega@insa-lyon.fr	M. Jocelyn BONJOUR INSA Lyon Laboratoire CETHIL Bâtiment Sadi-Carnot 9, rue de la Physique 69621 Villeurbanne CEDEX jocelyn.bonjour@insa-lyon.fr
ScSo	<u>ScSo*</u> https://edsciencessociales.universite-lyon.fr Sec. : Mélina FAVETON INSA : J.Y. TOUSSAINT Tél : 04.78.69.77.79 melina.faveton@univ-lyon2.fr	M. Christian MONTES Université Lumière Lyon 2 86 Rue Pasteur 69365 Lyon CEDEX 07 christian.montes@univ-lyon2.fr

*ScSo : Histoire, Géographie, Aménagement, Urbanisme, Archéologie, Science politique, Sociologie, Anthropologie

Acknowledgement

This manuscript ends with a few words for the many people who have helped and supported me during these four years. The work of a thesis is far from being a solitary work and I hope that these few thanks will be able to express a part of my gratitude for the generosity and the contributions that these people have given to my work.

First of all, I would like to thank my thesis supervisor, Prof. Benyebka Bou-Saïd, for the trust and kindness he has given me during these many years. His immense knowledge and his scientific open-mindedness allowed me to work on this huge project that shaped the researcher I am today. I sincerely believe that you never meet someone by chance and I am happy to say that he has guided me in the best possible way. He taught me a lot, both scientifically, by constantly arousing my curiosity, and humanly, by his support and his coaching of my French.

I would also like to thank Mrs. Pascale Kulisa, for her great availability and patience, her numerous pieces of advice, and her moral support, which have all been a very precious help during the last two years of the most critical period of the Ph.D. study, especially in the period of doubts. I benefited from flawless help that allowed me to fully develop my research skills.

This work would not have been possible without the financial support of the China Scholarship Council (CSC), which allowed me to devote myself to the elaboration of this thesis. I would like to thank the CSC for the financial support given to this research project.

I would also like to express my sincere appreciation to all my committee members: Prof. Corneliu Balan, Prof. Francesco Massi, Dr. Pascale Kulisa, Prof. Loïc Boussel, Prof. Antoine Millon, Dr. Monica Sigovan, Dr. Xavier Escriva, CEO Marine Menut, Prof. Patrick Lermusiaux, and also the president of my jury Prof. Michel Fillon. Thank you for generously offering your time, support, advice, and goodwill throughout the revision of this manuscript. Thank you for making my defense an enjoyable moment, and for their insightful remarks and suggestions.

This project is a collaboration among several people from very different fields, who helped me enormously in the realization of this work and with whom I enriched myself a little more each day. My thanks and gratitude go first of all to the hospital practitioners, specially Prof. Patrick Lermusiaux for all his precious advice, his help, and his kindness. Thanks to Dr. Marine Menut and Dr. Xavier Escriva for their support and their many contributions concerning the computational part of this thesis. Thanks to Monica Sigovan for the clinical data. Thanks also to Anaïs Moravia, who studied the same pathology but focused on the experimental part, which helped me a lot for a part of the last chapter of my Ph.D. manuscript.

I would also like to give a special thanks to Jingjing Zhang's family, herself, her husband Prof. Paolo Massioni, and her two lovely daughters. Jing's cooking skills made me not so homesick. And

their friendliness, great humor, brilliance, and social skills have given me a lot of happiness and encouragement during my Ph.D. study.

Finally, as simple words are often the strongest, I would like to thank my parents for their support since the beginning of my studies. The difficulties we have encountered have made me, I hope, always a little stronger. Therefore, in the new journey ahead, no matter how difficult it may be, I will go on confidently with gratitude, friendship, responsibility, expectations, and dreams.

学无止境，砥砺前行。

少年强则国强，少年智则国智！

此时此刻，我深深地体会到，没有国家留学基金委的全力支持，就不会有我继续深造的机会。没有祖国强盛国力作为后盾，也不会有学成报效祖国的强大内心驱动力。

特此再次感谢中国政府和中国留学基金！

Abstract

Cardiovascular diseases (CVDs) are the leading cause of mortality in the European Union and accounted for about 36% of all deaths in 2019 (Timmis et al., 2020). Among these diseases, aortic dissection is relatively unknown and difficult to treat, with a survival rate for most severe cases not exceeding 10%. This pathology occurs when an injury leads to a localized tear of the innermost layer of the aorta, called the entry port. It allows blood to flow between the layers of the aortic wall, forcing the layers apart and creating a false lumen. The dissection of these layers may extend over a long portion of the thoracic and abdominal aorta.

Endovascular treatment seeks to obliterate the entrances to the false lumen with a stent. The currently available surgical tools for endovascular procedures are selected only from information based on medical imaging techniques. The images are carried out before the intervention and therefore do not consider the deformation of the vascular structure by the implementation of the prosthesis. While many biomechanical studies have been done on the endovascular treatment of aneurysms of the abdominal aorta, there are, however, very few studies on aortic dissections. However, there are few studies as well on the postoperative demonstration of blood flow phenomena in the aortic dissection endovascular treatment. It is crucial to study the hemodynamic of blood in the aorta after an intervention, because the deployment of a stent leads to modifications in the blood flow. For the surgeons, the procedure can only be performed empirically, using MRI-4D images to view the post-operative flow of the patient's blood in the aorta with the stent. The numerical simulation method, instead allows us to simulate the complete endovascular procedure for an adapted recommendation during surgical planning.

This thesis aims to present a numerical tool, from the open-source software FOAM-Extend[®], allowing for Multiphysics numerical simulations, performing the fluid-structure coupling between the hemodynamics and the arterial deformation to assist in the planning process. In addition, using Abaqus software, we realized the placement of the surgical tools in a “biomechano-faithful” aortic dissection model (Pan et al., 2020). This model will be able to predict the deformation of the flap and the artery wall during the implementation of the tools. Also, with the numerical simulation, we could obtain the postoperative hemodynamic in the aorta, to predict the modification of flow. Finally, the numerical simulation results are compared with the MRI data to have a validation of the numerical models. There is a parallel thesis (Moravia, 2021) that focuses on flows in aorta phantoms PIV applied in AD (same geometry) and enables the confrontation and inter-validation of both model methods at the time of the study.

Keywords: Biomechanics. Cardiovascular diseases. Virtual Surgery. Aortic dissection. Endovascular. Numerical simulation. Hemodynamic. Fluid-structure interaction. 4D-MRI

Résumé

Les maladies cardiovasculaires sont la principale cause de mortalité dans l'Union européenne et représentent environ 36% de tous les décès en 2019 (Timmis et al., 2020). Parmi ces maladies, la dissection aortique est relativement méconnue et difficile à traiter, avec un taux de survie pour les cas les plus graves ne dépassant pas 10%. Cette pathologie survient dans l'aorte et se caractérise par l'irruption de sang à l'intérieur de la paroi de l'aorte. Elle correspond à une déchirure localisée des couches internes de la paroi aortique, appelée porte d'entrée, par laquelle le sang sous pression pénètre et décolle les différentes couches qui constituent la paroi de l'aorte. La dissection de ces couches peut s'étendre sur une longue portion de l'aorte thoracique et abdominale.

Le traitement endovasculaire vise à oblitérer les entrées de la faux lumen à l'aide d'un stent. Les outils chirurgicaux actuellement disponibles pour les procédures endovasculaires sont sélectionnés uniquement à partir d'informations basées sur les techniques d'imagerie médicale. Les images sont réalisées avant l'intervention et ne prennent donc pas en compte la déformation de la structure vasculaire par la mise en place de la prothèse. Si de nombreuses études biomécaniques ont été réalisées sur le traitement endovasculaire des anévrismes de l'aorte abdominale, il existe en revanche très peu d'études de ce type sur les dissections aortiques. Et il y a peu d'études sur la démonstration postopératoire des phénomènes de flux sanguin dans le traitement endovasculaire de la dissection aortique. Il est crucial d'étudier l'hémodynamique dans l'aorte après une intervention car le déploiement d'un stent entraîne des modifications du flux sanguin. Pour les chirurgiens, la procédure ne peut être réalisée que de manière empirique, en utilisant des images IRM-4D pour visualiser le flux post-opératoire du sang du patient dans l'aorte avec le stent. Mais la méthode de simulation numérique nous permet de simuler la procédure endovasculaire complète pour une recommandation adaptée lors de la planification chirurgicale.

Cette thèse a pour but de présenter un outil numérique, issu du logiciel open-source FOAM-Extend®, permettant des simulations numériques multiphysiques réalisant le couplage fluide-structure entre l'hémodynamique et la déformation artérielle pour aider au processus de planification. En outre, à l'aide du logiciel Abaqus, nous réalisons le placement des outils chirurgicaux dans un modèle de dissection aortique "bio-fidèle" (Pan et al., 2020). Cela permettra de prédire la déformation du flap et de la paroi de l'artère lors de la mise en place des outils. Et aussi, avec la simulation numérique, nous pourrons réaliser l'hémodynamique dans l'aorte en postopératoire pour prédire la modification du flux. Enfin, les résultats de la simulation numérique sont comparés aux données de l'IRM pour avoir une validation des modèles numériques. En outre, il y a une thèse parallèle (Moravia, 2021) qui se concentre sur les écoulements dans des fantômes d'aorte avec applications de la PIV en AD (même géométrie) qui permet la confrontation et l'inter-validation des deux méthodes de modélisation au moment de l'étude.

Mots clés : Biomécanique. Maladies Cardiovasculaires. Chirurgie Virtuelle. La dissection aortique. Endovasculaire. Simulation numérique. Hémodynamique. Interaction fluide-structure. IRM-4D

Résumé long

Les maladies cardiovasculaires sont la première cause de mortalité dans le monde, et les problèmes pluridisciplinaires posés par ces pathologies nécessitent une diversité, une transversalité et une complémentarité des méthodes de résolution de problèmes de mécanique. Cette étude se concentre sur l'aorte, plus précisément l'aorte thoracique, l'arc aortique en forme de canne d'où partent les artères qui alimentent le cerveau et les bras. L'une de ces maladies vasculaires consiste en une dissection aortique, une affection rare et grave caractérisée par l'irruption de sang à l'intérieur de la paroi de l'aorte. Une dissection aortique (DA) peut être rapidement mortelle car elle ne peut fournir suffisamment de sang au cœur ou l'aorte se rompt. Sa formation est un processus complexe impliquant à la fois une combinaison de facteurs génétiques et une mauvaise santé cardiovasculaire due à l'hypertension artérielle, à l'hypercholestérolémie, au tabagisme et à l'obésité comme facteurs de risque.

Il existe deux types d'interventions chirurgicales pour prévenir la rupture d'une dissection aortique : la chirurgie ouverte traditionnelle et la chirurgie endovasculaire. La chirurgie ouverte consiste à implanter une prothèse synthétique à l'endroit de la dissection et à retirer le tissu pathologique, en pratiquant ainsi une incision aortique primaire. La chirurgie endovasculaire consiste à insérer une endoprothèse à travers le fémur jusqu'à la dissection afin de recanaliser le flux sanguin par l'endoprothèse. Par rapport au traitement chirurgical classique, cette procédure peut réduire le risque de mortalité précoce et de parapésie et peut également réduire la durée du séjour à l'hôpital et les complications générales imposées par la chirurgie ouverte. Malgré tous les avantages de la technique endovasculaire, sa durabilité à long terme reste discutable en raison de complications qui ne sont pas encore totalement comprises. Ces complications comprennent les endofuites de type I, qui sont des fuites proximales ou distales au niveau des zones d'étanchéité et qui restent les complications les plus graves dues à un défaut d'adhérence de l'endoprothèse à la paroi aortique. La migration, qui est un autre type de complication possible, devient moins fréquente avec les nouvelles prothèses dotées de systèmes de fixation plus fiables. Par conséquent, il nous manque une compréhension de l'hémodynamique dans l'aorte en postopératoire. Il est également crucial de comprendre la mécanique du flux sanguin du patient dans les vaisseaux sanguins après la procédure endovasculaire.

Dans le contexte d'une population vieillissante, le traitement endovasculaire de la dissection aortique s'est considérablement développé ces dernières années, constituant une alternative à la chirurgie ouverte et représentant la seule option thérapeutique chez les patients présentant des comorbidités sévères et ne se prêtant pas à la chirurgie traditionnelle. En pratique, la décision de traitement endovasculaire de cette pathologie repose principalement sur le niveau de dissection, la tortuosité de l'artère iliaque et l'état de santé du patient. Le déploiement d'une endoprothèse dans une morphologie de dissection aortique complexe est difficile en raison de la courbure de l'arc qui génère des forces complexes sur l'endoprothèse. Cela peut entraîner des endofuites précoces pendant et après le déploiement. C'est pourquoi les essais cliniques ont constamment

montré l'importance de l'évaluation préopératoire de la morphologie aortique pour la réussite de la chirurgie endovasculaire de la dissection aortique.

Le traitement de la maladie est souvent difficile et empirique, il faut alors de nouveaux critères pour proposer une solution fiable pour la localisation et la supervision préopératoire précise de la libération du stent. Les techniques avancées de modélisation et de simulation des structures mécaniques des artères et du flux sanguin, associées à l'amélioration des techniques d'imagerie médicale, peuvent permettre de mieux comprendre le comportement de la paroi artérielle, mais aussi d'analyser et de prévoir l'ensemble de la procédure endovasculaire. L'intégration d'une modélisation précise et réaliste des interactions entre les outils et les tissus devient alors nécessaire pour proposer une solution personnalisée afin de choisir un outil de libération et un stent adapté. En outre, il est préférable d'observer l'évolution de la distribution des flux sanguins après l'opération pour comprendre l'hémodynamique du sang dans l'aorte. Cela permet de mieux prévenir les complications postopératoires.

- Résumé du 1er chapitre

Ce chapitre se concentre sur la description médicale de la pathologie associée à la dissection aortique et présente les avantages de la chirurgie endovasculaire par rapport à la chirurgie ouverte. Les complications après une chirurgie endovasculaire sont considérées d'un point de vue mécanique. Il met également en évidence le rôle très important de la simulation numérique dans les solutions chirurgicales, et les défis chirurgicaux. La partie concernée par cette étude couvre essentiellement l'ensemble de l'aorte, en particulier la crosse aortique et la dissection aortique thoracique. La décision d'effectuer un traitement endovasculaire de la dissection aortique est principalement basée sur les mesures à l'entrée de la dissection, la morphologie de la dissection aortique, la tortuosité des artères iliaques et l'état de santé du patient. La prise en charge de cette maladie est souvent délicate et empirique, et de nouveaux critères sont nécessaires pour proposer un protocole opératoire fiable pour le positionnement et le contrôle peropératoire précis de l'endoprothèse. Dans ce contexte, notre recherche est basée sur la caractérisation du comportement mécanique de la paroi aortique ainsi que sur les caractéristiques hémodynamiques spécifiques au patient, qui sont essentielles pour le processus d'aide au diagnostic et à la planification clinique. Le contexte médical décrit au chapitre 1 démontre la nécessité de nouvelles techniques de planification. Notre intérêt se porte sur la caractérisation de la pathologie de la dissection aortique et de ses caractéristiques mécaniques, qui sont essentielles pour le diagnostic et le processus de planification clinique. L'approche envisagée s'inscrit donc dans une moindre mesure dans le cadre des procédures médicales et chirurgicales assistées par ordinateur afin de proposer une solution opérationnelle pour la localisation précise et le contrôle préopératoire de la pose du stent mais surtout, la recherche et la proposition d'une recommandation personnalisée pour le choix d'un système de pose et d'un stent approprié. Si de nombreuses études biomécaniques ont été réalisées sur le traitement endovasculaire des anévrismes de l'aorte abdominale, il existe en revanche très peu d'études de ce type sur les dissections aortiques. Ainsi, une bonne compréhension de la pathologie de type B pour préparer l'opération devient importante. L'objectif de cette thèse est donc de définir les critères permettant de déterminer la procédure à suivre et d'améliorer le taux de succès de ce type d'opération.

- Résumé du 2ème chapitre

Tout d’abord, pour atteindre l’objectif de ce projet, nous devons comprendre le comportement mécanique de la paroi aortique et les caractéristiques hémodynamiques du patient pour diagnostiquer les caractéristiques pathologiques personnalisées de la dissection aortique et aider le chirurgien à planifier le traitement endovasculaire. La compréhension et la caractérisation mécanique du comportement des tissus biologiques sont d’une importance capitale pour comprendre l’hémodynamique et les maladies vasculaires. De nombreux chercheurs s’intéressent depuis plusieurs années aux simulations numériques de l’hémodynamique, permettant de corréler la localisation des dissections avec la surface des régions où le flux sanguin est perturbé.

Cependant, ces phénomènes de recirculation du flux sanguin n’expliquant pas totalement l’évolution des lésions artérielles, une grande attention a été portée aux propriétés mécaniques des artères. Bien que des tests *in vivo* basés sur des techniques d’échographie ou d’imagerie par résonance magnétique aient été développés, il n’existe toujours pas de méthode directe de mesure non invasive de la pression dans les grosses artères comme l’aorte. Les propriétés mécaniques ne peuvent donc pas être obtenues directement. Cette limitation a conduit les chercheurs à rechercher des moyens indirects pour obtenir une estimation de ces propriétés. La plupart des méthodes sont basées sur une estimation de la vitesse de propagation de l’onde de pression, généralement à partir de la mesure du flux sanguin par échographie ou IRM. Bien que ces méthodes non invasives tendent à remplacer les techniques invasives pour la mesure des propriétés mécaniques de la paroi artérielle, des méthodes *ex-vivo* sont encore nécessaires pour caractériser les artères de manière fiable sur le plan mécanique. Elles évitent également l’influence des erreurs inhérentes aux méthodes non invasives et sont encore largement utilisées dans la littérature. Pour simuler numériquement la procédure endovasculaire et parallèlement à la caractérisation des tissus biologiques, il est également important de connaître le comportement mécanique des outils chirurgicaux impliqués dans les opérations chirurgicales et en contact direct avec les artères. Les stents et les outils chirurgicaux commerciaux ont des dimensions fixes et existent en plusieurs tailles pour s’adapter au mieux à la morphologie de toutes les dissections aortiques. L’Agence française de sécurité sanitaire des produits de santé (AFSSAPS) exige des tests mécaniques statiques et dynamiques de ces dispositifs médicaux avant leur implantation sur le marché vasculaire afin de vérifier leur dimensionnement et leur résistance à long terme. Ils reproduisent la procédure d’implantation et les contraintes *in-vivo* correspondant à une durée de vie minimale de 10 ans. Par conséquent, nous devons tenir compte non seulement de la rhéologie du sang et de la paroi artérielle, mais aussi des caractéristiques mécaniques des outils et de la façon dont ils affectent la paroi artérielle tout au long du traitement endovasculaire.

Dans le deuxième chapitre, nous nous concentrons sur la caractérisation et le modèle mécaniques. Le flux sanguin joue un rôle essentiel dans le développement de cette pathologie. Ainsi, la rhéologie du sang et ses différents modèles sont abordés. De plus, la paroi artérielle, en particulier la partie intimale, est essentielle pour influencer les phénomènes hémodynamiques dans la situation physiologique. Ainsi, la compréhension du mécanisme de la paroi artérielle est également présentée dans ce chapitre. L’augmentation des pathologies vasculaires et l’innovation des techniques de traitement ont conduit à un réel besoin de comprendre à la fois le comportement des artères et la rhéologie du sang. Certains auteurs ont constaté que des contraintes pariétales faibles et oscillantes favorisent le développement d’anévrismes par leur impact sur la forme et la structure des cellules endothéliales.

Le rôle du flux sanguin dans le développement de ces pathologies ne peut être négligé. La rhéologie du sang avec ses différents comportements est considérée dans notre étude. Dans la littérature, les modèles de viscosité appliqués au sang sont une approche relativement large de son comportement. Grâce aux progrès de l'imagerie médicale et de l'IRM de flux, il est possible d'obtenir des informations importantes telles que les champs de vitesse et les pressions endovasculaires, en plus de l'imagerie de l'aorte thoracique obtenue par scanner. Avec ces données expérimentales obtenues in-vivo, il devient possible de valider les calculs en mécanique des fluides et le modèle rhéologique choisi pour l'écoulement sanguin. De plus, l'évolution des techniques d'imagerie médicale permet de fournir des informations plus précises sur le comportement artériel et d'améliorer les modèles, notamment pour caractériser le comportement de la paroi de la dissection aortique. Les méthodes de caractérisation des matériaux ont permis de mettre en évidence le caractère non linéaire, anisotrope et viscoélastique de la paroi aortique et le comportement hétérogène entre parois saines et malades. La technique de corrélation d'images utilisée dans ce travail de recherche permet de mesurer le champ de déformation de la paroi artérielle lors de tests de gonflement et de traction uniaxiale. Les modèles proposés par [Fung et al. \(1979\)](#), [Ogden \(1972\)](#), [Humphrey \(1995\)](#) sont complexes ou parfois trop éloignés de la réalité. Pour cette raison, nous avons choisi d'utiliser le modèle de Mooney-Rivlin, qui est approprié pour notre étude. Le modèle de Mooney-Rivlin choisi pour cette étude a ses limites, principalement en termes d'isotropie, alors que des modèles plus élaborés prenant en compte, par exemple, le caractère orthotrope existent déjà ([Holzapfel et al., 2000](#), [Gasser and Holzapfel, 2006](#)). Cependant, en raison de la grande variabilité entre les individus, selon leur âge, leur sexe, leurs conditions physiques, on peut considérer que le modèle de Mooney-Rivlin donne des résultats raisonnables dans le cadre de ce projet de recherche.

En outre, nous étudierons dans ce chapitre les propriétés mécaniques des outils chirurgicaux et des stents utilisés dans les traitements endovasculaires. La caractérisation des matériaux non biologiques, des composants des outils chirurgicaux et des dispositifs médicaux permet une meilleure compréhension du comportement mécanique de ces différentes pièces pour la modélisation complète de l'acte chirurgical. Le nitinol, un alliage à mémoire de forme, est un matériau complexe à caractériser mécaniquement en raison de sa variabilité importante selon l'expérimentation et l'utilisation. La modélisation numérique de ce matériau a été abordée dans de nombreux travaux ([Altnji et al., 2015](#), [Menut, 2017](#)) et les différences en termes de résultats mettent en évidence l'importance de la modélisation du stent, des propriétés du matériau et en particulier celles du textile sur la réponse mécanique des stents. Enfin, les guides chirurgicaux ont une géométrie et une composition complexes, adaptées à leur utilisation. Le travail de [Menut \(2017\)](#) pour les essais de flexion trois points est un complément aux essais de traction réalisés par [Mouktadiri \(2013\)](#). Pour les guides testés, la différence de rigidité dans la zone de transition est due à la géométrie interne du guide, dont le revêtement TFE (trafluoroéthylène) glisse sur l'âme en acier inoxydable du guide. L'influence du revêtement sur le guide en acier n'a pas été étudiée ici, car sa faible rigidité par rapport à l'acier a été négligée. Des études numériques validées par des résultats expérimentaux sur fantômes existent dans la littérature ([Wang et al., 2015](#)) et montrent l'importance d'une approche robuste pour simuler le comportement des guides en radiologie interventionnelle vasculaire. Cependant, en pratique clinique, le comportement du guide est affecté par le flux sanguin et la déformation périodique des vaisseaux, en particulier de l'aorte thoracique soumise à des déplacements et déformations plus importants que le reste du circuit artériel. La

simulation des comportements des instruments chirurgicaux dans un environnement dynamique est donc un problème qui concerne la rhéologie des parois vasculaires et du sang, que nous abordons dans le chapitre suivant.

- Résumé du 3ème chapitre

Dans le troisième chapitre, nous présentons le développement du modèle numérique pour la simulation de l'hémodynamique dans le logiciel libre OpenFOAM dans des modèles de dissection aortique, en tenant compte du comportement complexe du flux sanguin. Pour identifier correctement le circuit hémodynamique, il est nécessaire de développer un modèle 3D bio-fidèle suffisamment sophistiqué. Avec le logiciel OpenFOAM extend, qui s'appelle OFOM-Extend, nous réalisons un module de couplage fluide-structure. La prise en compte de la déformation du trajet aortique au cours de l'opération nous permettrait de préconiser un stent parfaitement adapté et personnalisé à des cas cliniques complexes. Nous développons une simulation de la montée des outils chirurgicaux dans une dissection aortique pathologique. Les progrès de l'imagerie médicale permettent la reconstruction virtuelle des organes d'un individu selon une procédure automatique, précise et rapide. De plus, ces mêmes outils permettront la mesure des champs de vitesse et rendront possible la validation in-vivo et non-intrusive des résultats obtenus par des simulations numériques. Ces avancées méthodologiques permettent de réaliser des simulations spécifiques aux patients afin de mieux comprendre l'impact de la morphologie de chacun d'entre eux.

Ces dernières années, les simulations numériques en mécanique des fluides ont été de plus en plus utilisées pour modéliser des géométries complexes afin de comprendre et de prévoir l'hémodynamique artérielle dans les pathologies cardiovasculaires. Ce travail numérique fait suite à des expériences sur des échantillons de tissus aortiques, qui caractérisent le comportement hyperélastique de la paroi artérielle. Avec les résultats concernant la modélisation du comportement de la structure artérielle, il était alors nécessaire de se concentrer sur la modélisation précise et réaliste du comportement du sang et de son interaction avec la paroi.

Dans cette étude, nous avons modélisé le comportement du sang avec deux modèles : Le fluide newtonien et le fluide de Carreau-Yasuda. Nous avons observé qu'il n'y a pas de différence significative lorsque nous comparons les caractéristiques de vitesse et de WSS. Nous avons donc supposé que le sang est un fluide newtonien. Les conditions aux limites de Windkessel implémentées dans les logiciels OpenFOAM et FOAM-Extend ont permis de prendre en compte la résistance du reste du circuit artériel, qui n'est pas modélisé, et la compliance des artères. Les paramètres arbitraires de ce modèle sont un point négatif pour son utilisation à grande échelle sans nécessairement obtenir des données de flux dynamiques, car les valeurs numériques doivent être recalibrées sur chaque patient. Actuellement, les conditions aux limites des sorties dans les modèles fluides sont soit des conditions sur les pressions, comme le modèle de Windkessel, soit des conditions sur les vitesses, donc sur la distribution des flux entre les troncs artériels. Cependant, ces conditions sur les vitesses de sortie conduisent souvent à des instabilités dans les calculs numériques. Les données issues de l'IRM 4D sont d'une importance primordiale dans la validation de la simulation hémodynamique. De plus, l'amélioration exponentielle des techniques d'imagerie médicale rapproche de plus en plus les cliniciens et les mécaniciens. Les données in-vivo telles que les flux en temps réel obtenus par les cliniciens sur les patients permettent des avancées significatives dans la modélisation numérique.

Cet aspect sera présentée dans le dernier chapitre.

L'aorte thoracique, qui comprend les parties de la dissection aortique, est une des artères (flap) qui se déforme le plus sous l'effet du pouls cardiaque, d'où la nécessité de simuler l'interaction entre le fluide et la structure pour se rapprocher des conditions physiologiques. Le couplage utilisant FOAM-Extend a été validé dans ce cas et nous avons observé clairement le mouvement du flap avec des parois déformables. En raison de l'incroyable complexité du couplage nécessaire pour simuler un tel phénomène, il est relativement difficile de le reproduire dans un modèle de difficulté AD à notre disposition. Nous avons donc débogué de nombreux paramètres dans le schéma numérique pour assurer sa convergence. Ainsi, les techniques numériques offrent une alternative potentielle pour analyser l'hémodynamique dans la DA et inclure le mouvement de la paroi dans la simulation. Cela mérite une étude plus approfondie pour voir si le travail supplémentaire nécessaire pour inclure le mouvement de la paroi dans les modèles de DA est justifié dans le cadre d'une application clinique.

En parallèle des simulations d'interaction fluide-structure et en prévision de la modélisation complète de la procédure chirurgicale, nous avons pu reprendre le travail de [Mouktadiri \(2013\)](#) et [Menut \(2017\)](#) sur l'insertion des outils chirurgicaux dans l'aorte avec une pathologie de DA et l'adapter à l'aorte entière. Ce travail présente une difficulté supplémentaire induite par la flexion des outils au niveau des troncs supra-aortiques. Les simulations numériques de cette étude ont été réalisées avec une hypothèse forte de comportement élastique pour la paroi vasculaire.

- Résumé du 4ème chapitre

Le dernier chapitre valide le modèle CFD bio-fidèle avec les données de l'IRM 4D, dont l'accord est mis en évidence. Cette recherche décrit une méthode permettant d'effectuer des simulations de DA spécifiques aux patients en utilisant les données anatomiques et d'écoulement les plus importantes disponibles *in vivo*. Dans cette partie, le modèle de paroi rigide utilisé pour les simulations CFD donne les premières estimations de flux par rapport à l'imagerie dynamique, en imposant des conditions limites physiologiquement correctes et individualisées. Les validations par rapport aux mesures *in vivo* révèlent un haut degré de concordance en général. Les résultats de cette étude devraient contribuer à une meilleure compréhension des schémas d'écoulement et des conditions hémodynamiques dans les dissections aortiques de type B, avec l'objectif à long terme d'identifier les facteurs biomécaniques qui peuvent être utilisés pour prédire la probabilité de dégénérescence et de rupture anévrysmale ultérieure chez ces patients en préopératoire et en postopératoire. Comme l'indiquent des recherches récentes ([Thubrikar et al., 1999](#), [Xiang et al., 2011](#), [Chiu and Chien, 2011](#), [Meng et al., 2014](#)), les marqueurs de la dynamique des fluides tels que les caractéristiques du WSS et les pressions FL & TL ont un impact significatif sur la progression à long terme de la DA. Une planification clinique éclairée ne peut pas reposer uniquement sur des données géométriques. Elle doit également tenir compte de l'environnement hémodynamique pathologique et compliqué qui caractérise les cas complexes de DA. On ne saurait trop insister sur l'importance d'une telle stratégie synergique pour la recherche sur la DA et son application clinique. Assurer la validité et l'exactitude des simulations est une étape essentielle du transfert de ces méthodes vers la clinique. Les méthodes expérimentales créées dans cette étude servent de référence pour valider les résultats générés *in silico*. Une fois validés, les modèles CFD peuvent être utilisés pour prédire avec précision

les indicateurs hémodynamiques tels que le WSS qui sont difficiles à mesurer expérimentalement et impossibles à évaluer *in vivo*. En outre, les modèles *in silico* peuvent simuler diverses situations interventionnelles (par exemple, *Chapitre 3.8 Modélisation de la montée des outils chirurgicaux*). Et une nouvelle méthode individualisée a été développée, intégrant des outils expérimentaux et numériques guidés par l'imagerie clinique. Les deux modèles *in vitro* (Moravia, 2021) et *in silico* ont incorporé une géométrie de DA anatomiquement précise, un flux pulsatile et des BC dynamiques. Les deux modèles comportaient un haut degré d'intégration des informations à de nombreux niveaux et étaient influencés par les données cliniques. Les modèles de PIV Moravia (2021) expérimental comportaient un flux pulsatile contrôlé par ordinateur, un modèle d'AD spécifique au patient et les caractéristiques correspondantes du flux sanguin (modèle de Carreau-Yasuda). Cette étude montre comment les techniques *in vitro* et *in silico* peuvent être créées de concert pour recréer avec précision l'hémodynamique spécifique au patient de cas compliqués de DA, offrant ainsi un nouveau paradigme pour le traitement de la DA ou d'autres maladies vasculaires. En outre, l'expérience de PIV vise à fournir un cadre robuste pour la réalisation d'études hémodynamiques expérimentales et numériques précises de la pathologie de la DA à l'aide de données cliniques non invasives et d'investigations comme outil d'amélioration des résultats cliniques et sont souvent validées par rapport à des données expérimentales *in vitro*.

- Conclusion

Le développement de l'imagerie médicale et l'acquisition de données géométriques du système cardiovasculaire d'un patient constituent une évolution significative de la simulation numérique. L'avantage des simulations multi-physiques de la pose d'un stent avec déformation de la paroi artérielle et écoulement hémodynamique est un domaine de recherche appliquée ayant un réel impact pour la communauté clinique. Bien qu'il y ait eu de nombreuses études biomécaniques sur le traitement des dissections aortiques par technique endovasculaire, il y a encore peu d'études consacrées aux dissections aortiques, en particulier celles de l'écoulement en vrai et faux chanel. Les simulations numériques pourront alors identifier les paramètres biomécaniques responsables d'éventuels échecs du traitement endovasculaire et apporter des éléments d'analyse pour améliorer les stents utilisés, tant au niveau de la durée du stent lui-même que du traitement chirurgical. Cette thèse avait pour but de modéliser la procédure endovasculaire complète (Figure 1) pour la DA afin de comprendre l'origine de ces complications et ainsi proposer de nouveaux critères pour une solution opérationnelle fiable pour une localisation et un contrôle précis de la pose de stent-graft. Cependant, dans la pratique clinique, le comportement des outils chirurgicaux et le succès de la pose de l'endoprothèse sont affectés par le flux sanguin et la déformation périodique du vaisseau, en particulier, l'aorte thoracique soumise à des déplacements et des déformations plus critiques que le reste du circuit artériel. Par conséquent, la simulation numérique de l'hémodynamique dans la DA et le comportement des instruments chirurgicaux dans un environnement dynamique de la DA sont des recherches qui concernent à la fois la rhéologie des artères et du sang.

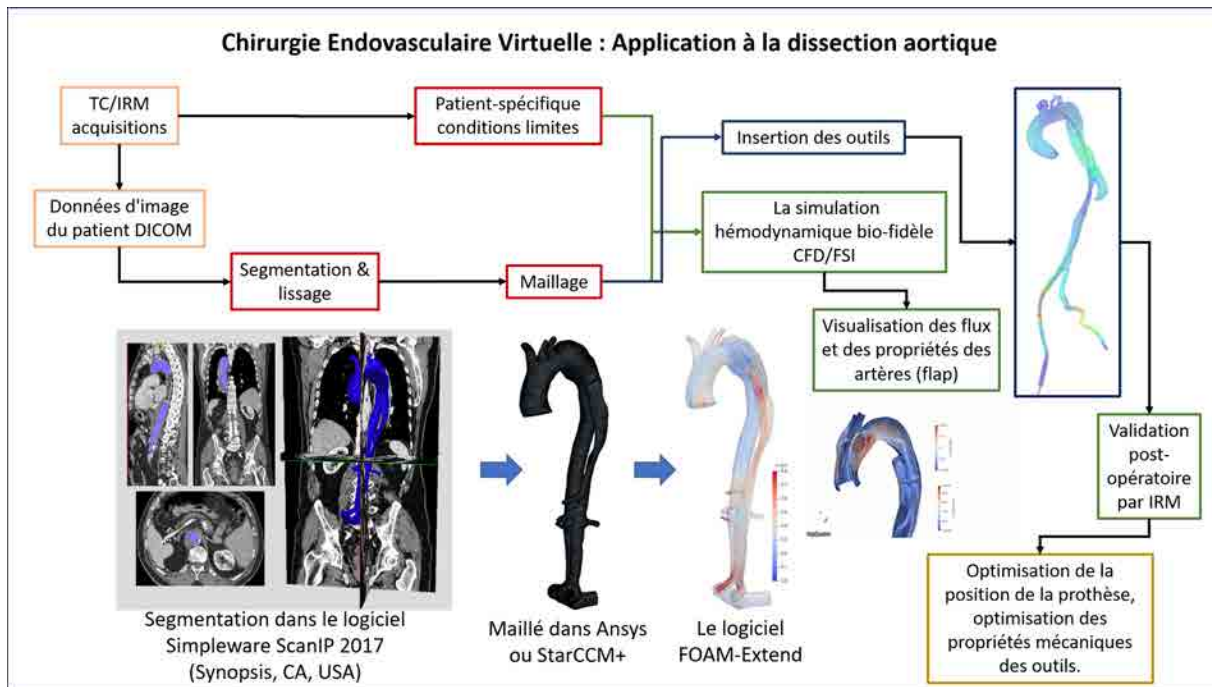


Figure 1: La procédure de chirurgie endovasculaire virtuelle : application à la dissection aortique

Contents

Abstract	8
List of Figures	22
List of Tables	29
General introduction	30
1 Clinical context and targets	33
1.1 Cardiovascular flow system	34
1.2 Vascular pathology	37
1.3 Aorta	37
1.3.1 Global location of the aorta	37
1.3.2 The different parts of the aorta	38
1.4 Aortic dissection(AD) and pathologies	39
1.4.1 Definition	39
1.4.2 Causes	40
1.4.3 Epidemiology and type of AD	40
1.4.4 The complication of AD	43
1.5 Aortic repair surgeries for AD	43
1.6 Scientific position of research	46
1.6.1 Diagnosis of AD	46
1.6.2 The operating scenario	47
1.6.3 Possible complications with endovascular operation	48
1.6.4 Improvement of diagnostic methods from a mechanical point of view	48
1.7 Conclusions and strategies	49
2 Mechanical models and characterization	51
2.1 Introduction	53
2.2 Blood rheology	53
2.2.1 Blood function and composition	53
2.2.2 Blood rheology	55
2.2.2.1 Rheology and hemorheology	55
2.2.2.2 Plasma viscosity	57
2.2.2.3 Red blood cells: aggregation, dispersion and deformability	57
2.2.2.4 Rheological properties of blood	59
2.2.3 Hemodynamical flow	60
2.2.4 Mathematical models	64
2.2.5 Physical principles	65

2.2.5.1	Blood flow simplified models	67
2.3	Rheology of the vascular wall	67
2.3.1	Constitution of the arterial wall	67
2.3.2	Mechanical properties of arteries	73
2.3.3	Different mechanical behavior models	75
2.3.3.1	Isotropic hyperelastic models	75
2.3.3.2	Anisotropic hyperelastic models	77
2.3.4	Experimental tests on arteries	79
2.3.4.1	Pressurization tests	79
2.3.4.2	Uniaxial traction test	80
2.3.4.3	Biaxial traction test	82
2.3.4.4	Aortic expansion test	83
2.3.4.5	The indentation method	85
2.4	Mechanical of endoprotheses and tools	86
2.4.1	The endoprotheses	87
2.4.2	The surgical guides	88
2.4.2.1	Mechanical properties of the guides	89
2.4.3	The catheters	90
2.5	Conclusions and strategies	91
3	Basic Equations and numerical simulation	93
3.1	Introduction	95
3.2	Introduction of fluid mechanics	96
3.2.1	Mathematical Modeling	97
3.3	Introduction of the CFD	98
3.3.1	The OpenFOAM Open-Source software	99
3.4	Numerical patient-specific geometry of an AD	100
3.4.1	Acquisition methods	100
3.4.2	Fluxes measured by 2D and 4D PC-MRI	102
3.4.3	Segmentation from medical imaging	103
3.4.4	Fluid domain meshing	104
3.4.5	Boundary conditions	108
3.4.5.1	Conditions at the entry	108
3.4.5.2	Conditions at the exit	110
3.4.5.2.1	Mathematical modeling of the cardiovascular system	110
3.4.5.2.2	Windkessel	111
3.4.5.2.3	Implementation of the 3-element Windkessel model	115
3.4.5.2.4	Windkessel parameters	116
3.5	Data analysis	117
3.6	Bio-faithful model with rigid walls	118
3.6.1	Newtonian fluid	118
3.6.2	Comparison with the Carreau-Yasuda model	123
3.7	Fluid-structure coupling	129
3.7.1	Necessity of a fluid-structure coupling	129

3.7.2	Fluid-structure coupling with FOAM-Extend	130
3.7.2.1	Discretization	133
3.7.3	FSI model of AD patient-specific	134
3.7.3.1	Mesh of FSI model	134
3.7.3.2	Boundary conditions	135
3.7.3.3	Results	137
3.7.3.3.1	Comparison between CFD model and FSI model	137
3.7.3.3.2	Influence of the d'Younge module	140
3.7.3.4	Discussion and conclusion	142
3.8	Modeling for the rise of surgical tools	143
3.8.1	Numerical models	143
3.8.2	Boundary conditions	146
3.8.2.1	Aortic environment	146
3.8.2.2	contact	147
3.8.3	Results of tool insertion	148
3.8.3.1	Results of guidewire insertion	148
3.8.3.2	Results of catheter insertion	150
3.8.4	Discussion	151
3.9	Conclusion	152
4	Validation	153
4.1	Introduction	154
4.2	AD case study	155
4.2.1	Data MRI for AD2 & AD3	156
4.2.1.1	AD2	156
4.2.1.2	AD3	160
4.3	Results & Comparison with MRI	163
4.3.1	AD2	163
4.3.2	AD3	165
4.3.2.1	Preoperative	165
4.3.2.2	Postoperative	166
4.3.2.3	Preoperative & Postoperative	167
4.3.3	Discussion	175
4.4	Comparison with <i>in vitro</i>	175
4.4.1	3D printed aorta model	175
4.4.2	PIV	176
4.4.3	AD1	180
4.4.4	AD2	182
4.4.5	Discussion	186
4.5	Discussion and conclusion	187
	General conclusion	189
	Perspectives	192

A	Poiseuille flow adapted to a non-circular face	194
A.1	Methodology	194
A.2	Matlab [®] Code	195
B	Implementation of the model with rigid walls in OpenFOAM	198
C	Implementation of the model with FSI in FOAM-Extend	211
C.1	Fluid domain	211
C.2	Solid domain	221
	Bibliography	234

List of Figures

1	La procédure de chirurgie endovasculaire virtuelle : application à la dissection aortique	17
1.1	Human aorta antomy	35
1.2	Pressures and volume debits are representative of the human cardiac cycle: the dotted line is the pressure measured in the aorta (based on the work of Themes (2016)) . .	36
1.3	Location of the aorta in the body (image : Dr Claude VAISLIC [©])	38
1.4	Aortic arch (image : Dr Claude VAISLIC [©])	38
1.5	Diagram of an aortic dissection formation (image: J.Heuser [©])	40
1.6	Aortic dissection with examples entry and exit sites	41
1.7	Classification of aortic dissections, according to DeBakey and Stanford Classification(image : Gawinecka et al. (2017))	42
1.8	Diagram of a classic surgical procedure: a synthetic prosthesis is implanted in place of the dissection:(A)Interpretation of an acute type A aortic dissection-the dotted line indicates the dissection;(B)After the entire underside of the aortic arch is removed, the head vessels are connected to the remaining aorta through a thin peninsula of tissue;(C)The graft is matched to the aorta and sutured with a fine needle to reconstruct the distal anastomosis;(D)Intraoperative photograph show the distal anastomosis configuration;(E)Intraoperative photograph of the completed transverse arch peninsula style repair. (Image: Chiu and Miller (2016)).	44
1.9	Diagram of an endovascular procedure: the stent is gradually deployed in a descending aortic dissection:(A) The presence of the IVUS(intra-vascular ultrasound) catheter in the true lumen;(B) Primary intimal rupture over the descending aorta;(C)Stent graft covering primary intimal tear.(Image : Uchida and Sadahiro (2018))	45
1.10	CT images of 51 year-old male diagnosed with subacute uncomplicated type B aortic dissection,(A)Pre-operation;(B)2 months after Endovascular treatment;(C) CT images demonstrated favorable remodeling of the dissected descending aorta after one year of intervention. (Image: Uchida and Sadahiro (2018))	45
1.11	Differentiate true lumens and false lumens	47
1.12	The delivery system is advanced into the aortic arch.(Image: adapted from Leshnower and Chen (2018))	47
1.13	Brand Gore [©] : flexible endoprosthesis adapted for endovascular surgery of the thoracic aorta	49
2.1	Blood composition	54
2.2	(a) Scanning electron microscopy of red blood cells ×1800 (b) The average dimensions of a red blood cell (c) In the small vessels, the red blood cells form aggregates called "Rouleaux" ×250 (Mescher, 2013)	55

2.3	(1) Shear stress versus shear rate diagram for Newtonian (solid line) and non-Newtonian fluids in a simple shear flow. The dotted line represents a non-Newtonian fluid with a yield stress. The top dashed line indicates shear-thinning fluid without yield stress. The bottom dashed line represents shear-thickening fluid without yield stress. (Bao et al., 2017) (2) Viscosity-shear rate relationships for Newtonian (solid line) and non-Newtonian (dashed line) fluids	56
2.4	Relationship between viscosity and hematocrit values of blood at four varying shear rates at 37°C. (Chien et al., 1966)	58
2.5	Variations of relative viscosity as a function of shear rate for three hematocrit 45% suspensions: Normal RBCs are in plasma (NP), albumin-Ringer RBCs are in albumin (NA), and hardened RBCs are in albumin-Ringer (HA) ((Chien, 1970))	59
2.6	Rheological behavior of blood. (a) Stress as a function of the shear rate of plasma and blood (b) Relationship between blood viscosity and shear rate (Menut, 2017) . .	60
2.7	Hypothesis on the role of wall shear stress (WSS) in atherosclerotic plaque initiation and growth. Blood flow velocity (arrows) in a tangential view of an artery showing endothelial cells and intima. (a) Low shear stress induces endothelial wall dysfunction by increasing its permeability (b) Arterial remodeling and intimal thickening affect the tolerance of WSS (c) Advanced stenosis progression (Pedersen et al., 1999) . . .	61
2.8	3D flow analysis: (A) detection of the systolic peak, (B, C, D) manual segmentation at peak systolic and calculation of the centerline, (E) an example of 3D flow results obtained in the thoracic aorta (Sigovan et al., 2015)	62
2.9	Estimation of pulse wave velocity in a patient with significant elongation and rotation of the descending thoracic aorta (Markl et al., 2010)	62
2.10	(Left) CT volume render of the thoracic aorta demonstrating the dissection septum, (Centre) 2D PC-MRI data at the aortic inflow and several locations across the aorta, (Right) 4D PC-MRI data (Dillon-Murphy et al., 2016)	63
2.11	Comparison between CFD and 4D PC-MRI streamlines at peak systole and mid diastole. Additionally, CT imaging data (left) at two sites are presented to demonstrate probable secondary tears that were not seen on the 4D PC-MRI data (Dillon-Murphy et al., 2016)	63
2.12	Velocity profiles for different values of the Womersley number (Hellmuth, 2017) . . .	64
2.13	Microscopy in polarized light of sections of (a) intima, (b) media, (c) adventitia of a thoracic aorta (horizontal and vertical directions of the image represent the orthoradial and axial directions of the artery, respectively) (Schriebl et al., 2012) . .	69
2.14	Schematic of the arterial wall structure with its three layers: intima (I), media (M) and adventitia (A) (Holzapfel et al., 2000)	70
2.15	A comparison of the 3 layers of the largest artery and vein: the aorta (a) and the vena cava (b). (I) Intima (IEL) Internal elastic lamina (M) Media (EF) Elastic fibers (A) Adventitia (V) Small vessels. (Mescher, 2013).	71
2.16	Histology of the normal aorta of a child (A) and an elderly adult (B). With aging, elastic fibers fragment, collagen becomes more apparent, and smooth muscle cells decrease (magnification x 450) (O'Rourke et al., 1998)	72

2.17 (a) A normal and dissected aorta, as well as the location of calcifications, are shown. (b) CT of patients with aortic dissection and observed the calcification at the outer edge of false lumen (de Jong et al., 2014).	72
2.18 Stress-strain plots for a human vena cava sample. The circles represent loading, and the squares represent unloading (Meyers and Chawla, 2008)	74
2.19 The effects of residual stresses in the longitudinal and orthoradial directions of a healthy aorta (Holzapfel et al., 2007)	75
2.20 Preferred directions of collagen fibers introduced in anisotropic models (a) undeformed configuration (b) deformed configuration (Holzapfel and Ogden, 2003)	78
2.21 (Left) Image of the thoracic aorta section used for testing (Middle) Green-Lagrange strains in the initial configuration (Right) Cauchy tensor stresses in the deformed configuration (Avril et al., 2010).	80
2.22 (Left) Stress versus relative elongation in the longitudinal direction of a healthy aorta (Middle & Right) Stress versus relative elongation in the longitudinal and orthoradial directions of a pathological aorta with AAA (Raghavan et al., 1996).	81
2.23 (Left) Five biaxial tensile stress-stretch curves for a porcine aorta, with the fitted elastic model(dashed line) (Right) Uniaxial and biaxial tensile stress-stretch curves for a human femoral artery (Prendergast et al., 2003).	82
2.24 (A) Sample cleaned (B) The inside of the thoracic arch reveals no signs of calcification for this fresh sample (C) Installation of the speckled sample on its support (D) Aorta immersed in water before the experiment (E) Rupture on the aortic isthmus (Menut et al., 2015)	83
2.25 Results of swelling tests on a human aortic arch. Experimental data and fitting curves for a 5-parameter Mooney-Rivlin polynomial model (adapted from Menut (2017)) . .	85
2.26 Mapping of the elastic modulus as a function of the degree of calcification for the different layers of the aorta (adapted from Mouktadiri (2013)). The orders of magnitude of arterial wall stiffness vary from a few kPa for healthy areas to a few MPa for the calcified areas	86
2.27 2 Nitinol thoracic endoprostheses: Gore & Medtronic	87
2.28 Comparison of cyclic tensile test curves (1 cycle represented) for Gore and Medtronic Nitinol stents (Menut, 2017)	88
2.29 Illustration of a surgical guide with a flexible point preventing damage to the arterial wall (Image: Merit Medical [©])	89
2.30 Guidewire	89
2.31 Evolution of stiffness along the transition zone of the Cook and Amplatz guides (Menut, 2017)	90
2.32 (A-B) Catheter with an undeployed stent inside (images from Medtronic [©]) (C) Traction testing of the stent-containing portion speckled in white on a black background (Mouktadiri, 2013)	91
3.1 General steps for CFD simulation	99
3.2 Graph shown that with the number of dimensions and scan duration grows, the complexity and information richness of flow data increases (Markl et al., 2016) . . .	101

3.3	(Left) Comparison of 2D and 4D flow rates calculated in-vivo through 2 slices located at the ascending and descending aorta. Both methods show very similar results that will be used for numerical simulations; (Right) Flowlines based on 4D MRI results(adapted from (Menut, 2017)).	102
3.4	Segmentation process based on medical imaging with commercial software Simpleware ScanIP 2017 (Synopsis, CA, USA). The 3D volume is chosen on the 3D space parts.	104
3.5	Comparison of the number of adjacent meshes for a tetrahedral (left) and polyhedral (right) (image from Balafas (2014))	105
3.6	Polyhedral mesh generated with the commercial software Star-CCM+ [©] (338265 cells)	106
3.7	Tetrahedral mesh generated with the commercial software ANSYS [©] (1575416 cells)	107
3.8	Centers of the entrance surface meshes of the ascending aorta represented in 2D . .	109
3.9	(Left) Velocity profile for a Poiseuille flow adapted to a non-circular surface at $t = 0s$; (Middle) Velocity profile for a Poiseuille flow adapted to a non-circular surface at systolic; (Right) Curves of imposed velocity profiles at the entrance of the ascending aorta at different times of the cardiac cycle.	110
3.10	Windkessel concept. The large arteries are associated with the air chamber (Windkessel). The combination of compliance, associated with aortic valves and peripheral resistance, leads to a rather constant peripheral flow (Westerhof et al., 2009).	112
3.11	The two-element Windkessel model is analogous to the flow in an arterial system, an electrical circuit formed by a current generator, a resistor R , and a capacitor C connected in parallel.	112
3.12	The three-element Windkessel model introduces an additional resistor Z_C connected in series with the two-element Windkessel model.	113
3.13	The four-element Windkessel model introduces an inductance L modeling the low-frequency blood inertia in parallel with the impedance Z_C connected in series with the two-element Windkessel model.	113
3.14	An example of measured impedance at the aortic inlet and impedances predicted by the two-element, three-element and four-element Windkessel model (Westerhof et al., 2009)	114
3.15	The three-element Windkessel model with the hydraulic analogy. The equation (3.7) is associated with this circuit model.	116
3.16	Diagram of the configuration of the numerical model with rigid walls on OpenFOAM	119
3.17	Convergence of the pressure measured with OpenFOAM over 8 cardiac cycles on the input and each output of the aorta CFD Newtonian model	120
3.18	Flow rates measured with OpenFOAM over 8 cardiac cycles on the input and each output of the aorta CFD Newtonian model	121
3.19	(Left) Velocity profiles on several sections along the aorta; (Right) Streamlines with velocity in AD	122
3.20	Velocity profiles on several sections along the aorta for the Newtonian and Carreau-Yasuda models	124
3.21	Velocity profiles with streamline along the aorta for the Newtonian and Carreau-Yasuda models at peak systole and the diastolic period	125

3.22	Flow rate on section C for the Newtonian and Carreau-Yasuda models with a cardiac cycle	125
3.23	Pressure on section C (TL & FL section) for the Newtonian and Carreau-Yasuda models with a cardiac cycle	126
3.24	Wall shear stress (WSS) at peak of systole ($t=0.12$ s) for the Newtonian and Carreau-Yasuda models	126
3.25	WSS during diastole ($t=0.4$ s) for the Newtonian and Carreau-Yasuda models	127
3.26	Comparison of TWASS bewteen the Newtonian and Carreau-Yasuda models	127
3.27	Comparison of OSI bewteen the Newtonian and Carreau-Yasuda models	128
3.28	Comparison of RRT bewteen the Newtonian and Carreau-Yasuda models	128
3.29	Schematic of monolithic and partitioned approaches for FSI	132
3.30	Solving process for a fluid-structure interaction problem with weak coupling and strong coupling using the partitioned approach.	133
3.31	Simplified scheme of (Left) the IQN-ILS technique, and (Right) Aitken relaxation (adapted from (Degroote et al., 2009))	134
3.32	tetrahedral mesh generated with the commercial software ANSYS®	135
3.33	Comparison of velocity profiles on several sections along the aorta between CFD and FSI models during the cardiac cycle	138
3.34	Comparison of the streamline during systole and diastole between CFD and FSI models	138
3.35	Comparison of the pressure at peak systole between CFD and FSI models on the place of Section C	139
3.36	Comparison of the WSS at peak systole between CFD and FSI models	140
3.37	Displacement of the artery at various time instances with Young's modulus = 300 MPa	141
3.38	Displacement of IF region with Young's modulus = 300 MPa at peak systole	141
3.39	Displacement of IF region with various Young's modulus at peak systole	142
3.40	A: Segmentation process with software Simpleware ScanIP and views in the three sections of space; B: The model generated after segmentation; C: View of the aortic dissection	144
3.41	Modeling of the rigid guidewire whose elastic mechanical properties vary according to different transition zones (Menut, 2017)	145
3.42	(Left)Modeling of the introducer for the navigation of the release system; (Right) Mesh of introducer	145
3.43	Modeling of the catheter (stent holder) whose elastic mechanical properties are derived from results of Mouktadiri (2013)	146
3.44	(Left) Aortic model in its environment; (Right) Complete modeling of the model of the rise of surgical tools.	147
3.45	Penetration method (Menut, 2017)	148
3.46	Von Mises stresses observed on the Amplatz guide during rise in the thoracic aorta at different times	149
3.47	Displacement of aorta observed on the Amplatz guide during rise in the thoracic aorta at same times as above	149
3.48	Von Mises stresses observed on the catheter during rise in the thoracic aorta at different times	150

3.49	Displacement of aorta observed on the catheter during rise in the thoracic aorta at same times as above	151
4.1	Three bio-faithful AD cases	155
4.2	Three bio-faithful AD cases	156
4.3	A section of the ascending aorta is selected so that velocity vectors can be measured by dynamic imaging. An average flow over the area can be generated to fulfill the input condition of the model.	157
4.4	Flow rates measured by 2D PC-MRI on a patient with AD2 in 5 planes positioned by the operator at the level of the ascending and descending aorta and supra-aortic trunks.	158
4.5	Polyhedral mesh generated with the commercial software Star-CCM+ [©] (1043286 cells)	159
4.6	4D-MRI flow data with helical flow	160
4.7	Reconstruction of the bio-faithful model with MRI data, AD3 preoperative & post-operative	161
4.8	Polyhedral mesh generated with the commercial software Star-CCM+ [©] (1438364 cells)	162
4.9	Polyhedral mesh generated with the commercial software Star-CCM+ [©] (1642729 cells)	162
4.10	Streamline of the velocity profile at several periods during the cardiac cycle	164
4.11	Velocity profiles on several sections along the aorta and compared with 4D-MRI	164
4.12	Comparison of MRI data and CFD simulation of preoperative for flow rates	165
4.13	Comparison the flow streamline between 4D-MRI data and CFD simulation of pre-operative	166
4.14	Velocity profiles on several sections along the aorta and compared with 4D-MRI	166
4.15	Comparison of MRI data and CFD simulation of postoperative for flow rates	167
4.16	Flow streamline comparison between 4D-MRI data and postoperative CFD model	167
4.17	Fluid reflow from FL to TL for the postoperative	168
4.18	Flow rate compared between the preoperative and postoperative CFD model	169
4.19	Comparison of flow rates in 4 branches arteries on descending thoracic in preoperative and postoperative CFD models	169
4.20	Pressure compared between the preoperative and postoperative CFD model on each boundary	170
4.21	TAWSS distributions for preoperative and postoperative	171
4.22	OSI distributions for preoperative and postoperative	172
4.23	RRT distributions for preoperative and postoperative	173
4.24	LNH distributions for preoperative and postoperative	174
4.25	3D printing to print a complete model of the aorta	176
4.26	Detail of 3D printing model of AD1 & AD2	176
4.27	PIV experimental setup in AD configuration ((Moravia, 2021))	177
4.28	Boundary conditions at inlet (ascending thoracic aorta) and the major outlet (descending thoracic aorta)	178
4.29	Schematic illustration of the experimental platform and the corresponding CFD numerical simulation properties	179
4.30	Comparison of PIV and numerical simulation velocity results for AD1 at four instants	181
4.31	3D observation on velocity vectors of CFD model for AD1 at four instants	182

4.32	Comparison of PIV and numerical simulation velocity results for AD2 at three instants	184
4.33	3D observation on velocity vectors of CFD model for AD1 at four instants	186
4.34	The procedure of computer aided surgery: application to AD	191
4.35	Progressive and realistic deployment of a stent (adapted from Altnji et al. (2015))	193
A.1	A diagram illustrating how to transfer a radial velocity profile onto the nodes of a 2D boundary surface (Mynard and Nithiarasu, 2008)	194

List of Tables

1.1	Differentiation between true lumen and false lumen in AD (Erbel et al., 2001) . . .	41
1.2	Difference between Type A and Type B (Rizzoli et al., 1997)	43
2.1	The Non-Newtonian fluid models are often used to describe the rheology of blood. .	65
2.2	Average dimensions of the vascular tree (according to O'Rourke et al. (1998))	66
2.3	Principal strain energy density functions for isotropic incompressible hyperelastic models (Holzapfel, 2000)	77
2.4	Principal strain energy density functions for incompressible anisotropic hyperelastic models	79
2.5	Coefficients of the 5-parameter hyperelastic Mooney-Rivlin law (equation 2.1) were chosen for the model associated with swelling tests on the human aortic arch.	85
2.6	Table comparing the calculated elasticity modules between Gore & Medtronic (adapted from Menut (2017))	88
3.1	Mesh sensitivity study based on the maximum value of shear stress at peak systole. .	108
3.2	Hydraulic-electrical analogy for 0D models	111
3.3	Windkessel model parameters applied to fluid model outputs(Menut, 2017)	117
3.4	Reynolds number	123
3.5	Numerical values from Razavi et al. (2011) for the Carreau-Yasuda model.	124
3.6	The maximum TAWSS and RRT comparison bewteen the Newtonian and Carreau-Yasuda models	129
3.7	Pressure compared between FSI and CFD model on the place of Section C (entry site of dissection)	139
3.8	Comparison of maximum values of WSS for several time periods between FSI and CFD model	140
3.9	Modeling of the Ampltz guidewire whose elastic mechanical properties vary according to different transition zones (adapted from Menut (2017))	145
4.1	The cardiac cycle of AD1, AD2 and AD3	156
4.2	Windkessel model parameters applied to AD2 fluid model outputs and adjusted with MRI data	160
4.3	Windkessel model parameters applied to AD3 fluid model outputs and adjusted with MRI data	163
4.4	The cardiac cycle of AD3 (preoperative & postoperative)	163
4.5	Numerical values for the Carreau-Yasuda model corresponding to experimental fluid properties	179
4.6	In all AD models, PIV synchronization parameters are used to photograph 12 cycle instants during the cardiac cycle	180

General introduction

Cardiovascular diseases are the leading cause of death in the world, and the multi-disciplinary problems posed by these pathologies require a diversity, transversality and complementarity of methods. This study focuses on the aorta, specifically the thoracic aorta, the cane-shaped aortic arch from which arteries supply the brain and arms originate. One of these vascular diseases consists in forming an aortic dissection, a rare and severe condition characterized by the irruption of blood inside the wall of the aorta. After aortic dissection, it can be deadly quickly because it cannot provide enough blood to the heart or the aorta ruptures. Their formation is a complex process involving both a combination of genetic factors and poor cardiovascular health due to high blood pressure, high cholesterol, smoking, and obesity as risk factors.

There are two types of surgeries to prevent the rupture of aortic dissection: traditional open surgery and endovascular surgery. Open surgery consists in implanting a synthetic prosthesis at the place of the dissection and removing the pathological tissue, thus making a primary aortic incision. Endovascular surgery consists in inserting a stent graft through the femur to the dissection in order to recanalize the blood flow by the stent. Compared to the classical surgery treatment, this procedure can reduce the risk of early mortality and paraplegia and also can reduce the duration of the stay in hospital and the general complications imposed by open surgery. Despite all the advantages of the endovascular technique, its long-term durability remains questionable due to complications that are not yet fully understood. These complications include type I endoleaks, which are proximal or distal leakage at the level of the sealing zones and remain the most serious complications due to a failure of the stent graft to adhere to the aortic wall. Migration, which is another type of possible complication, is becoming less frequent with newer prostheses with more reliable fixation systems. Therefore, we lack an understanding of hemodynamics in the aorta with postoperative. It is also crucial to figure out patient's blood flow mechanics through the blood vessels after the endovascular procedure.

However, in the context of an aging population, the endovascular treatment for aortic dissection has grown considerably in recent years, constituting an alternative to open surgery and representing the only therapeutic option in patients with severe comorbidities who are not suitable for traditional surgery.

In practical terms, the endovascular treatment decision for this pathology is based primarily on the level of dissection, iliac artery tortuosity, and patient health status. Stent deployment in complex aortic dissection morphology is difficult because of the curvature of the arch generating complex forces on the stent graft. It may lead to precocious endoleaks during and after deployment. Therefore, clinical trials have consistently shown the importance of preoperative assessment of aortic morphology for successful endovascular surgery of aortic dissection.

The treatment of the disease is often difficult and empirical, then require new criteria to propose a reliable solution for the localization and the precise pre-operative supervision of the release

of the stent. The advanced techniques of modeling and simulation of the arteries' mechanical structures and blood flow, merged with the improvement of medical imaging techniques, which can allow to better understand the behavior of the arterial wall and also to analyze and predict the whole endovascular procedure. The integration of precise and realistic modeling of the interactions between the tools and the tissues becomes then necessary for the proposal of a personalized solution to choose an adapted release tool and stent. In addition, it is better to the observation of the phenomenon of blood after operation to understand the hemodynamic of blood in the aorta. This can better prevent postoperative complications.

In this context, our research is based on the characterization of the mechanical behavior of the aortic wall as well as on the patient-specific hemodynamic characteristics, which are essential for the diagnostic and clinical planning support process. Therefore, the approach considered in the research project is first to identify the mechanical behavior of the aortic dissection and then to identify the behavior of the blood flow to perform a patient-specific numerical simulation with the interaction between the fluid and the structure, and compared with CFD rigid wall simulation.

In the first chapter, the medical context and the positioning of the problem are presented. Vascular pathologies and their treatments are discussed as well as the possible complications. Also, the pathology of aortic dissection and the protocol for diagnosing this pathology are described. Through biomedical techniques will improve the endovascular intervention.

In the second chapter, we focus on mechanical characterization and modeling. The blood flow plays a vital role in the development of this pathology. Thus, the blood rheology with its different models is discussed. Also, the arterial wall, particularly the intimal part, is essential to influence the hemodynamics phenomena in the physiological situation. In this way, the comprehension of the mechanism of the arterial wall is also presented in this chapter. In addition, the mechanical behavior of surgical tools and stents used in endovascular treatment will be investigated in this chapter.

In the third chapter, we present the development of the numerical model for the simulation of the hemodynamics in open-source software OpenFOAM® in aortic dissection models, taking into account the complex behavior of blood flow. To correctly identify the hemodynamic circuit, it is necessary to develop a sufficiently sophisticated 3D bio-faithful model. With the OpenFOAM® extend software OFOM-Extend, we realize a coupling fluid-structure module. Consideration of the deformation of the aortic pathway during the operation would allow us to recommend a stent perfectly adapted and personalized to complex clinical cases. We develop a simulation of the rise of the surgical tools in a pathological dissection aorta. The progress in medical imaging allows the virtual reconstruction of the organs of an individual according to an automatic, precise, and fast procedure. Moreover, these same tools will enable the measurement of velocity fields and make possible the in-vivo and non-intrusive validation of the results obtained by numerical simulations. These methodological advances allow patient-specific simulations to better understand the morphology of each patient.

The last chapter validates the bio-faithful CFD model with 4D-MRI data, which has a highlight

agreement. And a new, individualized method was developed, integrating experimental and numerical tools guided by clinical imaging. Both *in vitro* (Moravia, 2021) and *in silico* models incorporated anatomically precise AD geometry and pulsatile flow and dynamic BCs. Both models included a high degree of information integration at many levels and were influenced by clinical data.

The development of medical imaging and the acquisition of geometric data of the cardiovascular system of a patient constitutes a significant evolution in numerical simulation. The advantage of multi-physical simulations of stent placement with arterial wall deformation and hemodynamic flow is an area of applied research with real impact for the clinical community. Although there have been many biomechanical studies on the treatment of aortic dissections by endovascular technique, there are still few studies devoted to aortic dissections, in particular those of flow in true and false channel.

Numerical simulations will then be able to identify the biomechanical parameters responsible for possible failures of the endovascular treatment and bring elements of analysis to improve the stents used, both in terms of the duration of the stent itself and the surgical treatment.

Clinical context and targets

This chapter focuses on the medical description of the pathology associated with aortic dissection and presents the advantages of endovascular surgery over open surgery. The complications after endovascular surgery are considered from a mechanical point of view. Also, highlight the numerical simulation plays a very important role in surgical solutions, and surgical challenges.

Contents

1.1	Cardiovascular flow system	34
1.2	Vascular pathology	37
1.3	Aorta	37
1.3.1	Global location of the aorta	37
1.3.2	The different parts of the aorta	38
1.4	Aortic dissection(AD) and pathologies	39
1.4.1	Definition	39
1.4.2	Causes	40
1.4.3	Epidemiology and type of AD	40
1.4.4	The complication of AD	43
1.5	Aortic repair surgeries for AD	43
1.6	Scientific position of research	46
1.6.1	Diagnosis of AD	46
1.6.2	The operating scenario	47
1.6.3	Possible complications with endovascular operation	48
1.6.4	Improvement of diagnostic methods from a mechanical point of view	48
1.7	Conclusions and strategies	49

1.1 Cardiovascular flow system

The cardiovascular system is also called the "circulatory system". It is composed of the heart, arteries, capillaries and veins. It is a closed circulatory pipeline in which blood flows, supplies organs and tissues with oxygen, various nutriment, hormones, etc., and transports wastes from tissue metabolism to excretory organs to maintain a stable and metabolic environment in the body. Carry out and support normal life activities. A system composed of the heart, arteries, capillaries, veins, and blood flowing through them. The heart can automatically contract and relax rhythmically under the control of the nervous system, ensuring that blood circulates in a certain direction. Arteries connect the heart to capillaries and carry blood from the heart to the tissues. The capillaries connect the arteries to veins, and form a network. They are the site of material exchange between blood and tissue. The vein connects the capillaries to the heart to collect blood and flow back to the heart.

Therefore, the arteries and veins supplying blood to the whole body are called **systemic circulation** (in red on the Figure 1.1). Its function is to carry oxygenated blood from the heart to all the organs of the body and then to return this venous blood to the heart. The blood passes from the atrium to the ventricle in the left heart, from where it is expelled under high pressure (110 – 140 mm Hg) into the aorta, the main distribution pathway. Additionally, branchings ensure oxygenation and waste collection of tissues in the body. The fluid is then returned to the heart through veins for injection into the pulmonary sub-system.

The body has another circulation pathway, namely **pulmonary circulation** (in blue on the Figure 1.1). Like the systemic circulation, the pulmonary circulation also starts and ends in the heart. The blood comes from the body and is drained by the veins to the right heart at a pressure barely higher than atmospheric pressure. Then the pulmonary circulation transports carbon dioxide-rich venous blood under low pressure (25 – 30 mm Hg) is sent from the right ventricle to the lungs. The pulmonary artery divides into more fine arterial ducts until the pulmonary capillaries at the level of which the exchanges with the pulmonary alveoli take place: the blood loses CO_2 and gains O_2 . The oxygenated blood then flows into the increasingly large venous channels until it reaches the two pulmonary veins, which open into the atrium of the left heart. And begins the process of the next systemic circulation.

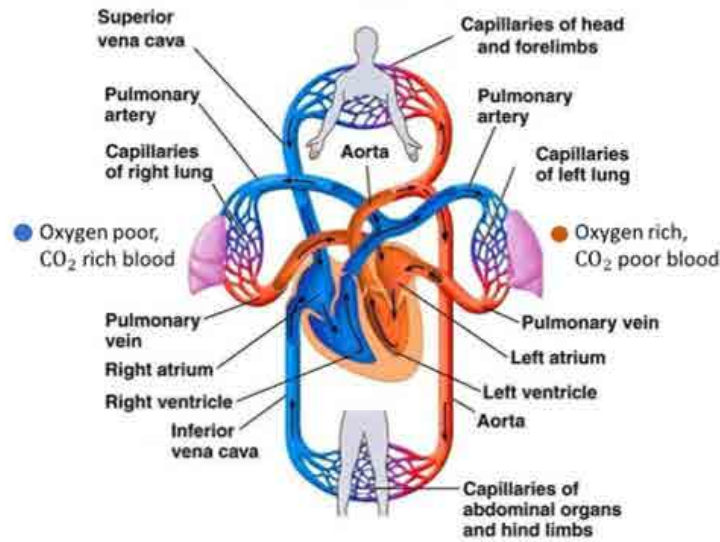


Figure 1.1: Human aorta anatomy

To ensure cross-flow between the pulmonary circulation and the systemic circulation, the heart pumps blood from one system to another. Therefore, the heart is like a double pump composed of four chambers: right and left atrium (blood enters the heart), and right and left ventricle (blood is pumped out of the heart). This dual-pump function divides the pulsatile cardiac cycle into two phases: diastole and systole. The heart supplies the necessary energy for blood circulation in a periodic way by a pulsatile phenomenon with an average frequency of 70 to 75 beats per minute. The arteries leaving the heart have particular mechanical properties that exploit this pulsatile phenomenon called the Windkessel effect. Their elasticity allows them to dilate during blood ejection (systole) by storing pressure part of the mechanical energy supplied by the heart and then releasing it during diastole. Therefore, the pressure and velocity of the blood vary periodically, but this mechanism ensures that the pressure and velocity of the blood in the capillaries remain more or less constant (Fung, 2013). The resistance to blood flow varies according to the diameter of the vessel and its muscle fiber content: the smaller the vessel, the greater its resistance, thus causing a strong decrease in pressure and velocity. About 50% of resistance is observed in arterioles, 20% in large arteries and capillaries, and only 10% in veins. The speed of the blood varies according to the cardiac cycle and the diameter of the vessel. It differs from 100cm/s in the ascending thoracic aorta to 1cm/s in the capillaries (Kojić et al., 2008).

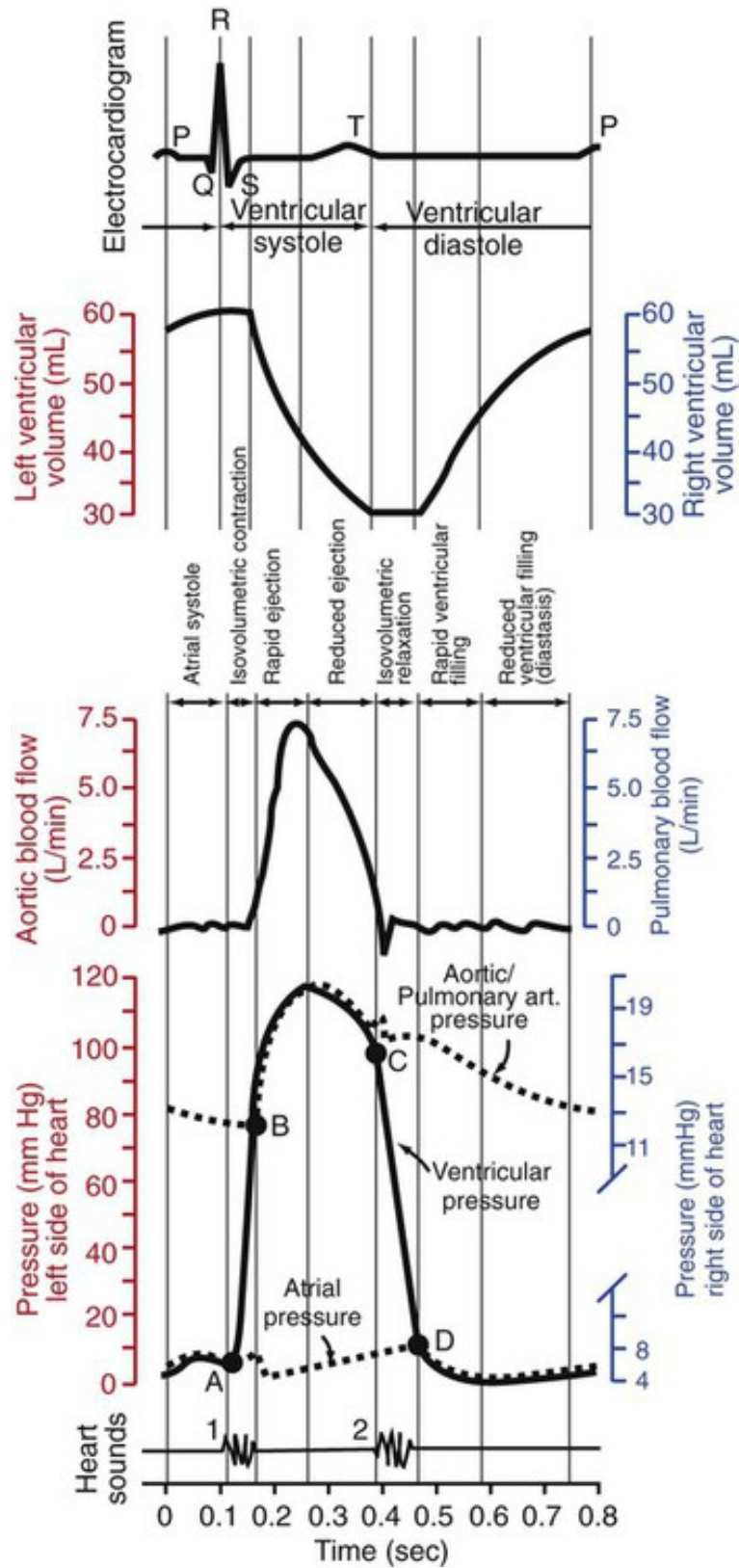


Figure 1.2: Pressures and volume debits are representative of the human cardiac cycle: the dotted line is the pressure measured in the aorta (based on the work of [Themes \(2016\)](#))

Representative pressures and flows of the human cardiac cycle are shown in the Figure 1.2. Arterial pressure is maximal during systole, and minimal in diastole: in large vessels such as the aorta, this pressure is, at rest, between 120mmHg and 80mmHg in systole and diastole, respectively. As the vessel diameter decreases, this pressure can drop to 20 mm Hg in the capillaries and the end of the arterial circuit. In the arterial circuit of the lungs, this pressure tends to be even lower because of less powerful contractions of the right ventricle and the structure of the vessels at this site, which have more non-elastic fibers.

1.2 Vascular pathology

Cardiovascular diseases are a group of heart and blood vessel disorders that include:

- Coronary heart disease: diseases of the blood vessels supplying the heart muscle.
- Cerebrovascular disease: diseases of the blood vessels supplying the brain.
- Peripheral arterial disease: diseases of the blood vessels supplying the arms and legs.
- Rheumatic heart disease: damage to the heart muscle and heart valves caused by rheumatic fever caused by streptococci.
- Congenital heart disease: structural malformations of the heart present at birth.
- Deep vein thrombosis and pulmonary embolism: the presence of a blood clot in a leg vein, which can dislodge and move to the heart and lungs.

Cardiovascular disease is the number one cause of death worldwide: more people die each year from cardiovascular disease than any other reason. Heart attacks and strokes are usually emergencies, mainly due to blockages that prevent blood from flowing to the heart or brain. This happens most often because of a fatty layer built up on the inner walls of the blood supplying vessels to the heart or brain. Strokes can also be caused by bleeding from a blood vessel or blood clot in the brain. Heart attacks and strokes are usually caused by the co-existence of multiple risk factors, such as tobacco use, unhealthy diet and obesity, lack of physical activity and harmful alcohol use, high blood pressure, diabetes and hyperlipidemia.

Therefore, the study of the aorta is a critical topic that is very beneficial for the treatment of vascular pathology.

1.3 Aorta

1.3.1 Global location of the aorta

According to [Claude \(2021\)](#), the aorta has two parts: a part which is located in the rib cage, which is called the thoracic aorta, and a part which is located in the belly, which is called the abdominal aorta. The thorax and abdomen are separated by a horizontally stretched muscle called the diaphragm. In the rib cage, the aorta takes the form of a cane with a part that goes up (ascending), a horizontal part called the butt, and a descending part that will extend into the belly (Figure 1.3) crossing the diaphragm.

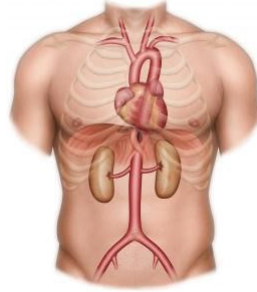


Figure 1.3: Location of the aorta in the body (image : Dr Claude VAISLIC[©])

It arises from the heart's left ventricle and extends to the abdomen, where it branches off into two smaller arteries (the common iliac arteries). It brings oxygenated blood to all parts of the body via the circulation, except for the functional circulation of the lung (pulmonary artery). We will choose to focus in this section on the existing connections with the thoracic aorta.

1.3.2 The different parts of the aorta

According to Figure 1.4, the aorta is classically divided into the thoracic aorta and the abdominal aorta, relative to the diaphragm. The thoracic aorta has three parts: ascending, transverse, and descending. This part presents another element belonging to the aorta: the aortic isthmus.

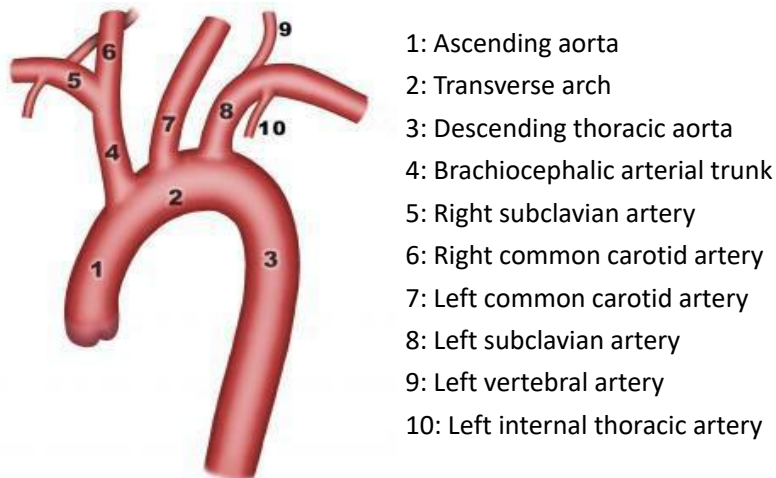


Figure 1.4: Aortic arch (image : Dr Claude VAISLIC[©])

Ascending aorta is the initial segment of the aorta. It emerges from the left ventricle, from which it is separated by the aortic valve. The two coronary arteries of the heart originate from the base of the aorta just above the aortic valve. It is positioned in a pericardial sheath common with the pulmonary artery. These two arteries wind together so that the aorta arises dorsally

in relation to the pulmonary artery, but then the aorta twists latero-ventrally to end up ventral with the pulmonary artery.

Transverse aorta (Aortic arch) passes over the pulmonary artery and the left main bronchus and remains linked to the right pulmonary artery by the Botall arterial ligament, a remnant of the ductus arteriosus. Three vessels arise from this aortic arch, the brachiocephalic arterial trunk, the left common carotid artery, and the left subclavian artery. We can also see behind the beginning of the thyroid artery (or middle thyroid artery) between the origins of the brachiocephalic arterial trunk and the left carotid artery, located posterior to this arch, but it did not come out of it. Generally speaking, the branches of the horizontal aorta supply the head, neck and arms.

Descending thoracic aorta descends into the trunk, into the mediastinum, behind the heart, and in front of the esophagus in its upper part, behind in its lower part. This part is relatively fixed compared to the other two segments. The junction between the horizontal and descending aorta is called the "aortic isthmus". It then crosses the diaphragm at the level of the aortic hiatus, located at the level of the 12th thoracic vertebra, and becomes the abdominal aorta.

Aortic isthmus can be defined as the junction zone between the arch of the aorta and the descending aorta (Ouattara, 2013). Located downstream from the emergence of the left subclavian artery, the aortic isthmus is the attachment of the ligament arteriosum, a remnant of the embryonic ductus arteriosus, which attaches the aorta to the left pulmonary artery. Thus, the aortic isthmus is individualized as a border zone between the mobile portion (the arch of the aorta) and the fixed portion (the descending aorta) of the thoracic aorta. Finally, the aortic isthmus, due to its embryological origin, is a vascular structure of less resistance. All of these anatomical arrangements make it a zone of vulnerability during thoracic trauma with sudden deceleration causing shearing phenomena.

1.4 Aortic dissection(AD) and pathologies

1.4.1 Definition

Cardiovascular disease is the world's largest cause of death, and it is estimated that 17.9 million people are killed every year. The importance of cardiovascular diseases is expected to increase with the aging of the population (demographics), obesity (epidemiological factors) and the intensification of treatment (screening, early detection, etc.). Among these diseases, aortic dissection (AD) is relatively little known and difficult to treat, with a survival rate for the more serious cases not exceeding ten percent. Aortic dissection affects about three people per 100000 (Olsson et al., 2006, Clouse et al., 2004), and AD occurs most frequently between the ages of 50 to 70 years old and affects males in approximately two-thirds of cases (Meszaros et al., 2000).

The main risk factors are high blood pressure, as well as pre-existing pathologies affecting the wall properties. This condition occurs in the aorta and is characterized by the emergence of blood inside the wall of the aorta (Wik, 2021), see Figure 1.5.

Dissection corresponds to a localized tear in the inner layers of the aortic wall, called the entry site, through which the blood under pressure penetrates and removes the various layers that make up the

wall of the aorta. And it will cause an aortic aneurysm. Dissection of these layers may extend over a long portion of the ascending aorta, aortic cross, or descending aorta. It constitutes a surgical emergency.

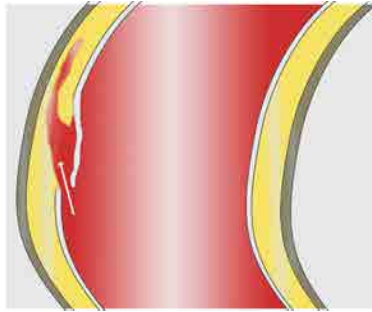


Figure 1.5: Diagram of an aortic dissection formation (image: J.Heuser[©])

1.4.2 Causes

1. Hypertension and atherosclerosis: about 67 % to 80 % of patients with aortic dissection (AD) are combined with hypertension (Golledge and Eagle, 2008), and in addition to an increase in the absolute value of blood pressure, an increase in the rate of change of blood pressure is also an important trigger for AD. Atherosclerosis can thicken the intima of the arteries, which leads to malnutrition of the intima of the arterial wall, which is also an important precipitating factor for AD.
2. Two genetic disorders are common in AD patients: Marfan syndrome and Ehlers-Danlos syndrome, which are familial and often develop in patients at a young age.
3. Congenital aortic malformations: such as aortic constriction (stenosis), ductus arteriosus (aorta connected to the pulmonary artery), and aortic valve defects.
4. Injury: severe trauma can cause tearing of the aortic isthmus, and medically induced injuries can also lead to AD.

1.4.3 Epidemiology and type of AD

Depending on the case, several possible ending outcomes may occur. With this type of pathology, blood flows into two ducts: the **true lumen(TL)** (the initial path taken by blood), and the **false lumen(FL)** (the channel created between the layers of the wall). The two aortic lumens are separated by a layer of intimal tissue called the intimal flap (Criado, 2011), as shown on Figure 1.6. The cause of death is often due to rupture of the aortic wall, weakened by dissection.

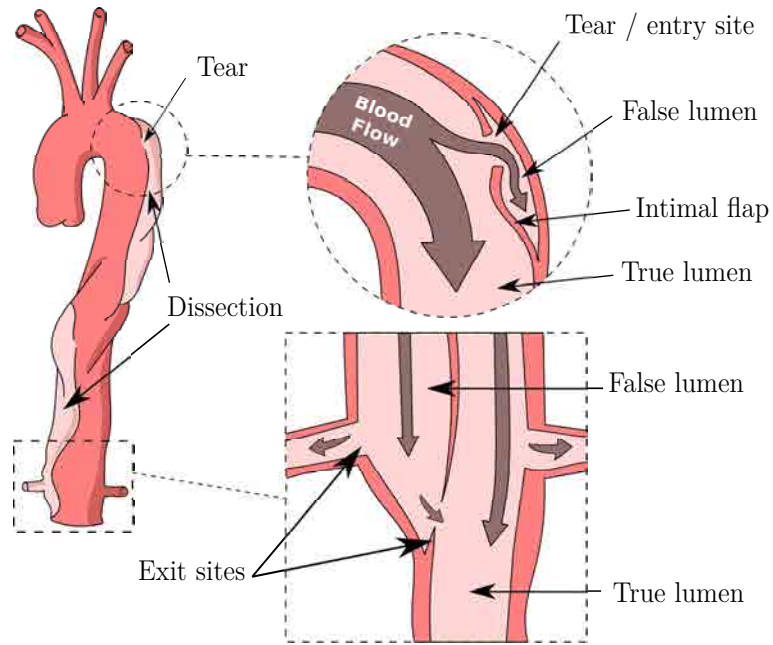


Figure 1.6: Aortic dissection with examples entry and exit sites

The extent (starting point and ending point) of a dissection can be described considering the wall thickness and the intimal flap. Depending on the flow in the false lumen or tears in the intimal flap, aortic dissections can be distinguished (Table 1.1).

Table 1.1: Differentiation between true lumen and false lumen in AD ([Erbel et al., 2001](#))

	True lumen	False lumen
Size	most often true < false	most often false > true
Pulsation	systolic expansion	systolic compression
Flow direction	systolic antegrade flow	systolic antegrade flow reduced or retrograde flow
Localization within the aortic arch	inner contour	outer contour
Signs of slowflow	rare	frequent
Thrombus	rare	frequent

There are several different classification methods for aortic dissection. The most commonly used clinically are DeBakey typing and Stanford typing, see Figure 1.7.

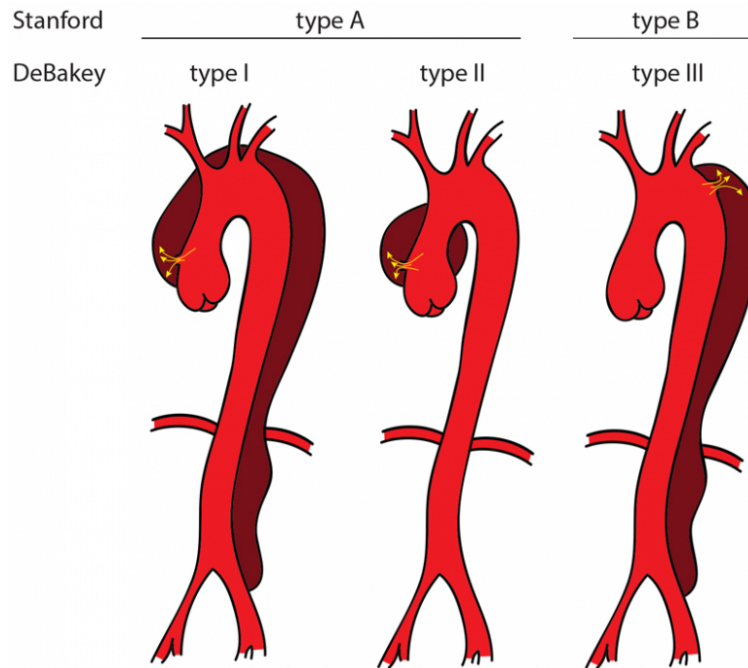


Figure 1.7: Classification of aortic dissections, according to DeBakey and Stanford Classification(image : [Gawinecka et al. \(2017\)](#))

The DeBakey classification ([De Bakey et al., 1965](#)) is an anatomical classification of aortic dissections based on the origin of the dissection and its downstream extension (including the extension of the dissection to the ascending aorta, to the aortic arch, or to the descending aorta):

- Type I – Begins at the ascending aorta, to the aortic arch and descending portion.
- Type II – Begins and localizes only at the ascending aorta.
- Type III – Begins and localizes at the descending aorta.

The Stanford Classification([Daily, 1970](#)) is divided in two categories: A and B. This classification depends on the entry point of the dissection as well as its extent.

Key information is whether the entry point is in the ascending or descending aorta. This location strongly influences the rate of mortality and the choice of the type of intervention. The Table 1.2 shows the differences between type A and type B.

- Type A dissection involves the ascending aorta and/or aortic arch, and the descending aorta may also be involved. Intimal tear originates from the ascending aorta, aortic arch, or descending aorta (rarely). So type A dissection is a clinical emergency and associated with a high mortality rate.
- Type B dissection involves the descending aorta and/or extends to the abdominal aorta, but does not involve the ascending aorta and the aortic arch. It differs in that the surgeons must choose the method of intervention. This type is more conducive to endovascular treatment, and much less problematic than open surgery operation (which has a paraplegia risk of 30%).

Table 1.2: Difference between Type A and Type B (Rizzoli et al., 1997)

	Type A	Type B
Incidence	65-85% of cases	30-35% of cases
Average age	50 years old	65 years old
Acute mortality(without treatment)	$\geq 90\%$	40%
Treatment	emergency surgery	medical, endovascular
Surgical mortality	10 %	19-32 %

Thus, as the classification situation describes: Type A involves the ascending aorta but may extend into the arch and descending aorta(DeBakey type I and II); Type B involves the descending aorta only(DeBakey type III).In Stanford type A, the ascending aorta is always engaged. In Stanford type B, the dissection is distal to the origin of the left subclavian artery. The Stanford system also helps to delineate two distinct risk groups for management.

1.4.4 The complication of AD

The condition strongly weakens the aortic wall and disrupt blood flows, which can cause multiple complications:

Dissection at ascending aorta:

- massive aortic valve insufficiency by tilting of a cusp of the latter, resulting in severe heart failure;
- rupture in the pericardium leading to profuse pericardial effusion with compression of the heart (tamponade), which may progress to heart failure and cardio-circulatory arrest;
- dissection by extension of the coronary arteries with occlusion of the latter and constitution of myocardial infarction;

Dissection at descending aorta:

- rupture of the aorta with massive fatal internal bleeding;
- progression of the dissection on the different arteries with occlusion of the latter (or significant decrease in their flow) gives a picture of localized ischemia (cerebrovascular accident if it is an encephalic artery use, renal infarction if it is a renal artery).

In practice, the most serious complications involve the heart and only occur if the dissection involves the ascending aorta. The latter therefore constitutes an absolute surgical emergency. Dissections of the descending aorta(Stanford type B) must first be treated medically (with drugs), and surgery is then discussed on a case-by-case basis.

1.5 Aortic repair surgeries for AD

Surgery may be needed when AD reaches a critical state. It takes place when the patient experience sharp pain, the aorta rapidly deletes, the aorta ruptures and/or aorta branches become

too distressed to fuel essential organs properly. Depending on the degree of severity and the dissection location, a medical treatment is given, and for most serious cases, different types of surgical procedures can be practiced.

There are two possible treatment techniques for aortic dissection:

- **Open surgery treatment** is used urgently in the event of a ruptured aortic dissection, but also for preventive treatments, consists in implanting a synthetic prosthesis in place of the aortic dissection. This technique has the advantage of being efficient and reliable but remains a heavy intervention with many risks and cardiac and respiratory complications. AD Stanford type A is mostly treated with this surgical method (Fann et al., 1995).

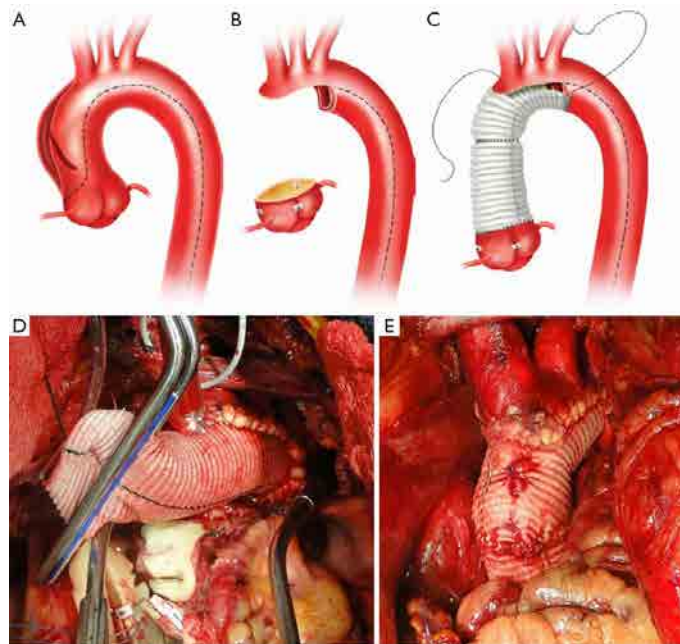


Figure 1.8: Diagram of a classic surgical procedure: a synthetic prosthesis is implanted in place of the dissection;(A) Interpretation of an acute type A aortic dissection-the dotted line indicates the dissection;(B) After the entire underside of the aortic arch is removed, the head vessels are connected to the remaining aorta through a thin peninsula of tissue;(C) The graft is matched to the aorta and sutured with a fine needle to reconstruct the distal anastomosis;(D) Intraoperative photograph show the distal anastomosis configuration;(E) Intraoperative photograph of the completed transverse arch peninsula style repair.

(Image: Chiu and Miller (2016)).

- **Endovascular aortic Repair (EVAR)** is a minimally invasive treatment for AA (Aortic aneurysm) and AD. Repair is performed surgically by making a small open incision in the femoral artery and inserting a catheter to reach the AA or AD region. In the case of AD, it involves sliding the stent graft over the femur to the level of the aortic dissection to redirect blood flow by obliterating the entrances to the false lumen. Compared with traditional surgical treatment, this operation can reduce early mortality and paraplegia. It can also reduce hospital stay and overall complications, including neurological, cardiac, respiratory, renal and bleeding complications, without significantly increasing the need for reoperation during the mid-term follow-up period (Cheng et al., 2010). Although this technology has

all the advantages, it has not been fully verified. In fact, the long-term development of endoprostheses and the complications resulting from their installation have not been fully controlled.

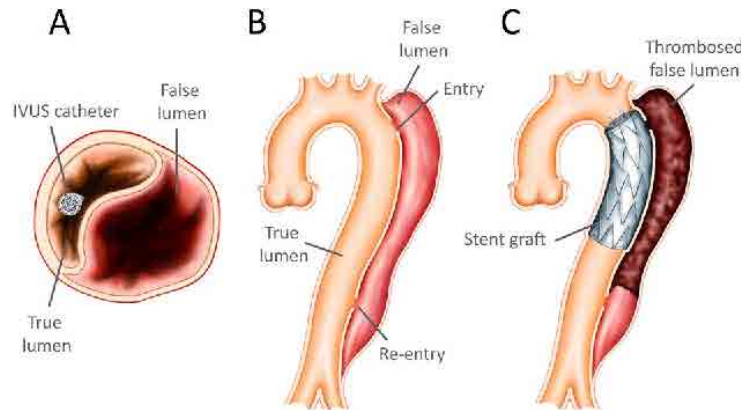


Figure 1.9: Diagram of an endovascular procedure: the stent is gradually deployed in a descending aortic dissection:(A) The presence of the IVUS(intra-vascular ultrasound) catheter in the true lumen;(B) Primary intimal rupture over the descending aorta;(C)Stent graft covering primary intimal tear.(Image : [Uchida and Sadahiro \(2018\)](#))

As a consequence, type B is increasingly treated by the endovascular procedure ([Hanna et al., 2014](#)) ([Nienaber et al., 2013](#)).But,the tools of endovascular procedures currently available to surgeons are based only on information from medical imaging techniques([Dake et al., 1999](#)) ([Uchida and Sadahiro, 2018](#)) ([Lombardi et al., 2020](#)) (Figure 1.10).

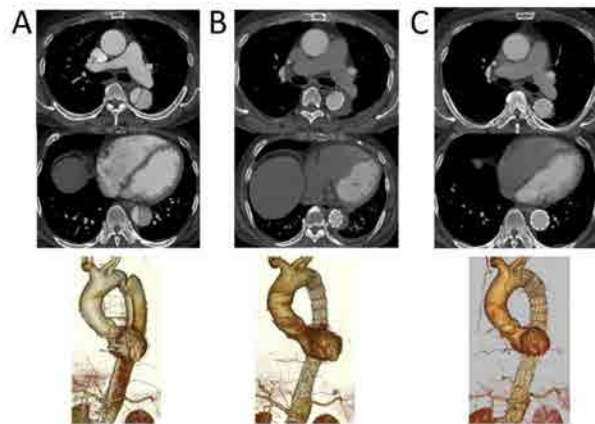


Figure 1.10: CT images of 51 year-old male diagnosed with subacute uncomplicated type B aortic dissection,(A)Pre-operation;(B)2 months after Endovascular treatment;(C) CT images demonstrated favorable remodeling of the dissected descending aorta after one year of intervention. (Image:[Uchida and Sadahiro \(2018\)](#))

1.6 Scientific position of research

1.6.1 Diagnosis of AD

Detecting an aortic dissection can be tricky because the symptoms are like those of a variety of health problems. Doctors often suspect an aortic dissection if the following signs and symptoms are present:

- Most patients have sudden onset of chest and back pain, type A mainly in the anterior chest and interscapular region, type B mainly in the back and abdomen.
- Blood pressure asymmetry >20 mmHg between the 2 arms or abolition-decrease of a peripheral pulse abnormality of the standard chest X-ray
- Abnormality of the thoracic standard X-ray (mediastinal enlargement, abnormality of the cardiac silhouette, pleurisy)

Although these signs and symptoms suggest, aortic dissection more sensitive imaging techniques are needed. Commonly used imaging procedures include:

- The thoracic scanner (computed tomography (CT-scan) & magnetic resonance imaging (MRI)) with an injection of contrast medium into the vascular system shows a double contrast of the aorta, which is "separated" in two by the "flap". It allows a clear delineation of its extension (Yang et al., 2014a). CT scans are relatively quick and noninvasive, and the extent of the entrapment and true or false lumen can be determined by contrast image enhancement. MRI can produce high image resolutions in the absence of contrasting agents, but can be time-consuming and is not recommended for use in hemodynamically unstable patients.
- Transesophageal echocardiogram (TEE) consists in having the patient swallow, under local anesthesia, an ultrasound probe attached to an endoscope. The examination allows a good visualization of almost the entire thoracic aorta. In the case of dissection, the "flap" is clearly objectified, as well as, sometimes, the entry and exit site (Patil and Nierich, 2016).
- Electrocardiography (ECG) is systematically performed in the presence of any chest pain. It may show signs of left ventricular hypertrophy secondary to untreated or poorly treated hypertension. It may also show signs of a developing infarction or repolarization disorders in a quarter of cases (Biagini et al., 2007).

Multiple modalities (CT, MRI scan, and echocardiography) may supplement each other to support the diagnosis, but it depends on the circumstances. The general diagnostic precision of these various modalities is comparable. To achieve the diagnostic objectives, first, we identify the diagnostic and classify the dissection/delineate the extent; then distinguish true and false lumens (Figure 1.11), also localize intimal tear, intimal flap, entry sites (Liu et al., 2018), and differentiate between communicating and non-communicating dissection. We need also to evaluate side branch involvement (i.e., coronary, carotid, subclavian, and renal arteries), detect and grade aortic regurgitation, monitor extravasation (periaortic or mediastinal hematoma, pleural or pericardial effusion, tamponade).

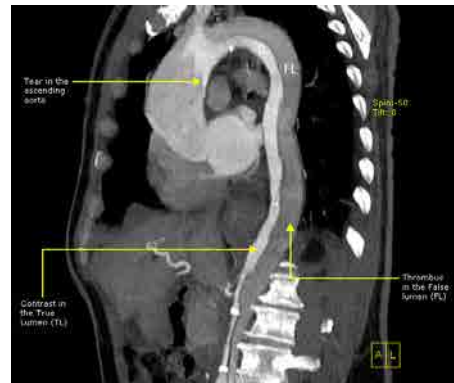
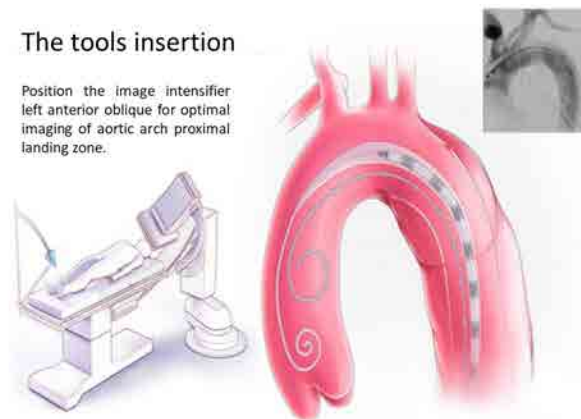


Figure 1.11: Differentiate true lumens and false lumens

1.6.2 The operating scenario

Before an endovascular operation, the surgeon performs a preoperative plan, which consists in analyzing the preoperative data of the patient's examinations. These data generally contain a CT angiography, an examination that allows the visualization of the blood vessels (veins or arteries) after injecting an iodinated contrast product, opaque to X-rays. This examination makes it possible to verify that the patient's anatomy is compatible with endovascular intervention and choose the stent-graft dimensions adapted to the disease and the patient's morphology. This step is called the *sizing*. Several anatomical landmarks are placed on the CT angiography images and are used to take length and diameter measurements. The endoprosthesis models vary by their constitution, their mechanical properties, the range of sizes available, but also by the dimensions and properties of the catheter. It is up to the surgeon to choose the model that he thinks best suits the patient, according to all the data he has in his knowledge and considering the morphology, the accesses, but most often his experience with the medical devices.

Figure 1.12: The delivery system is advanced into the aortic arch.(Image: adapted from [Leshnower and Chen \(2018\)](#))

During surgery, the surgeon inserts several tools into the arteries before the stent is deployed(Figure 1.12). He begins by inserting a flexible guide to initiate the deformation of iliac arteries and abdominal aorta to make them as straight as possible. The surgeon then inserts a more

rigid guide, which generates more significant deformations and straightens the vessels. The iliac arteries generally encounter the most deformation and can undergo displacements of the order of a centimeter. The surgeon then inserts the catheter, the most rigid tool with a diameter of about 5 to 7 mm, containing the stent. Its rigidity is relatively high compared to the vascular structure, which requires that the patient's anatomy be favorable (the iliac arteries not too tortuous, nor too calcified) to be able to introduce the device without risk via the femoral routes.

1.6.3 Possible complications with endovascular operation

Despite the advantages of this technique, such as shorter hospital stay, smaller incisions, faster recovery, and lower morbidities and mortality, current long-term clinical outcomes do not differ significantly in terms of comparison with conventional surgery. However, due to the complications generated by their implementation, the level of reliability of these new treatment techniques remains a subject of discussion, and lifelong CT surveillance is mandatory annually ([Ten Bosch et al., 2010](#)).

The main complications that can arise are as follows:

- **Before surgery:** The feasibility of interventional vascular therapy is directly related to each patient's vascular shape, which depends on the degree of arterial curvature and the characteristics of the vessel wall. However, patients with more complicated pathology, such as extremely tortuous arteries and high calcification degrees, will make it difficult to transport the stent in the blood vessel during the operation. That will lead to higher stress concentration on the vessel wall and the hidden danger of vessel rupture ([Vorp et al., 2003](#), [Walraevens et al., 2008](#)), which may increase death risk. On the other hand, patients and doctors are excessively exposed to X-rays when the vascular stent is inserted into the blood vessel, which causes a certain degree of harm to their health.
- **Postoperative:** Phenomena of stent migration, breakage, folds, endoleaks, thrombosis in the thoracic and abdomen walls will be observed ([Atkins et al., 2006](#)). These phenomena have not been completely avoided for 40% of patients who have been treated after one year ([White et al., 2011](#)). The deformation of the artery under the stent tools' action is not considered, and another cause could be the improper size of the stent, the poor placement of the release catheter, or the improper selection of the stent ([Khanna, 2011](#)). If the size of the stent exceeds 30 %, it will negatively affect the results of vascular interventional surgery ([Tolenaar et al., 2013](#)). And the study of ([Liu et al., 2016](#)) shows that if a rate of oversizing $\leq 5\%$ may be a optimal choice for TEVAR of type B dissection.

1.6.4 Improvement of diagnostic methods from a mechanical point of view

The computerized tomography (CT) images are carried out before the intervention and therefore do not consider the deformation of the vascular structure by the implementation tools of the prosthesis. These tools do not allow for anticipation of events that may unfold during the course of treatment, which can lead to both poor sizing (length, diameter) but also poor positioning of the stent.

The experience of the surgeon permits carrying out delicate procedures and managing the unexpected. Nevertheless, it is impossible to predict the consequences of this positioning in terms of flow.

Endovascular treatment seeks to obliterate the entrances to the false lumen with a stent. In this latter case, it is difficult for the surgeon to know beforehand the place where the stent will be the most effective (entry site, reentry, output, etc.). Therefore, the positioning of the stent is an essential element for the success of the operation. This position leads to a new flow distribution that should be specified for the clinician. Poor redistribution of flow can be harmful for the health of the patient. In addition, the implantation of a stent in the aortic arch poses more significant technical and technological difficulties than in the treatment of the aortic dissection due to the angulations, the extension of the dissection, the origin of the supra-aortic trunks, and the proximity of the aortic valves. If the angle is acute and the dissection is extensive, the procedure may still be challenging to perform, even if the curved prostheses have improved well. In some areas where the supra-aortic trunks cannot be preserved, it is necessary to combine the endovascular procedure with bridges between those trunks and the ascending aorta.

Important research is currently underway to develop new prostheses specifically for the aortic arch. For example, prostheses with side portals make it possible to keep the aortic arch, and the hybrid prostheses associate a traditional prosthesis with an endoprosthesis which makes it possible, under extracorporeal circulation, to treat the patient with a single procedure and achieve encouraging results (7% of deaths, 3% of paraplegia) (BECQUEMIN et al., 2010). In Figure 1.13, a Gore stent-graft is shown, specially adapted for the curvature of the thoracic aorta because of its flexibility.



Figure 1.13: Brand Gore[©] : flexible endoprosthesis adapted for endovascular surgery of the thoracic aorta

In recent years, endovascular treatments have emerged to simplify the treatment of DA. These techniques are practical and offer an alternative to open surgery (Jang et al., 2017). For some patients, they constitute the only possible treatment. Nevertheless, due to the geometry of the site (angled shape) and its position in the anatomy (exit of the heart), the stents are subjected to strong solicitations linked to the turbulent, pulsatory, and unsteady character of the blood flow. These phenomena can lead to early damage, endoleaks, and migration.

1.7 Conclusions and strategies

The area of attention in this study was to basically cover the entire aorta, especially the aortic arch and thoracic aortic dissection. The decision to perform endovascular treatment of aortic dissection is mainly based on measurements of the entry of the dissection, the morphology of the

aortic dissection, the tortuosity of the iliac arteries, and the condition of the patient's health. The management of this disease is often difficult and empirical, and new criteria are needed to propose a reliable operating protocol for the positioning and precise intraoperative control of the stent-graft.

The medical background described in Chapter 1 demonstrates the need for new planning techniques. Our interest is focused on the characterization of the pathology of aortic dissection and its mechanical features, which are essential for diagnosis and clinical planning process.

The envisaged approach is thus to a lesser extent within the framework of computer-assisted medical and surgical procedures in to propose an operational solution for the precise localization and preoperative control of the stent delivery but above all, the research and proposal of a personalized recommendation for the choice of an appropriate delivery system and a stent.

While many biomechanical studies have been done on the endovascular treatment of aneurysms of the abdominal aorta, there are, however, very few such studies on aortic dissections. Thus, a good understanding of the type B pathology to prepare for the operation becomes important. Therefore, the objective of this thesis is to find the criteria that make it possible to determine the procedure to be followed and improve the success rate of this type of operation.

Mechanical models and characterization

As the blood flow plays an essential role in the appearance of this pathology, this chapter presents the composition and rheology of the blood. Understanding the mechanism of the arterial wall is essential to carry out the hemodynamics in physiological situations and during different vascular diseases. The choice of hypothesis law allowed us to fit a mathematical model to the literature's results and mechanically characterize the arterial wall's behavior for our numerical simulations. Also, for the endovascular treatment, the mechanical behavior of surgical tools and stents will be performed.

Contents

2.1	Introduction	53
2.2	Blood rheology	53
2.2.1	Blood function and composition	53
2.2.2	Blood rheology	55
2.2.2.1	Rheology and hemorheology	55
2.2.2.2	Plasma viscosity	57
2.2.2.3	Red blood cells: aggregation, dispersion and deformability	57
2.2.2.4	Rheological properties of blood	59
2.2.3	Hemodynamical flow	60
2.2.4	Mathematical models	64
2.2.5	Physical principles	65
2.2.5.1	Blood flow simplified models	67
2.3	Rheology of the vascular wall	67
2.3.1	Constitution of the arterial wall	67
2.3.2	Mechanical properties of arteries	73
2.3.3	Different mechanical behavior models	75
2.3.3.1	Isotropic hyperelastic models	75
2.3.3.2	Anisotropic hyperelastic models	77
2.3.4	Experimental tests on arteries	79
2.3.4.1	Pressurization tests	79
2.3.4.2	Uniaxial traction test	80
2.3.4.3	Biaxial traction test	82
2.3.4.4	Aortic expansion test	83
2.3.4.5	The indentation method	85
2.4	Mechanical of endoprotheses and tools	86
2.4.1	The endoprotheses	87
2.4.2	The surgical guides	88
2.4.2.1	Mechanical properties of the guides	89

2.4.3 The catheters	90
2.5 Conclusions and strategies	91

2.1 Introduction

We need to figure out the mechanical behavior of the aortic wall and the patient's hemodynamic characteristics to diagnose the pathological features of aortic dissection and help the surgeon with the planning of endovascular treatment. The understanding and mechanical characterization of the behavior of biological tissues is of paramount importance to understand hemodynamics and vascular diseases. Many researchers (Robicsek and Thubrikar, 1994, Dillon-Murphy et al., 2016) have been interested in numerical simulations of hemodynamics for several years, allowing the location of dissections to be correlated with the area of regions where blood flow is disturbed.

However, as these blood flow recirculation phenomena do not fully explain the evolution of arterial lesions, a great deal of attention has been paid to the mechanical properties of arteries. Although in-vivo tests based on ultrasound or magnetic resonance imaging techniques have been developed (Avril et al., 2009), there is still no direct method of non-invasive pressure measurement in large arteries such as the aorta. Mechanical properties cannot then be obtained directly.

This limitation has led researchers to investigate indirect means to obtain an estimate of these properties. Most methods are based on an estimate of the propagation velocity of the pressure wave, usually from the measurement of blood flow by ultrasound or MRI (Lehmann et al., 1993, Hardy et al., 1994). Although these non-invasive methods are tending to replace invasive techniques when measuring the mechanical properties of the arterial wall, ex-vivo methods are still needed to characterize arteries mechanically reliably. They also avoid the influence of errors inherent to non-invasive methods and are still widely used in the literature.

To numerically simulate the endovascular procedure and in parallel with the characterization of the biological tissues, it is also important to know the mechanical behavior of the surgical tools involved in the surgical operations and direct contact with the arteries. Commercial stents and surgical tools have fixed dimensions and exist in several sizes to best fit the morphology of all aortic dissections. The French Health Products Safety Agency (AFSSAPS) requires static and dynamic mechanical testing of these medical devices prior to their implantation in the vascular market to verify their sizing and long-term resistance. They reproduce the implantation procedure and the in-vivo stresses corresponding to a minimum life span of 10 years. As a result, we must consider not only the rheology of blood and arterial wall, but also the mechanical characteristics of the tools and how they affect the artery wall throughout the endovascular treatment.

2.2 Blood rheology

This section describes the mechanical and physical characteristics of blood to better understand the different behavioral models better.

2.2.1 Blood function and composition

In humans, the blood volume is 5 to 6 liters, and the average cardiac output at rest is 5.5 L/min. With physical effort, this flow can reach up to 25 L/min. The blood is distributed to the different parts of the human body and then drained by vessels of various types. But this system is not a simple distribution circuit, and it also plays the role of reservoirs: a high-pressure reservoir in the

arterial part, exploiting the distensibility properties of the arteries, and a low-pressure reservoir in the venous region, which influences the high deformability characteristics of the veins (Fung, 2013).

Blood is composed of cells suspended in a saline solution containing various proteins, called plasma. These cells occupy about 50% of the total volume and are distributed as follows:

- 97% are red blood cells (erythrocytes).
- 1% are white blood cells (leukocytes).
- Approximately less than 1% are platelets (thrombocytes).

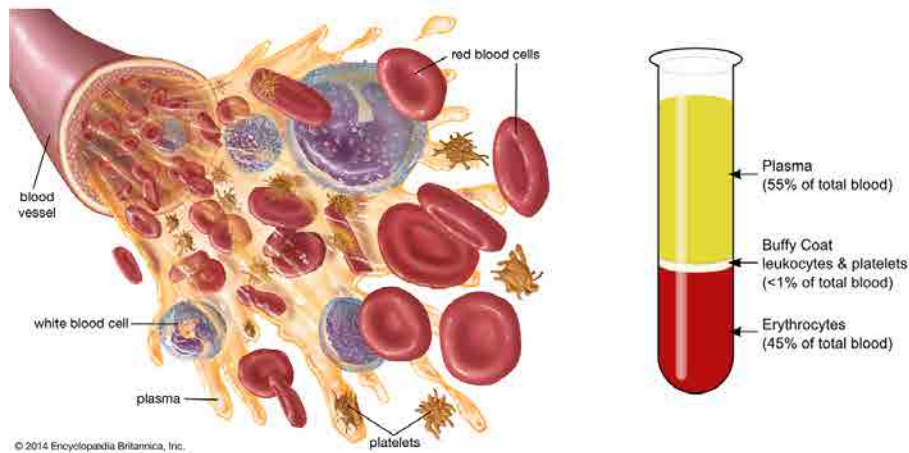


Figure 2.1: Blood composition

Plasma is the extracellular fluid of blood. The plasma composition is highly complex and includes proteins, lipids, inorganic salts, sugars, amino acids, metabolic wastes, and large amounts of water. The plasma serves as a channel of transport for the following constitutive cells.

Red blood cells (RBCs), also called as erythrocyte, is the most numerous type of blood cell in the blood. They are disk-shaped, biconcave cells without a nucleus, with a diameter of 8 to 9 μm (Figure 2.2), and filled with a protein with an iron nucleus, called hemoglobin, to which oxygen is bound. Hemoglobin allows the transport of oxygen to the tissues and carbon dioxide to the lungs. There are 4 to 6 million of them per mm^3 of blood.

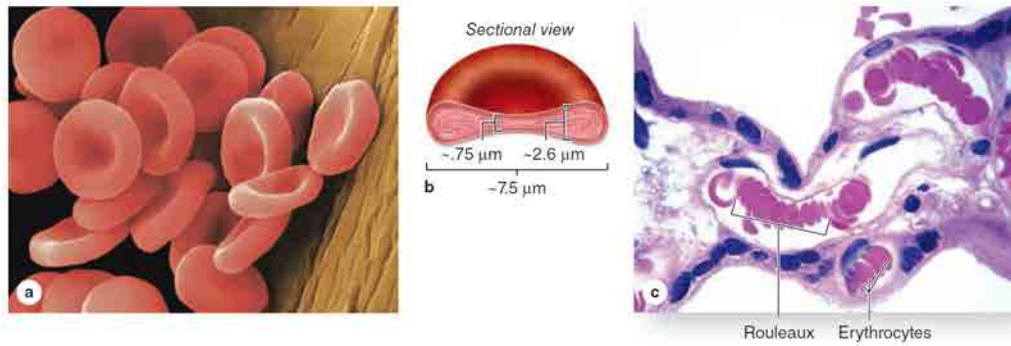


Figure 2.2: (a) Scanning electron microscopy of red blood cells $\times 1800$ (b) The average dimensions of a red blood cell (c) In the small vessels, the red blood cells form aggregates called "Rouleaux" $\times 250$ (Mescher, 2013)

White blood cells (WBCs), also known as leukocytes, are roughly spherical and nucleated, which are part of the immune system and are in charge of destroying and removing old or abnormal cells and cellular debris, in addition to attacking pathogens and external objects. There are 5 to 10 thousand of them per mm^3 of blood.

Platelets are also referred to as thrombocytes, and their main function is blood clotting. The fibrin clumps together in a grid to gather red blood cells to form clots, which stop more blood from being lost and help stop bacteria from entering the body.

Hematocrit is a term that refers to the amount of produced components in blood. The characteristics of the flowing blood depend mainly on the hematocrit. It is the volume of blood cells (RBCs, WBCs, and platelets) as a proportion of the total volume of blood. Because 97 – 99% of blood cells are red blood cells, hematocrit is frequently associated with blood RBC ratio. Hematocrit values fluctuate amongst individuals for various reasons, including gender, illness, low oxygen environment, and dehydration.

2.2.2 Blood rheology

2.2.2.1 Rheology and hemorheology

The science of rheology is the study of material deformation and flow. Hemorheological rheology is the study of the characteristics of blood flow in its physiological context. It entails examining the interplay of blood components, flow characteristics, the interaction of blood and vascular walls, and physiological parameters such as temperature, pressure, and diseases (Errill, 1969).

Understanding the degree of deformation (or flow) of a material is essential because the force exerted per unit area must be considered (Chien et al., 2012). The deforming force, referred to as stress, may be made up of several different components, including the following: (1) Shear stress, defined as the force operating parallel to the surface per unit area; (2) Normal stress, described as the force acting perpendicular to the surface per unit area. For the latter is to be defined as a pressure in a fluid. Strain is a phrase that refers to the degree of deformation, and it also has several components linked with the various stress components. For example, shear stress leads to shear strain, which is sometimes referred to as shear rate, in which successive layers of material move parallel to one another.

Early fluid-mechanics research discovered that for a pipe of fixed diameter and length, the resistance to flow depends on the flow conditions within the pipe (Errill, 1969). During the second part of the 1800s, experimental data showed that flow was proportional to the pressure drop, which (reflected) resistance to flow. Under these conditions, it has been shown that the liquid particles travel smoothly on neighboring planes (laminae) parallel to the tube wall; this form of flow is termed laminar flow (Lowe and Barbenel, 2019). As the fluid flow rate increases, there is a tendency for fluid movement to become erratic, with swirling and uneven patterns. Turbulent flow is defined as a state of chaotic flow in which turbulence increases with the flow rate. The pressure drop is proportional to the square of the flow speed for these conditions: for the same pipe and fluid, resistance to flow is more considerable with turbulence (Tennekes and Lumley, 2018).

In laminar flow circumstances, a shear stress-shear rate relationship is utilized to determine the fluidity of liquids (Errill, 1969). This connection represents the internal resistance between fluid layers (laminae) and the fluid's viscosity; a liquid's viscosity may be estimated by dividing the shear stress (resistance to flow) by the shear rate (rate of flow) (Lowe and Barbenel, 2019). Liquids may be classified into two broad categories based on their rheological properties (Figure 2.3): (1) Newtonian fluids have a viscosity that is unaffected by changes in shear rate or shear stress. The slope of the shear stress-shear rate relationship is constant for these fluids across the shear stress range tested, and hence the viscosity is constant; (2) Non-Newtonian fluids are those in which the apparent viscosity of a fluid depends on the amount of the shear stress or shear rate. As the shear rate is raised, the apparent viscosity of a non-Newtonian fluid can drop (shear-thinning behavior) or rise (shear-thickening behavior). Non-Newtonian fluids may exhibit a yield stress, below which the shear rate is zero (there is no flow), resulting in an infinite apparent viscosity (Rampling, 2019). The flow behavior of non-Newtonian fluids may also be time-dependent; at a fixed shear rate, the viscosity of thixotropic fluids decreases with time (Chien et al., 2012). Notably, the viscosity of a liquid varies with its temperature for both groups of fluids. For example, the dynamic viscosity of water is 0.89 cP (mPa.s) at about 25°C, and at 37°C has a viscosity of 0.6913 mPa.s. In addition, the ratio of shear stress τ to shear rate $\dot{\gamma}$ is the apparent dynamic viscosity μ :

$$\mu = \frac{\tau}{\dot{\gamma}}$$

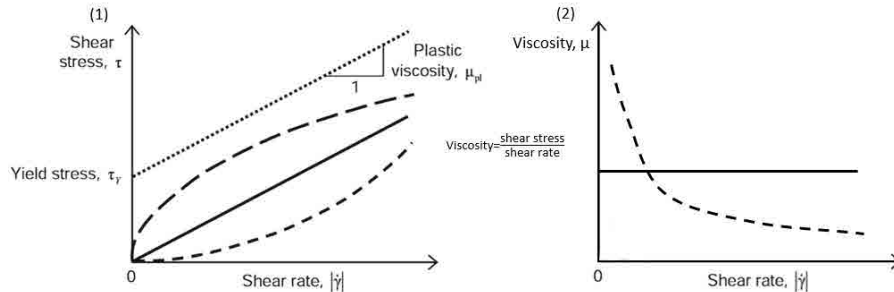


Figure 2.3: (1) Shear stress versus shear rate diagram for Newtonian (solid line) and non-Newtonian fluids in a simple shear flow. The dotted line represents a non-Newtonian fluid with a yield stress. The top dashed line indicates shear-thinning fluid without yield stress. The bottom dashed line represents shear-thickening fluid without yield stress. (Bao et al., 2017) (2) Viscosity-shear rate relationships for Newtonian (solid line) and non-Newtonian (dashed line) fluids

Hemorheology is concerned with blood flow and its deformation behavior and the constituents that shape it (i.e., red blood cells, white blood cells, platelets). Blood rheological properties are crucial to the study of vascular mechanics: the subtleties of blood rheology are still being investigated, and blood rheology is altered in a variety of disease states. Clinical and experimental evidence demonstrates unequivocally that blood flow behavior is a crucial driver of optimal tissue perfusion. Therefore, blood rheology detection has become an indispensable and essential tool for clinical medicine and research.

Blood may be thought of as a tissue made of multiple types of cells (red blood cells, white blood cells, and platelets) and a liquid intercellular medium from a biological perspective (i.e., plasma). Blood may be conceived of as a two-phase liquid from a rheological perspective; it may also be thought of as a solid-fluid suspension with the cellular constituents constituting the solid phase. However, due to the liquid-like behavior of red blood cells under shear, blood may also be considered as a liquid-liquid emulsion.

2.2.2.2 Plasma viscosity

Because plasma serves as the suspending phase for the cellular components in blood, any change in its viscosity has a direct effect on blood viscosity independently of hematocrit or cellular element characteristics. Plasma viscosity ranges typically between 1.10 and 1.35 cP at 37°C (Lowe and Barbenel, 2019), but in pathological conditions and after tissue damage, maybe it will be higher (this value could be up to 2 cP). Although plasma is a Newtonian fluid, some have reported non-Newtonian behavior due to technological artifacts (Baskurt and Meiselman, 2003). Because plasma has a crucial component called plasma proteins, the most important matrix proteins in the blood include between 6 and 8 grams of proteins per 100 milliliters. The bulk of these proteins is split into albumin and globulin fractions (Lacombe et al., 1988). Also present in plasma is fibrinogen, a soluble protein that is transformed into an insoluble, polymerized form known as fibrin during the clotting process (Baskurt et al., 2007). Fibrinogen is also a significant determinant of blood flow behavior since this protein plays a critical role in the reversible aggregation of Red blood cells. Therefore, a substantial amount of the non-Newtonian flow characteristics are determined by fibrinogen (Merrill et al., 1963b). Plasma viscosity is a practical, non-specific indication of disease processes and is elevated in pathophysiological situations associated with acute-phase responses (Somer and Meiselman, 1993). Acute-phase reactants, including fibrinogen, significantly influence the non-specific rise in plasma viscosity in disease processes. Plasma viscosity may rise by up to 5–6 cP in individuals with aberrant protein levels, as observed in so-called paraproteinemias (Lowe, 2019).

2.2.2.3 Red blood cells: aggregation, dispersion and deformability

The red blood cell is the most numerous type of blood cell in the blood. Therefore, the characteristics of the flowing blood depend mainly also on the aggregation and deformation properties of red blood cells (Chien, 1975).

The cellular phase contributes to the total viscosity rise and imparts non-Newtonian features. As seen in Figure 2.4, viscosity falls as the shear rate of the fluid increases. Thus, the fluid is described as "shear-thinning". To emphasize the critical function of the cellular phase, increasing hematocrit in blood results in an increase in absolute viscosity and a steepening of the shear-thinning slope

(Chien et al., 1966).

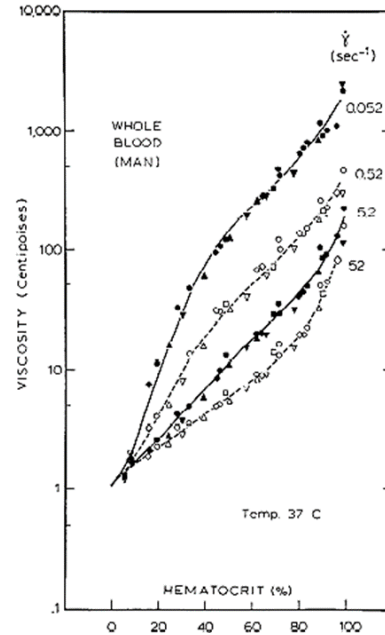


Figure 2.4: Relationship between viscosity and hematocrit values of blood at four varying shear rates at 37°C. (Chien et al., 1966)

Two principal reversible mechanisms in RBCs are identified to explain blood shear-thinning:

- **Deformability:** RBCs are deformable elastic entities that deform under external pressure. When flowing under a laminar high shear rate, RBCs align and elongate in the flow direction. On the other hand, RBCs revert to roundness at low shear rates and rotate in the fluid.
- **Aggregation:** When RBCs are suspended in autologous plasma and viewed under light microscopy at rest, they cluster into huge aggregates like a stack of coins (Figure 2.2(c)). These aggregates, referred to as "rouleaux", are readily dispersed by fluid forces (e.g., by applying pressure to the coverslip to generate a local flow) but immediately re-form when the fluid forces are removed (Chien and Sung, 1987). Aggregation is highly dependent on the nature of the suspending medium. For example, fibrous proteins found in plasma promote aggregation. In addition, modifications to the media (Either experimental needs or physiological changes due to pathology) affect the RBC aggregation process.

Many studies have considered the viscosity of blood through the aggregation properties of red blood cells (Chien et al., 1978, Chien and Sung, 1987, Donner et al., 1988, Haider et al., 2004). The rheo-fluidification curves in the Figure 2.5 represent the decrease in blood viscosity as the shear rate $\dot{\gamma}$ increases. They demonstrate the changes in the organized structure of the blood as a result of the reversible aggregation and disaggregation of red blood cells.

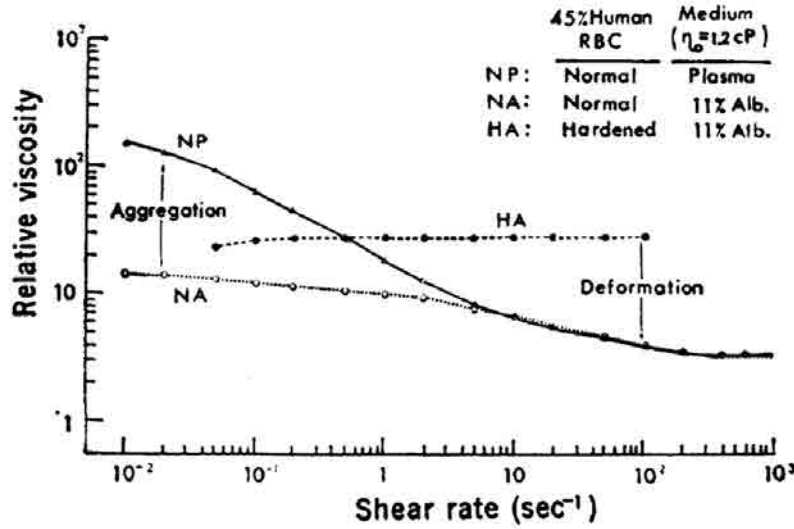


Figure 2.5: Variations of relative viscosity as a function of shear rate for three hematocrit 45% suspensions: Normal RBCs are in plasma (NP), albumin-Ringer RBCs are in albumin (NA), and hardened RBCs are in albumin-Ringer (HA) ((Chien, 1970))

- At low shear, red blood cells are associated in arrays of rolls or as individual rolls (Figure 2.2(c)). This is because the blood has a high viscosity, and the elastic deformation of these rolls imparts a viscoelastic behavior to it.
- At high shear, red blood cells are dispersed, orient themselves in the flow, and deformed. Thus, the low viscosity is determined mainly by the red blood cell's particular mechanical characteristics, particularly its deformability.
- At moderate shear, viscosity is essentially governed by complex equilibrium phenomena between aggregation and disaggregation of red blood cells. Roller disaggregation provides an explanation for the thixotropy of blood (Lacombe et al., 1988, Jaffrin and Goubel, 1998): the viscosity decreases with time when constant stress is applied.

2.2.2.4 Rheological properties of blood

The behavior of blood is therefore dependent on the organized structure of the red blood cells. Such a relationship between viscosity and structure leads to time-dependent effects. The response of the blood during a cardiac cycle can consist of two phases: a first systolic phase during which the shear is high and therefore the viscosity of the blood is low, and a second diastolic phase during which the shear is lowest and the viscosity of the blood increases. The Figure 2.6 illustrates this rheological behavior of blood: the rheogram (Figure 2.6(a)) demonstrates that the viscosity of blood decreases with increasing shear, which means the blood becomes more flowable. The rolls of RBCs are formed at low shear, and when subjected to higher shear forces, these aggregates deform in the presence of weak blood flow. There is then a stress threshold below which the blood hardly flows. Thus, there is a stress threshold τ_c below which the flow will not occur (Merrill et al., 1963a).

We consider that at low and high shear rates, blood can be regarded as Newtonian fluid (Figure 2.6(b)) with respectively average viscosities $\mu_0 = 50 \text{ mPa.s}$ and $\mu_\infty = 5 \text{ mPa.s}$.

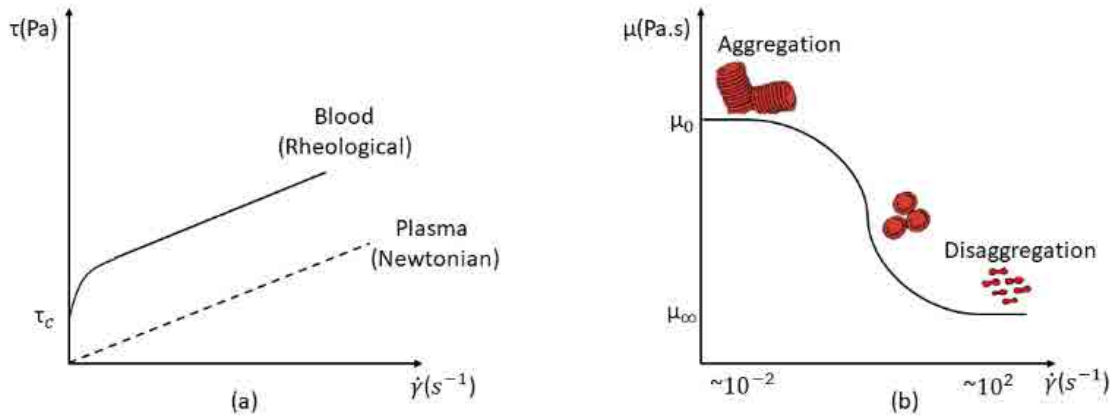


Figure 2.6: Rheological behavior of blood. (a) Stress as a function of the shear rate of plasma and blood (b) Relationship between blood viscosity and shear rate (Memut, 2017)

Hematocrit also has an important role in considering, and its influence has been studied extensively (Wells Jr and EW, 1961, Merrill et al., 1963a, Strumia et al., 1963, Chien et al., 1966). In a healthy patient, the hematocrit rate is between 40 and 50%, but pathologies can make this rate decrease or increase. In some pathological cases, it can reach 60-70%, increasing the viscosity of the blood very strongly. When the hematocrit is less than 20%, the aggregation of red blood cells is practically non-existent, and the blood has a Newtonian behavior: its viscosity no longer varies with the shear rate.

The rheological behavior of blood significantly influences its flow by its viscosity which is affected by four main factors: hematocrit, temperature (Eckmann et al., 2000), arterial pressure, and vessel diameter (Pries et al., 1992), and therefore by the flow's continuous or unsteady character. The arterial system is constituted of a complex network with contractions, vessel dilatations, and elbows that provide the flows with complex behaviors, including recirculation zones. The non-Newtonian behavior of the blood cannot be neglected, and it becomes necessary to model the flow with an appropriate model that approximates the physiological behavior during a cardiac cycle.

2.2.3 Hemodynamical flow

The location of the thoracic aorta in the human body is one of the difficulties of the endovascular procedure for the aortic dissection pathology treatment. Deployment complications may occur due to the location of primary entry tear of dissection, the diameter of the true lumen and false lumen, the angulation and tortuosity of the artery (Figure 2.9), the location of the supra-aortic trunk, and its positioning directly at the exit of the heart, inducing high stress from blood flow.

The role of hemodynamics in aortic dissection formation is well recognized in the literature. Authors (Robicsek and Thubrikar, 1994, Seta and Cohen, 2014, Osswald et al., 2017) have shown the existence of preferential sites for aortic dissection formation and have found that low and oscillating parietal stress favors dissection development by its impact on the shape and structure of endothelial cells. Low wall shear stress induces endothelial injury, arterial remodeling, and adaptive intimal thickening with the accumulation of cells tend to increase shear stress (Figure 2.7(b)), leading to

atheromatous plaque formation (Figure 2.7(c)) triggered by the presence of additional risk factors (smoking, hypertension, diabetes, etc.).

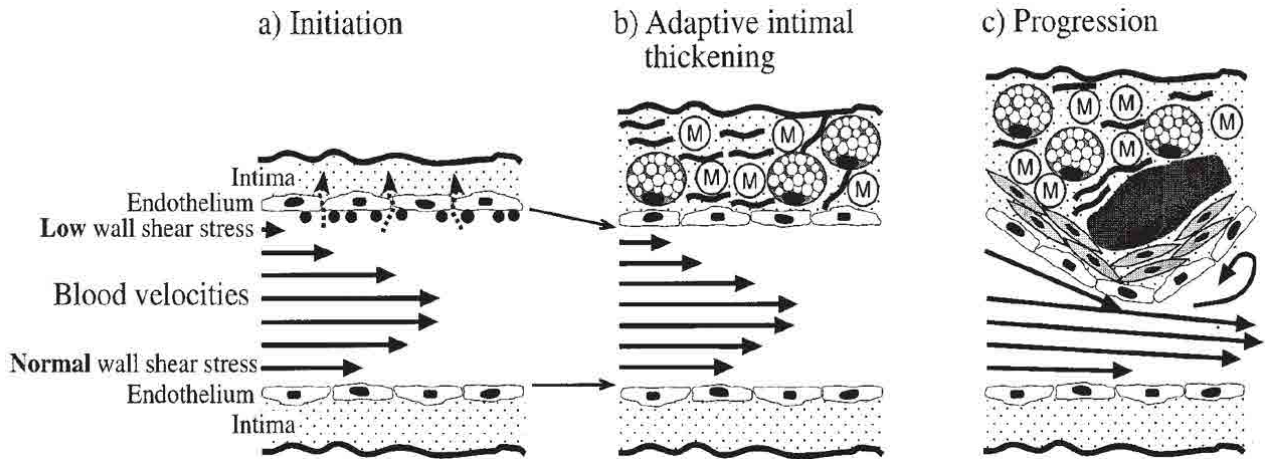


Figure 2.7: Hypothesis on the role of wall shear stress (WSS) in atherosclerotic plaque initiation and growth. Blood flow velocity (arrows) in a tangential view of an artery showing endothelial cells and intima.

(a) Low shear stress induces endothelial wall dysfunction by increasing its permeability (b) Arterial remodeling and intimal thickening affect the tolerance of WSS (c) Advanced stenosis progression (Pedersen et al., 1999)

The improvement of medical imaging techniques (Hope et al., 2010, François et al., 2013, Millon et al., 2014, Sherrah et al., 2015, Sigovan et al., 2015) allows providing more precise information on the rheological behavior of blood. In addition to the use of ultrasound imaging, which is often hampered by the organs covering the arterial vessels, the radiologist now has multiple magnetic resonance angiography (MRA) sequences that can be applied to most arterial sites and that enable a dynamic exploration of the main vascular pathologies. After having had limited indications, the non-contrast sequences, have a renewed interest, thanks to the recent technological improvements and signs in exploring the intracranial vascularization and the thoracic aorta. The work of Sigovan et al. (2015) and Markl et al. (2010) presented in Figures 2.8 and 2.9 show the kind of studies that are now available with the new dynamic imaging techniques, called 4D MRI, and obtaining flow rates and velocity profiles at different moments of the cardiac cycle. The study of Allen et al. (2019) demonstrates that hemodynamic evaluation using 4D flow MRI is a useful method for seeing and characterizing fenestrations in patients with dissection flap. This kind of research is particularly interesting in comparing rheological models and validating their hypotheses during numerical simulations in computational fluid dynamics.

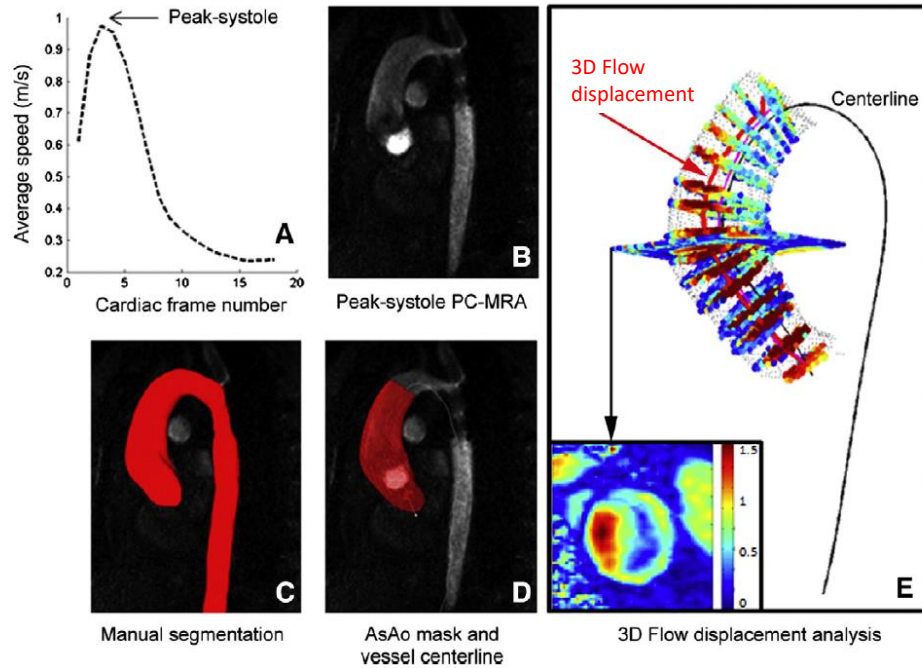


Figure 2.8: 3D flow analysis: (A) detection of the systolic peak, (B, C, D) manual segmentation at peak systolic and calculation of the centerline, (E) an example of 3D flow results obtained in the thoracic aorta (Sigovan et al., 2015)

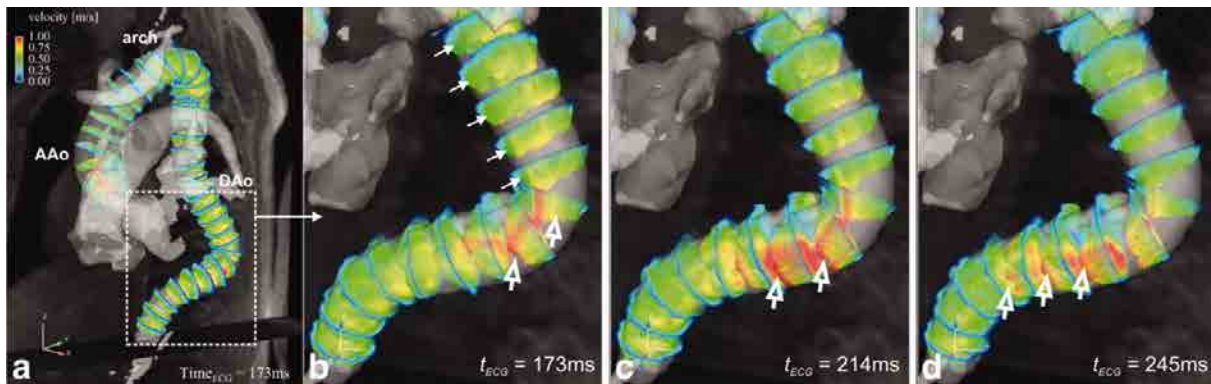


Figure 2.9: Estimation of pulse wave velocity in a patient with significant elongation and rotation of the descending thoracic aorta (Markl et al., 2010)

For example, this is the case for the work of Karmonik et al. (2011), Dillon-Murphy et al. (2016), Bonfanti et al. (2017), Munshi et al. (2020) that use computational fluid dynamics (CFD) models based on imaging to simulate the flow in aortic dissection. Patient-specific geometries and velocity data are reconstructed using CT or MRI. Figure 2.10 illustrates the difference between CT and MRI. Figure 2.11 shows that tears may be observed in the CTA, but the 4D PC-MRI data cannot determine their locations since no distinct change in the velocity field indicates a re-entry between the true and false lumen. In addition, in some studies, CFD simulations performed for measured flow conditions are primarily compared with in vivo 4D MRI measurements. For example, a comparison with a Newtonian flow model in an acute type B dissection located at the aortic isthmus is shown

in Figure 2.11. It illustrates an impressive similarity in the results. In some cases, CFD simulations could help to determine which surgical procedure is most suitable to reform flow in the aortic dissection pathology while also preserving blood flow. In addition, numerical modeling based on medical imaging can provide advice to clinicians by indicating possible complications based on the simulation results and the expected potential for achieving success in improving the flow with the AD pathology before operation.

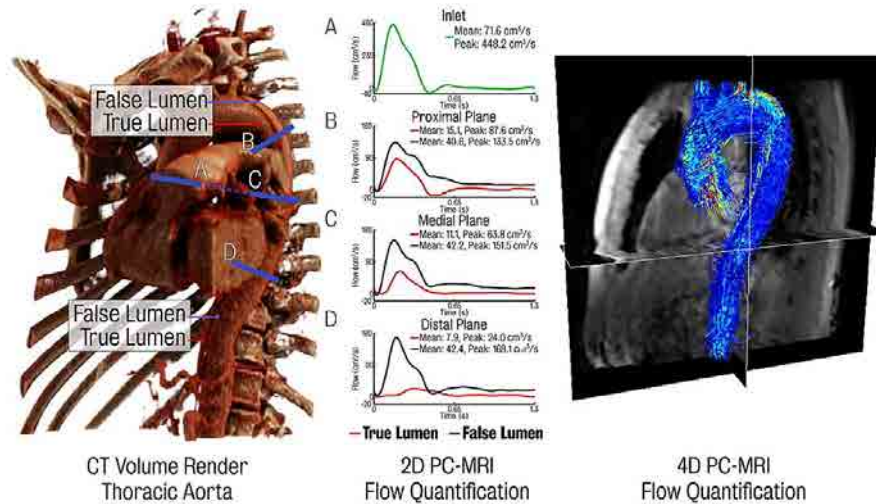


Figure 2.10: (Left) CT volume render of the thoracic aorta demonstrating the dissection septum, (Centre) 2D PC-MRI data at the aortic inflow and several locations across the aorta, (Right) 4D PC-MRI data (Dillon-Murphy et al., 2016)

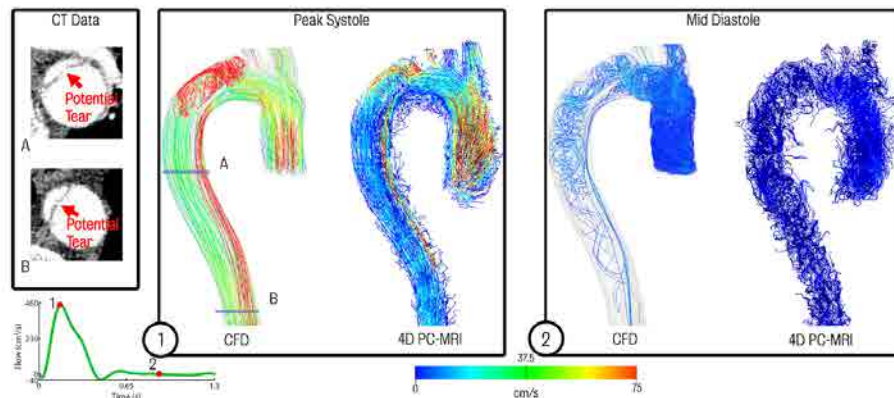


Figure 2.11: Comparison between CFD and 4D PC-MRI streamlines at peak systole and mid diastole. Additionally, CT imaging data (left) at two sites are presented to demonstrate probable secondary tears that were not seen on the 4D PC-MRI data (Dillon-Murphy et al., 2016)

The observation of velocity profiles in arteries demonstrates a periodic laminar flow behavior in a circular cylindrical pipe. Indeed, in a permanent regime, the law relating the pressure to the speed is the Poiseuille law. In an oscillatory regime, this relation becomes more complex, and the study of such a flow was approached by several authors whose most significant results were contributed by Womersley (1955) and Uchida (1956) who characterized the velocity profiles by a non-dimensional

number α , called Womersley :

$$\alpha = R \sqrt{\frac{\rho \omega}{\mu}}$$

with R the arterial diameter (m), ρ the blood density (kg/m^3), ω the oscillation frequency (rad/s) and μ the blood viscosity (Pa.s). Therefore, the relation between pressure and velocity in the oscillating regime is time-dependent, and the velocity profiles that it generates deviate from the parabolic shape as α grows (Fung, 2013). At rest, this number varies from 10^{-3} for the capillaries to 20 for the aorta for the human circulation. When $\alpha = 1$, we then have a Poiseuille profile (Figure 2.12).

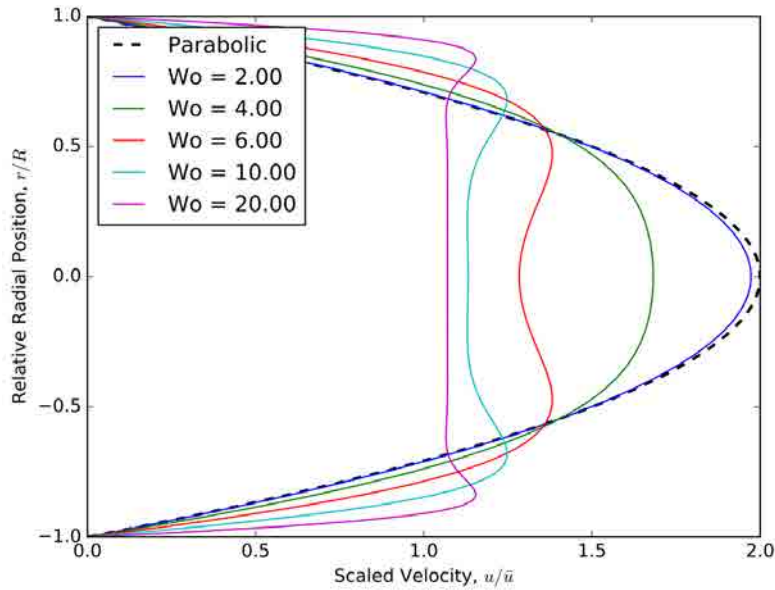


Figure 2.12: Velocity profiles for different values of the Womersley number (Hellmuth, 2017)

2.2.4 Mathematical models

The rheological behavior of blood significantly influences its flow. It is a complex fluid, and its different elements lead to significant changes in its rheological properties. Therefore, modeling the flow of blood implies choosing an appropriate model that closely approximates its physiological behavior during a cardiac cycle, that is, to capture one or several of its rheological properties. Since the shear thinning and viscoelastic properties decrease rapidly as the microstructure of red blood cells decomposes, it is essential to consider in which non-Newtonian properties of the flow regime and for the simulation domain are important. Indeed, in medium and large arteries, viscosity influences hemodynamics, but it is mainly in some capillaries, small vessels with diameters close to the size of cells, where the non-Newtonian property of blood is more predominant.

It is necessary to examine the behavior of blood at both low and high blood shear rates to provide a comprehensive explanation of hemodynamic events. The effect of viscosity on shear rate is usually well taken into consideration when selecting suitable parameters that match the experimental findings for each non-Newtonian model. There are many behavioral equations to represent the viscous

property of blood. In general, these models are divided into Newtonian and non-Newtonian models. There are different variants among the non-Newtonian models: the power law, Casson and Carreau models are the most widely used and make the viscosity variable. On the other hand, blood is also represented as a Newtonian fluid, which is a reasonable approximation in various situations, including the flow through large vessels at medium and high shear rates. For a Newtonian fluid, a constant is commonly used, called the high shear rate blood viscosity, which has a value of 3.5 mPa.s.

The fact that no model, Newtonian or non-Newtonian, is capable of capturing all the aspects of the blood's complexity necessitates the employment of several models to describe various characteristics of the blood rheology. These models, whether Newtonian or non-Newtonian, clearly vary in meaningful ways, and consequently, they may yield wildly disparate outcomes from one another. In addition, the findings vary substantially between Newtonian and non-Newtonian models in most of situations. The complexity and capacity to represent various physical events of the non-Newtonian models vary from one another. Table 2.1 provides a non-exhaustive list of Generalized Newtonian models with the form of their equations, the constants used, and in which the properties are used. When using these models, blood is treated as a homogeneous fluid, and the only particularity of these models is the consideration of the variation in viscosity as a function of shear rate.

Table 2.1: The Non-Newtonian fluid models are often used to describe the rheology of blood.

Model (Non-Newtonian Properties)	Equation	Constants
Power law(shear thinning)	$\mu = k\dot{\gamma}^{n-1}$	$n = 0.828$, $k = 0.00927$ Pa.s (Kim et al., 2000) $n = 0.708$, $k = 0.017$ Pa.s (Shibeshi and Collins, 2005)
Powell-Eyring(shear thinning)	$\mu = \mu_{\infty} + \frac{(\mu_0 - \mu_{\infty}) \sinh^{-1}(\lambda\dot{\gamma})}{\lambda\dot{\gamma}}$	$\mu_0 = 0.056$ Pa.s, $\mu_{\infty} = 0.00345$ Pa.s, $\lambda = 5.383$ s, (Sequeira and Janela, 2007)
Carreau(shear thinning)	$\mu = \mu_{\infty} + \frac{\mu_0 - \mu_{\infty}}{(1 + (\lambda\dot{\gamma})^a)^{2/(n-1)}}$	$\mu_0 = 0.16$ Pa.s, $\mu_{\infty} = 0.0035$ Pa.s, $\lambda = 8.2$ s, $n = 0.2128$, $a = 0.64$ (Abraham et al., 2005)
Carreau-Yasuda(shear thinning)	$\mu = \mu_{\infty} + \frac{\mu_0 - \mu_{\infty}}{(1 + (\lambda\dot{\gamma})^2)^{2/(n-1)}}$	$\mu_0 = 0.056$ Pa.s, $\mu_{\infty} = 0.00345$ Pa.s, $\lambda = 3.313$ s, $n = 0.3568$ (Cho and Kensey, 1991)
Cross(shear thinning)	$\mu = \mu_{\infty} + \frac{\mu_0 - \mu_{\infty}}{1 + (\lambda\dot{\gamma})^m}$	$\mu_0 = 0.056$ Pa.s, $\mu_{\infty} = 0.00345$ Pa.s, $\lambda = 1.007$ s, $m = 1.028$ (Cross, 1965)
Casson(yield stress)	$\mu = (\sqrt{\mu_c} + \sqrt{\tau_c / \dot{\gamma}})^2$	$\mu_c = 0.0035$ Pa.s, $\tau_c = 0.005$ N (Shibeshi and Collins, 2005)

2.2.5 Physical principles

Various studies in the literature show that wall shear stress has a significant role in the behavior of the vessel wall. The forming of the dissection, the movement of the flap, and the placement of

a stent also strongly disturb the local hemodynamics and often generate an increase of this stress. Many researchers have focused on the evaluation of this stress in different ways. Some use medical imaging techniques to measure the velocity gradient at the wall and, assuming Newtonian behavior, can deduce this stress's value. Other researchers attempt to calculate it numerically with rheological blood models, but the lack of experimental validation data and the significant disparity between the models make this method still uncertain (Baaijens et al., 1993, Gijsen et al., 1999).

The influence of non-Newtonian effects is greatly dependent on the shape and size of the flow conduits. Thus, various non-Newtonian rheological behavior and consequently different flow modeling methods should be used for different sections of the circulatory system. In addition, there are many differences in blood transportation mechanisms in this region, such as bulk flow in big arteries compared to diffusion or perfusion in capillaries.

We can distinguish the vascular tree by the magnitude in 3 parts (Table 2.2): large blood vessels which primarily apply to arteries and veins, medium blood vessels which involve the terminal of arteries and veins, and small blood vessels which include capillaries and possibly arterioles.

Table 2.2: Average dimensions of the vascular tree (according to O'Rourke et al. (1998))

Name	Level	Inlet diameter (mm)	Outlet diameter (mm)	Average inlet diameter (mm)	Total surface (cm ²)	Number
Aorte	1	20	7	20	3.2	1
Large arteries	2	1.8 – 10	1.8	3.2	3.4	20
Main branches	3	1.0 – 4.0	1	3.4	3.4	260
Secondary branches	4	0.4 – 2.0	0.4	0.8	4	800
	5	0.2 – 0.8	0.2	0.31	5	7×10^3
Tertiary branches	6	0.1 – 0.4	0.1	0.16	6	3×10^4
Terminal arteries	7	0.04 – 0.2	0.04	0.08	10	2×10^5
Terminal branches	8	0.025 – 0.1	0.025	0.032	16	2×10^6
Arterioles	9	0.015 – 0.06	0.015	0.02	25	8×10^6
	10	0.008 – 0.03	0.008	0.012	35	3×10^7
Capillaries	11	0.008 – 0.01	0.008	0.008	80	2×10^8

The work of Trimarchi et al. (2011) shows that at the level of acute type B aortic dissection, the median aorta diameter was 4.1 cm (range 2.1–13.0 cm). As a result, we regard blood to behave basically like a Newtonian fluid in the presence of aortic dissection. One explanation is that blood in such large lumens and cavities is often treated to very high shear rates. Therefore, the non-Newtonian effects that occur at low shear rates dissipate (Perktold et al., 1999). Additionally, the blood seems to be a homogenous continuous media at this large scale due to the decreasing impact of blood cell aggregation (Box et al., 2005). At this size, the contact between blood cells is also limited due to their prominent elastic characteristics. However, for a complete bio-faithful aortic dissection model, non-Newtonian effects are significant even in the cavities and arteries and should be included in the flow model. Another point is that some areas of the large vessel network can contain low-shear zones, such as bends and bifurcation junctions (Lou and Yang, 1993). Thus non-Newtonian effects in large vessels may be significant in some cases, such as when these zones play a bring to the attention in blood flow due to a diseased condition.

Numerous mathematical and numerical models have been developed to simulate the flow of blood via large individual arteries. For Newtonian fluids, these models include the one-dimensional

elastic Navier-Stokes and the rigid Hagen-Poiseuille, as well as a variety of other non-Newtonian rheological models, such as Cross and Carreau-Yasuda, as previously mentioned. Blood flow properties in single large arteries are derived analytically or numerically from these mathematical models, for example, using finite element or finite difference methods. Most non-Newtonian fluid models used are generalized Newtonian models, which do not account for time-dependent elastic or thixotropic effects. Additionally, analytical non-Newtonian models are typically applicable to rigid tubes alone. However, some efforts have been made in this context to extend Poiseuille flow to non-Newtonian rheological elastic vessels (Vajravelu et al., 2011). It is also possible to develop non-Newtonian models for elastic vessels using numerical methods.

2.2.5.1 Blood flow simplified models

Even in big arteries, when the Reynolds and Womersley numbers are high, the fluid's viscosity has a significant impact on the flow. Flow-induced viscous stresses play an important role in determining the stability and turbulence of arteries and whether the streamline will separate (diverge) from the vessel wall at branching points or at segments where a sudden change in cross section occurs, such as in stenosis or dissection. As a physical phenomenon, viscosity is a dissipation mechanism, and as such, it should manifest itself in the attenuation of velocity and pressure in the direction of propagation. However, it is discovered that the effect of viscoelastic dissipation in the vessel wall is significantly greater than the effect of viscous dissipation in the blood. As a result, we must consider the coupled fluid-structure interaction (FSI) issue while developing our solution. On the third chapter, we will implement not only the blood flow numerical simulation with computational fluid dynamics (CFD), but also the FSI simulation to observe and validate the interaction between the fluid and solid.

Hence, considering the large vessels, we assume that the blood flow is a Newtonian fluid. And in Chapter 3 we will verify our hypothesis by a numerical simulation of the blood flow.

2.3 Rheology of the vascular wall

2.3.1 Constitution of the arterial wall

Understanding the mechanical behavior and hence the physiology of the arterial wall is essential for understanding hemodynamics in physiological situations and various vascular disease situations, as the mechanical properties of the arterial wall greatly influence the characteristics of blood flow.

The blood vessel wall has a layered structure with three fundamental constituents: the elastin fibers, the collagen fibers, and the smooth muscle fibers that perform a very particular function. On the one hand, the viscoelastic behavior of the walls modifies the pulse waveform of cardiac output and attenuates pressure waves and blood flow in the arterial system. On the other hand, the activity of the smooth muscles in the arterial wall regulates and adapts the blood flow to the oxygen requirements of the various organs (Jaffrin and Goubel, 1998).

All vascular walls (arteries, veins, heart) are lined internally with a layer of flat cells called the endothelium. This cell formation provides a smooth surface for the blood to pass through

and remains permeable to water and red blood cells. The arterial walls are usually circular in cross-section. The thickness of the artery wall varies along the artery tree but the ratio of thickness to diameter remains close to a constant of about 0.1 for adults (Jaffrin and Goubel, 1998). The proportions of the different fibers also vary along the arterial tree: the number of smooth muscle fibers increases as one moves away from the heart, progressively shifting from an elastic artery to a muscular artery.

We can distinguish two types of arteries:

- Elastic arteries, such as the aorta and carotid arteries, are located near the heart and have a larger diameter than other arteries. They have more elastin fibers to dampen the pressure wave coming from the heart.
- Muscular arteries (distal arteries), such as the femoral and cerebral arteries, are smaller than the elastic arteries and are considered viscoelastic structures. As the distance from the heart increases, the proportion of elastin fibers decreases, and the ratio of smooth muscle cells increases.

Elastin and collagen are proteins assembled in the form of fibers. They are responsible for the elastic behavior of the wall for relatively small deformations under normal physiological pressure conditions. Elastin is an expandable fiber with an elastic modulus of 10^2 kPa (Bank et al., 1996) that is primarily responsible for the aorta's elastic properties at modest strain. When subjected to small deformations, elastin fibers have a constant elastic modulus of about 600 kPa. When pressure rises throughout the cardiac cycle, elastin stores energy and assists the tissue in resuming its original form when pressure decreases. Collagen fibers contribute to the stiffness and strength of vessel walls. The stiffness of collagen is about 1000 times higher than that of elastin which makes a negligible contribution at low strains. However, once in tension, it gives the arterial wall significant stiffness. This stiffness depends on the arrangement of the fibers (Jaffrin and Goubel, 1998). Moreover, fibers display low-level organization at low pressures and high-level circumferential alignment as pressure increases. The artery stiffens, thus limiting aortic distension.

These different fibers of the arterial wall have a preferential orientation, which has been extensively studied in the literature to understand and better model the mechanical behavior of the wall. Figure 2.13 illustrates the preferred direction of these fibers and shows two distinct types of fibers (Schriebl et al., 2012). They are found in different layers oriented helicoidally with an angle varying about 45° in relation to the orthoradial direction. In addition, the smooth muscle fibers make little contribution to the mechanical behavior of the arteries. However, by contraction, they regulate their elasticity and their diameter to respond to the various physiological demands during the cardiac cycle. These components are distributed and oriented differently along the vessel to accommodate a variety of loads. For instance, the thoracic aorta's elastin-collagen ratio is about 60%, while the abdominal aorta's ratio is 70% (O'Rourke et al., 1998).

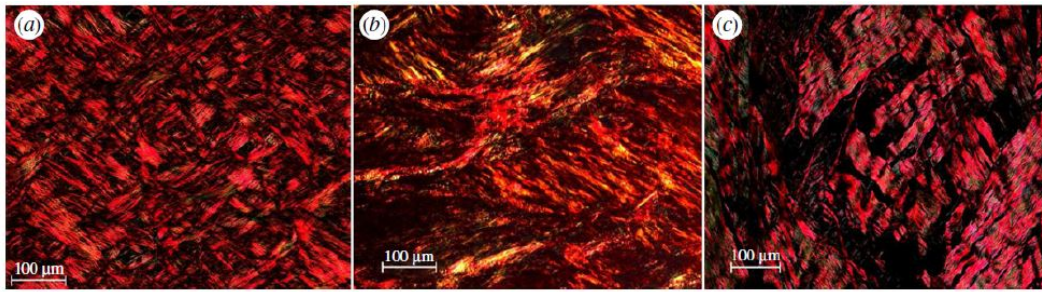


Figure 2.13: Microscopy in polarized light of sections of (a) intima, (b) media, (c) adventitia of a thoracic aorta (horizontal and vertical directions of the image represent the orthoradial and axial directions of the artery, respectively) (Schriefel et al., 2012)

Arterial wall is composed of three concentric and relatively well-separated layers or tunics: intima, media, and adventitia (Figure 2.14).

Intima :

The intima is the innermost layer of the artery. It consists of a single layer of endothelial cells lining the inner surface of the wall in contact with the blood. These cells interlock to form a smooth surface that helps reduce friction between the blood and the inner surface of the vessel. They rest on a thin subendothelial layer whose thickness varies with topography, age, and disease. However, for young and healthy muscular arteries, this layer is almost non-existent, and the very thin intima has a very low contribution to the mechanical behavior of the artery. But with older and diseased arteries, this contribution becomes essential as the intima thickens and becomes stiffer. Thus, pathological intimal changes are associated with significant alterations in the mechanical behavior of the artery, distinguishing them from healthy arteries (Learoyd and Taylor, 1966) . For example, aortic dissection occurs when a rupture in the aortic intima allows blood to push its way through the vessel's other layers, producing an intimal flap that splits the aorta into a true and false lumen.

Media :

The media is the middle layer of the artery. It is usually the thickest wall layer and consists of an arranged network of smooth muscle cells separated by fine elastin and collagen fibers. The helical orientation of the smooth muscle fibers leads to a decrease in the artery's diameter during their contraction and an increase in diameter during their relaxation. Due to the high concentration of these smooth muscle cells, the media is mainly responsible for the viscoelastic character of the artery.

Adventitia :

The adventitia is the outer layer of the arterial wall. It contains mainly collagen and nerves, allowing the stimulation of smooth muscle cells. Its thickness depends primarily on the artery's type (elastic or muscular), its physiological function, and location. Collagen fibers are oriented in helices and serve to reinforce the arterial wall, contributing to its stability.

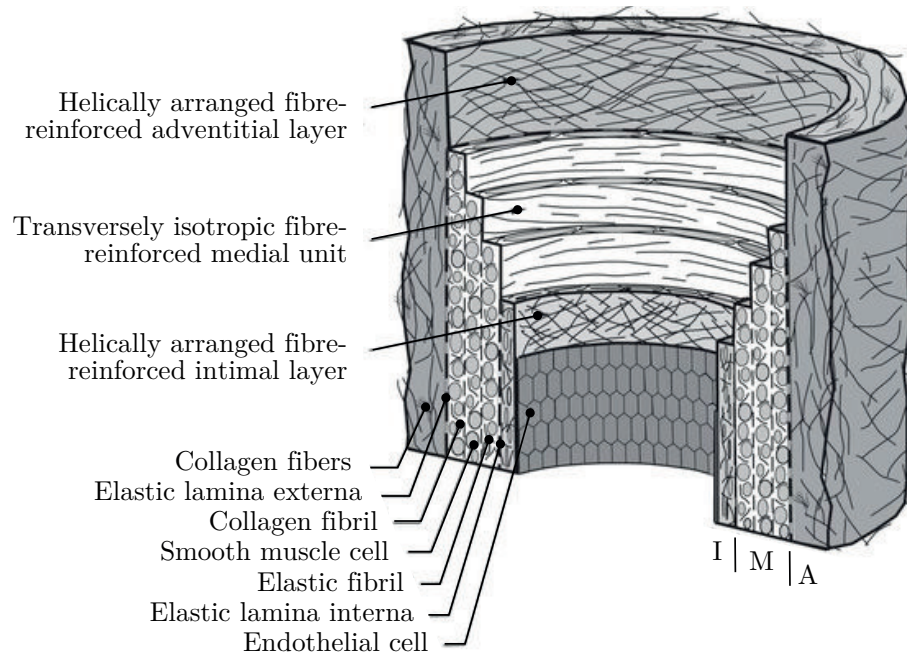


Figure 2.14: Schematic of the arterial wall structure with its three layers: intima (I), media (M) and adventitia (A) (Holzapfel et al., 2000)

The proportions of the layers of the vascular wall and their composition vary according to the location of the vessel in the arterial tree and their function. Arteries, which carry oxygen, have a thicker middle layer than veins, which carry blood back to the heart. Figure 2.15 illustrates these observations by comparing the aorta and the vena cava, roughly similar in diameter. The media in the aorta contains a lot of elastin and is thicker than the media in the vein. The latter has numerous lamellae of elastin and smooth muscle cells. Unlike the media, the adventitia is thicker in the vein than in the aorta.

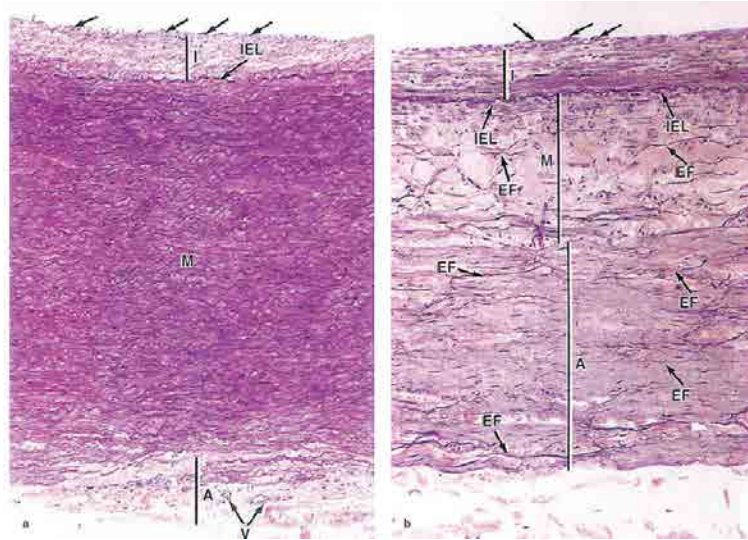


Figure 2.15: A comparison of the 3 layers of the largest artery and vein: the aorta (a) and the vena cava (b). (I) Intima (IEL) Internal elastic lamina (M) Media (EF) Elastic fibers (A) Adventitia (V) Small vessels. (Mescher, 2013).

This description is for a normal, healthy aorta; nevertheless, arteries undergo modification during life due to physiological load, age (Figure 2.16), and diseases. Each of the aortic wall components, i.e., elastin, collagen fibers, and smooth muscle cells, will change with age. With aging, elastin fibers fragment, collagen becomes more apparent at the expense of smooth muscle cells. The aortic wall weakening leads to the dilation of the lumen and elongation of the aorta, which generally characterizes it in older people. These changes are accompanied by changes in the structure of the wall, especially the middle layer. Tension on the aortic wall increases shear stress, and this process is accelerated by hypertension, especially when pulsatile forces are high. The combination of hereditary, degenerative, mechanical, and hemodynamic factors adversely affects the medial layer of the aortic wall, leading to dilation of the artery and setting the stage for diseases such as an aneurysm or aortic dissection.

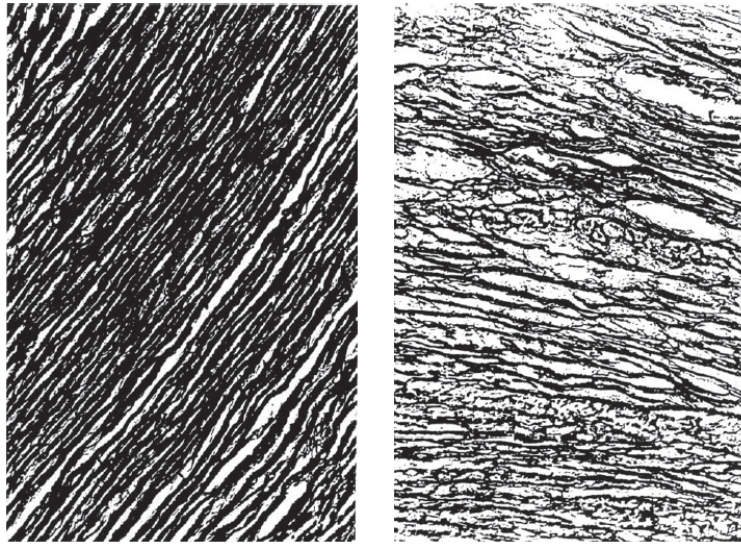


Figure 2.16: Histology of the normal aorta of a child (A) and an elderly adult (B). With aging, elastic fibers fragment, collagen becomes more apparent, and smooth muscle cells decrease (magnification $\times 450$) (O'Rourke et al., 1998)

What's more, it is usually accompanied by calcification of the arterial wall in aortic aneurysm or aortic dissection disease. Arterial wall calcification is a manifestation of abnormal deposits of calcium and phosphorus in the vessel wall. Aortic dissection is sometimes associated with calcifications of the false lumen's outer wall (Hachiya et al., 1993). Because the intima has been ripped away at the false lumen's edge, it is very probable that these calcifications are situated in the tunica medium or tunica adventitia (Figure 2.17). Therefore, in aortic dissection disease, the rheology of the artery should consider the calcification phenomenon.

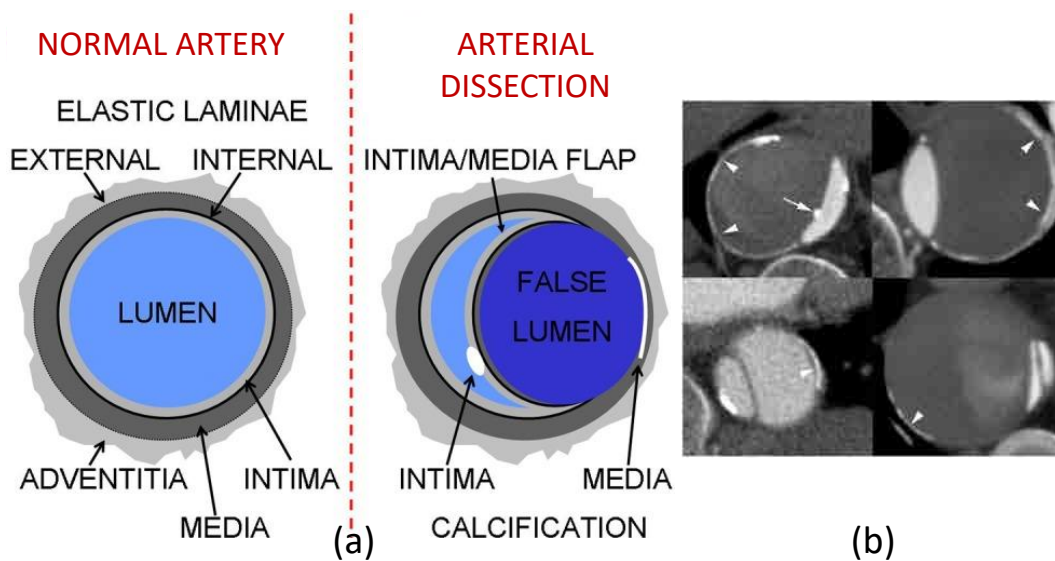


Figure 2.17: (a) A normal and dissected aorta, as well as the location of calcifications, are shown. (b) CT of patients with aortic dissection and observed the calcification at the outer edge of false lumen (de Jong et al., 2014).

2.3.2 Mechanical properties of arteries

It is necessary to understand the mechanical behavior of the aortic tissue since it is highly stressed during stent deployment. Many hypotheses formulated to understand its behavior better are detailed below.

Incompressibility :

Experimental measurements in traction and inflation show that the arterial wall is virtually incompressible, comparing their volume before traction and in the stretched state. The results of these studies (Carew et al., 1968) indicate that the volume change was only 0.165% when the arterial segment was inflated in vivo by a pressure of 181 mm Hg. The slight volume changes observed result from the expulsion of water from the tissue: they are negligible and allow the arterial wall to be treated as an incompressible material.

Anisotropy :

The mechanical behavior of the arterial wall is not isotropic. When arterial samples are subjected to an equivalent force in the longitudinal and orthoradial directions, the mechanical behavior of the tissue is different. However, due to the architecture of the aortic wall, the tissue has a different mechanical reaction. Arterial tissue may be regarded as an orthotropic material, even though it is often referred to as isotropic if the degree of anisotropy is small or the internal pressure variations are small (Peterson et al., 1960).

Nonlinear large deformations :

Arterial walls undergo large deformations when subjected to physiological pressure. Deformation caused by pressure variations during the cardiac cycle is 1 – 2% for muscular arteries and can reach 10 – 15% for elastic arteries such as the aorta or carotid artery. The wall is easily deformed at low pressure because the collagen fibers forming loose loops are not stressed, and only the elastin fibers are stretched. At higher pressure, the wall becomes rigid as the collagen fibers are also stretched (Peterson et al., 1960, Jaffrin and Goubel, 1998).

Viscoelasticity :

A hysteresis loop (Figure 2.18) appears on the pressure-strain plot during experimental tests with dynamic loading of an arterial wall sample. It implies that the wall's stress state is determined not only by the corresponding deformation but also by previous deformations. The components of the wall can no longer be considered elastic and therefore constitute a viscoelastic material. Simple tensile tests show both stretching and relaxation.

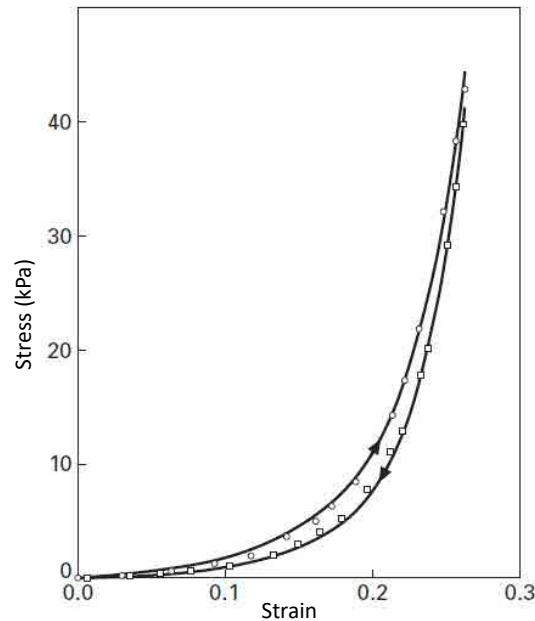


Figure 2.18: Stress-strain plots for a human vena cava sample. The circles represent loading, and the squares represent unloading (Meyers and Chawla, 2008)

Residual stresses :

The arteries underwent retraction after longitudinal and circumferential cutting. The arterial segments opened to form approximately a sector of a circle (Vaishnav and Vossoughi, 1987). Figure 2.19 (Holzapfel et al., 2007) shows that the segments are spontaneously opened. This form constitutes a zero-stress state and reveals the existence of zero transverse pressure pre-stresses. The inner part of the wall is under compression, and the outer part is under tension. The opening angle is generally the parameter chosen to describe the level of prestress in the arterial segment. Experimental work has shown a variation in the opening angle along the arterial tree. Fung and Liu (1989) showed that this angle is about 180° for the ascending aorta. These results were also subsequently demonstrated as Holzapfel et al. (2007), having performed a study on a human aorta, observed that the deformations lasted 16 hours after cutting the aorta. The opening angle was more than 180° in the circumferential direction, while a small curvature was formed in the longitudinal direction (Figure 2.19). According to them, these residual strains are not equal in the three layers of the artery and in the two cutting directions, which means that the distribution of residual stress in the arterial wall is not the same.

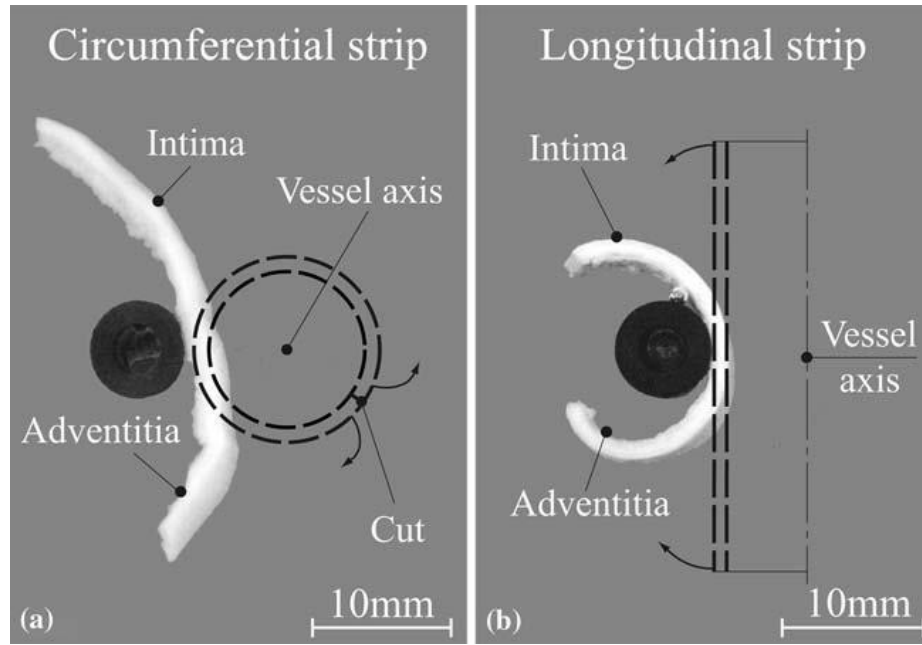


Figure 2.19: The effects of residual stresses in the longitudinal and orthoradial directions of a healthy aorta (Holzapfel et al., 2007)

2.3.3 Different mechanical behavior models

The study of the mechanical behavior of the materials of the vascular wall allows us to know its response to a given solicitation. The objective of mechanical behavior models is to reproduce numerically and as close as possible the observations made experimentally. Each model can therefore be formulated from the fundamental equilibrium relations of the mechanics of continuous media. Relations of elastic, hyperelastic, viscoelastic or poroelastic behavior have been used to describe the mechanical properties of arterial tissue. Hyperelasticity reflects the highly nonlinear behavior of a material, whereas viscoelasticity includes time-dependent mechanical responses and is appropriate for modeling relaxation phenomena. On the other hand, poroelasticity considers the material as a fluid-saturated medium and is suitable for studying fluid movements in the arterial wall. Some models of isotropic and anisotropic behavior used in the literature to describe the mechanical behavior of arterial tissue are presented in this section.

2.3.3.1 Isotropic hyperelastic models

A hyperelastic model assumes a potential internal energy density Ψ , a scalar function of the deformation measure. We consider a solid subjected to large deformations. F is the gradient tensor of the transformation from the initial configuration Ω_0 to the current deformed configuration Ω_t . We note X the position of a point in Ω_0 and x the position of this same point after deformation in Ω_t . The gradient tensor of the transformation is written as:

$$F = \text{grad}_X(x)$$

This tensor is not ideal to describe the deformation of the structure. It is not zero for rigid body motions, and it represents all the deformation: the change in length of the infinitesimal elements

and their orientation. However, a pure rotational movement does not generate stresses, and it is preferable to use a measure of deformation that does not consider this rigid rotation. Therefore, it is preferable to use the straight Cauchy-Green strain tensor :

$$C = F^T F = U^2$$

with U the elongation tensor defined in terms of the principal elongation ratios λ_1, λ_2 and λ_3 :

$$U = \begin{pmatrix} \lambda_1 & 0 & 0 \\ 0 & \lambda_2 & 0 \\ 0 & 0 & \lambda_3 \end{pmatrix}$$

The three invariants of the Cauchy-Green tensor C are given by :

$$\begin{aligned} I_1 &= tr(C) \\ I_2 &= \frac{1}{2}[tr(C)^2 - tr(C^2)] \\ I_3 &= J^2 = det(C) \end{aligned}$$

where J is the Jacobian of the transformation, which characterizes the variation in the volume of the material. For an incompressible material, $J = 1$. The arterial wall can be considered incompressible under [Bergel \(1961\)](#) physiological conditions. However, the state of deformation alone does not allow the determination of the state of stress, known at a hydrostatic pressure noted p . The tension is then written in the form :

$$S = 2 \frac{\delta \Psi}{\delta C} - p C^{-1}$$

where Ψ is the strain energy density, and S is the Piola-Kirchhoff II stress tensor.

There are many isotropic hyperelastic models in the literature. Their main strain energy density functions are summarized in Table 2.3. Polynomial models are the most common and were introduced by [Rivlin and Saunders \(1951\)](#). They are formulated in terms of deformation invariants of the Cauchy-Green tensor and are often called the generalized Rivlin models. A little earlier, a specific model was developed by [Mooney \(1940\)](#) and [Rivlin \(1948\)](#), called the Mooney-Rivlin model. It constitutes a particular form of the generalized model. The Ogden model ([Ogden, 1972](#)) is formulated in terms of elongation ratios and material constants, whereas the models of Neo-Hookean (1943)([Kim et al., 2012](#)), [Demiray \(1972\)](#), [Vito and Hickey \(1980\)](#) and [Yeoh \(1990\)](#) depend only on the first deformation invariant. The model of [Raghavan and Vorp \(2000\)](#) is a quadratic model, and the parameters have been identified with uniaxial traction tests.

Table 2.3: Principal strain energy density functions for isotropic incompressible hyperelastic models (Holzapfel, 2000)

Model	Function
Mooney (1940)	$\Psi = \Psi(I_1, I_2) = C_{10}(I_1 - 3) + C_{01}(I_2 - 3)$ C_{10} and C_{01} are material parameters characterizing the deflection tensor of the deformations, $\mu = 2(C_{10} + C_{01})$ is the initial shear modulus.
Neo-Hookean (1943)	$\Psi = \Psi(I_1) = C_{10}(I_1 - 3)$ (Kim et al., 2012) C_{10} is a material parameter.
Ogden (1972)	$\Psi = \Psi(\lambda_1, \lambda_2, \lambda_3) = \sum_{i=1}^N \frac{\mu_i}{\alpha_i} (\lambda_1^{\alpha_i} + \lambda_2^{\alpha_i} + \lambda_3^{\alpha_i} - 3)$ λ_i are the principal aspect ratios of the left Cauchy-Green tensor, N, α_i, μ_i are material parameters, $\mu = \frac{1}{2} \sum_{i=1}^N \alpha_i \mu_i$ is the initial shear modulus.
Demiray (1972)	$\Psi = \Psi(I_1) = \frac{\mu}{2\alpha} (e^{\alpha(I_1-3)} - 1)$ μ and α are positive constants : μ is the shear modulus and α is the degree of non-linearity of the material.
Yeoh (1990)	$\Psi = \Psi(I_1) = C_1(I_1 - 3) + C_2(I_1 - 3)^2 + C_3(I_1 - 3)^3$ C_1, C_2 and C_3 are material parameters, $\mu = 2C_1$ is the initial shear modulus.
Raghavan and Vorp (2000)	$\Psi = \Psi(I_1) = \alpha(I_1 - 3) + \beta(I_2 - 3)^2$ α and β are material parameters.

2.3.3.2 Anisotropic hyperelastic models

An important mechanical property of soft tissue is the anisotropy that results from tensile stress. This finding is associated with the different collagen fibers distributed in the material that give it directional properties (Holzapfel and Ogden, 2003). Uni-axial traction tests (Raghavan et al., 1996) first observed the nonlinear and anisotropic behavior of the aortic wall, the observations of which led to the establishment of different models. These models (Table 2.4) are either based on the decomposition of the strain energy potential into an isotropic and an anisotropic part. They are expressed about Green-Lagrange finite deformations in the circumferential and axial directions ($E_{\theta\theta}, E_{zz}$) and defined with material dependent parameters. For example, the exponential model of Fung et al. (1979) observed the mechanical behavior of rabbit arteries subjected to internal pressure and longitudinal stretch. They observed the behavior of biological tissues during repeated loading and unloading. This model has been widely used and adapted in the literature, but Humphrey (1995) proposed the most general form. Takamizawa and Hayashi (1987) showed that the strain energy functions of the exponential form better described the mechanical behavior of canine carotid arteries than the polynomial forms. They proposed a logarithmic model considering residual stresses. Other models have an approach based on the invariants of the Cauchy-Green tensor and have been formulated to come closer to the experimental results (Gasser and Holzapfel, 2006, Basciano and Kleinstreuer, 2009, Rodríguez et al., 2009, Babu et al., 2015). In order to take into account the

anisotropy mainly due to the collagen fibers of the aortic tissue, two preferred directions of these fibers are introduced in the anisotropic models (Figure 2.20). These directions are defined by :

$$M = \cos \phi e_1 + \cos \phi e_2, M' = \cos \phi e_1 - \cos \phi e_2$$

where the angle ϕ is a constant and e_1, e_2 are the directions of the Cartesian reference frame. These two vectors allow us to define new invariants to characterize the anisotropy of the material:

$$I_4 = MCM, I_4 = M'CM'$$

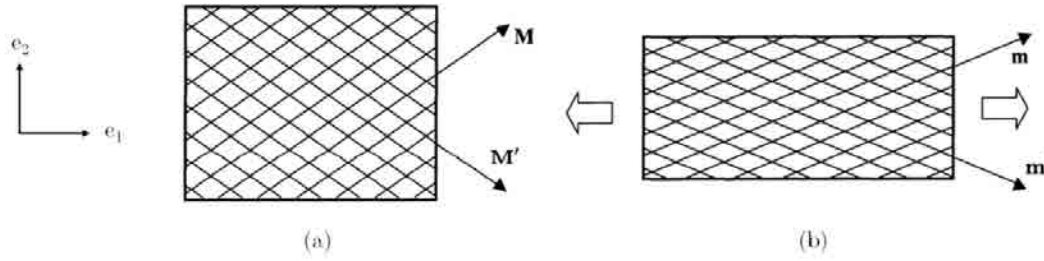


Figure 2.20: Preferred directions of collagen fibers introduced in anisotropic models (a) undeformed configuration (b) deformed configuration (Holzapfel and Ogden, 2003)

Model of Rodríguez et al. (2009) contains a parameter ρ that characterizes the degree of anisotropy of the material: when $\rho = 0$, the material becomes isotropic. The parameters I_4^0 and I_6^0 characterize the initial waviness of the collagen fibers. The set of parameters of these models is obtained by an optimization process using experimental data.

The primary energy functions, detailed in Table 2.4, describe the anisotropic hyperelastic mechanical behavior of arterial walls. They have been established with a phenomenological approach that describes the macroscopic behavior of the tissue based on experimental data. However, this modeling does not allow a correlation between the deformation mechanisms and the known microscopic structure of the material since the parameters of the models have no direct significance with the latter.

Table 2.4: Principal strain energy density functions for incompressible anisotropic hyperelastic models

Model	Function
Fung et al. (1979)	$\Psi = \frac{C}{2\rho_0} e^Q$ <p>with $Q = \alpha_1(E_{\theta\theta}^2 - E_{\theta\theta}^{*2}) + \alpha_2(E_{zz}^2 - E_{zz}^{*2}) + 2\alpha_4(E_{\theta\theta}E_{zz} - E_{\theta\theta}^{*2}E_{zz}^{*2})$</p>
Takamizawa and Hayashi (1987)	$\Psi = -C \ln(1 - \frac{1}{2}E_{\theta\theta}\epsilon_\theta^2 - \frac{1}{2}E_{zz}\epsilon_z^2 - E_{\theta z}\epsilon_\theta\epsilon_z)$
Humphrey (1995)	$\Psi = D_1(e^Q - 1)$ <p>with $Q = \alpha_1 E_{\theta\theta}^2 + \alpha_2 E_{zz}^2 + \alpha_3 E_{rr}^2 + 2\alpha_4 E_{\theta\theta}E_{zz} + 2\alpha_5 E_{zz}E_{rr} + 2\alpha_6 E_{rr}E_{\theta\theta} + \alpha_7 E_{\theta z}^2 + \alpha_8 E_{rz}^2 + \alpha_9 E_{r\theta}^2$</p>
Rodríguez et al. (2009)	$\Psi = U(J) + C_{10}(I_1 - 3) +$ $\frac{k_1}{2k_2} (e^{k_2[(1-\rho)(I_1-3)^2 + \rho(I_4 - I_4^0)^2]} - 1)$ $\frac{k_3}{2k_4} (e^{k_4[(1-\rho)(I_1-3)^2 + \rho(I_6 - I_6^0)^2]} - 1)$
Basciano and Kleinstreuer (2009)	$\Psi = \alpha(I_C - 3)^2 + \beta(IV_C - 1)^6 + \delta(VI_C - 1)^6$
Babu et al. (2015)	$\Psi = \frac{k_1}{2k_2} \sum_{i=4,6} (e^{k_2(I_i-1)^2} - 1)$

2.3.4 Experimental tests on arteries

There are different techniques for mechanical characterization of aortic tissue: pressurization tests, uniaxial and biaxial tensile tests, aortic expansion test, and indentation methods. These methods have demonstrated the nonlinear, anisotropic, and viscoelastic character of the aortic wall and the heterogeneous behavior of both healthy and diseased walls.

2.3.4.1 Pressurization tests

Pressurization tests characterize the swelling of the aorta under the effect of internal pressure. This method is performed both ex-vivo (Roy, 1881, Bergel, 1961, Wolinsky and Glagov, 1964) and in-vivo (Peterson et al., 1960, Imura et al., 1990) and is often applied to animal arteries but more recently to human aortas (Menut, 2017). During these tests, the evolution of the diameter is measured and evaluated as a function of pressure. In 1880, Roy (1881) studied rabbit and dog aorta samples and showed that aortic tissue did not follow Hooke's law: the extension of the aorta is not proportional to the force applied to it. Subsequent studies (Bergel, 1961) then showed that the elastic modulus of the aortic wall is relatively low when swelling occurs at pressures below the diastolic aortic pressure but increases very rapidly with increasing pressure. Later, Wolinsky and Glagov (1964) then focused on the structure of the aortic media in the rabbit to understand this behavior. Under physiological pressures, the media behaves as a two-phase material: collagen fibers aligned along the circumference of the vessel support tangential forces while the elastin network distributes the forces uniformly over the wall. With in-vivo experiments and measurements, some

authors (Peterson et al., 1960, Imura et al., 1990) have highlighted the viscoelastic character of the arterial wall and its stiffness according to the cardiac cycle. More recently, ex-vivo swelling tests performed on a thoracic aorta section (Figure 2.21, Avril et al. (2010)), coupled with image correlation displacement field measurements, have allowed to fit, using an inverse method, a model of anisotropic hyperelastic behavior.

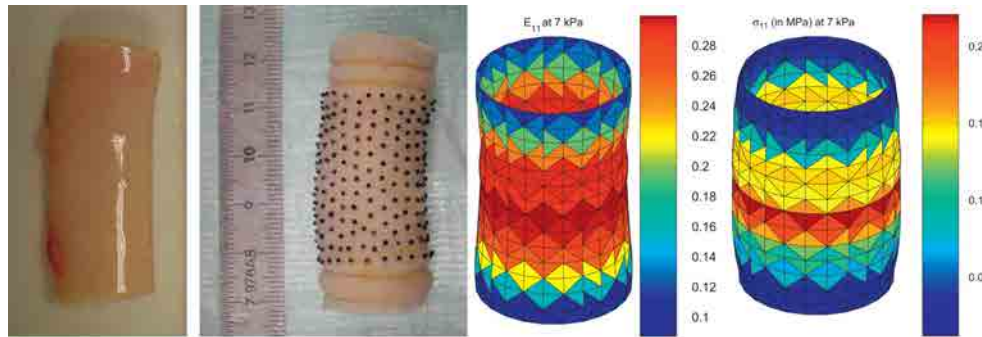


Figure 2.21: (Left) Image of the thoracic aorta section used for testing (Middle) Green-Lagrange strains in the initial configuration (Right) Cauchy tensor stresses in the deformed configuration (Avril et al., 2010).

In conclusion, all the curves showing the progression of stresses as a function of arterial deformation show its stiffening with age and pathology and the significant disparity between the individuals. The measurement of the modulus of elasticity does not provide a precise indication of the actual mechanical behavior of the tissue. It is very often supplemented by standard uni-axial and bi-axial tensile tests.

2.3.4.2 Uniaxial traction test

Uni-axial tensile tests involve a sample held at both ends and stretched at constant speed. The required tensile force as a function of elongation is then determined. A tensile curve can be drawn from these tests from which the modulus of elasticity, yield strength, and tensile strength can be deduced. The work of Raghavan et al. (1996) shows uniaxial tensile curves obtained on human samples taken in the longitudinal direction from healthy aortas and samples taken in the longitudinal and orthoradial directions from pathological aortas with abdominal aortic aneurysms (AAA) (Figure 2.22). This figure shows the nonlinear hyperelastic behavior of healthy and pathological arterial tissue and the strain and stress values reached before sample rupture.

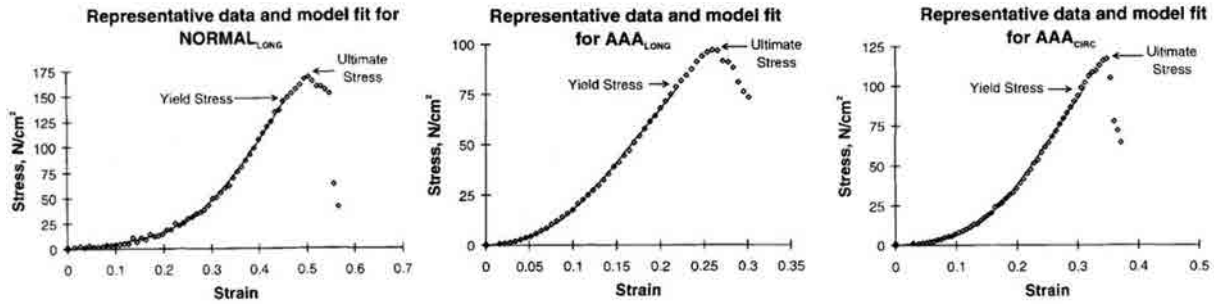


Figure 2.22: (Left) Stress versus relative elongation in the longitudinal direction of a healthy aorta (Middle & Right) Stress versus relative elongation in the longitudinal and orthoradial directions of a pathological aorta with AAA (Raghavan et al., 1996).

Maximum strains at failure are in the range of 50% for healthy aorta and 25 to 35% in the longitudinal and orthoradial directions for the pathological aorta. At the same strain level, the stresses are higher for the diseased aorta than for the healthy aorta, indicating greater stiffness of the diseased arterial tissue. This stiffness also appears to be greater in the longitudinal direction than in the orthoradial direction for the pathological aorta.

There is much work on AAA, but there are relatively few studies on aortic dissection, especially dissection of aortic intima and media. The recently work of Sommer et al. (2008), Ríos-Ruiz et al. (2021) investigated the processes through which fissures propagate after aortic dissection. They performed uniaxial tension tests in the radial direction on healthy porcine or human abdominal aortas to determine the dissection strength. We can refer to the work of Menut (2017) who perform experimental uniaxial tension on the abdominal aorta for our study of the arterial wall dissection. Nevertheless, the models proposed by Ogden (1972), Vito and Hickey (1980), Fung et al. (1979), Humphrey (1995) are too complex or sometimes too far from reality. There are many isotropic hyperelastic models in the literature (Chapter 2 - 2.3.4 Different models of mechanical behavior). The polynomial models, introduced by Rivlin and Saunders (1951), are the most widespread and formulated in terms of deformation invariants of the Cauchy-Green tensor. For this reason, Menut (2017) have chosen to use the Mooney-Rivlin model, which has limitations, mainly in terms of isotropy. Nevertheless, given the wide range of individual differences in age, gender, and physical condition, this model seems to be acceptable. As the two parameters Mooney-Rivlin model could not represent the non linearities of the material correctly and the seven parameters model was not complex enough to identify these parameters, Menut (2017) chosen the five parameters model, a compromise between nonlinearity and complexity Rivlin and Saunders (1951).

The strain energy function W chosen to calculate the coefficients of the fitting curve depends on the invariants of the Cauchy-Green tensor. It has the following form:

$$W = C_{10}(I_1 - 3) + C_{01}(I_2 - 3) + C_{20}(I_1 - 3)^2 + C_{11}(I_1 - 3)(I_2 - 3) + C_{02}(I_2 - 3)^2 \quad (2.1)$$

The limitations of this study are mainly related to the description of the vessel wall, the type of mechanical stresses exerted on the samples, and the isotropic homogeneous law used to describe

their behavior. The aortic wall is not isotropic, and its properties differ in the longitudinal and circumferential directions. Therefore, it is not representative of stressing the material in a single direction but all its stress directions.

2.3.4.3 Biaxial traction test

Bi-axial tensile tests consist of applying stress in two perpendicular directions to a single sample. [Prendergast et al. \(2003\)](#) performed uni-axial and bi-axial tensile tests on porcine aortas and human femoral arteries. By the inverse method, these ex-vivo tests allowed to fit a model of isotropic hyperelastic behavior. A little later, the work of [Avril et al. \(2010\)](#) incorporated the anisotropy of the arterial wall. The stress-stretch curves in Figure 2.23 represent an average of longitudinal and orthoradial stresses. They show that the porcine aorta is less stiff than the human femoral artery, an expected result in view of previous results ([Bergel, 1961](#), [Wolinsky and Glagov, 1964](#)) who have already studied the hyperelasticity of animal arterial tissues. The work of [Prendergast et al. \(2003\)](#) also shows a disparity of results between uni-axial and biaxial tensile tests, testifying to a greater stiffness under orthoradial stress than under longitudinal stress. This result, also observed by [Raghavan et al. \(1996\)](#) in uniaxial tensile tests, can be explained by the constitution of the arterial wall and the orientation of elastin fibers in the arterial tissue.

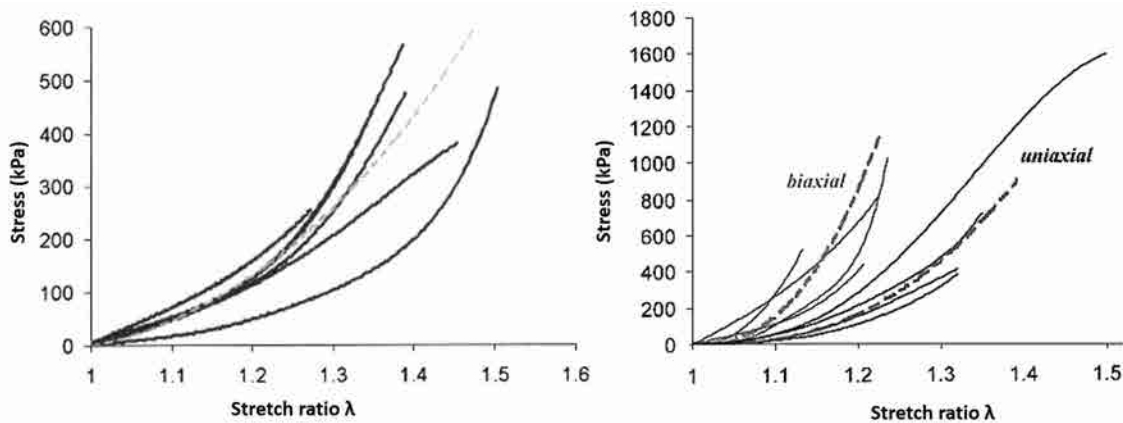


Figure 2.23: (Left) Five biaxial tensile stress-stretch curves for a porcine aorta, with the fitted elastic model (dashed line) (Right) Uniaxial and biaxial tensile stress-stretch curves for a human femoral artery ([Prendergast et al., 2003](#)).

Even while several biaxial tensile tests ([Azadani et al., 2012](#), [Kamenskiy et al., 2014](#)) have been done on healthy samples of the human ascending aorta, there are just a few investigations that have been conducted on dissected samples. The work recently realized by [Deplano et al. \(2019\)](#) performed biaxial tensile testing with samples of healthy and pathological human aortas, as was the case for the work of [Raghavan et al. \(1996\)](#) in uni-axial tensile testing only. [Deplano et al. \(2019\)](#) demonstrated that the flap acted as a linear and anisotropic material, which is consistent with the nonlinear and anisotropic mechanical behavior of the aortic wall. Simplifications were done to minimize computational time and we assumed that aortic wall and flap had a linear isotropic behavior, like in the work of [Menut \(2017\)](#).

2.3.4.4 Aortic expansion test

Pressurization tests, which characterize the swelling of the aorta under internal pressure, are particularly well suited to the morphology and physiology of the artery. Following the previous results obtained with the uniaxial tensile tests and the limitations of this type of mechanical solicitation, it becomes necessary to solicit the material under the most possible physiological conditions. Biaxial tensile tests would allow us to get closer to physical stresses to determine a non-linear behavior. However, they would require cutting the sample and would not consider the effects of residual stresses and strains. They have the advantage of being the most representative for studying the behavior of the aortic wall. In the study of [Menut et al. \(2015\)](#), it was thus chosen to measure the deformation field of the aortic arch by image correlation for a human aorta immersed in water (Figure 2.24). The immersion allows, first, to have better results for the measurement method and get closer to the physiological conditions of the artery. The strain field in the aortic arch of a human aorta submerged in water is measured in [Menut et al. \(2015\)](#), using the stereo-correlation method. Immersion enables more accurate measurement findings and the incorporation of residual stress and strain effects.

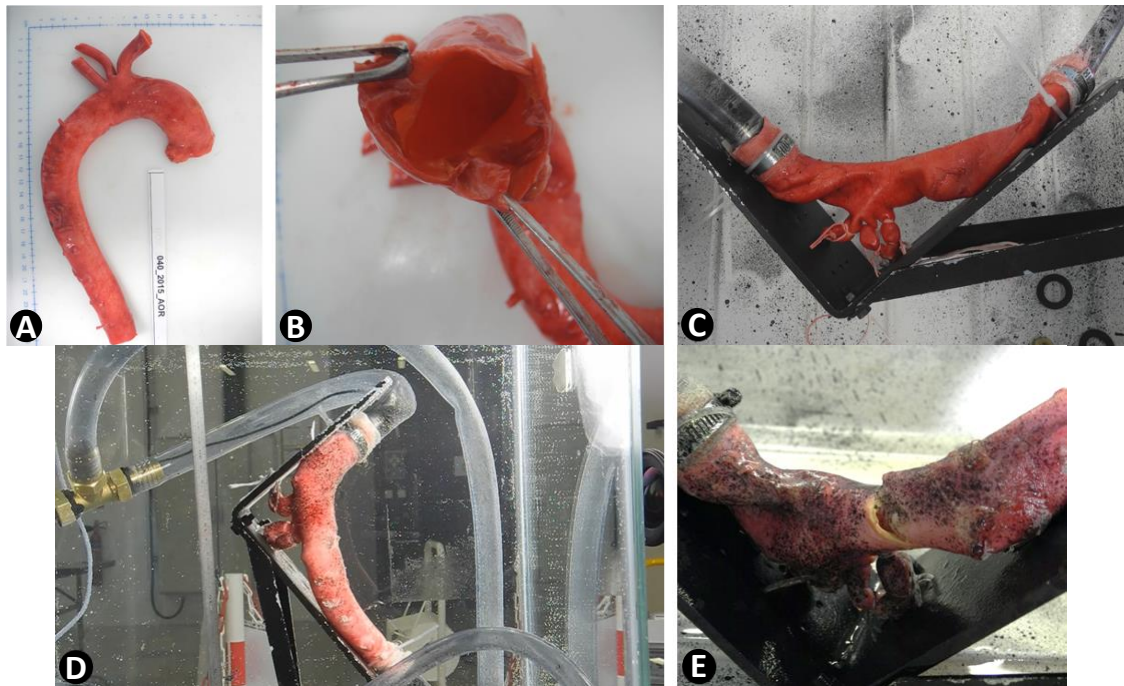


Figure 2.24: (A) Sample cleaned (B) The inside of the thoracic arch reveals no signs of calcification for this fresh sample (C) Installation of the speckled sample on its support (D) Aorta immersed in water before the experiment (E) Rupture on the aortic isthmus ([Menut et al., 2015](#))

The strain energy function W chosen to calculate the coefficients of the fitting curve for this experiment is the same as that selected for the uniaxial tensile tests with the work of [Menut \(2017\)](#) (Equation 2.1). The relationship between mechanical stress and elongation for an incompressible material in a pressurization test is expressed as a function of the principal elongations λ_i . The

principal stresses σ_i of the Cauchy tensor are written as :

$$\sigma_i = \lambda_i \frac{\partial W}{\partial \lambda_i} \quad (2.2)$$

With the hypothesis of an incompressible material, the invariants of the Cauchy-Green deformation tensor depend only on the elongation of the material and become for the swelling test (Mooney, 1940):

$$\begin{aligned} I_1 &= \lambda_1^2 + \lambda_2^2 + \frac{1}{\lambda_1^2 \lambda_2^2} \\ I_2 &= \lambda_1^2 \lambda_2^2 + \frac{1}{\lambda_1^2} + \frac{1}{\lambda_2^2} \\ I_3 &= \lambda_1^2 \lambda_2^2 \lambda_3^2 = 1 \end{aligned}$$

Therefore, the relationships 2.3 and 2.4 can be derived, which relate principal stresses with elongations and strain invariants. These relationships are used for the fitting curve in Figure 2.25, based on the results of swelling tests performed on aortic arch samples (Menut, 2017).

$$\begin{aligned} \sigma_1 &= \lambda_1 [(C_{10} + 2C_{20}(I_1 - 3) + C_{11}(I_2 - 3))(2\lambda_1 - \frac{2}{\lambda_1^3 \lambda_2^2}) + \\ &\quad (C_{01} + C_{11}(I_1 - 3) + 2C_{02}(I_2 - 3))(2\lambda_1 \lambda_2^2 - \frac{2}{\lambda_1^3})] \end{aligned} \quad (2.3)$$

$$\begin{aligned} \sigma_2 &= \lambda_2 [(C_{01} + C_{11}(I_1 - 3) + 2C_{02}(I_2 - 3))(2\lambda_1^2 \lambda_2 - \frac{2}{\lambda_3^2}) + \\ &\quad (C_{10} + 2C_{20}(I_1 - 3) + C_{11}(I_2 - 3))(\lambda_1 \lambda_2 - \frac{2}{\lambda_1^2 \lambda_2^3})] \end{aligned} \quad (2.4)$$

The identification of the hyperelastic Mooney-Rivlin law parameters consisted of a least squares minimization of the deviation between the stress calculated with the experimental values and the stress calculated by the hyperelastic law according to the strain invariants. Table 2.5 summarizes the values of the identified coefficients compared with values from the work of Prendergast et al. (2003) on femoral aorta samples.

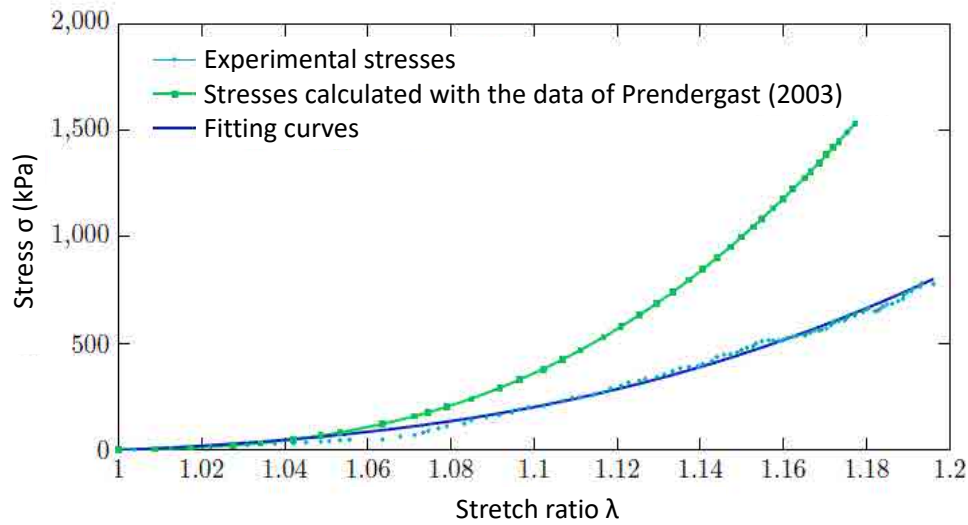


Figure 2.25: Results of swelling tests on a human aortic arch. Experimental data and fitting curves for a 5-parameter Mooney-Rivlin polynomial model (adapted from [Menut \(2017\)](#))

Table 2.5: Coefficients of the 5-parameter hyperelastic Mooney-Rivlin law (equation 2.1) were chosen for the model associated with swelling tests on the human aortic arch.

Coefficients	Values of Prendergast et al. (2003) (MPa)	Values of Menut (2017) (MPa)
C_{10}	0.01890	0.0746
C_{01}	0.00275	0
C_{20}	0.59042	0
C_{11}	0.85748	0.5134
C_{02}	0	0

Therefore, table 2.5 shows that the work of [Menut \(2017\)](#) could simplify the 5-parameter hyperelastic Mooney-Rivlin law to the 2-parameter elastic Mooney-Rivlin law. From that, we could assume that aortic wall and flap had a linear elastic and isotropic behavior.

2.3.4.5 The indentation method

Indentation method evaluate the hardness of the material by measuring the contact pressure during the indentation of an indenter (pyramidal, conical or spherical). The hardness is calculated either after the test, by measuring the indentation surface, or during the test, by measuring the indentation of the indenter, in both cases as a function of the applied load. The work of [Mouktadiri \(2013\)](#) illustrates this type of in-vitro test on different human arterial samples and focuses on the mechanical properties of the different layers of the arterial wall. This work has thus allowed us to map the nano-macro-mechanical properties of the intima, the media, and the adventitia, according to the degree of calcification and fat. These cartographies consider the arterial morphology to better represent each patient's specific anatomy. Using preoperative images of the parietal quality of arterial walls presented in Figure 2.26, each level of gray is related to a mechanical property in the form of elasticity modulus.

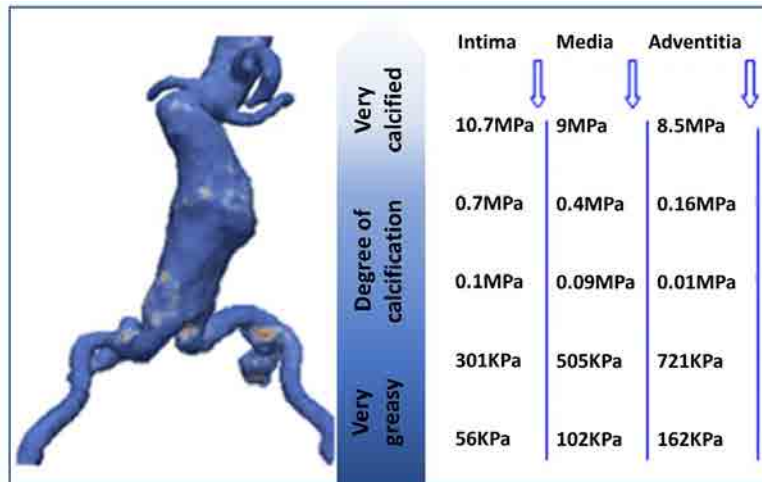


Figure 2.26: Mapping of the elastic modulus as a function of the degree of calcification for the different layers of the aorta (adapted from Mouktadiri (2013)). The orders of magnitude of arterial wall stiffness vary from a few kPa for healthy areas to a few MPa for the calcified areas

In a series of experiments carried out by Mouktadiri (2013) on arteries at macroscopic and nanoscopic scales, we have been able to distinguish between healthy, calcified, atheromatous, and fatty areas, which allowed us to identify the nonlinear character of the mechanical behavior of biological tissues and to demonstrate the independence to the loading rate at the nanoscopic scale (Figure 2.26). Furthermore, pathologic research have shown that the quantity of calcium in the tunica media is larger than the amount of calcium in the intima on average at all ages, which is adapted figure 2.26. And the others experiments do not consider the mechanical behavior of each layer of the aortic wall but its global behavior, in contrast to a study by Mouktadiri (2013) presented in section II-3.4.5 that maps the mechanical properties of the different layers of the arterial wall as a function of the degree of calcification and fat. Both in global and local behavior, the mechanical behavior of the arterial wall is strongly influenced by the concentration and structural arrangement of its constituents, such as collagen, elastin, and smooth muscle fibers.

The evolution of medical imaging techniques (Millon et al., 2014, Liu et al., 2019) allows us to provide more precise information on arterial behavior and to improve the models with a new wave of theoretical models, in particular, to characterize the behavior of the aortic dissection wall. The increasing number of vascular pathologies and the development of treatment techniques have led to a significant need to understand better both arterial behavior and the mechanism of the pathology. This understanding comes not only from the study of the arterial wall but also from the physiological stresses that are applied to it. As a result, we must take into account not only the rheology of the blood and arterial wall, but also the mechanical characteristics of the tools and how they affect the artery wall throughout the endovascular treatment.

2.4 Mechanical of endoprotheses and tools

Modeling endovascular treatment requires knowledge of the mechanical behavior of soft tissues as well as surgical tools and medical devices such as guides and stents.

2.4.1 The endoprotheses

An endoprothesis generally consists of metallic support, the stent, and a semi-permeable textile coating. This liner provides the seal to the system and can be made of woven or knitted polyethylene terephthalate (PET or Dacron), or expanded polytetrafluoroethylene (ePTFE). The stent gives the stent its structural rigidity as well as its ability to expand when removed from the stent holder. Therefore, we were interested in the mechanical behavior of Nitinol, which is the most common material in the stent. Almost all new generation stents are made of Nitinol (NiTi). The first-generation stents were made of stainless steel 316L.

These 3 thoracic stents-grafts are the more widely used in hospitals.

- Gore: new generation NiTi stent (Figure 2.27)
- Medtronic: new generation NiTi stent (Figure 2.27)
- Cook: first generation of 316L stainless steel stents (less use now)

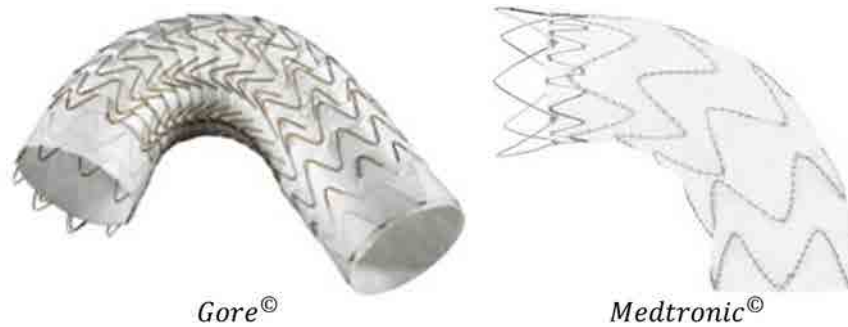


Figure 2.27: 2 Nitinol thoracic endoprotheses: Gore & Medtronic

In the work of [Menut \(2017\)](#), the uniaxial tensile tests were performed on Gore and Medtronic stent. Figure 2.28 compares the curves obtained with video extensometer for uniaxial tensile tests performed on Gore and Medtronic wires. A difference between the elastic modules of the Gore and Medtronic Nitinol wires can be observed. The values of the martensitic plateau remain, however, very close. For all stress-strain curves, an instability zone is observed at the end of the martensitic plateau. This zone marks the end of the solid-solid phase change.

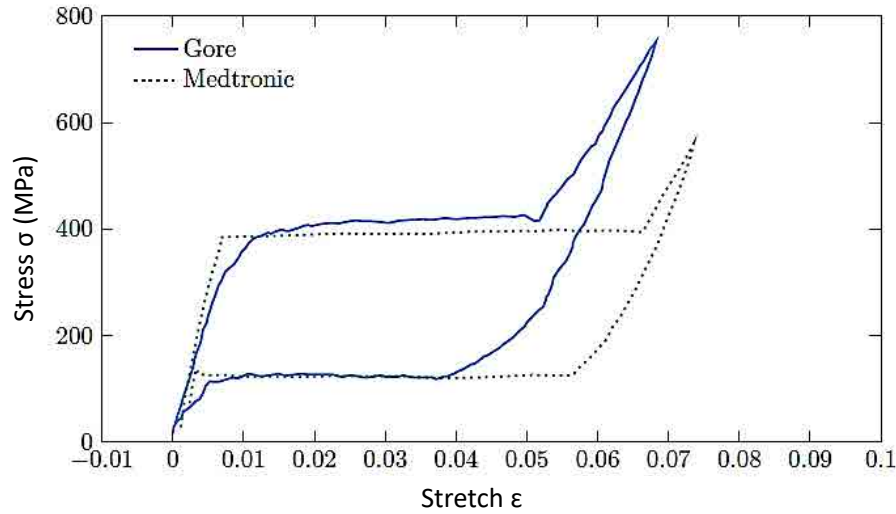


Figure 2.28: Comparison of cyclic tensile test curves (1 cycle represented) for Gore and Medtronic Nitinol stents (Menut, 2017)

Table 2.6 presents a summary of the values of the elasticity module calculated during the uniaxial tensile experiments between Gore and Medtronic stent.

Table 2.6: Table comparing the calculated elasticity modules between Gore & Medtronic (adapted from Menut (2017))

Parameters	Gore	Medtronic
Austenite modulus of elasticity E_a (MPa)	42030	64570
Martensitic modulus of elasticity E_m (MPa)	20330	22600
Martensitic transformation deformation	0.046	0.058

As such, we need to select the suitable stent for the patient based on the mechanical properties of the patient's vessel wall and the rheology of blood.

2.4.2 The surgical guides

During endovascular surgery, the surgeon inserts several tools into the arteries before deploying the stent-graft. First, a soft guide is inserted, followed by progressively stiffer guides to straighten the arteries to make them as straight as possible. The soft guidewire is then removed, and the catheter is moved up the rigid guidewire to the dissection area. To simulate the rise of the guides and the catheter to the ascending thoracic aorta numerically, it is necessary to know their mechanical properties. The guides are generally softer at one end to facilitate the contact of the guide with the vascular walls.

Two different guides (Figure 2.29) were tested in three-point bending in the work of (Menut, 2017).

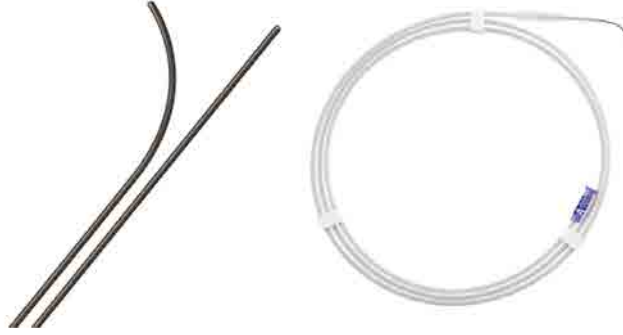


Figure 2.29: Illustration of a surgical guide with a flexible point preventing damage to the arterial wall (Image: Merit Medical©)

2.4.2.1 Mechanical properties of the guides

The characteristics of these guides (Figure 2.30) are as follows :

Amplatz Guide is a super rigid guide ($\phi=0.889$ mm) based on stainless steel, with an anti-adhesive TFE (tetrafluoroethylene) coating, a total length of 260 cm, and a straight and flexible tip length of 7 cm. The size of the transition zone is 11 cm, and the length of the rigid zone is 242 cm.

Cook Guide is an extra guide ($\phi=0.889$ mm) based on stainless steel, with TFE coating, a total length of 260 cm, and double-coated tip length 4 cm, consisting of external bobbin and gold for better visibility. The size of the transition zone is 11 cm, and the length of the rigid zone is 245 cm.



Figure 2.30: Guidewire

The evolution of the guide stiffness varies with the type of model (Figure 2.31) and along the transition zone. However, the guide is composed of a stainless steel wire and an extremely flexible coating. Therefore, we could consider that Young's modulus of the guide depends only on the steel wire whose diameter varies along the transition zone.

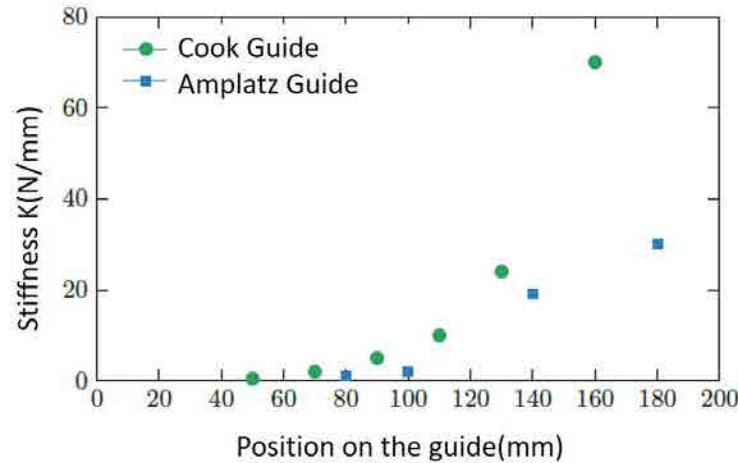


Figure 2.31: Evolution of stiffness along the transition zone of the Cook and Amplatz guides (Menut, 2017)

Finally, the average Young's modulus calculated for the guides is 187 GPa. This result agrees with the results of Mouktadiri (2013), who performed tensile tests on surgical guides. She found that the point of the different guides has Young's modulus between 700 MPa and 2000 MPa. Indeed, since the tip of the guide must ensure navigation in tortuous arteries and facilitate contact with the vascular walls, it must be flexible. The areas of the guides located after the tip are more rigid, with Young's modulus between 11800 MPa and 190000 MPa, their role being to straighten the arteries and facilitate navigation of the following tools.

2.4.3 The catheters

Experimentation was also performed on catheters, the surgical tools that contain the stent-graft before deployment in the treatment of aortic dissection pathology. These tests were realized in the laboratory during a previous thesis (Mouktadiri, 2013). They showed a variation of stiffness along the length of the catheter with a softer tip to facilitate its entry and navigation. Indeed, the catheters are composed of different materials (silicones, polyurethanes, or polytetrafluoroethylene), which are chosen to avoid any risk of coagulation or infection. Figure 2.32 (C) shows a traction test in which image correlation results were exploited on a catheter specimen from the stent-containing area. In the work of Mouktadiri (2013), several characterization methods were implemented, including image correlation, mechanical extensometer, and crosshead displacement measurement. The results obtained from the different measurements remain generally close, and Young's modulus value adopted for the catheter is 252 MPa.

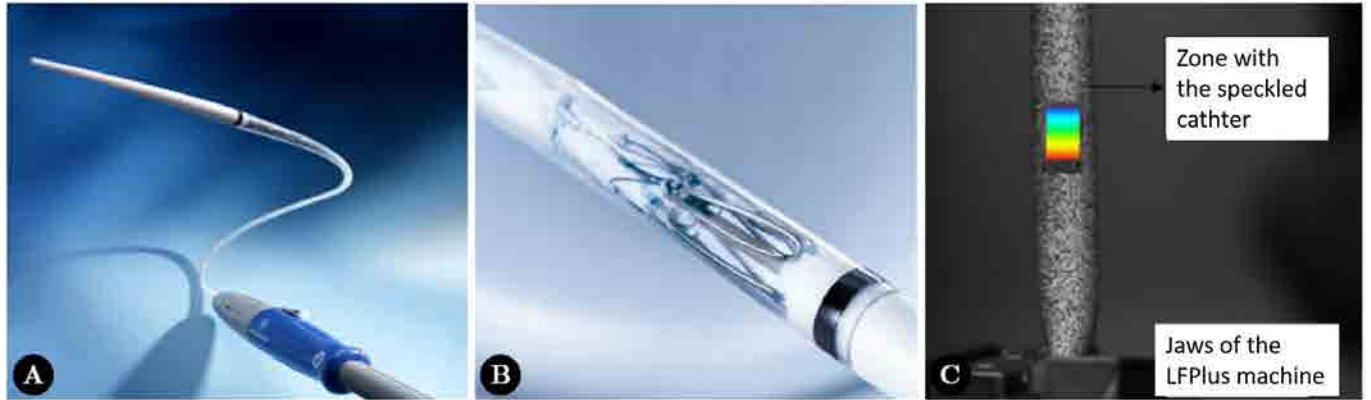


Figure 2.32: (A-B) Catheter with an undeployed stent inside (images from Medtronic©) (C) Traction testing of the stent-containing portion speckled in white on a black background (Mouktadiri, 2013)

The local mechanical characterization of the tools composing the delivery system remains a problem that has not yet been addressed. The measurement of local deformations appears to be a necessary tool for an accurate determination of mechanical properties. Tests of Mouktadiri (2013) on the mechanical characterization of endovascular tool samples have shown the feasibility of such a local characterization. Many samples from different catheters were tested in her work, including the most commonly used in the clinical setting. These tests allowed the establishment of cartography of mechanical properties for these tools.

2.5 Conclusions and strategies

The increase in vascular pathologies and the innovation of treatment techniques have led to a real need to understand both the behavior of arteries and the rheology of the blood. Some authors have found that low and oscillating parietal stress favors aneurysm development by its impact on the shape and structure of endothelial cells. The role of blood flow in the development of these pathologies cannot be neglected. The rheology of blood with its different behavioral patterns is considered in our study. In the literature, the viscosity models applied to blood have a relatively broad approach to its behavior.

Thanks to the progress of medical imaging and, flow MRI, it is possible to obtain much important information such as velocity fields and endovascular pressures, in addition to the imaging of the thoracic aorta obtained by CT-scanner. With these experimental data obtained in-vivo, it becomes possible to validate the calculations in fluid mechanics and the rheological model chosen for the blood flow. In addition, the evolution of medical imaging techniques (Millon et al., 2014, Sigovan et al., 2015) makes it possible to provide more precise information on arterial behavior and to improve the models, in particular, to characterize the behavior of the wall of the aortic dissection.

Material characterization methods have demonstrated the nonlinear, anisotropic, and viscoelastic character of the aortic wall and the heterogeneous behavior between healthy and diseased walls. The image correlation technique used in this research work allows the measurement of the deformation field of the arterial wall during swelling and uniaxial tensile tests. The models proposed by

Fung et al. (1979), Ogden (1972), Humphrey (1995) are complex or sometimes too far from reality. For this reason, we chose to use the model of Mooney-Rivlin, which is appropriate for our study. The Mooney-Rivlin model chosen for this study has its limitations, mainly in terms of isotropy. In contrast, more elaborate models taking into account, for example, the orthotropic character already exist (Holzapfel et al., 2000, Gasser and Holzapfel, 2006). However, due to the large variability between individuals, depending on their age, their sex, their physical conditions, the Mooney-Rivlin model can be considered as giving reasonable results in the framework of this research project.

The characterization of non-biological materials, components of surgical tools, and medical devices allows a better understanding of the mechanical behavior of these different parts for the complete modeling of the surgical act. Nitinol, a shape memory alloy, is a complex material to characterize mechanically because of its significant variability depending on experimentation and use. Numerical modelling of this material has been addressed in many works (Altnji et al., 2015, Menut, 2017) and the differences in terms of results highlight the importance of stent modelling, material properties and in particular those of the textile on the mechanical response of stents. Finally, surgical guides have a complex geometry and composition, appropriate for their use. The work of Menut (2017) for three-point bending tests is a complement to the tensile tests performed by Mouktadiri (2013). For the tested guides, the difference in stiffness in the transition zone is due to the internal geometry of the guide, whose TFE coating slides on the stainless steel core of the guide. The influence of the coating on the steel guide was not studied here, as its low stiffness compared to steel was neglected. Numerical studies validated by experimental results on phantoms exist in the literature (Wang et al., 2015) and show the importance of a robust approach to simulate guide behavior in vascular interventional radiology. However, in clinical practice, guidewire behavior is affected by blood flow and periodic vessel deformation, particularly of the thoracic aorta subject to more significant displacement and deformation than the rest of the arterial circuit. Simulating the behaviors of surgical instruments in a dynamic environment is, therefore, a problem that addresses the rheology of vascular walls and blood, which we discuss in the next chapter.

Basic Equations and numerical simulation

This chapter presents the development of the numerical model for the simulation of hemodynamics in an aortic dissection aorta. Using OpenFOAM[®] software for the calculation in fluid mechanics, and the interest of a fluid-structure interaction carried out with the OpenFOAM[®] extend program, OFOM-Extend[®]. In addition, the results of the simulation realized with Abaqus[®] for the rise of the surgical tools in a type B aortic dissection are presented in a first step without taking into account the stress generated by the blood.

Contents

3.1	Introduction	95
3.2	Introduction of fluid mechanics	96
3.2.1	Mathematical Modeling	97
3.3	Introduction of the CFD	98
3.3.1	The OpenFOAM Open-Source software	99
3.4	Numerical patient-specific geometry of an AD	100
3.4.1	Acquisition methods	100
3.4.2	Fluxes measured by 2D and 4D PC-MRI	102
3.4.3	Segmentation from medical imaging	103
3.4.4	Fluid domain meshing	104
3.4.5	Boundary conditions	108
3.4.5.1	Conditions at the entry	108
3.4.5.2	Conditions at the exit	110
3.4.5.2.1	Mathematical modeling of the cardiovascular system	110
3.4.5.2.2	Windkessel	111
3.4.5.2.3	Implementation of the 3-element Windkessel model	115
3.4.5.2.4	Windkessel parameters	116
3.5	Data analysis	117
3.6	Bio-faithful model with rigid walls	118
3.6.1	Newtonian fluid	118
3.6.2	Comparison with the Carreau-Yasuda model	123
3.7	Fluid-structure coupling	129
3.7.1	Necessity of a fluid-structure coupling	129
3.7.2	Fluid-structure coupling with FOAM-Extend	130
3.7.2.1	Discretization	133
3.7.3	FSI model of AD patient-specific	134
3.7.3.1	Mesh of FSI model	134
3.7.3.2	Boundary conditions	135

3.7.3.3	Results	137
3.7.3.3.1	Comparison between CFD model and FSI model	137
3.7.3.3.2	Influence of the d'Younge module	140
3.7.3.4	Discussion and conclusion	142
3.8	Modeling for the rise of surgical tools	143
3.8.1	Numerical models	143
3.8.2	Boundary conditions	146
3.8.2.1	Aortic environment	146
3.8.2.2	contact	147
3.8.3	Results of tool insertion	148
3.8.3.1	Results of guidewire insertion	148
3.8.3.2	Results of catheter insertion	150
3.8.4	Discussion	151
3.9	Conclusion	152

3.1 Introduction

The study of hemodynamics in arteries concerns first the prediction of blood pressure and flow at any place of the cardiovascular system, which is of major interest to the clinician in the pathophysiological investigation of a medical diagnosis. This approach is usually addressed by 0D and 1D modeling, based on simplified representations of the cardiovascular system components. Whereas 0D models provide a straightforward method for assessing hemodynamic interactions between cardiovascular organs, 1D models effectively represent the propagation effects of a pulse wave in the arterial network. These models have significantly reduced computational costs compared with higher dimensional fluid dynamics studies ([Shi et al., 2011](#)).

The prediction of blood flow dynamics on a local scale, particularly the parietal distribution of stresses on the endothelial layer, is also a significant challenge in hemodynamic modeling. Some authors have related the development of atherosclerosis to areas of low parietal stress ([Pedersen et al., 1999](#), [Siasos et al., 2018](#)), and the characterization of parietal stresses has been identified as a significant factor in most arterial pathologies in which altered tissue properties are involved. This characterization can only be considered with hemodynamic simulation tools that take into account the geometry of the structure.

The development of medical imaging (numerical process, improvement of resolutions, democratization of the access to the material in hospitals) and the acquisition of the geometrical data of the cardiovascular system of a patient constituted a significant evolution in the numerical hemodynamic simulation ([Markl et al., 2016](#)). These advances allow the virtual reconstruction of an individual's organs in an automatic, accurate, and fast procedure. Moreover, these same tools will enable the measurement of velocity fields and make possible the in-vivo and non-intrusive validation of the results obtained by numerical simulations. This methodological advance allows patient-specific simulations to better understand the morphology of each patient. However, among the precursor authors ([Taylor et al., 1998](#), [Moore et al., 1999](#), [Löhner et al., 2003](#)), difficulties persist, in particular concerning the boundary conditions, the material parameters, and the blood rheology.

Recently, the development of modeling in biology has enabled multi-scale modeling between phenomena of mechanotransduction on cells of the endothelial wall and blood circulation. This approach aims to understand better arterial diseases and the impact of tissue remodeling on hemodynamics in the long term ([Figueroa et al., 2006](#)). This methodology has been successfully applied to the study and treatment of arterial pathologies and assist in surgical procedures and surgical planning. As example, it has been used to predicting preoperative hemodynamics in the Fontan procedure ([Marsden et al., 2009](#)), pediatric cardiac surgery, and the design and optimization of aortic endovascular stents([Figueroa et al., 2009b](#), [Gallo et al., 2016](#)).

In treating aortic dissection pathology, the study of hemodynamics in the aortic arch and dissection's entry zone reveals new complexities compared to the abdominal aorta. On the one hand, due to the dynamics, as the Reynolds number at the systolic peak is located in the transition zone between the laminar and turbulent flow regimes. On the other hand, curvature effects are added

due to the natural geometry of the aortic arch: the centrifugal force generated by the curvature triggers secondary vortex flows called Dean vortices. The Dean number, characteristic of this effect, varies between 1000 and 3000 in the aortic arch. In this regime, a dipole of longitudinal vortices appears and propagates downstream of the aortic arch impacting the turbulence production. Moreover, the pulsatory character of flow in the aortic arch, characterized by the Womersley number that can reach values close to 20, is marked in this zone.

Finally, blood rheology, by its shear thinning and thixotropic nature, is strongly influenced by the unsteady character of shear stresses in the flow. Its consideration in hemodynamics with adapted behavior laws is then necessary. Several hemodynamic flow studies have been performed on realistic geometries of the thoracic aorta and confirm the perturbations, and the helical character of the flow observed in this area (Shahcheraghi et al., 2002, Morris et al., 2005, Watanabe and Matsuzawa, 2006, Liu et al., 2009). The prediction of hemodynamic stresses on an endovascular stent graft initially attached to the thoracic aorta was addressed by Figueroa et al. (2009a) and then by Mbodj et al. (2016) to predict oscillatory stresses on the thin stent structure, anticipate its migration, and thus predict possible future endoleaks.

In view of the preceding observations, the interest of multiphysics simulations of endovascular stent placement based on arterial wall deformation and hemodynamic flow provides a direction for applied research with real impact for the clinical communication community. This chapter presents the complex rheological model used to describe blood flow in the patient-specific aortic dissection, the mathematical modeling of the cardiovascular system, and the interest of fluid-structure coupling to validate results with in-vivo data for the future research.

3.2 Introduction of fluid mechanics

Fluid mechanics relies on the solution of partial differential equations based on principles of conservation of mass, momentum, and energy. They use variables describing a fluid flow, such as density, velocity, pressure, and viscosity, and consider the displacement of matter throughout the studied domain. The complex properties of this system of equations limit the possibilities of obtaining an analytical solution in most flows, hence the use of several approaches to analyzing different flows.

- the theoretical approach, which consists in the elaboration of simplified models to allow their resolution analytically,
- the experimental approach, which allows apprehending the results of the theoretical approach while bringing contributions on the understanding of certain observed phenomena,
- the numerical method solves a partial differential equation (PDE) system numerically for complex flows.

The development of the numerical approach in fluid mechanics makes it possible to reduce the time needed to analyze a flow, precisely control the various physical parameters of the simulation, and be economical compared to the costs of experimental tests. However, the progress of numerical simulation is also dependent on theoretical and experimental advances. The different approaches

allow improving the prediction capacities of the simulation tools by providing more and more accurate models and by allowing to compare the numerical results with reality. This is the case in many experimental works based on particle image velocimetry (PIV) techniques. Some authors (Guivier-Curien et al., 2009, Foucault et al., 2017) use this non-intrusive optical method to obtain flow velocity maps in in-vitro artery models with a perfectly controlled environment (material properties, fluid viscosity, flow rates, pressures, etc.).

3.2.1 Mathematical Modeling

The numerical solution of these flows implies the setting in equations of the problem, considering its assumptions and simplifications if necessary. The conservation equations formulated for Newtonian fluids are called the Navier-Stokes equations. They are based on the hypothesis that the fluid, on the scale of the investigation, is continuous, which means that it does not consist of discrete particles but instead of a continuous substance, leading to the condition that all fields of interest such as pressure, flow velocity, density and temperature are globally distinguishable. When it comes to blood flow in large artery vascular networks, the primary models used to describe and simulate blood flow is the one-dimensional Navier-Stokes finite element model for elastic networks (Formaggia et al., 2003, Sherwin et al., 2003).

These equations, in their differential form, for a Newtonian and incompressible fluid, are as follows:

- Continuity equation (mass conservation)

$$\nabla(\rho\vec{u}) = 0 \quad (3.1)$$

- Momentum balance equation

With Cauchy's equation:

$$\rho \frac{du_i}{dt} = \frac{\partial}{\partial x_j} (-p\delta_{ij}) + \frac{\partial}{\partial x_j} \left[\mu \left(\frac{\partial u_i}{\partial x_j} + \frac{\partial u_j}{\partial x_i} \right) \right] \quad (3.2)$$

For a Newtonian fluid:

$$\underbrace{\rho \frac{\partial \vec{u}}{\partial t} + \rho \nabla \vec{u} \cdot \vec{u}}_{\text{inertial terms}} = \underbrace{-\vec{\nabla} p}_{\text{pressure term}} + \underbrace{\mu \Delta \vec{u}}_{\text{viscous terme}} \quad (3.3)$$

- Heat equation (conservation of energy)

$$\frac{\partial T}{\partial t} + \vec{u} \nabla T = \kappa \Delta T \quad (3.4)$$

with \vec{u} the velocity field, p the pressure, ρ the density of the fluid, μ the dynamic viscosity, T the temperature and κ the thermal diffusivity.

The solution of these conservation equations is performed in the framework of a discretization method. There are several ways to formulate a solution scheme for fluid mechanics analysis. The oldest method is the Finite Difference Method (FDM). Despite being the most straightforward method available, its limited application to structured grids makes it of little use for the modern analysis of complex structures.

Another discretization system that can be used for fluid mechanics is the Finite Element Method (FEM). The advantage here lies in the fact that random geometries can be easily treated. With a robust mathematical background, fluid mechanics problems such as free surface problems can be treated. However, this method can be very time-consuming for complex issues.

The mathematical method of choice for most hydrodynamic codes is the finite volume method (FVM). The conservation equations are solved approximately, using a mesh of finite or control volumes, which are small disjoint volumes whose combination constitutes the field of study. The calculations are performed at the center of each control volume. The main advantage of this method is that it applies to any type of mesh and, allows the use of polyhedral meshes, which have the advantage of reducing the computational time compared to tetrahedral meshes.

3.3 Introduction of the CFD

Computational fluid dynamics (CFD) is a branch of fluid mechanics that analyzes and solves issues involving fluid flows via the use of numerical analysis and data structures. Besides, with the development of computer science in recent years, the advancement of computational fluid dynamics (CFD) enabled the use of 3D digital simulations to study patient-specific hemodynamics and to better understand the pathology and progression of various cardiovascular diseases. Limitations in the use of CFD simulations are related primarily to the model assumptions that are made when these simulations are performed, e.g., geometry, viscosity, distensibility, flow conditions. Simplified interpretations, however, have always been the cornerstone of understanding the physical world. Primarily because of its ability to quantify non-quantifiable factors in vivo, its repeatability, and its function as a diagnostic and therapeutic tool for a variety of cardiovascular disease problems. The use of CFD instead of in vitro studies facilitates modification of model parameters such as boundary conditions. Additionally, given the complexity of blood flow in intricate geometries, combining high-resolution simulation techniques and image-based measurements data has proven to be a reliable tool for realistic modeling of arterial blood flow (seen chapter II.2.3).

CFD simulations based on patient-specific models may be able to provide insight into the biomechanical behavior of blood flow in aortic dissection, allow for quantitative analysis of hemodynamic patterns, and predict clinical progression of aortic dissection, although the clinical value of these simulations has not yet been established. This research aims to simulate the complete endovascular procedure for a suitable recommendation during surgical planning. Using CFD, it is possible to assess certain hemodynamic parameters that are difficult to quantify in-vivo, such as wall shear stress.

In this project we choose to mesh the studied domain with the commercial software Star-CCM+[©]

and solve the Navier-Stokes equations with the open-source software OpenFOAM®.

3.3.1 The OpenFOAM Open-Source software

In the context of this study, one of the goals is to consider the appropriate rheological behavior of blood in complex locations of the human anatomy and patient-specific morphologies. It is necessary to use a powerful and accomplished CFD tool. The capability to handle complex geometries, non-structured, non-orthogonal and movable meshes, with a wide variety of solvers and interpolation schemes for the discretized system as well as numerical computation parallelization is essential. Considering these many criteria, the Open Source Field Operation and Manipulation (OpenFOAM) software, developed by OpenCFD Ltd of the ESI Group, appears to be a promising tool for this type of development. Figure 3.1 shows the basic construction of OpenFOAM. In OpenFOAM, the discretization of the flow governing equations is based on the finite volume method, including a resolution of the pressure and velocity by separate methods:

- **SIMPLE** (Semi-Implicit Method for Pressure Linked Equations) which is an appropriate choice for stationary flows (Barton, 1998),
- **PISO** (Pressure Implicit Splitting of Operators) which is used for transient flows, where more accurate intermediate solutions are required (Issa, 1986).
- **PIMPLE**(merged PISO-SIMPLE) which is used for transient flow, the accuracy of numerical simulations is improved, particularly when large time steps are used in a moving mesh.

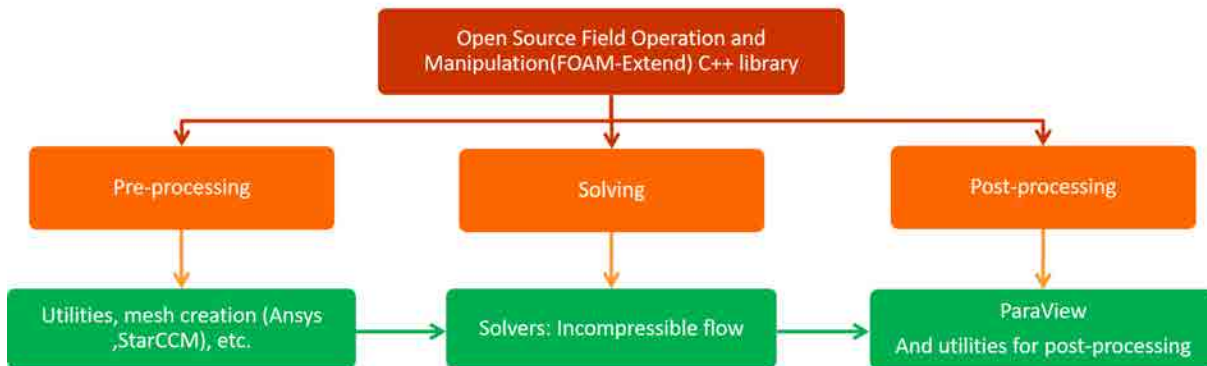


Figure 3.1: General steps for CFD simulation

Moreover, OpenFOAM allows the use of different numerical schemes for solving the different terms of the constitutive equation of the model, such as implicit Euler, explicit Euler and Crank-Nicholson for the discretization of the temporal derivatives. These features are only meant to describe the flexibility of the software, a more complete description of the numerical methods used in OpenFOAM, and the options of the different numerical schemes available in the work of

Jasak (1996).

The main advantage of OpenFOAM is the possibility to develop new solvers (in C++), which can be modified and compiled in an unlimited way, offering a straightforward implementation of complex mathematical models. This software has been widely used, tested, and validated with many existing solvers implemented for Newtonian fluid flows mainly, incompressible and compressible, laminar and turbulent, multiphase, etc. Although it has its own meshing tool, it can also import meshes from many other commercial software such as Fluent, Ansys, Star CCM+[©], and handle unstructured meshes in tetrahedra, hexahedra, and polyhedra prismatic and also movable meshes.

Even if OpenFOAM is difficult to use because of the absence of a graphical user interface, the development possibilities, and the fact that it is free to justify selecting this program for this research.

3.4 Numerical patient-specific geometry of an AD

3.4.1 Acquisition methods

Direct in-vivo assessment of blood flow, which plays an essential role in the development of cardiovascular disease, remains difficult despite advances in medical imaging. In particular, current imaging techniques are limited with respect to the assessment of certain blood flow characteristics that allow the global characterization of cardiovascular hemodynamics. These characteristics include complex changes in 3D blood flow schemes, the pulsatile nature of arterial flow with flow velocity variability, blood pressure estimation, and quantification of flow in small vessels.

Magnetic resonance imaging (MRI) techniques provide noninvasive, nonionizing methods for obtaining the accurate anatomic representation of the heart and its vessels during a cardiac cycle. In addition, the sensitivity of MRI to motion offers the ability to acquire blood flow information simultaneously with morphological data within a single measurement (Nayak et al., 2015). The characterization of dynamic blood flow components has advanced considerably in recent years with methodological advances in data acquisition, reconstruction, and analysis. These developments directly impact the ability to assess cardiac and vascular hemodynamics and have opened new possibilities both in aiding the treatment of vascular disease and the validation of accompanying numerical models.

Flow imaging with MRI is based on the phase contrast technique (PC-MRI), which is used to encode blood flow velocities along with the three spatial directions and thus allows the acquisition of spatial flow information simultaneously with morphological data. In current practice, PC-MRI is usually performed using two spatial dimensions (2D) defining sections chosen by the operator, with the velocity component directed perpendicular to these sections. More advanced flow MRI techniques also exist, allowing a more comprehensive assessment of blood flow characteristics. For example, one can find the 2D real-time PC-MRI technique for evaluating flow changes over short periods and evaluating these variations during an entire cardiac cycle and the 4D MRI for the complete analysis of blood flow in 3D over time.

Unlike echocardiography, the assessment of blood flow in the cardiovascular system by PC-MRI

is not limited by wave interference or probe angle. However, the evaluation of these flows for 2D MRI is performed through a section whose acquisition plane position remains difficult to assess and may lead to underestimating velocities during systole if it is not orthogonal to the evaluated flow. This difficulty is frequent in complex flows where changes in direction occur throughout the cardiac cycle. These underestimates can be improved by considering all flow directions during acquisition. Alternatively, 4D MRI allows three-dimensional, time-lapse visualization of blood flow at any location within an operator-selected 3D volume. Figure 3.2 shows the complexity of the trade-off between a large volume of flow data and acquisition times depending on the method chosen.

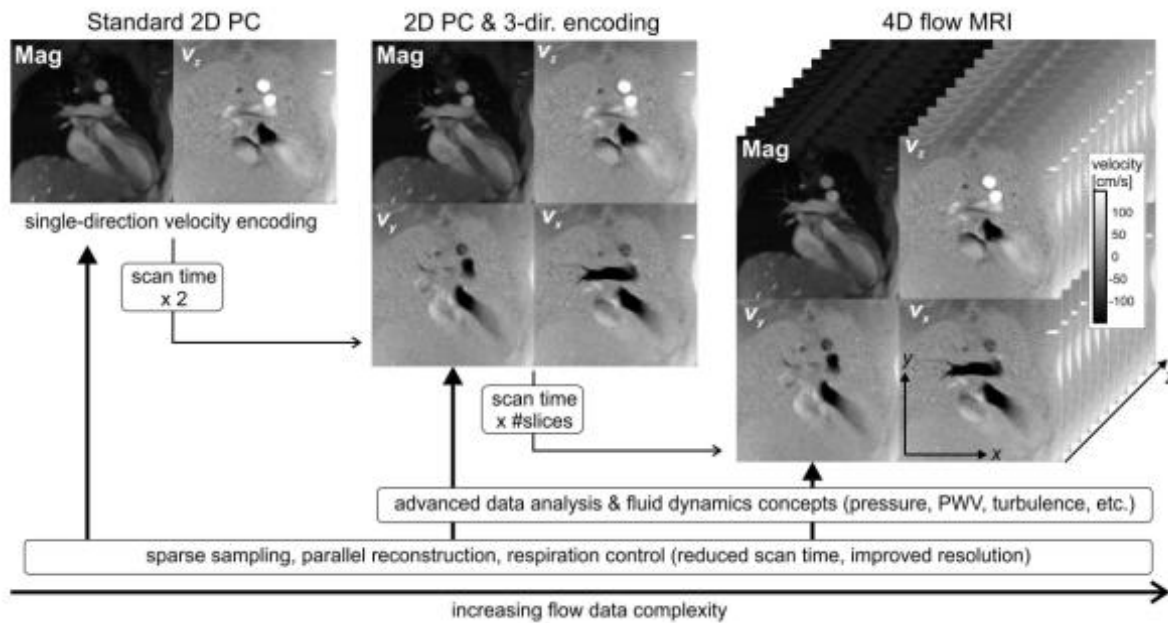


Figure 3.2: Graph shown that with the number of dimensions and scan duration grows, the complexity and information richness of flow data increases (Markl et al., 2016)

Several studies have compared the fluxes estimated by both 2D and 4D PC-MRI methods (Markl et al., 2003, Stalder et al., 2008) and generally found that the velocities were significantly underestimated when calculated in 2D with a single component orthogonal to the acquisition plane instead of considering all three spatial directions. However, the results obtained by considering all three directions for the in-plane velocity calculation remain consistent with those obtained by 4D MRI (Markl et al., 2016). These observations show the importance of considering all three directions of space in the calculation of flow velocities. However, the integration of these techniques into clinical protocols remains difficult due to the extended data acquisition time that requires additional data (Figure 3.2).

Recent improvements based on imaging techniques, however, have allowed the acquisition of 2D PC-MRI with velocities in the three directions of space during a single respiratory arrest, allowing clinical examination times on the order of 5 to 15 minutes (Markl et al., 2016). These advanced hemodynamic measurements provide quantitative information about the impact of vascular disease on the aortic or pulmonary blood flow, and many investigators have exploited these data to derive

new physiological hemodynamic parameters such as shear stress, pulse wave velocity, or pressure fields from reductive hypotheses.

3.4.2 Fluxes measured by 2D and 4D PC-MRI

Measurements in 2D PC-MRI with 3D velocity encoding were first performed on planes positioned by the operator at different locations. The slice planes were chosen such that the velocity fields and thus the flow rates could be calculated at the level of the ascending thoracic aorta, the supra-aortic trunks, and the descending thoracic aorta.

4D-PC-MRI measurements are also generally performed on the same patient to obtain velocity profiles at any time during the cardiac cycle over the entire volume of interest. There are a number of factors that compromise the accuracy of this method. These include limitations in spatial and temporal resolution leading to partial results in some areas. Other factors such as imperfections related to magnetic field disturbances can also call into question the accuracy. This is of particular concern for the in-vivo determination of velocity field-derived quantities such as shear stresses in complex flow regions in intracranial aneurysms, for example (Boussel et al., 2009). The work of Menut (2017) compared the flow values between the 2D and 4D methods, which are very close, and their comparison shown in Figure 3.3 attests to an accuracy of the 4D process similar to the 2D process in a healthy thoracic aorta.

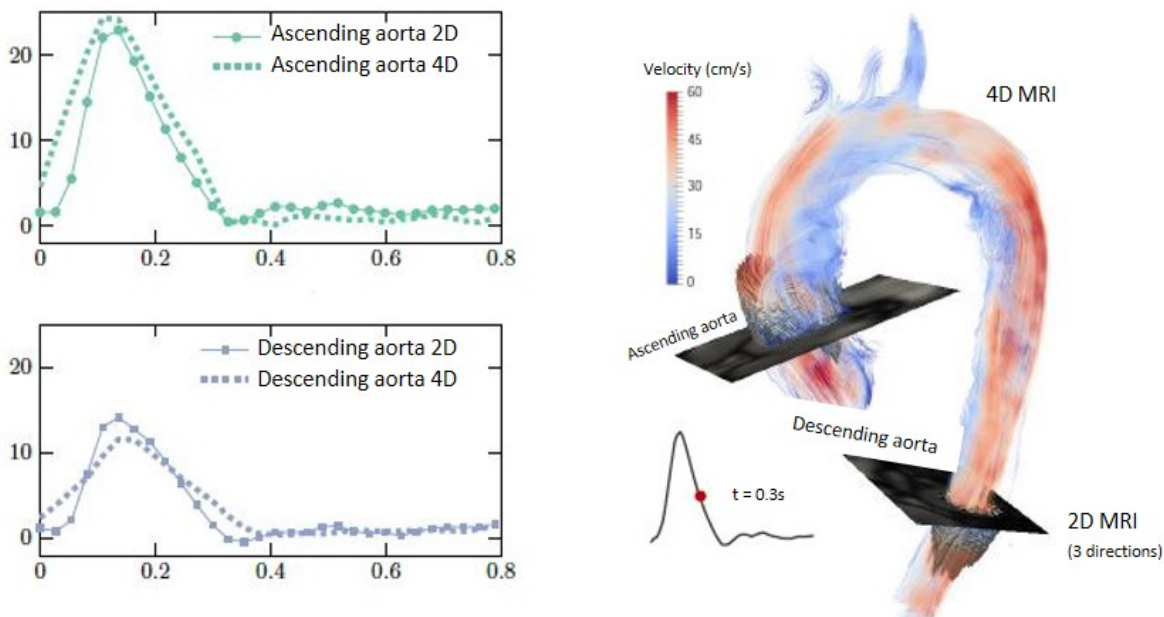


Figure 3.3: (Left) Comparison of 2D and 4D flow rates calculated in-vivo through 2 slices located at the ascending and descending aorta. Both methods show very similar results that will be used for numerical simulations; (Right) Flowlines based on 4D MRI results (adapted from (Menut, 2017)).

For this case with AD pathology, which will present in chapter 3 for hemodynamic simulation, dynamic flow measurements by 4D MRI were performed at the Hôpital de la Croix-Rousse on a voluntary healthy patient (Menut, 2017). Because no flow data was available for the present patient. But we have obtained the DICOM image for the reconstruction of the 3D bio-faithful model that was used in our numerical simulations.

3.4.3 Segmentation from medical imaging

According to the researchers, the semi-automated segmentation of blood arteries from medical pictures has a substantial impact on arterial disorders' diagnosis and surgical treatment planning. The digital extraction of a vascular network allows for the modeling of vessel architecture as well as blood flow in the network. When it comes to analyzing vessel diseases such as stenosis (Millon et al., 2014) or providing preoperative guidance for endovascular surgery, the quantitative information gained from these models is precious. In this context, the fast advancement of imaging methods has enabled the more common use of MRI sequences for 3D reconstruction in place of ionizing tomography to get better results. These non-invasive sequences do not need a contrast agent to see vessels and provide pictures with a high resolution, allowing for the detection of vessels with a relatively tiny diameter.

Image segmentation is a critical stage since the precision with which it is performed directly impacts the quality of the model used in numerical simulations. In this research, DICOM pictures from MRI were processed using the commercial software Simpleware ScanIP 2017 (Synopsis, CA, USA). The segmentation displayed in Figure 3.4 was done semi-automatically by choosing voxels (3D pixels) that belonged to a range of gray levels indicative of the aorta and placing them together. However, for the part of aortic dissection, especially for the dissection entry site, true lumen, and false lumen, it is crucial that the model is accurately remodeled. Therefore, each DICOM image must be manually confirmed for the dissection part to reconstruct a bio-fidelity geometry for the patient.

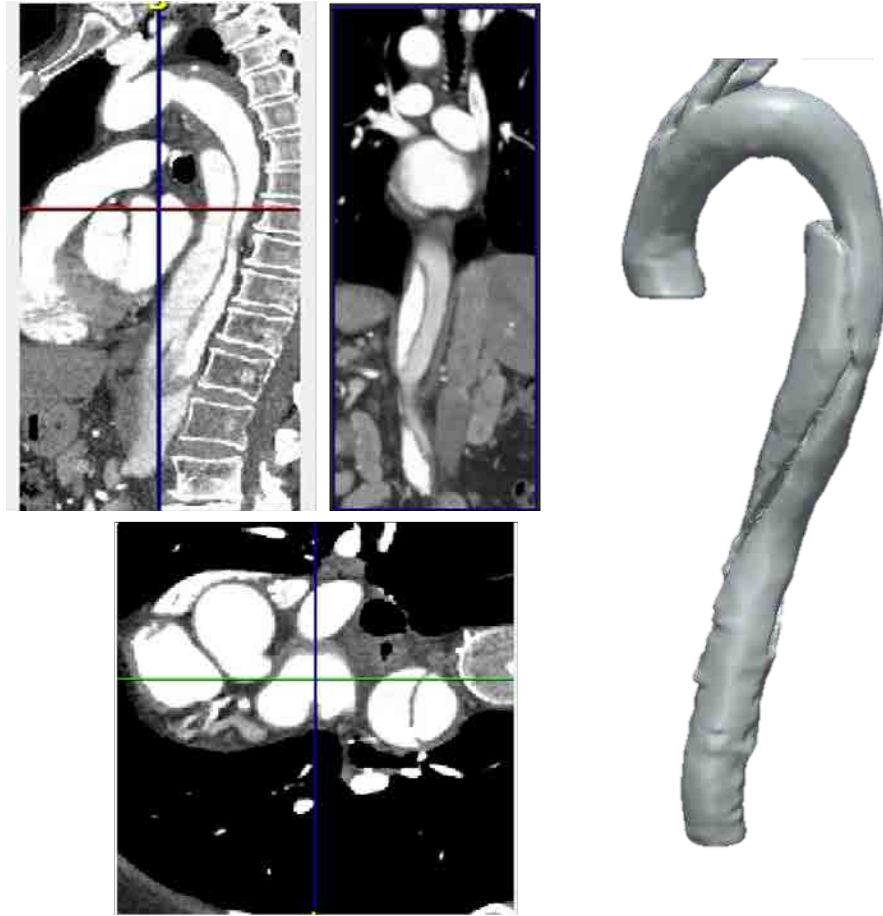


Figure 3.4: Segmentation process based on medical imaging with commercial software Simpleware ScanIP 2017 (Synopsis, CA, USA). The 3D volume is chosen on the 3D space parts.

3.4.4 Fluid domain meshing

The continuous growth of computational capabilities sees an increase in the complexities of numerical models that require more and more detailed analysis. For example, for this study, the consideration of the complex properties of blood. The fluid domain is characterized by complicated geometries, including the numerous bifurcations of human arteries, for which it is not always easy to establish a high-quality discretized model.

Whenever possible, numerical engineers prefer to use hexahedral meshes in 3D simulations. Indeed, hexahedra have geometrical properties that result in high-quality meshes inducing numerical stability in most cases. However, while for 2D domains, the automatic generation of quadrilaterals is generally possible, commercial software has not, to date, integrated a corresponding robust method for complex 3D domains. Nevertheless, significant progress is being made with the development of open-source codes such as Pyformex, which provides a program specifically adapted to the 3D hexahedral meshing of arteries (De Santis et al., 2011) or with the work of Al Akhras et al. (2017) on new techniques for parameterizing complex geometries.

The answer to these difficulties of meshing in hexahedra is the use of tetrahedra. Even being

the simplest possible volume elements, tetrahedral meshes can approximate any geometry. Their surfaces are plane segments, so the centroids of the faces and bodies are easily defined. Tetrahedral meshes have been well studied and developed, and they are also relatively easy to generate automatically. They are almost a standard application in automatic mesh generation techniques, and all major CFD solvers support tetrahedral meshes. On the other hand, however, tetrahedral meshes cannot be stretched too much, so for accuracy in boundary layers, long pipes, or small gaps, much more tetrahedral meshes than structured meshes (hexahedra) are required. Prismatic mesh layers can partially solve this problem.

Moreover, having only three neighboring cells (Figure 3.5), tetrahedra are not the optimal choice for computations in fluid mechanics because the calculation of gradients at the centers of the faces can become problematic, as the computation of the flow on a face is done by interpolating the information from the adjacent faces. One difficulty is the spatial location of the adjacent grid nodes since they may be almost in a plane, making it practically impossible to compute the gradient perpendicular to that plane. Another problem may be encountered when cells are adjacent to a boundary: even if only one face is the boundary face, the other three faces may be poorly distributed; especially when adjacent to lines or corners, a cell may have only two or one adjacent cells, which not only reduces accuracy but also causes severe numerical problems.

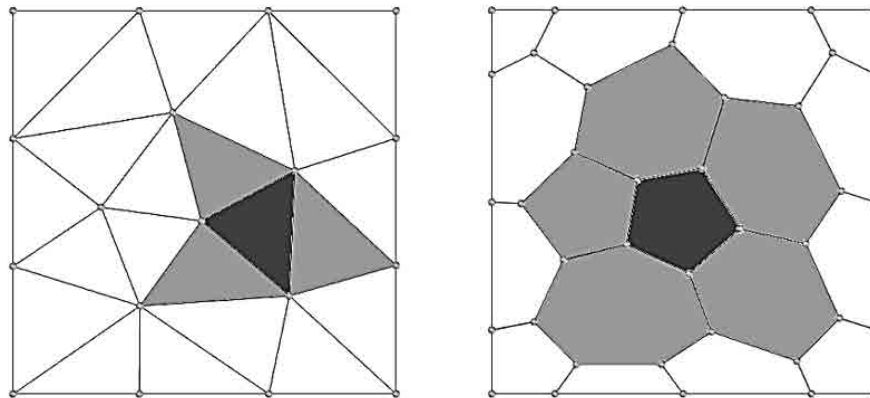


Figure 3.5: Comparison of the number of adjacent meshes for a tetrahedral (left) and polyhedral (right) (image from Balafas (2014))

To achieve accurate solutions and good convergence on tetrahedral meshes, special discretization techniques and many cells are required. These solutions are not optimal; the first approach makes the program more complex and harder to scale and maintain, while the second approach increases memory and computation time requirements. Polyhedral meshes provide the same automatic mesh generation capabilities as tetrahedral meshes and address these drawbacks. The main advantage of polyhedral meshes is that they have multiple neighboring cells (typically on the order of 10), and the gradient can be better approximated using polyhedral meshes compared to tetrahedral meshes (using linear shape functions and information about the nearest cell). Even near lines and corners, a polyhedral cell may have several neighboring cells, allowing reasonable prediction of gradients and local flow distributions. More adjacent cells imply more memory usage and more computational operations, which can be compensated from higher accuracy.

An alternative option to tetrahedral meshes has recently emerged, suggesting the use of polyhedral elements (Perić and Ferguson, 2005). Polyhedra have the same interests as tetrahedra, but their significant advantage is that they are surrounded by many neighbors (Figure 3.11). This makes the approximation of gradients much better than when using tetrahedra. In addition, they are less sensitive to stretching, and their irregular shape is not a restriction for fluid mechanics codes. However, polyhedra have a complex geometry that depends on the generation method and does not necessarily result in flat or convex faces. However, they allow for a significant reduction in computational time by reducing the number of meshes. The work of Balafas (2014) presents a detailed study on the use and methods of generating polyhedral meshes in fluid mechanics.

For the reasons stated above, we have decided to use a polyhedral mesh created using the commercial program Star-CCM+[©] for this investigation (Figure 3.6). In addition, we use the ANSYS program to create the tetrahedral mesh and compare it with the polyhedral mesh (Figure 3.7).

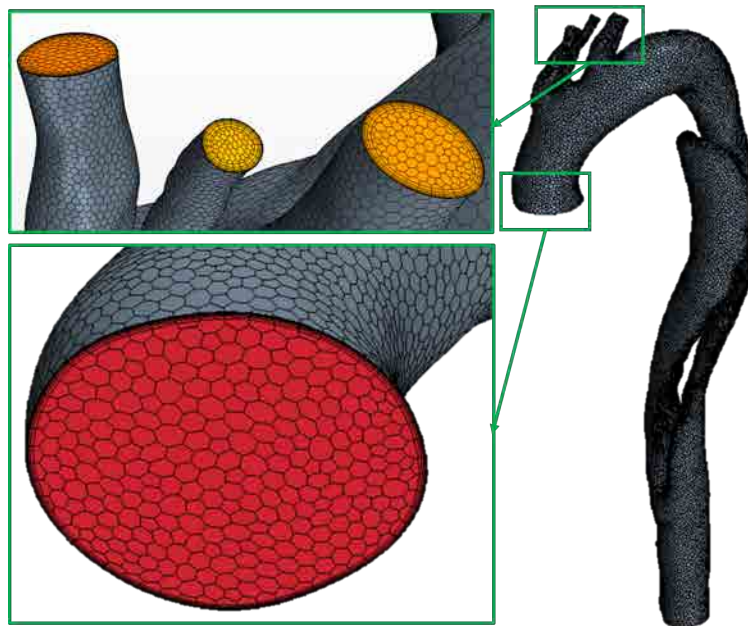


Figure 3.6: Polyhedral mesh generated with the commercial software Star-CCM+[©] (338265 cells)

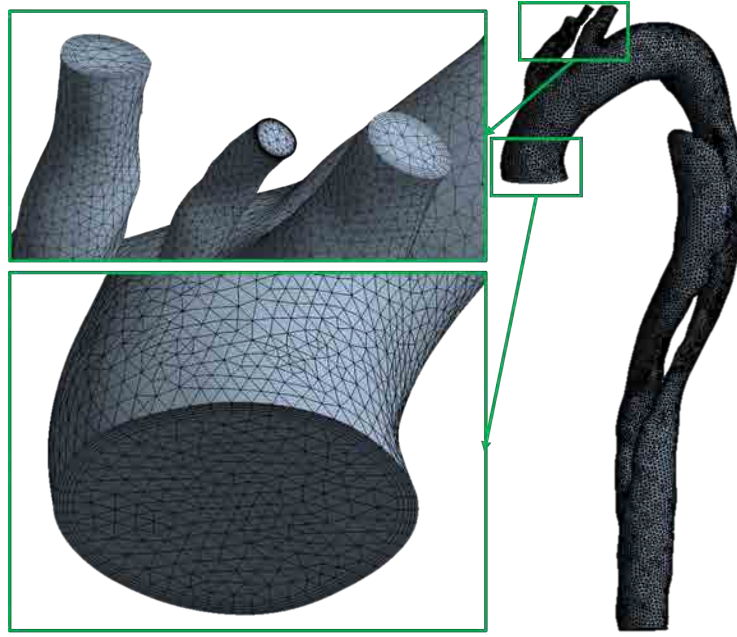


Figure 3.7: Tetrahedral mesh generated with the commercial software ANSYS® (1575416 cells)

A mesh sensitivity study was performed on these two mesh models (Polyhedral & Tetrahedral), based on the maximum numerical values of shear stresses at arterial bifurcations. The values were taken at the systolic peak, the phase of the cycle where the fluid velocities are the highest, the relevant criterion for this sensitivity study. For the polyhedral mesh, we study through three mesh sizes (2mm, 1mm, and 0.5mm) for the CFD simulation of AD. And we investigate the tetrahedral mesh using two different mesh sizes (2mm, 1mm). For 1mm size, we further refined the mesh around the flap of dissection to ensure the precision and convergence of the calculation. The numerical values in Table 3.1 show that the shear convergence is quite fast for coarse meshes. Because in the after work, we need to realize the simulation of fluid-structure interaction, according to the experience, the general near-wall surface with tetrahedron is more adaptable for dynamic mesh for fluid and solid. Therefore, we have chosen to generate a relatively accurate tetrahedral mesh with about 1575416 meshes (mesh size: 1mm (flap refinement)) for the FSI numerical model.

The sensitivity parameters β for mesh study represent the relative difference of the shear stress τ depending on the type of mesh respectively. This parameters are defined as:

$$\beta = \frac{\tau_{poly0.5mm} - \tau}{\tau_{poly0.5mm}} \quad (3.5)$$

Table 3.1: Mesh sensitivity study based on the maximum value of shear stress at peak systole.

Mesh type	Mesh size (mm)	Number of meshes $\times 10^3$	Shear stress τ (Pa)	Sensitivity parameter β (%)
Ployhedral	2mm	338	87.8	0.79%
	1mm	1043	88.2	0.34%
	0.5mm	3371	88.5	-
Tetrahedral	2mm	337	58.2	34.24%
	1mm	772	88.29	0.24%
	1mm(flap refinement)	1575	88.4	0.11%

3.4.5 Boundary conditions

Having completed validation of the rheological model developed for blood flow modeling and the acquisition of in-vivo data that will allow the geometrical reconstruction of a patient-specific model, the next step is the definition of the boundary conditions that will be used to resolve the fluid flow problem. When solving partial differential equations on the model borders, the boundary conditions will enable us to enforce the uniqueness of the solution and achieving the following results:

- The inlet surface of the aorta, on which a flow is applied that varies according to the cardiac cycle with a Poiseuille flow profile and flow from in-vivo dynamic imaging,
- The outlet surfaces of the supra-aortic trunks and descending thoracic aorta, to which conditions from a 3-element Windkessel model are applied,
- The free surface of the aorta is subject to a no slip at the wall condition, which means that the velocity of fluid near the aorta wall is the same as the velocity of the wall. In the case of the rheological model with rigid walls, this velocity is zero.

3.4.5.1 Conditions at the entry

There was no 4D-MRI flow data available for the this patient, so data from the work of [Menut \(2017\)](#) which worked with a healthy thoracic aorta. We used the same velocity field at ascending aorta, which is adapted with this case inlet. As a result, to impose this flow as an entrance condition in OpenFOAM, the flow must be translated into velocity vectors that are located at the center of each mesh on the entrance surface. The Poiseuille flow velocity profile was selected for this study, although this profile is appropriate for fully developed flows in circular pipes. As described in Chapter 2, a profile with Womersley flow is a popular option that is well suited to the oscillatory regime of the cardiac cycle and has been used in many studies. In contrast, even though Womersley flow is the solution for flows in arteries (such as those that drain into and return to the heart), it does not entirely fit the profile of blood ejection at the heart's outflow as shown in Figure 1. In the literature, Poiseuille flow is widely used to model physiological flow. Its popularity is based mainly on the fact that it is easy to use and understand and provides a reasonably accurate model that connects the mean pressure and flow values to the frictional resistance of the artery ([Stergiopoulos et al., 1992](#)). For these reasons, we decided to impose at the entrance a velocity profile based on a Poiseuille flow, which is more numerically stable because it does not include

negative velocities present in a Womersley-type flow.

The analytical form of the velocity profile of a Poiseuille flow, adapted to a perfectly cylindrical pipe, depends on the radius R of the tube and the maximum velocity v_{max} at the center of the disk :

$$v_r = v_{max}(1 - \frac{r^2}{R^2}) \quad (3.6)$$

This formula cannot be applied to the entrance surface of the model, which is not perfectly circular. To handle this problem, the method described in the work of [Mynard and Nithiarasu \(2008\)](#) was applied to the geometric data of the model. This method is described in Appendix A. The 3D velocity profile is plotted on the 2D inlet surface of the aorta. If the inlet were perfectly circular, then each mesh center could be assigned a velocity for each time step as a function of the radial distance r where it is located (equation 3.6). However, the entrance surface is generally not circular, and the velocities assigned to each mesh center are more complex(Figure3.8). So for the specific patient, we create the mesh for its numerical aortic model and then obtain the aortic inlet plane mesh to derive its inlet velocity.

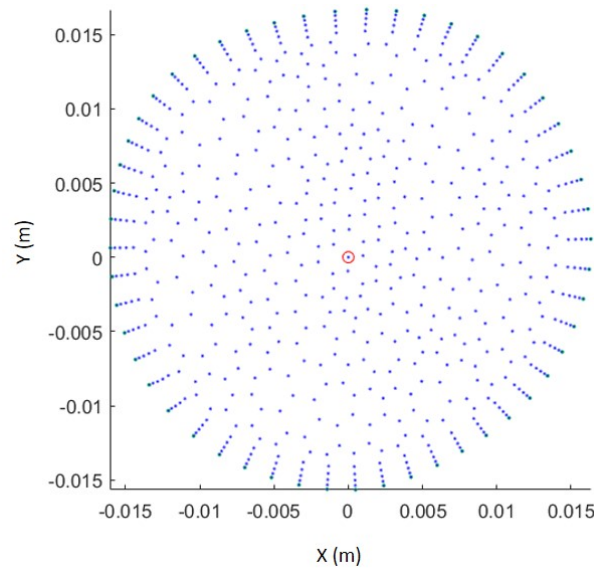


Figure 3.8: Centers of the entrance surface meshes of the ascending aorta represented in 2D

The Poiseuille profile fitting program has been developed in Matlab[®] and is available in Appendix A. The velocity plot performed with the developed method results in a relatively smooth 3D input velocity profile, as shown in Figure 3.9 at several instants of the cardiac cycle.

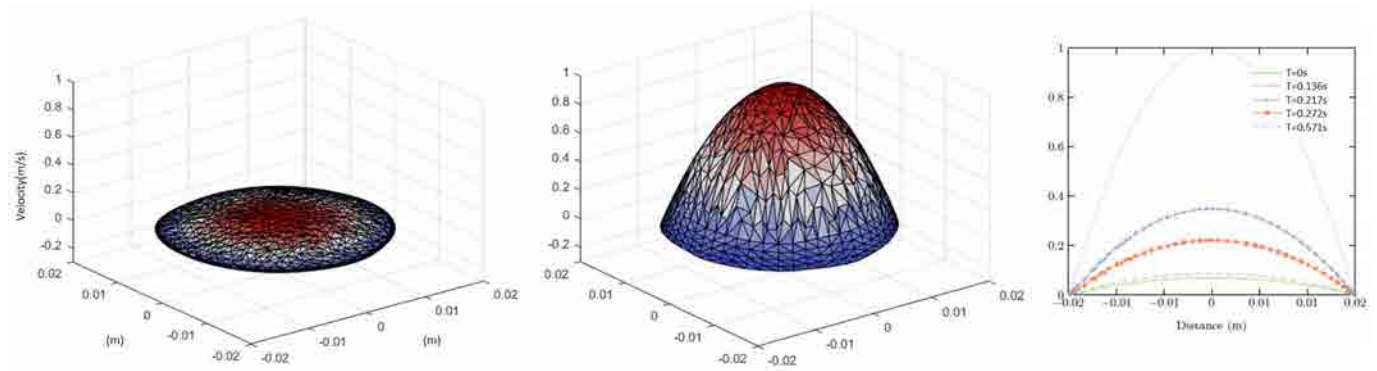


Figure 3.9: (Left) Velocity profile for a Poiseuille flow adapted to a non-circular surface at $t = 0$ s; (Middle) Velocity profile for a Poiseuille flow adapted to a non-circular surface at systolic; (Right) Curves of imposed velocity profiles at the entrance of the ascending aorta at different times of the cardiac cycle.

3.4.5.2 Conditions at the exit

3.4.5.2.1 Mathematical modeling of the cardiovascular system

The aorta and large arteries are incredibly elastic, serving as reservoirs that reduce the pulsing of blood flow imposed by the heart, which cause the heart to beat faster. Because of the complex geometry of the arteries and the existence of bifurcations, the blood flow wave is reflected and decreased in amplitude as it travels downstream of the vascular system. The elasticity of the blood vessels and the transition from larger to smaller arteries causes a significant decrease in blood pressure, which is referred to as Windkessel. During the systolic phase, the Windkessel effect helps to dampen the pressure change and preserve the blood perfusion to the organs. The impact, however, decreases with age as a result of the hardening of the arteries.

Blood flow in the cardiovascular system is governed by the laws of conservation of mass, momentum balance, and the interaction of blood with the artery wall, among other principles. This is why models based on the Navier-Stokes equations are used to explain the blood flow in a deformable aorta segment by investigating the interaction between the fluid and the structure. This class of models is split into three-dimensional (3D), two-dimensional (2D), and one-dimensional (1D) models, each of which is defined by a sequence of partial differential equations, as well as a zero-dimensional (0D) model, which is described by ordinary differential equations (ODE).

The selection of the appropriate dimension in the choice of model, from 0D to 3D, depends on the objectives and the desired accuracy. The 0D models, known as truncated logs, assume a uniform distribution of fundamental variables, such as pressure, flow rate, and volume at any time, while higher dimensional models distinguish the variation of these parameters in space and are useful for characterizing complex flows. The coupling of different models exists in the literature to solve the problem of boundary conditions that specify the behavior of the fluid at the entrance and exit of the considered domain. These conditions are needed numerically and the coupling of 3D-0D (Moghadam et al., 2013), 3D-1D (Formaggia et al., 2001) and 1D-0D (Marchandise et al., 2009) models can be used in order to eliminate the problem of measurements at the model output.

We chose a 0D model at the outlet of the arterial system branches that we developed in OpenFOAM for this study. The 0D model allows for varying, in a simple way, the pressure at the outlet of the branches during the whole cardiac cycle and thus to respect the physiological conditions of flow variation with the pressure, constituting, for this study, an acceptable compromise between model complexity and physiological reality.

3.4.5.2.2 Windkessel

In 0D models, a hydraulic-electric analogy is often applied. Indeed, the pressure gradient causes the blood to advance by opposing the hydraulic impedance, in the same way, that the potential difference causes the electric current to advance by opposing the circuit impedance. Hydraulic impedance represents the combined effect of frictional losses, the elasticity of the vessel wall, and inertia of the blood, similar to electrical impedance, which means the combination of resistance, capacitance, and inductance in an electrical circuit. By representing blood pressure and flow with electrical voltage and current, respectively, methods of electrical circuit analysis can be borrowed and applied to cardiovascular dynamics. This electrical analogy, summarized in Table 3.2, does not describe the nonlinearities that sometimes characterize cardiovascular mechanics, including, for example, the contribution of convective acceleration terms in the momentum equation and the nonlinear relationship between pressure and volume in a blood vessel. Nevertheless, these differences do not change the general nature of the hydraulic-electrical analogy and when necessary, such nonlinearities can be included in the solution of differential equations.

Table 3.2: Hydraulic-electrical analogy for 0D models

Arterial Hydraulics	Electrical System
Blood pressure	Voltage u
Blood flow	Current i
Vessel compliance	Capacity C
Vessel peripheral resistance	Resistance R
Ascending aorta compliance	Impedance Z_C
Inertia of circulating blood	Inductance L

Historically, 0D models have evolved and incorporated more complexities by adding components to capture particular physical phenomena. There is a wide range of 0D models available to simulate pressure and flow variations in an artery. The most widely used and simplest 0D model is the two-element Windkessel model, formulated by Otto Frank in 1899 (Sagawa et al., 1990). The word Windkessel, translated from German as "air chamber", refers to an elastic reservoir which, in a pulsating flow circuit, first fills with a particular volume and then releases an endless flow (Figure 3.10). Thanks to the elasticity of the compliant arteries, they exert the Windkessel effect by dampening the pulse of blood flow. The arteries then swell during systole and store blood volume before expelling it in diastole.

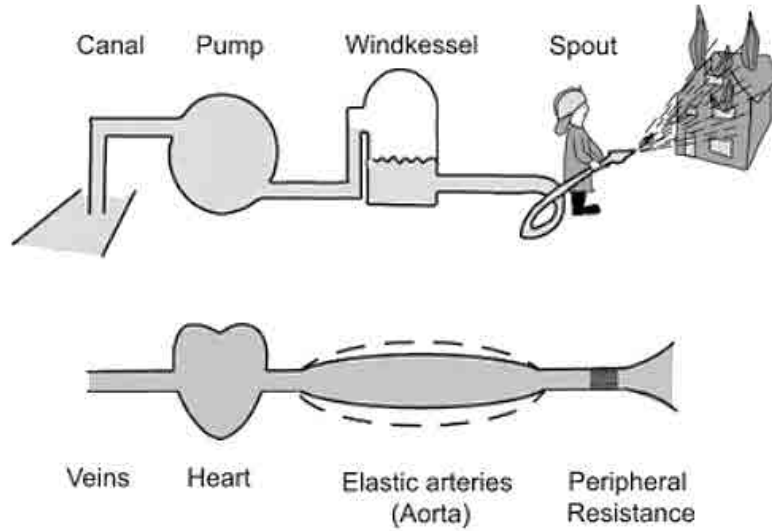


Figure 3.10: Windkessel concept. The large arteries are associated with the air chamber (Windkessel). The combination of compliance, associated with aortic valves and peripheral resistance, leads to a rather constant peripheral flow (Westerhof et al., 2009).

The two-element Windkessel model consists of a capacitance C connected in parallel with a resistance R (Figure 3.11). The capacitance describes the storage properties of large arteries which means their elastic properties, and the resistance describes the dissipative nature of small peripheral vessels, including arterioles and capillaries. This model was developed to represent the elementary characteristics of the arterial network only, the veins having been neglected and described as a zero-pressure field. However, it does not allow modeling the internal phenomena of the arteries, such as the propagation or reflection of the pulse wave. Moreover, when the aortic flow is used as an input to the system, this model produces aortic pressure waveforms that are far from the pressures found experimentally (Stergiopoulos et al., 1995).

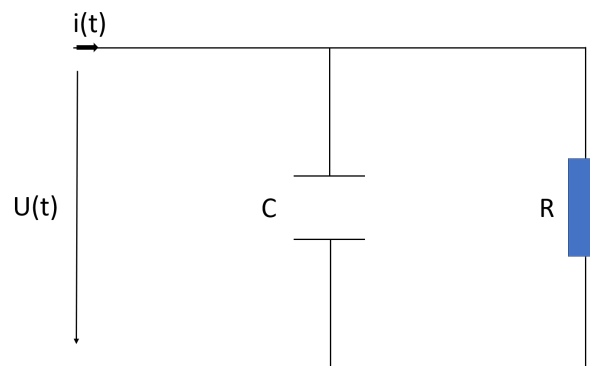


Figure 3.11: The two-element Windkessel model is analogous to the flow in an arterial system, an electrical circuit formed by a current generator, a resistor R , and a capacitor C connected in parallel.

To overcome this problem, the three-element Windkessel model (Westerhof et al., 2009) introduces an additional resistor Z_C connected in series with the two-element Windkessel model (Figure 3.12). This second resistor represents the aorta's characteristic impedance and considers the inertia and

compliance of the ascending thoracic aorta. The introduction of this Z_C resistor improves the model by producing realistic pressure and flow waveforms and by fitting the experimental data (Stergiopoulos et al., 1999b). This also allows to considerably improve the behavior of the model at medium and high frequencies. The 3-parameter model is the most widely used in systemic circulation modeling even though studies (Latson et al., 1987, Stergiopoulos et al., 1999b) show that the estimates of C and Z_C deviate significantly from the values obtained with the methods used in the literature: C tends to be overestimated and Z_C underestimated. This means that the three-element Windkessel model can produce realistic aortic pressures and flows, but only with parameters that differ quantitatively from vascular properties. At low frequencies, the input impedance of the system is also poorly estimated, a result visible in Figure 3.14.

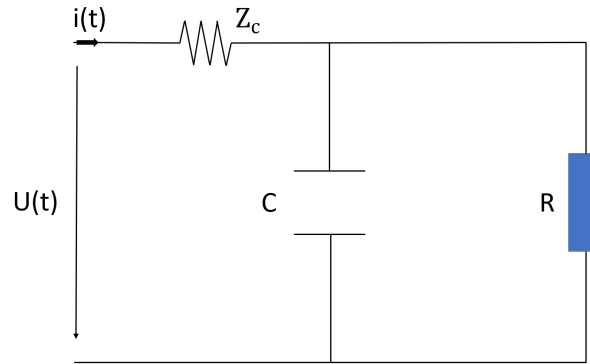


Figure 3.12: The three-element Windkessel model introduces an additional resistor Z_C connected in series with the two-element Windkessel model.

For this reason, the four-element Windkessel model (Figure 3.13), proposed by Burattini and Gnudi (1982), adds an inductance L in parallel with the impedance Z_C which represents the inertia of the whole arterial system and thus contributes to the low frequencies, allowing Z_C to take on the medium and high frequencies (Stergiopoulos et al., 1999b). However, this model reveals a particular difficulty in determining the value of the inductance.

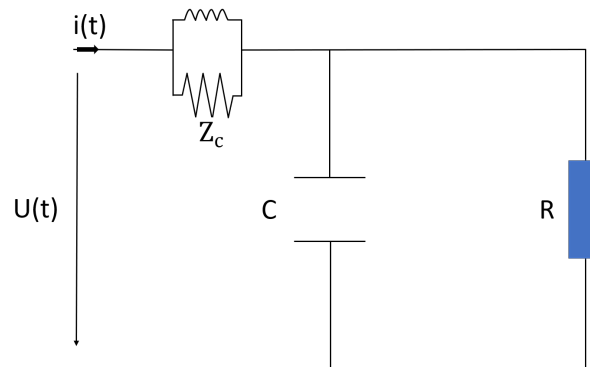


Figure 3.13: The four-element Windkessel model introduces an inductance L modeling the low-frequency blood inertia in parallel with the impedance Z_C connected in series with the two-element Windkessel model.

Figure 3.14 taken from the work of Westerhof et al. (2009) illustrates the differences between the Windkessel models in terms of impedance at the entrance to the thoracic aorta. Comparison with

the impedance calculated from experimental data highlights the shortcomings of the 2-element Windkessel model: for high frequencies, its modulus reduces to negligible values, and its phase angle reaches -90° . The experimentally calculated impedance shows that the modulus decreases to a fixed non-zero value and the phase angle oscillates around zero for high frequencies. The addition of a characteristic resistor in the 3-element Windkessel model allows for correcting this defect for high frequencies, and the modulus of the impedance approaches the experimental fixed value. However, the results achieved at low frequencies are not satisfactory. Finally, the addition of inductance in the 4-element Windkessel model allows getting closer to the experimental values of [Westerhof et al. \(2009\)](#). However, the complexity of determining the numerical values of the different elements of the circuit makes it a little-used model. For this reason, we choose to develop the 3-element Windkessel model to impose the boundary conditions of our numerical model.

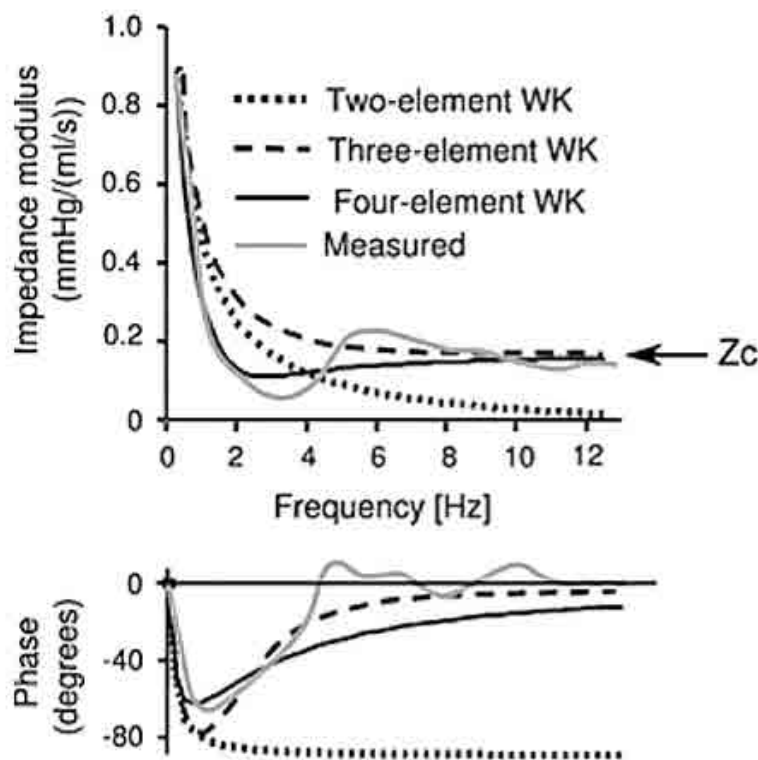


Figure 3.14: An example of measured impedance at the aortic inlet and impedances predicted by the two-element, three-element and four-element Windkessel model ([Westerhof et al., 2009](#))

The three-element Windkessel model does not represent the experimentally observed oscillations in impedance modulus and phase (Figure 3.14), so this aspect of the arterial system is not modeled. Many works have been dedicated to the calculation of Windkessel model parameters. Most of them use pressure and flow measurements ([Stergiopulos et al., 1994, 1995, 1999a](#)). The Windkessel models are straightforward models with ordinary differential equations, which provide a good understanding of the overall functioning of the arterial circuit and adequately describe the diastolic phase. Nevertheless, the difficulty of estimating the parameters, despite their physiological meaning, from pressure and flow measurements and the failure to take into account wave propagation phenomena, limits these models.

3.4.5.2.3 Implementation of the 3-element Windkessel model

- Implementation in OpenFOAM

Implementing the 3-element Windkessel model in OpenFOAM was based on a typical boundary condition implemented and coded in C in the software. From this condition, we developed the code `ImpedanceBC` with the implementation of new variables R_1 , R_2 , C , and p_0 respectively, the proximal resistance (also known as the compliance of the ascending aorta), the distal resistance (which is the hydraulic resistance of the vessel), the compliance of the vessel, and the initialization pressure at the boundary surface. The main code for this boundary condition is part of the source file `ImpedanceBC.C` and is presented as:

```
scalar Q_n = gSum(phi_prev);
scalar Q_nm1 = gSum(phi_2prev);
scalar Pmean_n = gSum(this->patch().magSf()*p_prev)/gSum(this
->patch().magSf());

scalar tau = R2_*C_;
scalar taudt = dt + tau;
scalar dtRT = dt*(R1_+R2_);
scalar R1tau = R1_*tau;
scalar dp_n = Pmean_n-p0_;
scalar dq_n = (Q_n-Q_nm1);

operator==( (tau*dp_n+dtRT*Q_n+R1tau*dq_n)/taudt + p0_ );
```

Q_n is the average mass flow rate at t_n , Q_{nm1} is the average mass flow rate at t_{n-1} , and $Pmean_n$ is the average pressure on the boundary surface. The declaration of the constants τ , τ_{dt} , $dtRT$, $R1\tau$, dp_n and dq_n allows an easier writing of the differential equation.

This code allows the resolution of the equation (3.7) which depends on the two resistances R_1 and R_2 , the compliance C , the flow rate Q and the pressure P . The electrical diagram with the hydraulic analogy is shown in Figure 3.15.

$$R_1 C \frac{dP}{dt}(t) + P(t) = (R_1 + R_2)Q(t) + R_1 R_2 C \frac{dQ}{dt}(t) \quad (3.7)$$

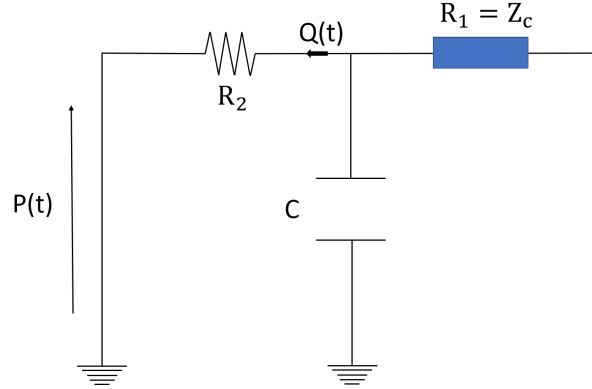


Figure 3.15: The three-element Windkessel model with the hydraulic analogy. The equation (3.7) is associated with this circuit model.

- Implementation in FOAM-Extend

An approach that is similar to this one is described in the preceding section. However, the environment for implementing the element Windkessel model in FAOM-Extend require the following modifications in the source file `ImpedanceBC.C`:

```
const scalar Qi = gSum(phi_curr);
const scalar Qim1 = gSum(phi_prev);
const scalar patchArea = gSum(this->patch().magSf());
const scalar Pmi = gSum(this->patch().magSf()*p_curr)/patchArea;
const scalar Pmim1 = gSum(this->patch().magSf()*p_prev)/patchArea;

scalar tau1 = Rd_*C_;
scalar tauD = 1.0/(dt + tau1);
scalar tau2 = dt*(Rd_+Rp_);
scalar tau3 = C_*Rd_*Rp_;
scalar dQi = (Qi-Qim1);
scalar p_next = Pout_+tauD*(tau1*Pmi+tau2*Qi+tau3*dQi);
operator==(p_next);
```

Q_i is the average mass flow rate at t_i , Q_{im1} is the average mass flow rate at t_{i-1} , Pm_i is the average pressure on the boundary surface at t_i , and Pm_{im1} is the average pressure on the boundary surface at t_{i-1} . The declaration of the constants τ_1 , τ_D , τ_2 , τ_3 , and dQ_i allows an easier writing of the differential equation.

3.4.5.2.4 Windkessel parameters

The Windkessel model parameters used for this case, R_1 , R_2 , and C were first set based on data from the work of Menut (2017), which used for a healthy thoracic aortic for the three supra-aortic trunks and descending aorta in the numerical model to assure the convergence of simulation.

The parameters of the Windkessel 0 three-element model used for the numerical simulations are available in Table 3.3. R_1 , R_2 , and C are the compliance of the ascending aorta, the vessel's hydraulic resistance, and the vessel's compliance, respectively.

Table 3.3: Windkessel model parameters applied to fluid model outputs(Menut, 2017)

	R_1 $\times 10^6 m^{-1} \cdot s^{-1}$	R_2 $\times 10^6 m^{-1} \cdot s^{-1}$	C $\times 10^{-7} m \cdot s^2$
Brachiocephalic artery	0.052500	0.8337	8.6334
Left common carotid artery	0.147000	2.23203	3.1003
Left subclavian artery	0.071985	1.2135	5.9511
Descending aorta	0.015442	0.2603	0.2774

3.5 Data analysis

After completing the simulations, we used ParaView[®], an open-source program for post-processing CFD/FSI simulations, to assess the following values. This program has a wide variety of filters that allow for the processing and presentation of all field variables associated with the flow, the solid, and the wall-fluid interface, including:

- The velocity field is used to identify the direction of blood flow from TL into FL (tracing the streamline that shows the direction in which a massless fluid element will travel at any point with time).
- For CFD simulation, the WSS is defined as the magnitude of traction owing to the viscous portion of the Cauchy stress tensor, τ , which is equal to the flow on the surface wall.

$$WSS = \|\mathbf{WSS}\|_2 = \left(\left\| \tau \cdot \mathbf{n}^f \right\| \right)_{\Gamma^{fs}} \quad (3.8)$$

- Time-Averaged Wall Shear Stress (TAWSS) is the average WSS magnitude during one cardiac cycle. It is defined as:

$$TAWSS = \frac{1}{T} \int_0^T |\tau_w| dt \quad (3.9)$$

where T is a cardiac cycle's duration, τ_w is WSS. TAWSS is an intriguing metric to investigate since it may be utilized to examine the WSS distribution on the artery and identify the low WSS areas. Generally, TAWSS for the arterial system is between 1 to 7 Pa form (Chiu and Chien, 2011). The work of Bassiouny et al. (1994) presented that low shear stress (<0.4 Pa), which is common in atherosclerosis-prone areas, promotes an atherogenic phenotype.

- Oscillatory Shear Index (OSI) was developed to account for the wall shear stress vector's cyclic deviance from its primary axial alignment (Ku et al., 1985) and it is defined as:

$$OSI = \frac{1}{2} \left(1 - \frac{\left\| \int_0^T \mathbf{WSS} dt \right\|}{\int_0^T \|\mathbf{WSS}\|_2 dt} \right) \quad (3.10)$$

OSI is an excellent predictor of plaque's initial placement. This variable's value fluctuates between 0 and 0.5. The higher the OSI, the greater the change in shear stress direction.

- Relative Residence Time (RRT) is criterion for disturbed blood flow. It is proportional to the magnitude of the TAWSS and OSI.

$$\text{RRT} = \frac{1}{(1 - 2\text{OSI})\text{TAWSS}} \quad (3.11)$$

RRT is suggested as a robust single metric for low and oscillating shear in low and oscillating conditions. The residence duration of the particles along the wall is closely related to the RRT (Himburg et al., 2004). A high RRT has been identified as being essential in the development of atherogenesis and in-stent restenosis (Hoi et al., 2011). When $\text{RRT} < 1$, the zone is high shear; when $\text{RRT} > 1$, the zones is both low and oscillating shear stress or areas with only low WSS.

3.6 Bio-faithful model with rigid walls

3.6.1 Newtonian fluid

The implementation of the model in OpenFOAM is done through the use of several source files allowing the user to enter the appropriate configuration for the calculation of the case with the appropriate boundary conditions. All these configuration files for the numerical simulation of the Newtonian case are available in Appendix B.

Figure 3.16 shows the set of boundary conditions entered into OpenFOAM for the fluid simulation with the Newtonian model. The boundary conditions are entered in the U, p files (Appendix B.1.2), including the Windkessel model parameters: R1, R2, and C. The properties of the Newtonian fluid are entered in the file transportProperties (Appendix B.3). The flow regime here is considered laminar, specified in the RASproperties and turbulenceProperties files (Appendix B.4.5). The viscoelastic properties of the fluid require a relatively small time step to capture the desired effects according to the imposed boundary conditions. So for the simulation convergence, the time step for the numerical calculation of blood where $\Delta t = 1 \times 10^{-5} \text{ s}$. The time step parameters, calculation duration, and writing of results are indicated in the controlDict file (appendix B.6). Finally, the solvers used to resolve the equations on the whole studied domain are precise in the files fvSchemes and fvSolutions (Appendix B.7.8).

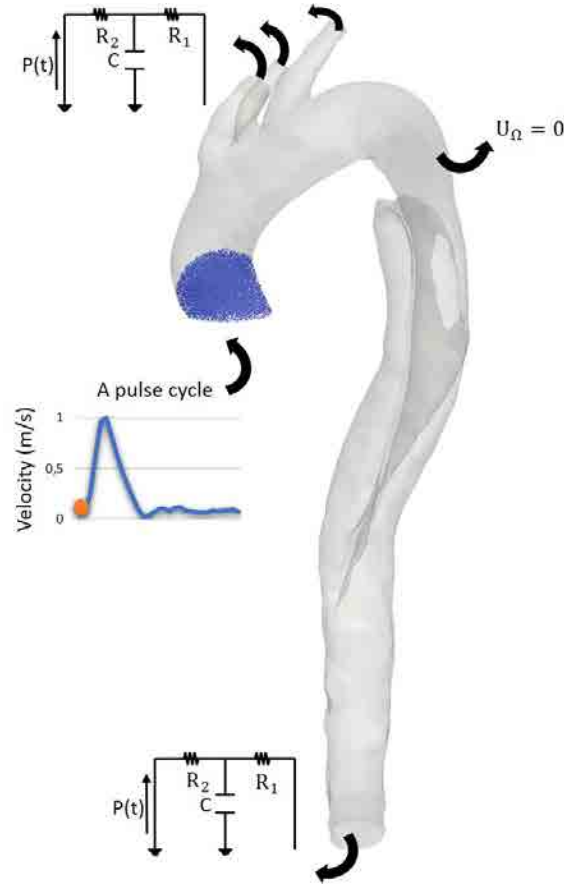


Figure 3.16: Diagram of the configuration of the numerical model with rigid walls on OpenFOAM

The numerical calculation of the pressure with a periodic behavior requires the simulation of several cardiac cycles to establish the pressure and the stresses in the fluid due to the relaxation parameters in dynamics. The periodic convergence of the pressure is illustrated in Figure 3.17. Figure 3.18 shows the stability of the flow values observed during the convergence of the pressure to ensure that the distribution of the flows in the different branches does not fluctuate. The values of these pressures and flows rates were taken at the model boundaries with the function of the probe, whose syntax is available in Appendix B.7.

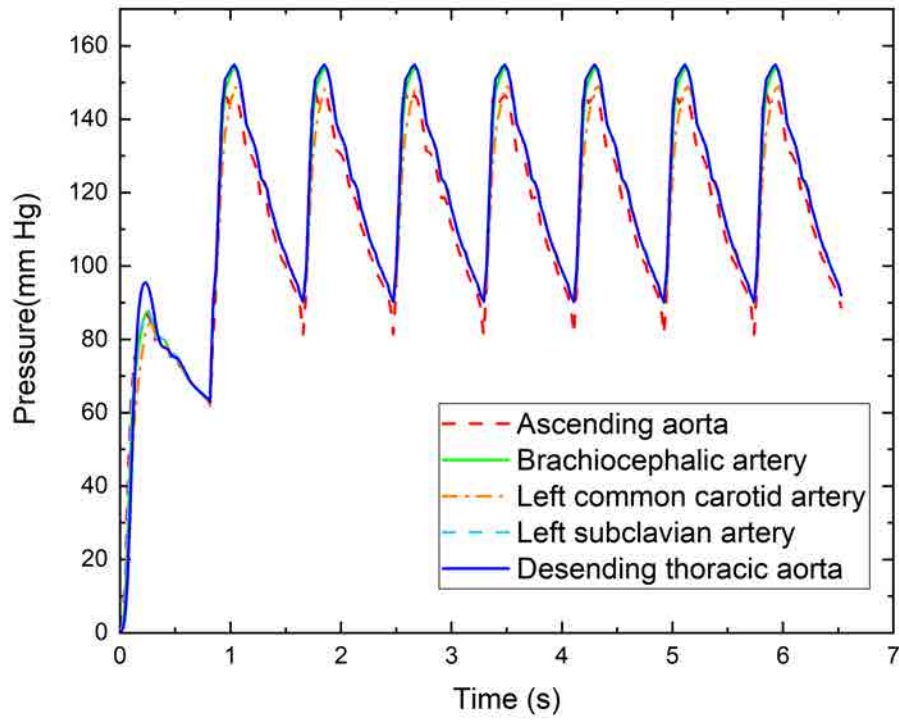


Figure 3.17: Convergence of the pressure measured with OpenFOAM over 8 cardiac cycles on the input and each output of the aorta CFD Newtonian model

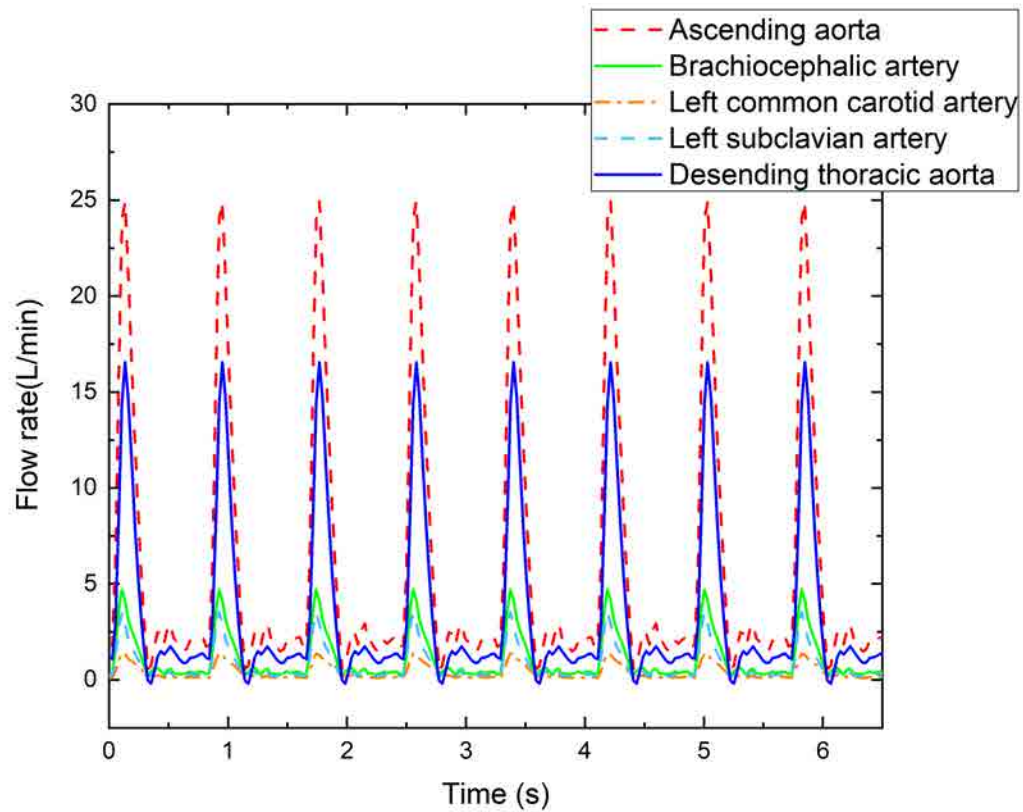


Figure 3.18: Flow rates measured with OpenFOAM over 8 cardiac cycles on the input and each output of the aorta CFD Newtonian model

As shown in Figure 3.19, the velocity profiles on different sections of the aorta were measured at various times during the peak systole of the patient ($t=0.12s$), throughout the flow decay ($t=0.2s$), at the end of the systole ($t=0.3s$), and the beginning of diastole ($t=0.42s$). At level C, we can observe that the blood flows into the False lumen and causing whirlpools inside the FL. We can also see blood moving up into the TL at level D in the figure 3.19 near the beginning of diastole, which is a nice touch.

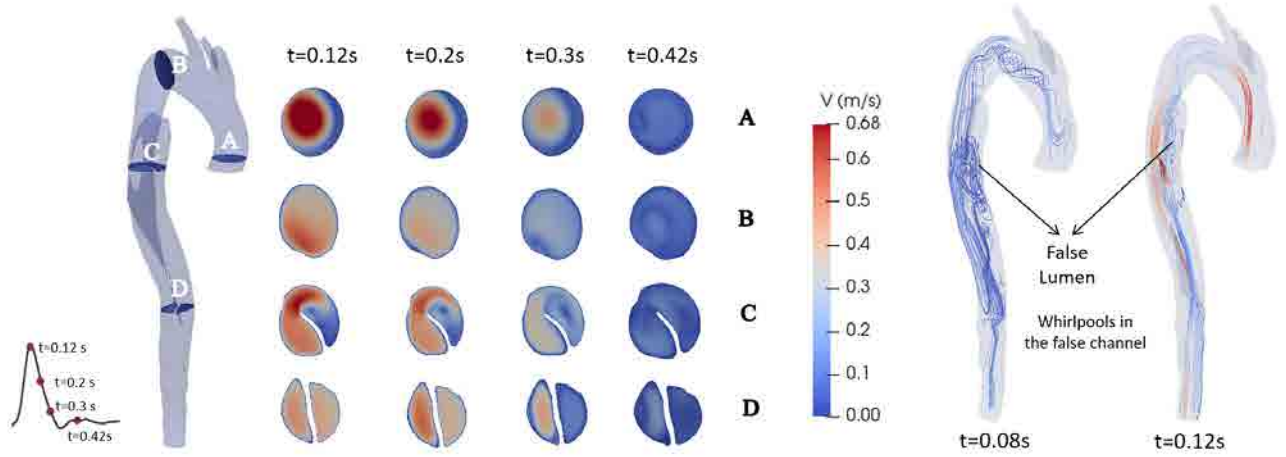


Figure 3.19: (Left) Velocity profiles on several sections along the aorta; (Right) Streamlines with velocity in AD

In the numerical simulation, we have assumed that the fluid is laminar. But in figure 3.19 there is turbulence flow present in the FL; we need to verify the Reynolds number to see if the hypothesis of laminar fluid is still working or not. The Reynolds number in tubes (Fung, 2013) is defined as

$$Re = \frac{\text{Inertial forces}}{\text{Viscous forces}} = \frac{\rho V D}{\mu} \quad (3.12)$$

with V is the average flow velocity (m/s), D is tube diameter(m), μ is fluid dynamic viscosity ($Pa.s$ or $N.s/m^2$), and ρ is fluid density (kg/m^3).

General pipe flow Reynolds number <2100 for laminar flow (also known as viscous flow, linear flow) state, more than 4000 for turbulent flow (also known as disturbance flow) state, $2100 \sim 4000$ for the transition flow state.

Table 3.4: Reynolds number

Section	Surface area (m^2)	Diameter (m)	Time (s)	Flow rate (L/min)	Average velocity(m/s)	Re
Ascending aorta	8.51×10^{-4}	3.29×10^{-2}	t=0.05	6.02	0.118	1176
			t=0.12	24.9	0.49	4867
			t=0.2	16.5	0.32	3224
			t=0.4	2.5	0.048	483
Brachiocephalic artery	5.91×10^{-5}	8.68×10^{-3}	t=0.05	1.5	0.424	1113
			t=0.12	4.13	1.16	3061
			t=0.2	2.55	0.72	1887
			t=0.4	0.64	0.18	471
Left common carotid artery	1.49×10^{-5}	4.35×10^{-3}	t=0.05	0.44	0.49	650
			t=0.12	1.3	1.46	1924
			t=0.2	0.97	1.08	1428
			t=0.4	0.23	0.257	339
Left subclavian artery	4.95×10^{-5}	7.94×10^{-3}	t=0.05	1.14	0.38	921
			t=0.12	2.94	0.99	2382
			t=0.2	1.68	0.569	1359
			t=0.4	0.43	0.15	349
Descending thoracic aorta	4.93×10^{-4}	2.51×10^{-2}	t=0.05	2.09	0.1	755
			t=0.12	16.55	0.56	4247
			t=0.2	11.32	0.38	2905
			t=0.4	1.18	0.04	302

We calculate the Reynolds number on the input and each output of the thoracic aorta throughout various instances of the cardiac cycle, respectively systolic and diastolic (Table 3.4). During the beginning phases of the cardiac cycle, the flow is laminar, with Re values less than 1200. At the moment of systolic, the flow reached the state transition status. Table 3.4 shows that the Re numbers are more than 2100 during systole and less than 2100 during diastole. Since the systolic period is relatively short and the Re numbers are not very large, we considered that the blood flow is laminar in all the numerical models.

3.6.2 Comparison with the Carreau-Yasuda model

The Carreau-Yasuda rheological model is widely used in the literature for modeling blood flows (O'Callaghan et al., 2006, Alimohammadi et al., 2015). It is a generalized Newtonian model with a two-step rheological viscosity law, detailed in Chapter 2. The comparison of numerical results between the Newtonian model and the Carreau model is interesting.

The Carreau-Yasuda model used in OpenFOAM is the **BirdCarreau** model with a viscosity that varies according to the following law ($\dot{\gamma}$ is the shear rate):

$$\mu = \mu_{\infty} + \frac{\mu_0 - \mu_{\infty}}{(1 + (k\dot{\gamma})^2)^{2/(n-1)}} \quad (3.13)$$

The model characteristics specified in the file **transportProperties** and whose numerical values of viscosities are divided by the density of the fluid are entered as follows in OpenFOAM:

BirdCarreauCoeffs

```

{
nu0      nu0    [ 0 2 -1 0 0 0 0 ] 5.283e-5;
nuInf    nuInf  [ 0 2 -1 0 0 0 0 ] 3.30189e-6;
k        k      [ 0 0 1 0 0 0 0 ] 3.313;
n        n      [ 0 0 0 0 0 0 0 ] 0.3568;
}

```

The numerical values of the different parameters of this law are those of the work of [Razavi et al. \(2011\)](#) summarized in Table 3.5.

Table 3.5: Numerical values from [Razavi et al. \(2011\)](#) for the Carreau-Yasuda model.

Coefficient	Definition	Value
η_∞	Dynamic viscosity of blood at high shear rate	0.00345 Pa.s
η_0	Dynamic blood viscosity at low shear rate	0.056 Pa.s
ρ	Volume mass of the blood	1060 kg.m ⁻³
λ	Blood relaxation time	3.313 s
n	Degree of power law	0.3568

Figure 3.20 shows velocity profiles during systole and diastole, respectively, taken from four sections along the thoracic aorta. These profiles are very close to those observed in the calculation based on a Newtonian model. The shear stresses of Carreau-Yasuda model (figure 3.25) are very low, which corresponds to the velocity distribution close to the Newtonian model.

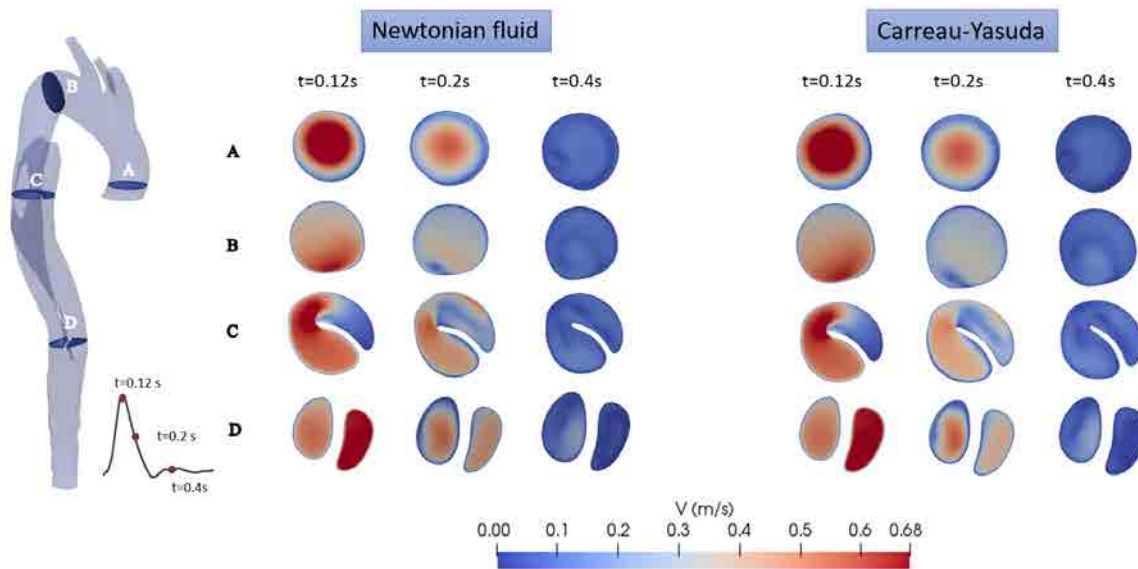


Figure 3.20: Velocity profiles on several sections along the aorta for the Newtonian and Carreau-Yasuda models

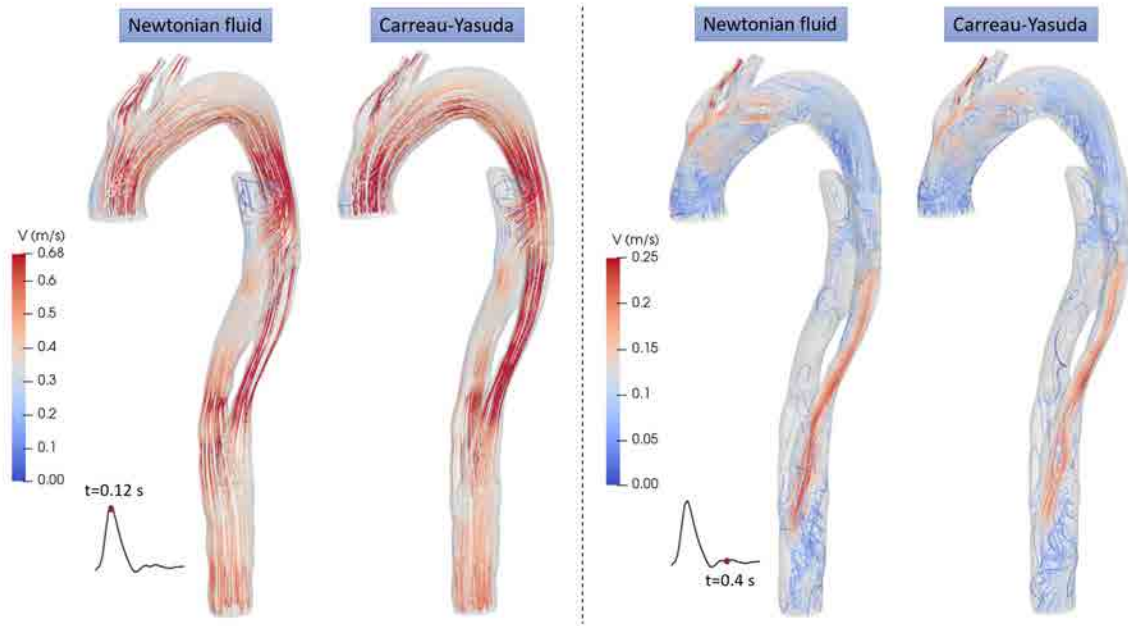


Figure 3.21: Velocity profiles with streamline along the aorta for the Newtonian and Carreau-Yasuda models at peak systole and the diastolic period

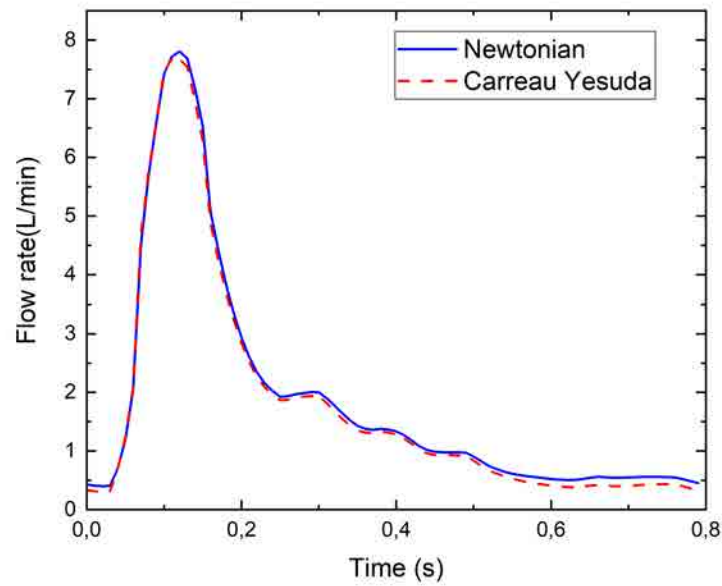


Figure 3.22: Flow rate on section C for the Newtonian and Carreau-Yasuda models with a cardiac cycle

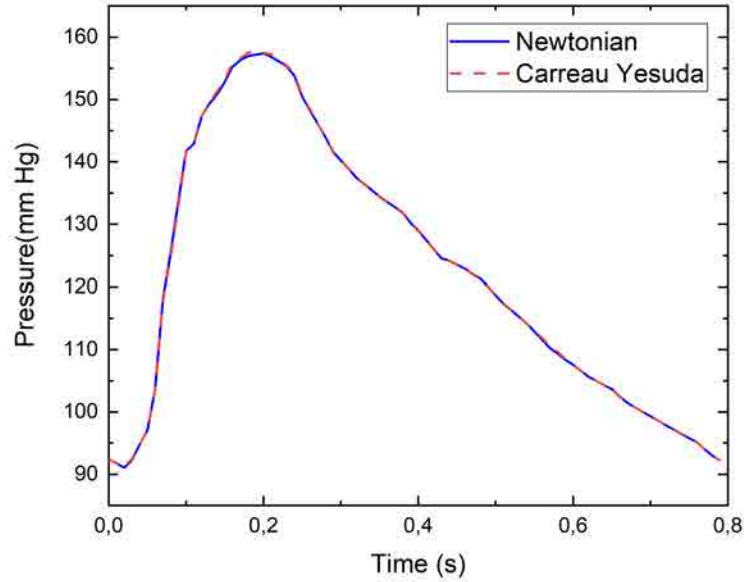


Figure 3.23: Pressure on section C (TL & FL section) for the Newtonian and Carreau-Yasuda models with a cardiac cycle

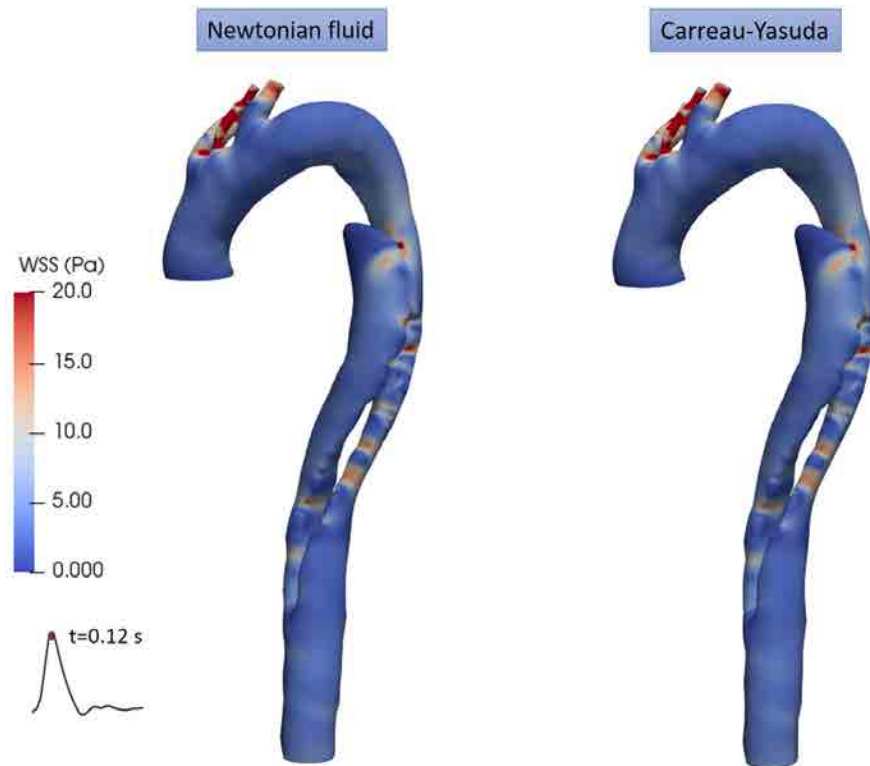


Figure 3.24: Wall shear stress (WSS) at peak of systole ($t=0.12$ s) for the Newtonian and Carreau-Yasuda models

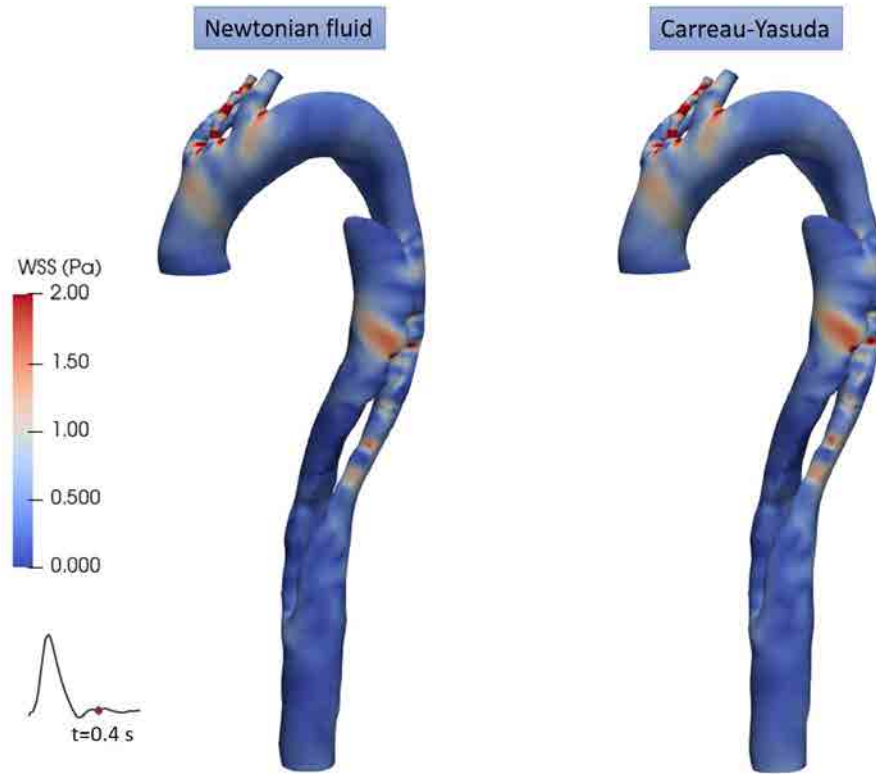


Figure 3.25: WSS during diastole (t=0.4s) for the Newtonian and Carreau-Yasuda models

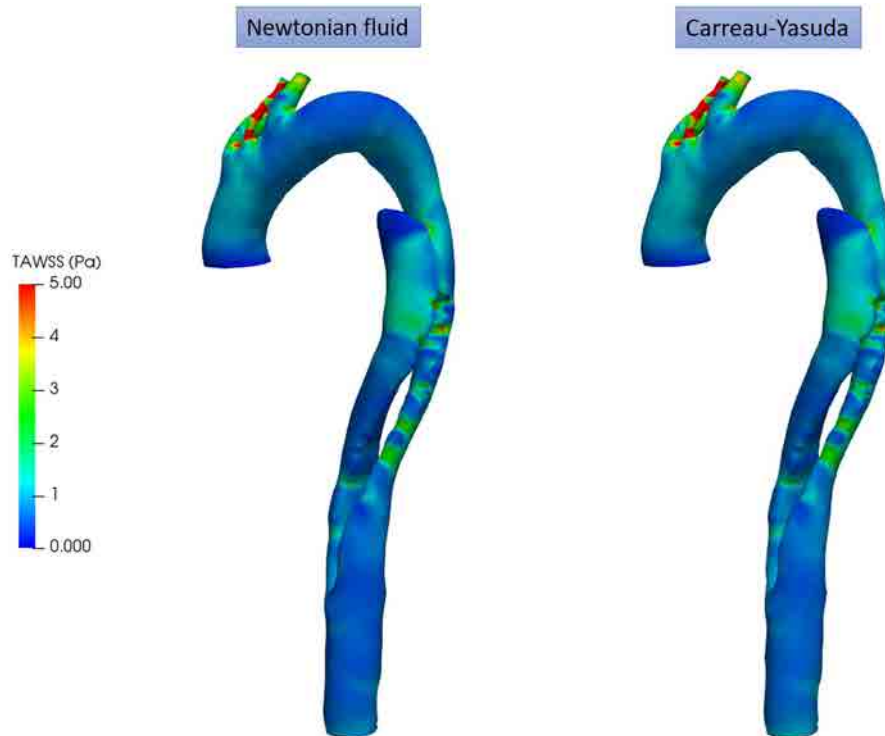


Figure 3.26: Comparison of TWASS between the Newtonian and Carreau-Yasuda models

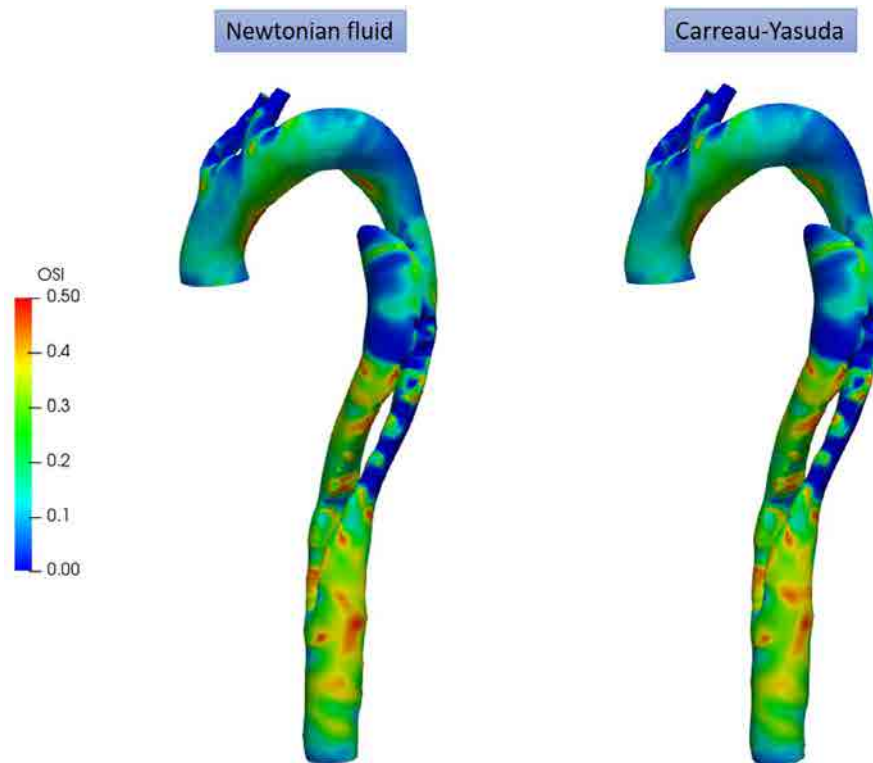


Figure 3.27: Comparison of OSI between the Newtonian and Carreau-Yasuda models

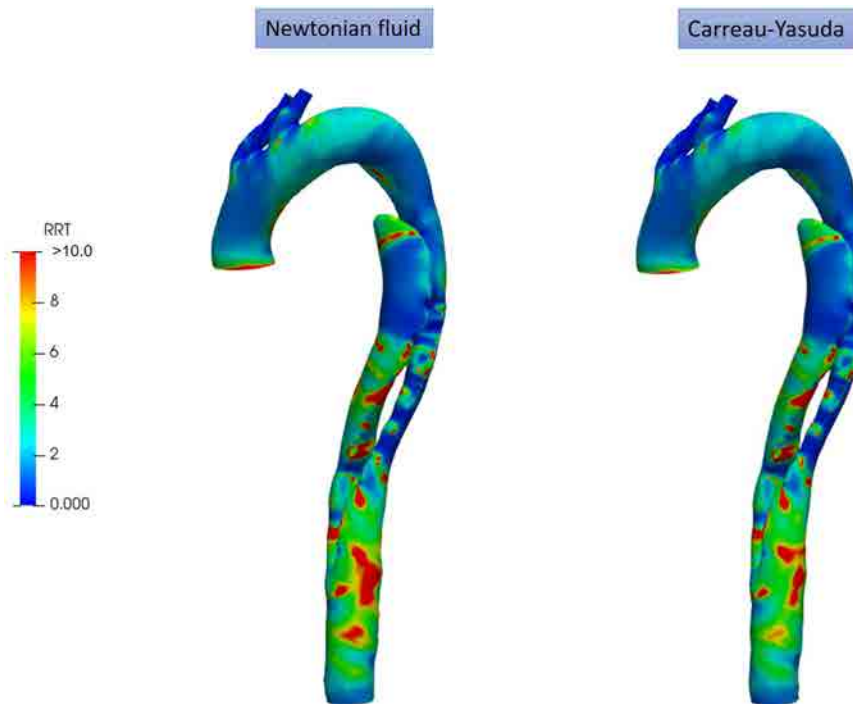


Figure 3.28: Comparison of RRT between the Newtonian and Carreau-Yasuda models

Table 3.6: The maximum TAWSS and RRT comparison between the Newtonian and Carreau-Yasuda models

	$TAWSS_{max}$ (Pa)	RRT_{max}
Newtonian	18.49	321.04
Carreau-Yasuda	19.01	197.81

The highest value of OSI, 0.5, indicates that the flow is entirely oscillatory. Table 3.6 shows that RRT maximum of Newtonian is higher than Carreau-Yasuda, and there are more regions of high RRT than Carreau-Yasuda fluids (Figure 3.28).

These results show that there are not significantly different between the Newtonian and Carreau-Yasuda models when we compared with velocity profile, average flow rate and pressure on section C where is the entry of AD, and also WSS, TAWSS, OSI and RRT of the thoracic aorta. So, the Newtonian model for this study fits well with the blood flow modeling. Meanwhile, due to the non-Newtonian blood's relaxing time, which means the fluid's viscoelastic characteristics, a concise time step is required to capture the desired effects, making computations costly. As a result, we assume that the blood flows in the following simulations are all Newtonian in behavior.

3.7 Fluid-structure coupling

3.7.1 Necessity of a fluid-structure coupling

Hemodynamics in arteries has two objectives. The first one concerns the prediction of blood pressure and flow, of significant interest for the clinician in the pathophysiological interpretation of a medical diagnosis at any point of the cardiovascular system globally and dynamically. The second objective is related to predicting the dynamics of the blood flow, which impacts the structure, particularly with the parietal stress distribution on the endothelial tunica. With the development of atherosclerosis in areas of low parietal stress, the characterization of parietal stresses is indicated as a major factor in most arterial pathogenesis and alteration of tissue properties. On the other hand, in this study, aortic wall compliance and internal pressure gradients influence vessel shape, affecting the flow domain, which varies during the cardiac cycle. This motion may be captured using fluid-structure interaction (FSI) simulations, which combine computational fluid dynamics (CFD) simulations of the fluid with finite element modeling of the aortic wall. In particular, FSI simulation could consider the dynamic interactions of the blood flow field and the dissection flap. It has been shown that flow at the dissection region is highly disturbed, and a significant flow enters the false lumen (FL), which may further enlarge the dissection. (Metz et al., 2010) validated FSI simulations of the interactions between the blood flow and the flap will provide insight into the dynamics of aortic dissections.

However, hemodynamic simulation methods must be used to characterize tissue behavior, and the artery deformation must be taken into consideration via FSI numerical simulations. Some of the papers have been published in the past five years that deal with flow-strengthening estimates in arteries (Qiao et al., 2019, Bäumlér et al., 2020). Up to this point, the issue of conducting substantial and accurate simulations in fluid-structure interaction in a time frame short enough to

give meaningful findings to surgeons has remained unsolved.

Several simplifying assumptions are incorporated into the computations, and certain boundary conditions are taken into consideration to decrease the computation time. In the field of blood flow, a lot of work has already been done regarding the flow and pressure boundary conditions, as for example with the work of [Formaggia et al. \(2001\)](#) whose three-dimensional FSI problem is coupled to a 1D system in order to get rid of the numerical problems of pulse wave feedback. After a few years, the issue was thoroughly investigated by the work of [Formaggia et al. \(2007\)](#), [Vignon-Clementel et al. \(2010\)](#), [Xiao et al. \(2013\)](#). They used ordinary differential equation models to simulate the downstream flows of the arterial system, which had previously not been considered.

However, despite these artificial boundary conditions for blood flow, few approaches consider the surrounding tissues of arteries to model boundary conditions on vessel walls. Most fluid-structure coupling studies consider a constant, and often zero, pressure applied to the outer part of the arterial wall. This simple boundary condition cannot support the artery and usually results in artificial motion of the arterial wall. In practice, this movement could induce much greater inaccuracies than those introduced by spurious reflections on the artificial boundaries of the model. One option could be to directly prescribe the displacements deduced from the dynamic sequence of a 4D MRI as time-dependent Dirichlet boundary conditions. But this approach would be directly influenced by the inaccuracies and noise in the data sequence, particularly related to the difficulties of time sampling. Moreover, such a model would have a relatively limited predictive character and would not model certain wave propagation phenomena in the arteries.

In the past two decades, computational techniques in FSI have advanced significantly, and numerous numerical simulation software packages are now available to tackle dynamic mesh issues and multi-physics problems. OpenFOAM® is a free and open-source software for computational fluid dynamics (CFD) simulations that is gaining popularity in academic and industry settings (Open Field Operation and Manipulation). Because one of its solutions is designed for FSI problems in a partitioned way, one of its branches, the foam-extend package, is considered to conduct the aortic dissection simulations in this case.

3.7.2 Fluid-structure coupling with FOAM-Extend

In fluid-structure interaction problems, one or more solid structures interact with an internal or surrounding fluid flow. Fluid-structure coupling problems play an important role in many scientific and engineering fields. However, the thorough numerical study of these problems remains a challenge due to their strong nonlinearity and multidisciplinary nature. Analytical solutions are impossible to obtain for most of these problems, and experiments have a limited scope. Numerical simulations are then employed to study the physics involved in the complex interaction between the fluid and the solid.

The equations governing FSI issues include nonlinear components, are coupled, and have an inherently temporal feature; in addition, in most instances, they must be solved in complicated geometries, which is challenging. Given these features, an analytical solution is almost difficult to

find in most situations when considering the currently available mathematical approaches, leaving the sole option to depend on computational methods to solve the problem. Like CFD, Finite Volume Method (FVM), Finite Element Method (FEM), and Finite Differences Method (FDM) are three of the most common mesh-numerical methods for FSI. These methods are designed to solve the governing equations using a temporal marching procedure in which the discretized equations are applied to elements or control volumes (computational mesh) into which the calculation domain is subdivided, yielding a system of equations.

Numerical approaches to solving these fluid-structure interaction problems can be classified into two methods, monolithic and partitioned (Ha et al., 2017), illustrated in Figure 3.29.

- **Monolithic approach** : it treats the fluid and structural dynamics in the same mathematical model to form a single equation for the entire problem. The fluid and structural equations are solved simultaneously with a single computational code. The conditions at the interface between the fluid and the solid are solved implicitly, guaranteeing unconditional stability. In general, monolithic schemes are accurate and stable, but very computationally expensive. Moreover, a monolithic approach is neither easy to implement nor to evolve. When the geometries or physical properties of the problem to be treated become complex, this method is no longer feasible since each medium requires specific numerical calculation procedures that the monolithic approach does not exploit.
- **Partitioned approach**: it treats the fluid and the structure as two computational domains that can be solved separately, with their discretization and numerical algorithm. Conditions at the interface are solved explicitly to share information between the fluid and structural solutions. A strong reason for using this approach is the possibility of integrating already available algorithms for solving the fluid and structure and thus reducing the development time of a monolithic code. The use of numerical algorithms validated and used to solve many problems allows for the robustness of both parts. Therefore, a successful partitioned method can solve FSI problem with complex fluids and structures. However, the challenge of this approach is to coordinate the algorithms to achieve an accurate and efficient fluid-structure interaction solution with minimal code modification. In particular, the interface that divides the fluid and the structure by its constant motion in time requires exceptional tracking that can lead to computational errors and instabilities.

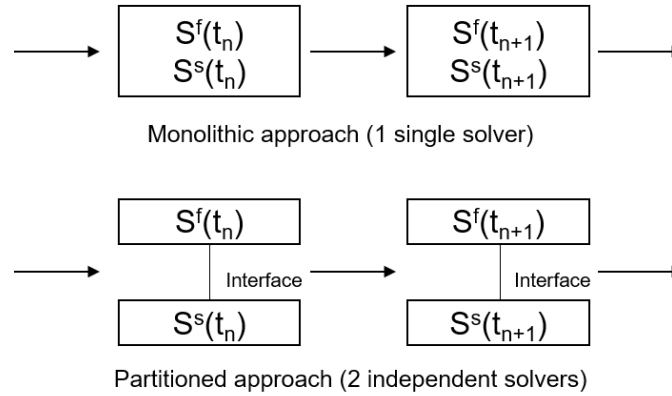


Figure 3.29: Schematic of monolithic and partitioned approaches for FSI

A comparison between these two approaches for numerical simulation of FSI problems is discussed in the work of Michler et al. (2004), where they are compared in terms of stability, accuracy, and computational cost. Partitioned schemes often require only one iteration between the fluid and the structure per time step, and, therefore, their computational cost is lower than that of monolithic schemes. On the other hand, the time lag between the integration of the fluid and the structure implies that the interface conditions cannot be completely satisfied, causing numerical instabilities. Although the stability and accuracy of partitioned schemes can be improved, they are still inferior to those of a monolithic scheme.

There are two types of coupling algorithms between the fluid and the structure in the partitioned approach: **strong coupling** and **weak coupling**, shown in Figure 3.30. These are also referred to as implicit (strong) and explicit (weak) coupling. The strong coupling has an additional loop in its solution algorithm, which ensures cohesion between the mesh deformation and the kinematic and dynamic conditions at the interface after each time step. This method often uses a sub-relaxation technique to speed up the coupling process and guarantee the algorithm's stability. The different methods of accelerating the calculations for strong coupling will not be detailed here, but a detailed description could be found in the work of Degroote et al. (2009).

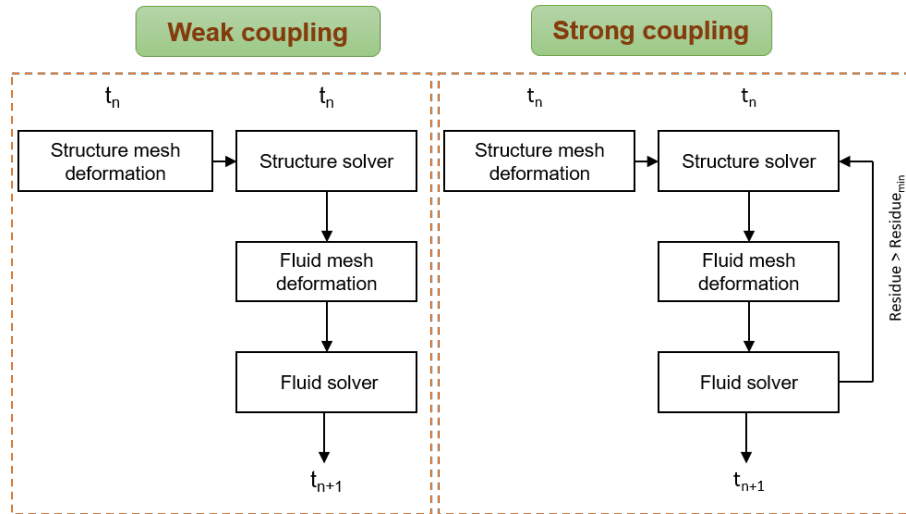


Figure 3.30: Solving process for a fluid-structure interaction problem with weak coupling and strong coupling using the partitioned approach.

A solver for fluid-structure interaction exists in the extended version of OpenFOAM, called FOAM-Extend. This solver uses a partitioned approach with strong coupling. Indeed, with the densities of the fluid and the structure being very close, a weak coupling will not capture the physics and the nonlinearities that this problem imposes Förster et al. (2007).

3.7.2.1 Discretization

With Newton–Raphson iterations, it is possible to solve for the location of the interface in partitioned simulations of fluid-structure interactions. There are several methods in FOAM-extend that could solve the problem of FSI. Schemes Interface Quasi-Newton-Implicit Jacobian Least-Squares (IQN-ILS) (Oliveira, 2017) and Aitken relaxation are mostly used in FAOM-Extend. The IQN-ILS algorithm is an implicit solution algorithm proposed by Degroote et al. (2009) in recent years. The Aitken algorithm (Küttler and Wall, 2008) is another implicit solution algorithm that is simple to implement and widely used, and its basic idea is based on the string truncation method. The IQN-ILS algorithm, a Newtonian iterative method, is faster than the Aitken algorithm in terms of convergence for most fluid-solid coupled problems. However, for pressure-driven fluid-structure coupled problems, the IQN-ILS algorithm cannot guarantee the stability of the computation while the Aitken algorithm has this ability. For partitioned FSI simulations, a simplified depiction of the IQN-ILS and Aitken relaxation algorithms is shown in Figure 3.31.

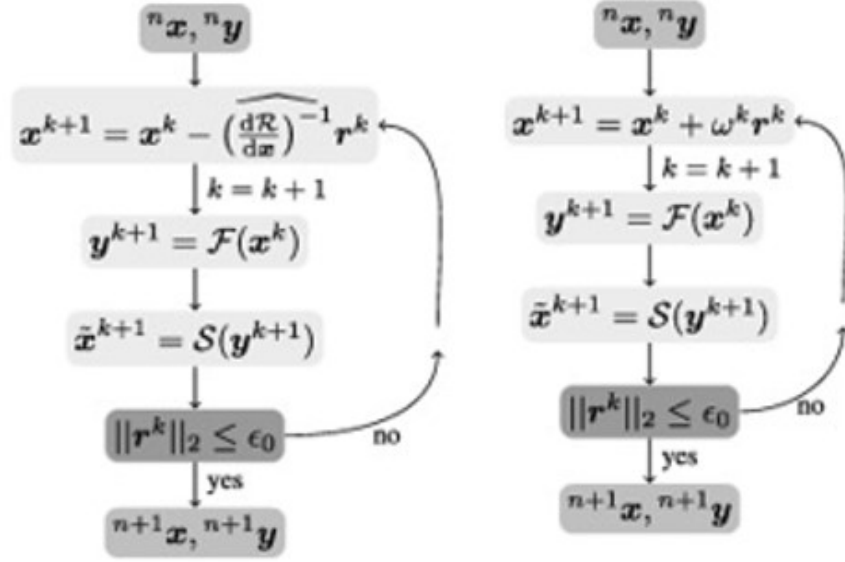


Figure 3.31: Simplified scheme of (Left) the IQN-ILS technique, and (Right) Aitken relaxation (adapted from (Degroote et al., 2009))

When using the IQN-ILS model, it is possible to write the interface quasi-Newton iterations together with the approximation for the inverse of the Jacobin as equation 3.14 .

$$\mathbf{x}^{k+1} = \mathbf{x}^k + \left(\widehat{\frac{dR}{d\mathbf{x}} \bigg|_{\mathbf{x}^k}} \right)^{-1} (-\mathbf{r}^k) \quad (3.14)$$

Furthermore, Aitken relaxation (equation 3.15) generates a scalar relaxation factor w^k that is dynamically changing for the fixed-point iterations inside a time step (Degroote et al., 2009).

$$\mathbf{x}^{k+1} = \mathbf{x}^k + w^k \mathbf{r}^k \quad (3.15)$$

with the relaxation factor w^k is calculated as follows:

$$w^k = -w^{k-1} \frac{(\mathbf{r}^{k-1})^T (\mathbf{r}^k - \mathbf{r}^{k-1})}{(\mathbf{r}^k - \mathbf{r}^{k-1})^T (\mathbf{r}^k - \mathbf{r}^{k-1})} \quad (3.16)$$

This shows that implementing the IQN-ILS technique is not much more complex than applying Aitken relaxation. For this project, we will use Aitken relaxation algorithm.

3.7.3 FSI model of AD patient-specific

The patient-specific model for the numerical simulation of fluid-structure interaction uses the fluid part explained in section 3.6 *Bio-faithful model with rigid walls* with a Newtonian fluid model and a structure part whose modeling is detailed below.

3.7.3.1 Mesh of FSI model

Setting up the fluid-structure interaction for a patient-specific model requires first establishing the structure part from the fluid part to have an interface in as perfect contact as possible with both the

structure and the fluid. This is a significant step to ensure the convergence of the calculation. The solid component was constructed in this manner using the exterior surface retrieved from the fluid model. One challenge is to construct a realistic model and mesh of flap. So using a fluid tetrahedral mesh with flap refinement is essential to be considered. Additionally, the wall thickness is difficult to determine owing to the low quality of the images. A geometrical operation was performed from this surface to create a thickness of 1 mm to wrap the fluid and generate tetrahedron. The intimal flap (IF) was created by filling the space between FL and TL, which varied in thickness throughout the dissection area from 1mm to 2.5mm. The use of tetrahedral in structural calculations allows, in the same way as in CFD, the generation of high-quality meshes inducing numerical stability in most cases.

Figure 3.32 depicts the model for creating the mesh for the structural component during the modeling phase.

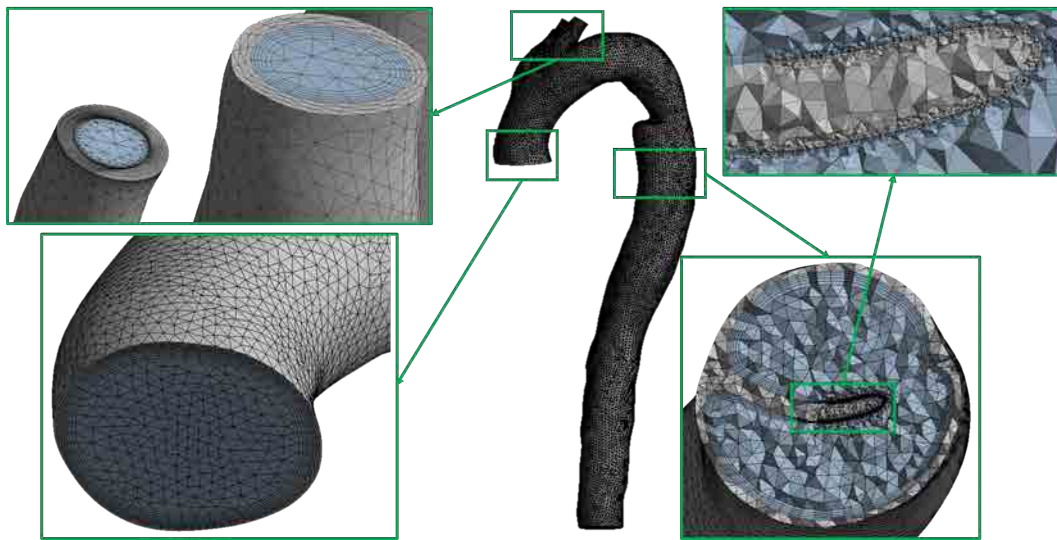


Figure 3.32: tetrahedral mesh generated with the commercial software ANSYS©

3.7.3.2 Boundary conditions

For the fluid part, we use the same boundary conditions as the CFD model for the blood fluid inlet at ascending aorta and outlet at brachiocephalic artery, left common carotid artery, left subclavian artery, and descending thoracic aorta boundary.

The structure is assumed to be elastic in this initial investigation of fluid-structure coupling, with Young's modulus of $E = 300$ MPa and a Poisson's ratio ν of 0.3. We relied on values obtained from the literature since it is still difficult to quantify specific characteristics in live tissues, such as Young's modulus and Poisson's ratio. So we performed three different elastic modulus simulations for the arterial wall in the fluid-structure coupling simulation. The initial one Young's modulus of $E = 300$ MPa, the artery is calcification with pathology which Young's modulus is $E = 3$ GPa. Also, Young's modulus is $E = 30$ GPa, which can represent a highly calcified wall and is mimicking the rigid wall properties.

By inspecting the governing equations, it becomes clear that the only unknown for the solid issue is the solid displacement field, which is both space- and time-dependent. As a result, appropriate boundary conditions are specified to resolve the issue. As with the fluid case, the starting condition is the numerical solution of the simulation with the wall excluded from the equation. A displacement field is derived from the flow solution's stress distribution on the wall and is therefore taken as the starting condition.

We used the following boundary conditions:

For the arteries, the inlet and outlets boundary of the arterial is applied as fixed displacement, which was set to zero.

Internal and external surfaces of flap and artery walls: a Neumann boundary condition was employed on the internal and outer surfaces of the solid domain, obtained from the elastic constitutive relation:

$$t^s = [(2\mu^s + \lambda^s) \nabla_0 \mathbf{u} + \mu^s \nabla_0^T \mathbf{u} + \lambda^s \text{tr}(\nabla_0 \mathbf{u}) \mathbf{I} - (\lambda^s + \mu^s) \nabla_0 \mathbf{u}] \cdot \mathbf{n}^s \quad (3.17)$$

where μ^s and ∇_s are the Lamé's parameters relating to the material's Young's modulus and Poisson's ratio: $\mu^s = \frac{E}{2(1+\nu^s)}$, and with t^s representing the traction per unit area on the surface, which is dependent on the stresses and pressures acting on it; and \mathbf{n}^s is the normal vectors pointing outward on the surface.

Equation 3.17 is rearranged to give:

$$(\nabla_0 \mathbf{u}) \cdot \mathbf{n} = \frac{t^s - [\mu^s \nabla_0^T \mathbf{u} + \lambda^s \text{tr}(\nabla_0 \mathbf{u}) \mathbf{I} - (\lambda^s + \mu^s) \nabla_0 \mathbf{u}] \cdot \mathbf{n}^s}{2\mu^s + \lambda^s} \quad (3.18)$$

which relates to the specification of a displacement gradient, commonly known as a Neuman boundary condition. The gradients in equation 3.18's right-hand side are calculated explicitly.

In terms of the boundary condition at the fluid-solid interface Γ^{fs} , the formulation presented here is commonly referred to as *the Dirichlet-Neumann formulation* of the FSI problem because the flow equations are solved for a specified velocity at Γ^{fs} due to the kinematic condition that ensures velocity continuity at this boundary :

$$(\mathbf{v}^f)_{\Gamma^{\text{fs}}} = (\mathbf{v}^s)_{\Gamma^{\text{fs}}} = \left(\frac{d\mathbf{u}}{dt} \right)_{\Gamma^{\text{fs}}} \quad (3.19)$$

with the interface traction on Γ^{fs} owing to the continuity dynamic condition is solved for the solid equation as follows:

$$\underbrace{(\sigma^f \cdot \mathbf{n}^f)_{\Gamma^{\text{fs}}}}_{t^f} + \underbrace{(\sigma^s \cdot \mathbf{n}^s)_{\Gamma^{\text{fs}}}}_{t^s} = 0 \quad (3.20)$$

where t^s is from equation 3.18, and \mathbf{n}^f and \mathbf{n}^s are the normal vectors pointing outward on Γ^{fs} .

On the external artery, equation 3.18 is still valid. Although, the traction t^s is solely attributable

to a uniform pressure being applied to it, as shown in the following equation:

$$t^s = -p\mathbf{n}^s \quad (3.21)$$

with p is about 97.3 mmHg on the outer surface and corresponds to the diastole pressure in the dissection region for this model.

The files for Foam-Extend to realize the FSI simulation are showing in Appendix C. Consider big arteries and formulate the following simple assumptions in order to include the viscosity of blood and the elasticity of the artery wall into the pulsatile flow analysis:

- The fluid is homogeneous and Newtonian.
- The wall material is isotropic and elastic.
- The fluid motion is laminar, incompressible.

3.7.3.3 Results

3.7.3.3.1 Comparison between CFD model and FSI model

We compared the results of CFD and FSI simulations through the previous model with Young's modulus of the artery eagle 300 MPa .

Figure 3.33 demonstrates velocity profiles obtained from four sections of the thoracic aorta during systole and diastole, respectively, throughout the cardiac cycle. And Figure3.34 shows the streamline flow characteristics in the proximal (proximal to the tear) of FL and TL. Mid-systole flow flowing through the middle FL & TL continues straight into the distal (distal to the exit of dissection) FL & TL, and streamlines may be seen extending down to the region's bottom.

We find that the velocity at peak systole is the same trend, but throughout the flow decay ($t=0.2s$), at the end of the systole ($t=0.3s$), and the beginning of diastole ($t=0.4s$), the dynamics in the FSI model are significantly different to the CFD model. The velocity in the aortic arch region and the proximal FL region is 2 or 3 times bigger than the results in the CFD model.

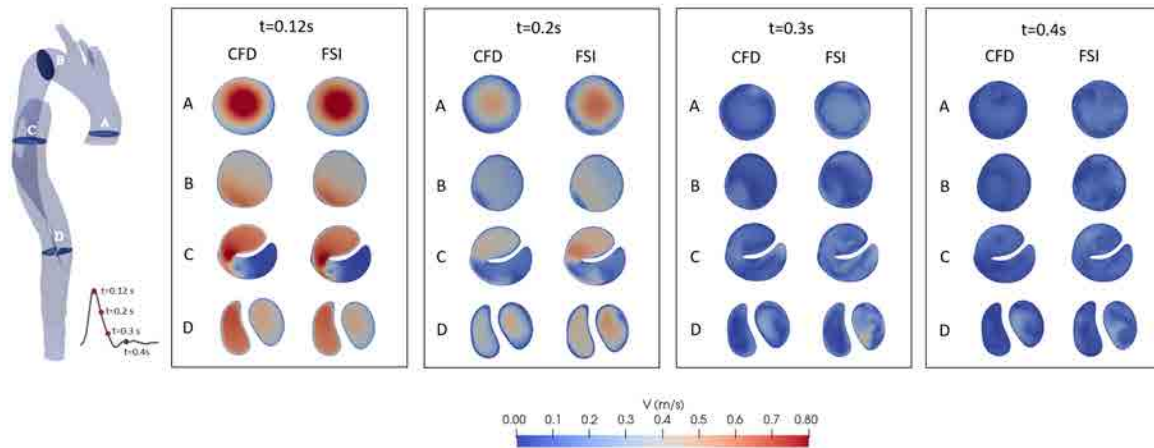


Figure 3.33: Comparison of velocity profiles on several sections along the aorta between CFD and FSI models during the cardiac cycle

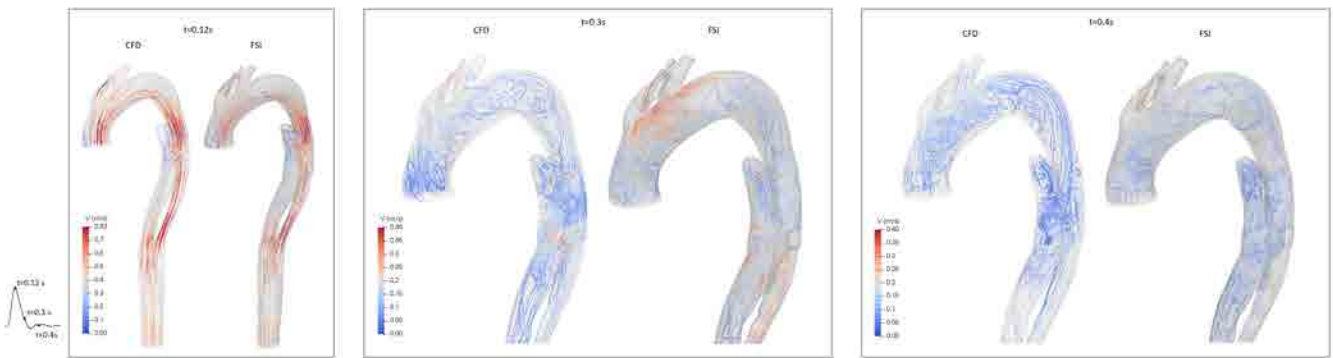


Figure 3.34: Comparison of the streamline during systole and diastole between CFD and FSI models

At peak systole, a pressure differential of about 20 mmHg exists between the FL and TL, which might be anticipated to produce significant flow between the two region (Figure 3.35). On the other hand, the flow continues to reach the distal FL at this moment, although at a relatively slow pace. The pressure gradient is reversed at the dirotic notch, yet the fluid in the distal FL is expelled when the pressure drops and the wall contracts. This is why in the systole deceleration, the velocity of FSI model is basically greater than that of CFD model. After diastole, the distal FL velocity is almost the same as TL, and the pressures between the lumina are roughly equal.

In addition, we compare the pressure on section C between FSI model and CFD model. Table 3.7 shows that because of the wall expansion at the systole, pressure is smaller than the CFD model. And at the dirotic notch and diastole, the wall contracts, pressure is greater than CFD model.

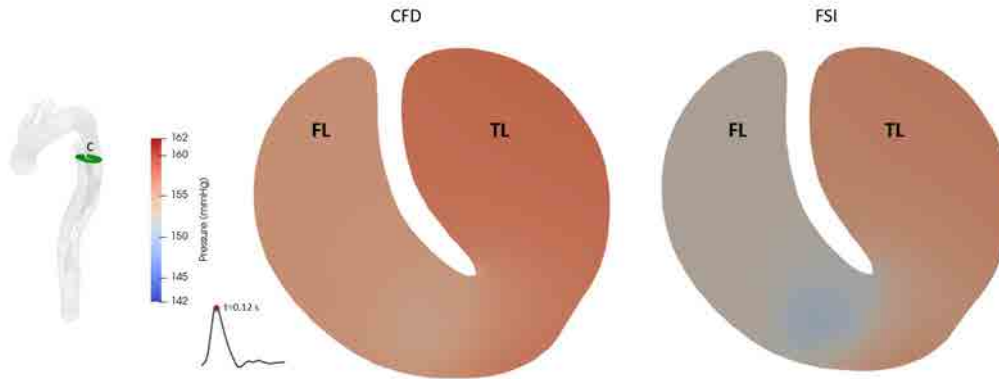


Figure 3.35: Comparison of the pressure at peak systole between CFD and FSI models on the place of Section C

Table 3.7: Pressure compared between FSI and CFD model on the place of Section C (entry site of dissection)

	FSI(mmHg)	CFD (mmHg)	$P^* = \frac{P_{FSI} - P_{CFD}}{P_{CFD}}$
t=0.12s	155.65	157.60	-1.24%
t=0.2s	164.75	167.08	-1.39%
t=0.3s	153.87	148.61	3.54%
t=0.4s	141.94	138.03	2.83%

While rigid wall simulations are incapable of simulating these complicated dynamics, the issue is whether the extra simulation work required to achieve this precision is worthwhile. Prediction of wall shear stresses is an essential outcome of these models. However, as shown in Figure 3.36, the differences between the rigid wall and FSI models for the WSS distribution are not substantial, and if just WSS is of relevance, FSI modeling may be unnecessary. Table 3.8 shows that the maximum value of wall shear stress compared for several periods, there is no significant difference in the values during the systolic period. And during the diastolic period, the FSI data will be larger than CFD, which is reasonable because at the aortic notch and diastole, the influence of the wall contracts.

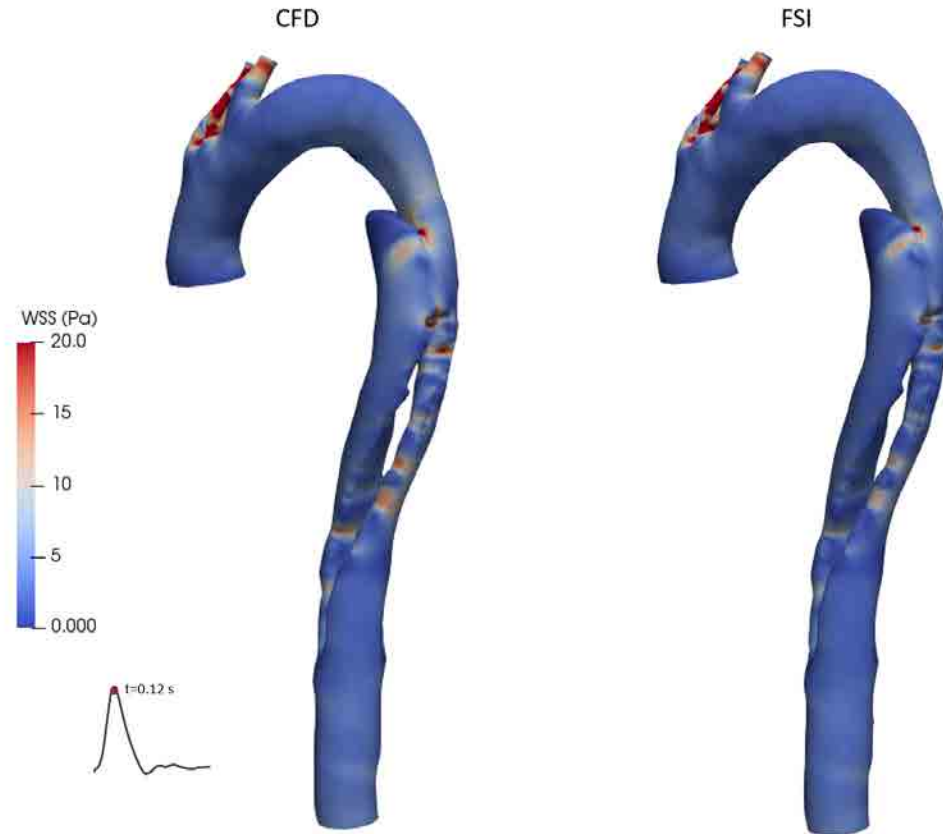


Figure 3.36: Comparison of the WSS at peak systole between CFD and FSI models

Table 3.8: Comparison of maximum values of WSS for several time periods between FSI and CFD model

	t=0.12s	t=0.2s	t=0.3s	t=0.4s
CFD	85.7 Pa	47.52 Pa	13.47 Pa	7.085 Pa
FSI	81.1 Pa	55.49 Pa	18.72 Pa	14.86 Pa

3.7.3.3.2 Influence of the d'Younge module

In this study, the elastic modulus is reported to be in the range of 300 MPa, 3 GPa, and 30 GPa, and we model the tissue by setting the Poisson ratio $\nu = 0.3$ in the whole structural domain.

In Figure 3.37, the displacement of the aorta wall is shown at four instances marked by inset graphs with Young's modulus of artery eagle 300 MPa. First, the ascending aorta has been pushed outward, increasing the aorta's volume, and the region of entry tear are displaced. And at diastole, the deformation around the entry tear is reverted to its original position. The more obvious displacement changes are in the proximity of TL during the cardiac cycle, and the distal FL & TL is closer to its original position. As shown in Figure 3.38, to illustrate the displacement of the region of entry tear, the highlighted black area in the inlay is expanded and color-coded. At peak systole, the edges of the entry tear are displaced by up to 0.2 mm, and the intimal flap (IF) is displaced by about 0.19 mm. As anticipated, the FL expands in sync with the TL contracting.

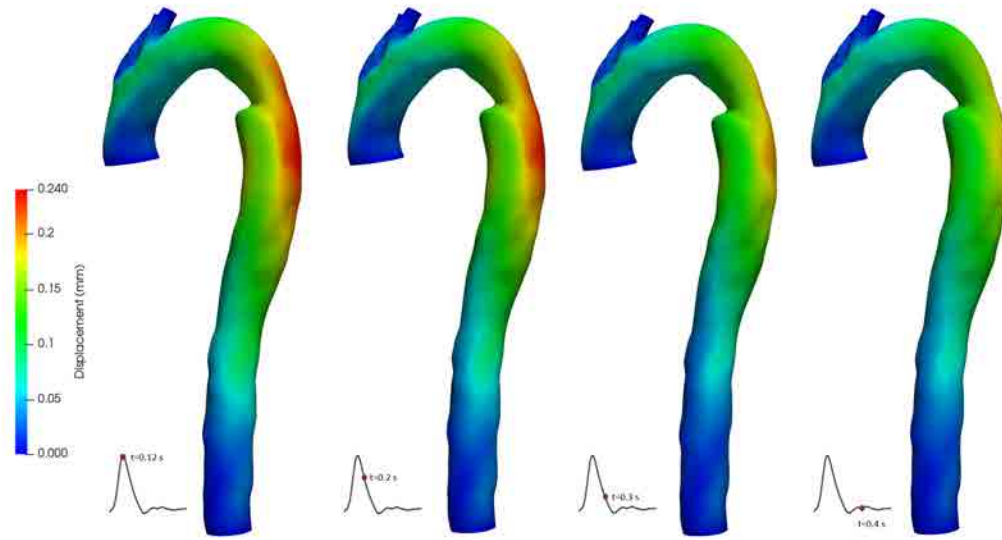


Figure 3.37: Displacement of the artery at various time instances with Young's modulus = 300 MPa

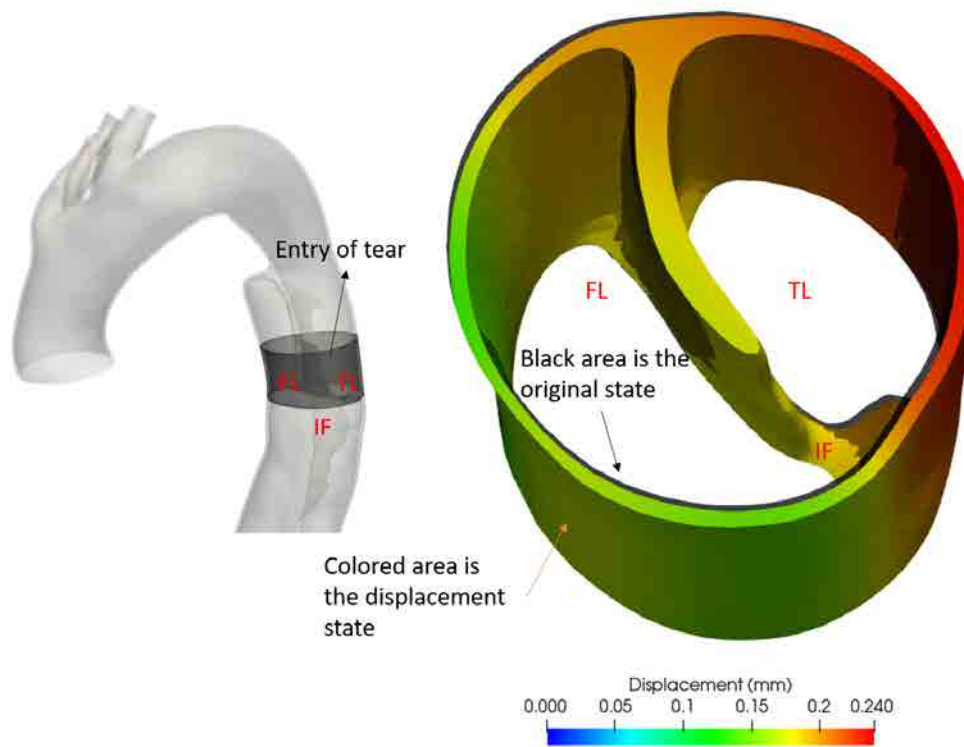


Figure 3.38: Displacement of IF region with Young's modulus = 300 MPa at peak systole

Figure 3.39 shows a significant influence on displacement values with different Young's modulus. They tend to deformation is the same. The scenario is justified because Young's modulus is a physical quantity that describes the ability of a solid material to resist deformation.

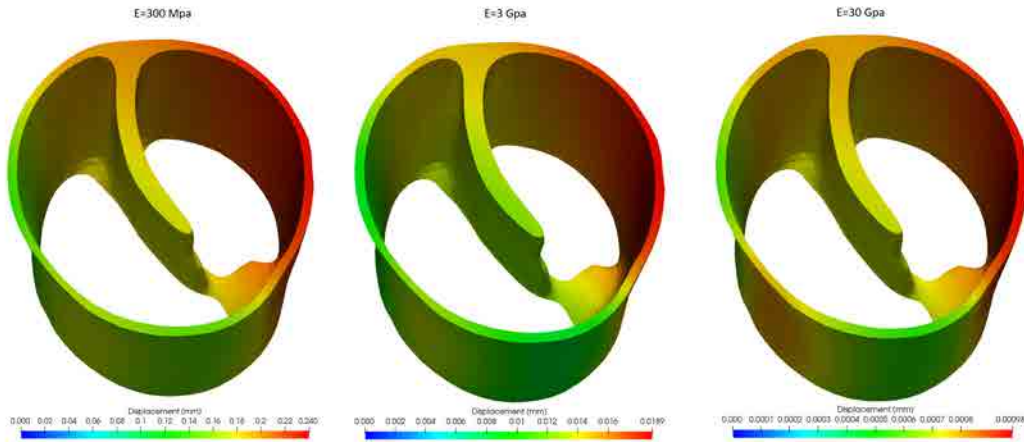


Figure 3.39: Displacement of IF region with various Young's modulus at peak systole

Due to the enormous intricacy of the connection required to mimic such phenomena of flap movement with the deformable wall, reproducing it in the current AD model available to us is rather challenging. We did not distinguish Young's modulus of the IF from other regions of the arterial wall to ensure convergence and stability of the calculation. In future work, Young's modulus of the intima should be explicitly set and follow the patient image datas' material properties.

3.7.3.4 Discussion and conclusion

The purpose of this research was to determine if the added complexity and, more importantly, the time needed to conduct patient-specific FSI simulations when modeling AD as a tool for interventional planning is warranted. In contrast to the three months needed for the FSI simulations on the cluster at our laboratory supercomputer, the rigid wall simulation completed three cycles in only one week and reached the convergence state. In future work, we should study the numerical scheme of foam-extend and adjust the parameters to reduce the computation time to speed up the convergence.

There is an increasing amount of research on FSI simulations of the AD (Alimohammadi et al., 2015, Qiao et al., 2019, Bäumlér et al., 2020), which use different models for the artery wall structure to capture the movement as accurately as possible. However, there is still no agreement on the optimal method for defining vessel wall characteristics solely from imaging data.

This issue is compounded in AD, which is often associated with increased vessel wall stiffness that is not uniformly distributed across the area (de Jong et al., 2014). The current simulation uses a basic Cauchy elasticity and isotropic model derived from experimental data (Menut, 2017) in Chapter 2, as well as a constant wall thickness throughout (except for the intimal flap), and as such may not accurately represent the wall dynamics. Yang et al. (2014b) reported considerably greater flap movements (1.8 mm – 10.2 mm). Qiao et al. (2019) discovered flap displacements of up to 0.15 mm in an FSI simulation of a simplified AD. It is unknown why there is such a difference between these results with the imaging mentioned above investigations.

This research produced a detailed tool of cross-sectional area changes using high-resolution data, which used open-source software. This tool offers a straightforward method to evaluate the geomet-

ric locations of the essential vessel wall motion (flap movement) and, therefore, can be a valuable clinical tool. Because the pathophysiology of AD is unknown, it is not completely obvious what data should be extracted from such FSI simulations.

Longitudinal research involving many patients is needed to discover key parameters/disease indicators and create clinically helpful benchmarks. Without such clear evidence, and considering that dissections develop from aneurysms, it is fair to infer that the pathophysiology of AD is comparable to that of aneurysms (Erbel et al., 2001). There is evidence that areas of high WSS are associated with AD; for example, it has been observed that reducing shear stress may help prevent dissection propagation (Nordon et al., 2011). Additionally, it has been shown that the sites of first tears correspond to areas of maximum pressure or WSS (Wen et al., 2010).

Thubrikar et al. (1999) also found a correlation between increased WSS and intimal tears. The areas of high WSS areas shown in Figure 3.36 did not differ substantially between the FSI and rigid wall simulations. However, a growing research of data indicates that areas with high OSI and low TAWSS are more prone to rupture (Xiang et al., 2011), calcification (Bassiouny et al., 1994), or wall thickening (Wen et al., 2010) in the setting of aneurysms. According to Meng et al. (2014), such areas exhibit a spectrum of endothelial dysfunction, including increased permeability and stickiness, and inflammatory responses (Chiu and Chien, 2011). And for these critical, the rigid model was shown to properly represent the fluid motion in these areas in this study. However, to study the motion characteristics of arteries, the FSI model outperforms rigid wall CFD simulations in reproducing thoracic aorta fluid hemodynamics. It becomes apparent that the lack of flap motion in rigid wall simulations has a significant effect on the predicted hemodynamic parameters, emphasizing the importance of FSI simulations in AD.

3.8 Modeling for the rise of surgical tools

The modeling of the rise of surgical tools is a strongly non-linear numerical problem, mainly due to numerous contacts between deformable, tortuous, and heterogeneous bodies and large displacements and complex material behavior such as arterial tissue. For this study, the Abaqus[©] software with an explicit method is used for numerical simulation. According to Mouktadiri (2013) observations, the implicit numerical method leads to several months' calculation time, mainly because each iteration needs to solve an extensive linear equations system, which requires a considerable amount of computing resources, disk space, and memory. Compared with an implicit method, an explicit temporal integration scheme leads to more reasonable computation time and guarantees more robustness in terms of numerical stability (better contact handling). Therefore, this work is particularly interested in considering the complex contacts between the aorta and surgical tools.

Here, we show the results of numerical simulations that were conducted only for the purpose of structure computation, that is, without considering the hemodynamic effects on the wall, which were performed before.

3.8.1 Numerical models

Clinical data from the medical imaging of a patient with the aortic dissection at the level of the descending aorta are collected in collaboration with vascular surgeons from Wuhan Tongji Hospital. In the preoperative period, the patient performs a three-dimensional scan with an injection of

contrast product to observe the arteries' positioning and understand the endovascular procedure. These tomodensitometry images allow us to produce a digital model of the entire aorta with the software Simpleware ScanIP 2017 (Synopsis, CA, USA). Figure 3.40 illustrates the segmentation process with the generation of the associated model comprising the thoracic aorta, the abdominal aorta, and the two iliac arteries necessary to simulate the rise of the tools from the beginning of the endovascular surgery.

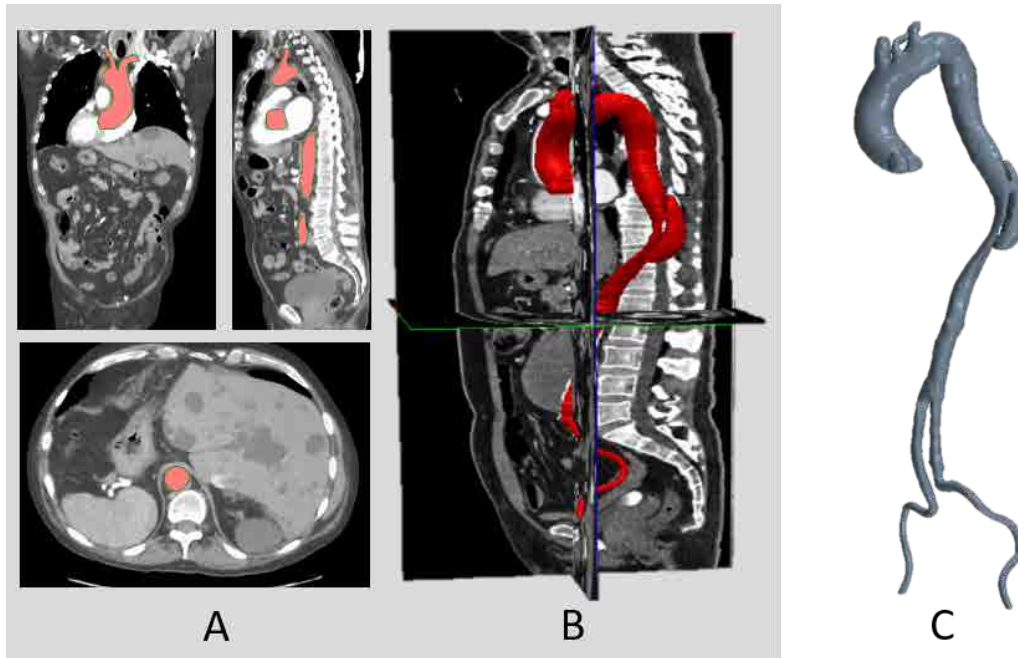


Figure 3.40: A: Segmentation process with software Simpleware ScanIP and views in the three sections of space; B: The model generated after segmentation; C: View of the aortic dissection

The model of the aorta has been meshed with triangular shell elements with a thickness of 1 mm. The shell elements are well suited to the model's geometry due to the low thickness of the arterial walls. At the aortic dissection area level, we hypothesize an elastic behavior with Young's modulus $E = 4.66$ MPa and a Poisson's ratio $\nu = 0.45$ due to the calcification at dissection area. The rest of the aorta is modeled with elastic behavior ($E = 3$ MPa and $\nu = 0.45$) according to the results of Mouktadiri (2013).

Based on the work of Menut (2017), the guide's rigidity affects the aorta's stress and displacement. The flexible guide produces a stress of 0.1 MPa in the iliac artery whereas the stiff guide generates 0.5 MPa. The iliac artery has 1.9 mm displacement by the flexible guide and 15 mm by the stiff guide. These findings are consistent with the surgical technique where the guides straighten the arteries and are used to rise the catheter at a later step. In this simulation, the guides of brands Amplatz (rigid) will be applied and modeled with beam elements. We have observed that the type of elements (linear or quadratic) has no impact on the stresses generated in the aorta, the aorta's displacement, and the guide's trajectory. Therefore, to optimize the calculation time, we choose linear elements, same choice for the guide rise in the abdominal aorta (Gindre et al., 2016). A convergence study allows elements of 1 mm size, that is to say, a ratio between the element's size

and the length of the guide of 2×10^{-3} .

According to [Menut \(2017\)](#), the elastic mechanical characteristics of the Amplatz (rigid) guides were determined via experimental measurements that were described in her study. We assumed that the guide's elastic mechanical properties change throughout the various transition zones (Figure 3.41) rather than modeling a guide with a diameter that varies along its length (as was done before). Table 3.9 summarizes Young's modulus and Poisson's ratio values that were acquired and utilized to simulate the various sections, and transition zones of the Amplatz (rigid), respectively.



Figure 3.41: Modeling of the rigid guidewire whose elastic mechanical properties vary according to different transition zones ([Menut, 2017](#))

Table 3.9: Modeling of the Amplatz guidewire whose elastic mechanical properties vary according to different transition zones (adapted from [Menut \(2017\)](#))

Zone (Figure 3.41)	Young's Modulus E (MPa)	Poisson's ratio ν
Tip	200	0.4
Transition zone A	360	0.4
Transition zone B	2270	0.4
Transition zone C	7745	0.4
Transition zone D	18300	0.4
Transition zone E	40500	0.4
Rigid zone	125000	0.4

The introducer (Figure 3.42) positioned by the surgeon at the femoral artery incision level and allowing the delivery system's navigation is modeled by a 2.5 mm thick tube, 50 mm long and 10 mm in diameter, allowing the insertion of the catheter inside. The mesh of the introducer is made with homogeneous and linear quadrangular shell elements of 6 mm length. Its behavior is elastic with Young's modulus $E = 500$ MPa and a Poisson's ratio $\nu = 0.45$ adapted from the results of [Mouktadiri \(2013\)](#).



Figure 3.42: (Left) Modeling of the introducer for the navigation of the release system; (Right) Mesh of introducer

In this case, the geometry of catheter (also known as a stent holder) is recreated based on experimental measurements data. One of the most frequently used catheters in the clinical environment

is manufactured by Medtronic and is 620 mm in length and 7.33 mm in diameter. For the catheter to follow the route established by the rigid guide in the vascular structure, its internal diameter is 0.889 mm. The catheter is made up of three components:

- a 100 mm long tip with a diameter ranging from 1 mm to 7.3 mm;
- a 154 mm long part containing the prosthesis to be released at the entry site of dissection;
- a 366 mm long part allowing the ascent through an internal iliac artery.

The mechanical characteristics of the catheter are derived from [Mouktadiri \(2013\)](#) findings and incorporated into the numerical model. The catheter is meshed with homogenous and linear quadrangular shell elements of 1 mm thick. From the results of mesh sensitivity inspection, it was feasible to set the size of the components at 2mm. The catheter model is shown in the following Figure 3.43.

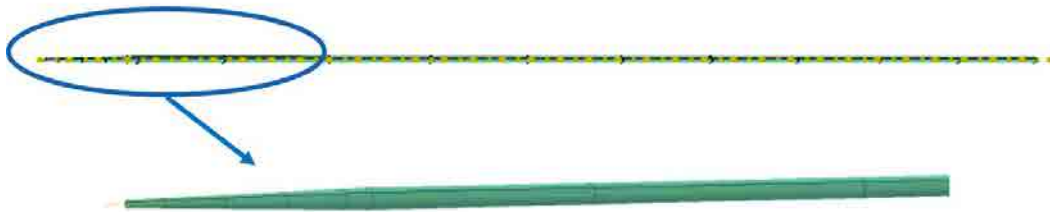


Figure 3.43: Modeling of the catheter (stent holder) whose elastic mechanical properties are derived from results of [Mouktadiri \(2013\)](#)

3.8.2 Boundary conditions

3.8.2.1 Aortic environment

To model the environment of the aorta, that means the surrounding tissues and organs. Springs were placed at the level of the different arteries that supply it and the level of the vertebral column's attachment zones to hold the model of the aorta (Figure 3.44). During the segmentation step, the scanner was used to identify the various locations on the body. To investigate the sensitivity of these springs to the stresses and displacements of the aorta, the stiffness of these springs varied between 0.1 and 1 N/mm.

The introducer which guidewire passes through and the guide are placed at the entrance of the iliac artery. The ends of the springs, two iliac arteries, and the introducer are modeled by embedding. Figure 3.44 shows the model after it has been constructed with all of the modeled components.

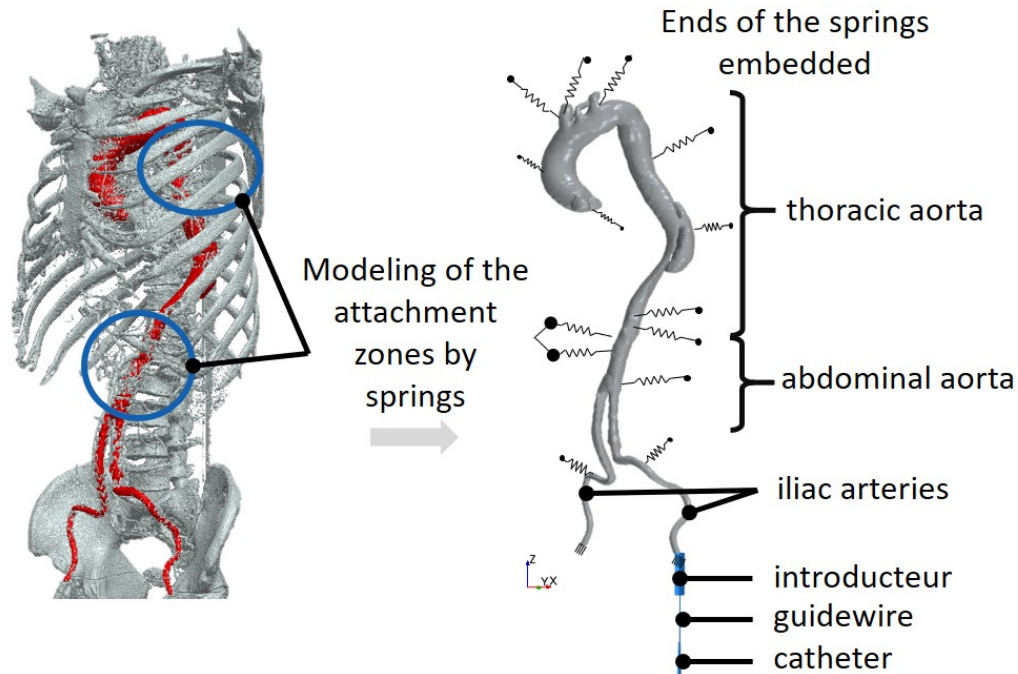


Figure 3.44: (Left) Aortic model in its environment; (Right) Complete modeling of the model of the rise of surgical tools.

The guidewires (flexible at first, then rigid) and the catheter, positioned in the center of the incised femoral artery, are raised progressively at 20 mm/s speed, just as the surgeon might do during surgery. This avoids the phenomena of buckling and numerical oscillations which can occur.

3.8.2.2 contact

It is possible to manage the contact between deformable bodies using a variety of methods. In the study of Mouktadiri (2013), many numerical techniques for addressing the issue of contact between various surgical instruments and the artery wall have been evaluated, namely the penalty and Lagrangian approaches described in detail (Mouktadiri, 2013), which may be summarized as follows:

The penalty method allows for slight penetration between two surfaces. This method is easy to implement because the contact force F is calculated explicitly by the product of the displacement with a penalty coefficient k (Figure 3.45).

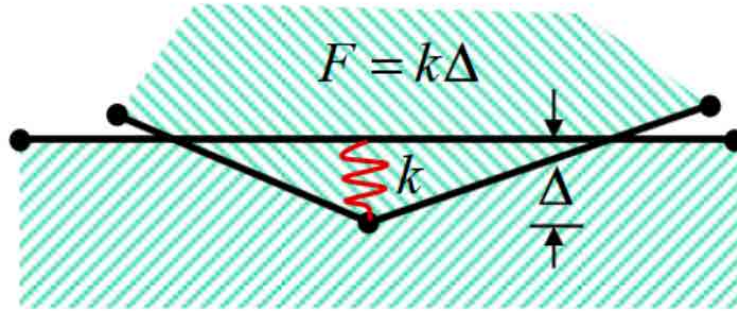


Figure 3.45: Penetration method (Menut, 2017)

The choice of this coefficient, which is sometimes referred to as the contact stiffness, impacts the outcome. A small value of this penalty coefficient leads to large penetrations that are not acceptable, while a too-large value causes oscillations and numerical instabilities. According to the work of Linck (2005), further information on numerical solutions of the contact issue by means of the penalty approach may be found there. The advantage of this method is that there is no change in the dimension of the initial system and thus no introduction of new unknowns in the solution system. The most significant drawback of this approach is the selection of the penalty coefficient, which directly impacts the outcomes of the analysis.

The method of Lagrange multipliers allows to respect a condition of non-penetration between the different deformable solids and avoid the problems related to the choice of penalty coefficients. On the other hand, it is more challenging to implement since, on the one hand, it requires the introduction of additional unknowns, called Lagrange multipliers. On the other hand, it generally involves the definition of a master surface and a slave surface. Contact conditions are then imposed on the slave nodes, which must not enter the domain delimited by the master surfaces. The Lagrange multipliers then correspond to the contact forces acting on the slave nodes.

The simulation of the rise of surgical tools in the thoracic aorta is a complex and highly nonlinear numerical problem. Several deformable bodies whose surfaces are potentially in contact are essential. Therefore, it is necessary to use a robust resolution algorithm, which is the source of a significant computation time. With the experience of Mouktadiri's (2013) work, the penalty method was chosen to model endovascular treatment of TAAs (thoracic aortic aneurysm), for its efficiency and reduced computation times. However, selecting the numerical value of the optimal penalty parameter is often tricky because it depends on the local stiffness of the structure. In this study, it was fixed following a sensitivity study on the Von Mises constraints.

3.8.3 Results of tool insertion

3.8.3.1 Results of guidewire insertion

The numerical results showed that the rigid guide had little influence on the Von Mises stresses (Figure 3.46) but a significant influence on the displacement values. The iliac arteries are the parts of the model most influenced by the insertion of the guide. This can be explained by the insertion of guide at the entrance of iliac arteries, which are therefore the first to undergo the deformation

imposed by the guide. However, our study focuses on the region of aortic dissection, where the deformation is less important (Figure 3.47).

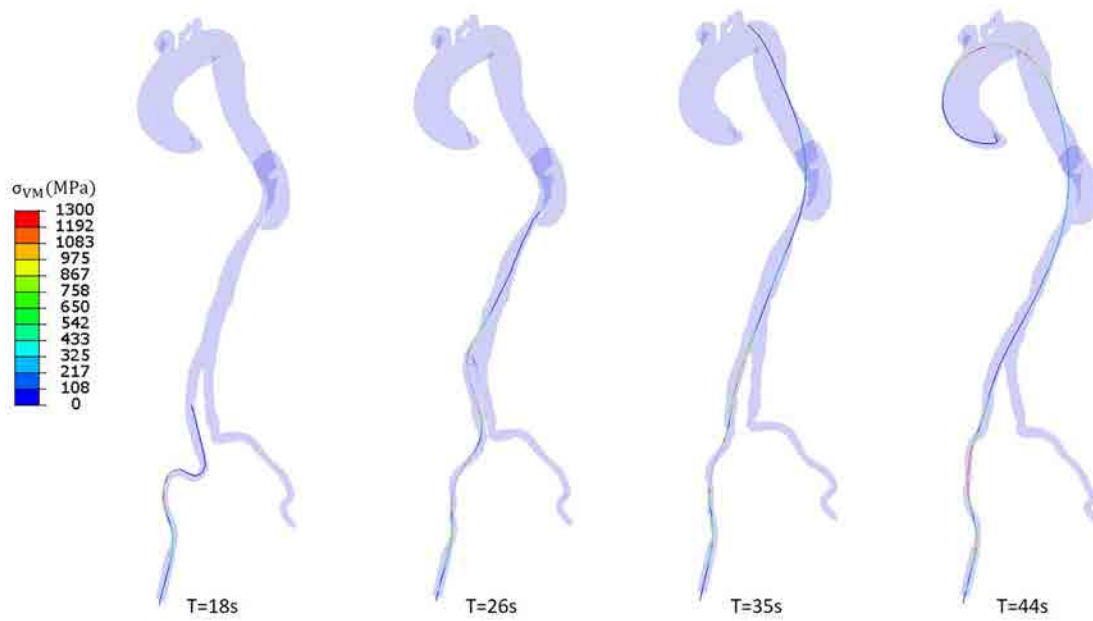


Figure 3.46: Von Mises stresses observed on the Amplatz guide during rise in the thoracic aorta at different times

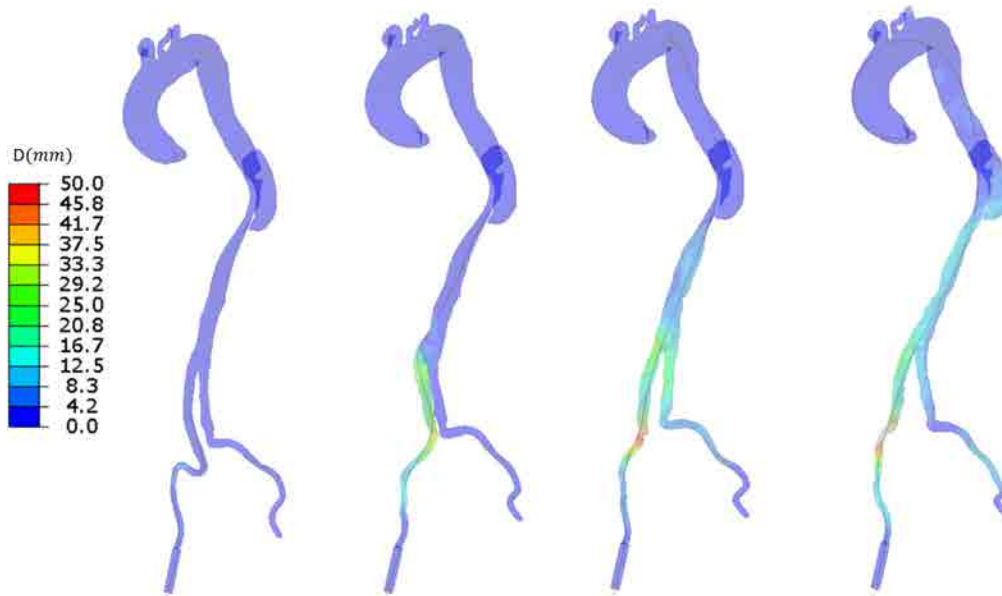


Figure 3.47: Displacement of aorta observed on the Amplatz guide during rise in the thoracic aorta at same times as above

3.8.3.2 Results of catheter insertion

The numerical simulations of the catheter ascent begin once the rigid guide is inserted into the TL of aortic dissection. The catheter ascent speed is fixed at 20 mm/s as for the guidewire, assuming that the surgeon changes the speed of the surgical process of a negligible amount. In addition, the vertical displacement of the guide once it has been mounted in the ascending thoracic aorta was blocked so that it would not rise with the catheter. In the same way, the surgeon maintains the guide during the catheter rising.

The catheter rising is shown below. Figure 3.48 illustrates the Von Mises stresses on the aorta at many different periods in time. The iliac region is considerably straightened by the presence of the compacted stent in the catheter. And resulting of the stiffness of catheter in this location, stresses in the iliac area are significantly increased.

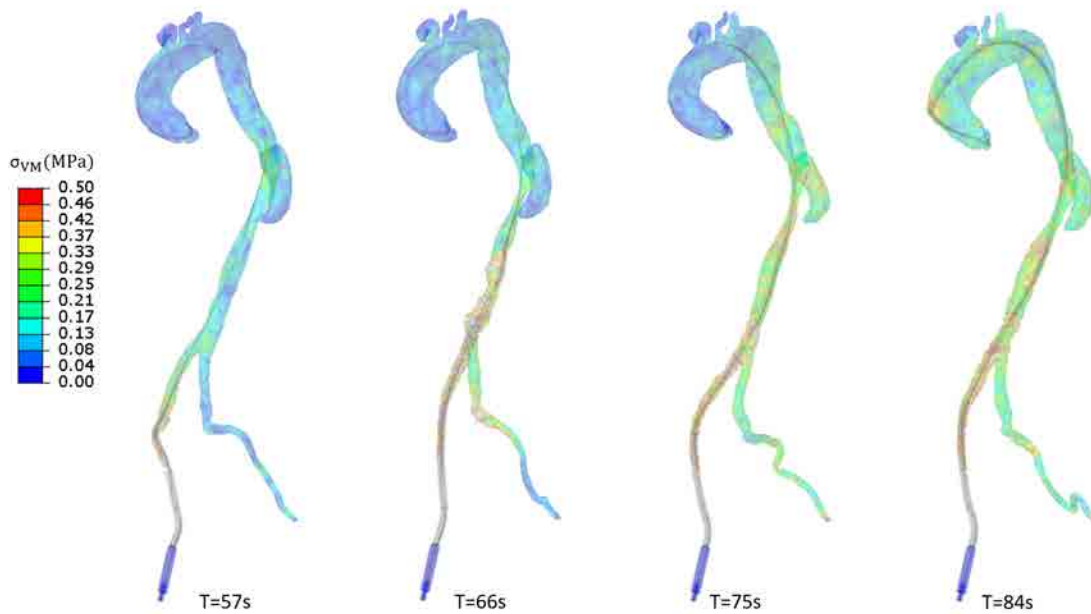


Figure 3.48: Von Mises stresses observed on the catheter during rise in the thoracic aorta at different times

The following figure 3.49 shows the displacement of aorta when the catheter rises in the aorta. Due to the relatively small diameter of iliac artery area, which is more affected by the catheter.

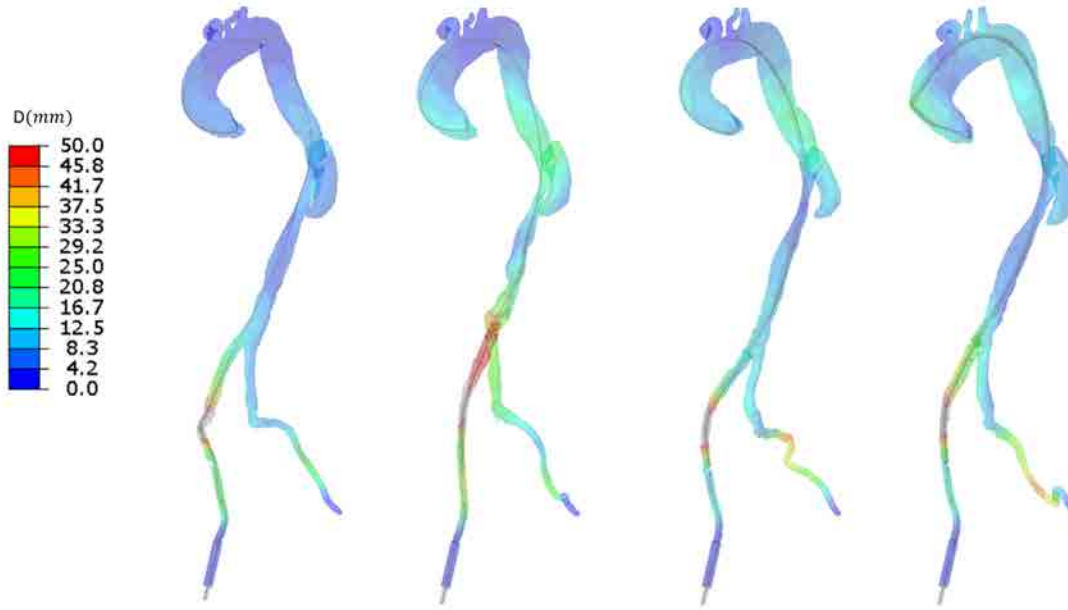


Figure 3.49: Displacement of aorta observed on the catheter during rise in the thoracic aorta at same times as above

3.8.4 Discussion

Numerical simulations were performed with a strong assumption of elastic and isotropic mechanical behavior. This reducing assumption is a first step in simulating the ascent of surgical tools in the thoracic aorta. The rise of these tools in the abdominal aorta has been simulated (Mouktadiri, 2013, Gindre et al., 2016), considering a hyperelastic isotropic model is already closer to the mechanical properties of the aortic tissue.

The modeling of the surrounding tissues of the aorta is rarely studied in the literature (Menut, 2017). Our study has chosen to model the aortic attachment zones at the spinal level by springs whose stiffness allows us to get closer to the intra-operative aortic deformation. However, the recent work of Moireau et al. (2012) proposes a mathematical model applied on the whole aortic surface to address this complex problem. From a biomechanical point of view, it allows a better description of the effect of the surrounding tissues and organs of the thoracic cavity on the aorta. From a numerical point of view, it improves the stability of the simulations by limiting migration in regions that are usually left free (aortic surface) and by relaxing some constraints in areas that are typically fixed (iliac ends, for example).

In this study, arterial calcification in aortic dissection was considered, which coincides with the CT images we obtained showing the location of calcification. The critical advantage of patient-specific simulations is that they can consider these calcifications, which greatly influence the deformations observed during the tool insertion. The results of the numerical simulation will therefore be very close to the intraoperative images.

3.9 Conclusion

In recent years, numerical simulations in fluid mechanics have been increasingly used to model complex geometries to understand and predict arterial hemodynamics in cardiovascular pathologies. This numerical work follows experiments on aortic tissue samples, which characterize the arterial wall's hyperelastic behavior. With the results concerning the modeling of the arterial structure behavior, it was then necessary to focus on the precise and realistic modeling of the blood behavior and its interaction with the wall.

In this study, we modeled the behavior of blood with two models: Newtonian fluid and Carreau-Yasuda fluid. We observed that there is not significant difference when we comparing velocity and WSS characteristics. So we assumed that blood is Newtonian fluid. The Windkessel boundary conditions implemented in the OpenFOAM® and FOAM-Extend software allowed the resistance of the rest of the arterial circuit, which is not modeled, and the compliance of arteries to be taken into account. The arbitrary parameters of this model are a negative point for its large-scale use without necessarily obtaining dynamic flow data, as the numerical values must be recalibrated on each patient. Currently, the boundary conditions on outputs in fluid models are either conditions on pressures, such as the Windkessel model, or conditions on velocities, thus on the distribution of flows between the arterial trunks. However, these conditions on the outlet velocities often lead to instabilities in the numerical calculations. Data from 4D MRI are of primary importance in the validation of hemodynamic simulation, and also the exponential improvement of medical imaging techniques is increasingly bringing clinicians and mechanics together. In-vivo data such as real-time flows obtained by clinicians on patients allow significant advances in numerical modeling. This study will present in the last Chapter.

The thoracic aorta, which includes the parts of aortic dissection, is one of the arteries (flap) that deforms the most under the effect of the cardiac pulse, hence the need for simulations of interaction between the fluid and the structure to approximate physiological conditions. The coupling using FOAM-extend has been validated in the case, we observed clearly the movement of flap with deformable walls. Due to the incredible complexity of the coupling necessary to simulate such a phenomenon, it is relatively difficult to reproduce it in a difficulty AD model at our disposal. So, we debugged many parameters in the numerical schema to ensure its convergence. Thus, numerical techniques offer a potential alternative for analyzing hemodynamics in AD and including wall motion in the simulation. This merits further study to see if the additional work needed to include wall motion into AD models is warranted in clinical translation.

In parallel with the fluid-structure interaction simulations and anticipation of the complete modeling of the surgical procedure, we were able to take up the work of [Mouktadiri \(2013\)](#) and [Menut \(2017\)](#) on the rise of surgical tools in the aorta with AD pathology and adapt it to the whole aorta. This work presents an additional difficulty induced by the bending of the tools at the supra-aortic trunks. The numerical simulations of this study were performed with a strong assumption of elastic behavior for the vascular wall.

Validation

Because of advancements in computing capacity, in silico models may simulate in vivo circumstances more closely via numerical simulation. Two cases of AD are presented in this last chapter for which we performed CFD simulations and compared to MRI data. The results of the numerical simulations have been validated with clinical data from medical imaging dynamically for the observation of in-vivo blood flow during a cardiac cycle, preoperatively and postoperatively. In addition, a comparison between in silico and in vitro is interesting to illustrate the physics of hemodynamic. Therefore, an implementation of Particle Image Velocimetry applied for the same case in the framework of another thesis is compared with numerical simulation and described in this chapter.

Contents

4.1	Introduction	154
4.2	AD case study	155
4.2.1	Data MRI for AD2 & AD3	156
4.2.1.1	AD2	156
4.2.1.2	AD3	160
4.3	Results & Comparison with MRI	163
4.3.1	AD2	163
4.3.2	AD3	165
4.3.2.1	Preoperative	165
4.3.2.2	Postoperative	166
4.3.2.3	Preoperative & Postoperative	167
4.3.3	Discussion	175
4.4	Comparison with <i>in vitro</i>	175
4.4.1	3D printed aorta model	175
4.4.2	PIV	176
4.4.3	AD1	180
4.4.4	AD2	182
4.4.5	Discussion	186
4.5	Discussion and conclusion	187

4.1 Introduction

The previous chapter illustrated the study for the numerical simulation of hemodynamic flow (CFD & FSI) with a bio-faithful AD model. However, the data from 4D MRI are critical for the validation of hemodynamic simulation, and the exponential development in medical imaging methods enables an ever-closer relationship between clinicians and mechanics to be established. In-vivo data, such as real-time flows collected by surgeon on patients, has enabled significant advancements in numerical modeling. A partnership with the Hospices Civils de Lyon on patients with AD and frequent follow-up results in the collection of two cases in this chapter. Both models accurately replicated the patient's physical characteristics, but they also imposed physiologically correct and individualized boundary conditions on the patient's body. One of these AD cases is very specific because the stent is normally released in the TL during endovascular surgery, whereas the surgeon released his catheter in the FL for this one case. This is very rare in the literature and in practice., so for this case, not only preoperative CFD simulation but also postoperative CFD simulation was performed.

On the other hand, *in vivo* data collection is restricted by the limitations of conventional medical imaging methods (resolution, availability, price, late diagnosis, etc.) and the capabilities of intrusive measuring tools. As a result, concluding the processes that cause AD is challenging. Despite the fact that 4D-MRI and 4Dflow assessments have significantly increased our understanding of AD development and treatment (Chen et al., 2021) as a time-resolved and volumetric imaging tool, some critical quantities of interest, such as WSS, are still difficult to assess (Stalder et al., 2008). Alternative methods, such as numerical modeling and *in vitro* experiments, may provide even more precise visualizations, assuming that the mimicked settings are representative of bio-faithful conditions, as shown by Bonfanti et al. (2020).

Several studies *in vitro*, ex vivo, and *in silico* are now being conducted to overcome the limitations of *in vivo* research (Alimohammadi et al., 2015, Deplano et al., 2019, Qiao et al., 2019). In most cases, these alternative approaches are used to obtain better visualizations of AD flows as well as multi-analysis possibilities (flow rate, pressure, wall displacements, etc.) using physical *in vitro* models (Soudah et al., 2015, Birjiniuk et al., 2015) and numerical simulations (Bonfanti et al., 2017). However, there is rarely literature about the work for combining an *in vitro* circulatory mock loop that replicates *in vivo* pulsatile flow conditions, non-Newtonian blood imitating fluid, and patient-specific AD phantoms into a single experiment before. And to compare with the results in numerical simulation, which are used the same initial and boundary condition *in vitro*. An essential goal of the current *in vitro* aortic flow simulator is to compare and verify numerical simulations with physical models of the same aortic phantoms to better understand how they work.

In this study, two Type-B AD was studied *in silico* using computational fluid dynamics (CFD) and *in vitro* utilizing a state-of-the-art mock circulatory loop and particle image velocimetry (PIV), developed by another Ph.D student who works in our laboratory. Both models accurately replicated the patient's physical characteristics from the segmentation precisely using the software Simflow ScanIP 2017 (Synopsis, CA, USA) in this study.

4.2 AD case study

There are three AD models (Figure 4.1) for this study. For AD1, which was used for hemodynamic in Chapter 3, only the model geometry was accessible, as presented in Chapter 3. But, AD2 and AD3 models are provided 4D-MRI scans. As a result of these measurements, the geometry and in-vivo flow velocity fields may be determined.

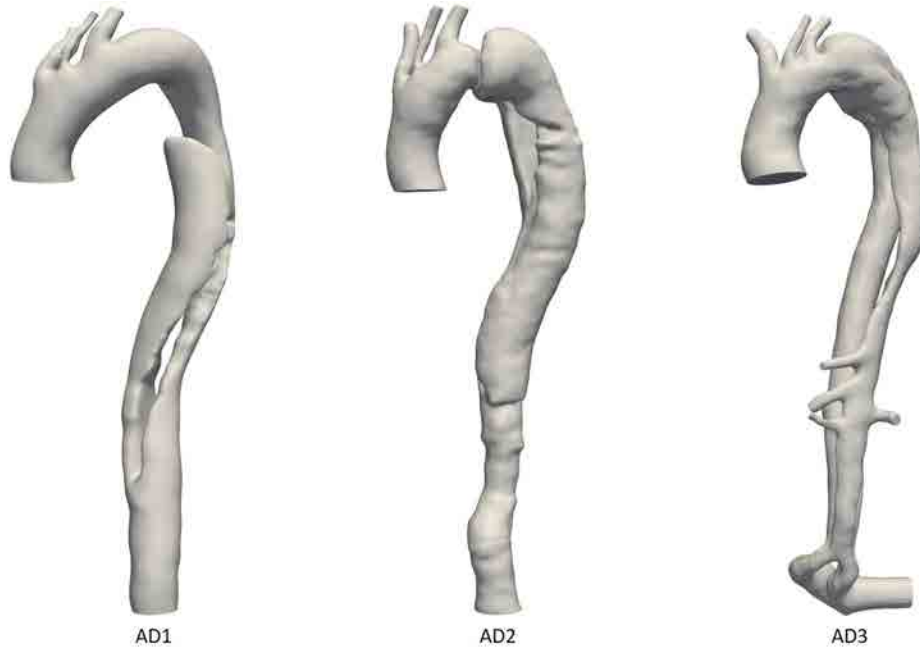


Figure 4.1: Three bio-faithful AD cases

- **AD1 model** of which we will perform the numerical simulation CFD with rigid wall and with boundary conditions which correspond to the experimental conditions and of which we will compare the results obtained by PIV
- **AD2 model**, which the entry site of dissection is located at the aortic arch. We received the 4D-MRI data and thus could realize the hemodynamic simulation with rigid wall and compare with both results from 4D-MRI data and PIV experiment.
- **AD3 model**, for which the entry site of the dissection is at the level of the aortic arch and the exit site is at the level of both iliac arteries. Thanks to the 4D-MRI data we performed the hemodynamic simulation with a rigid wall and compared with the two results of the 4D-MRI data with preoperative and postoperative. In addition, because the dimension of FL is larger than TL, the stent was used in FL during endovascular surgery for this patient.

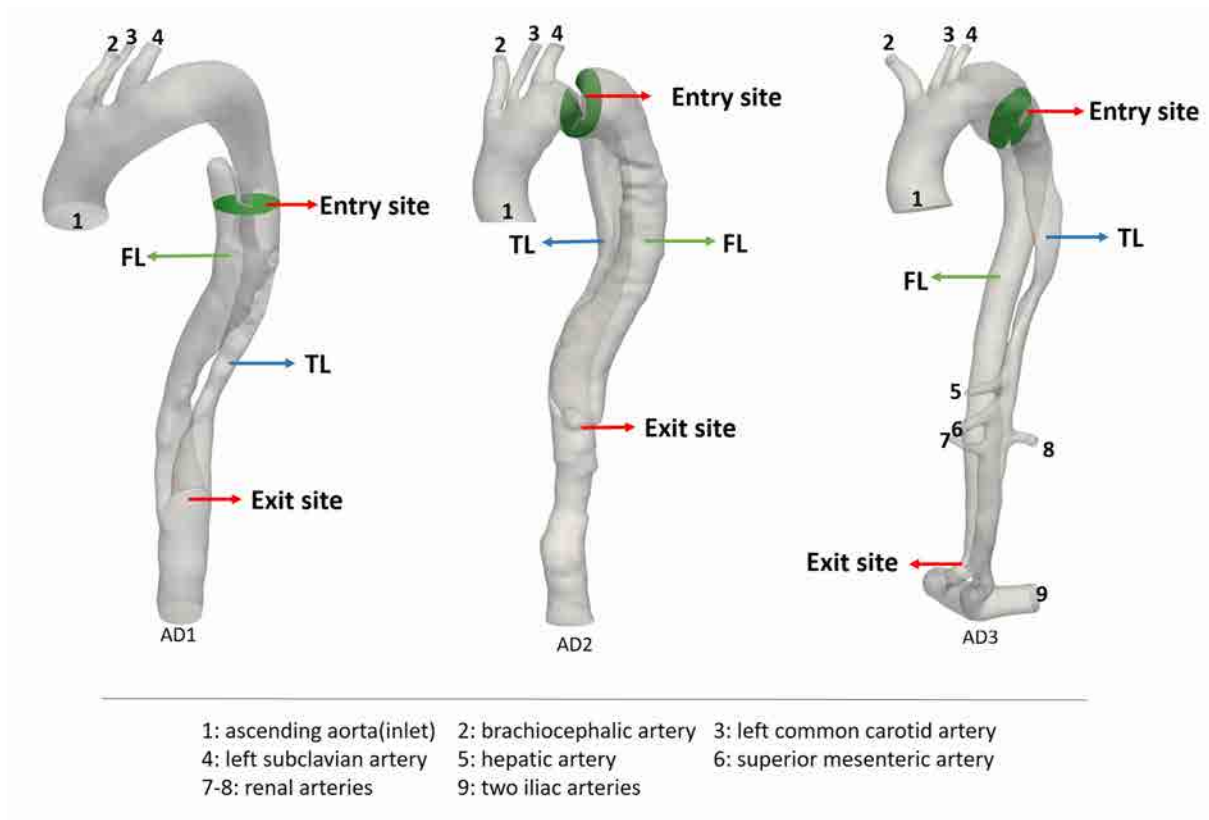


Figure 4.2: Three bio-faithful AD cases

Table 4.1 shows the peak systolic period and a preoperative cardiac cycle for three cases. AD1 used the data from Menut (2017). And the data of AD2 & AD3 from MRI data.

Table 4.1: The cardiac cycle of AD1, AD2 and AD3

Case	peak systolic (s)	a cardiac cycle (s)
AD1	0.12	0.816
AD2	0.108	1.081
AD3	0.131	1.311

4.2.1 Data MRI for AD2 & AD3

4.2.1.1 AD2

The AD2 case is a fascinating solution because of the observed false lumen's significant narrowing (54 percent decrease). The entrance condition is a velocity profile based on the flow rates measured by 2D PC-MRI with 3D velocity encoding. The velocity vectors are measured perpendicular to the cut made by the operator, and then from the surface measurement, the average flow rates during the cardiac cycle can be calculated. Figure 4.3 illustrates the process.

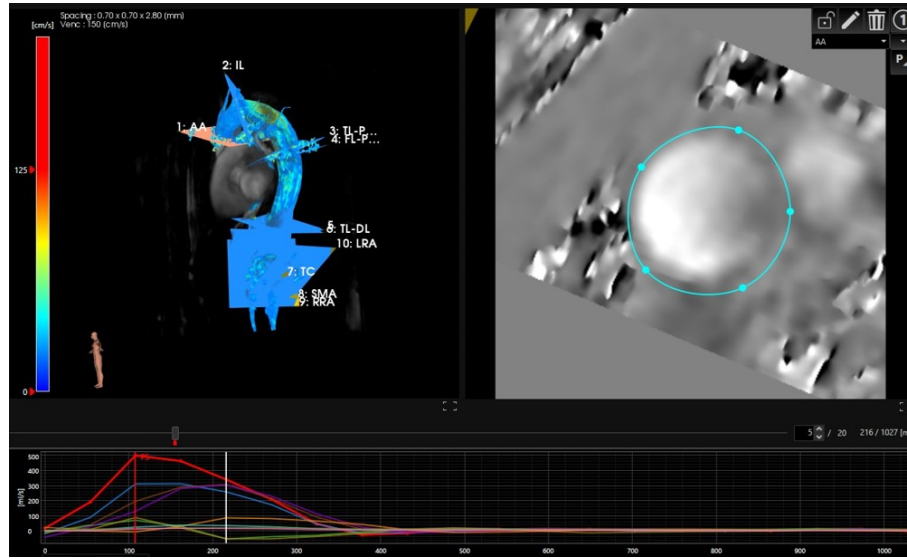


Figure 4.3: A section of the ascending aorta is selected so that velocity vectors can be measured by dynamic imaging. An average flow over the area can be generated to fulfill the input condition of the model.

Dynamic flow measurements by 4D MRI were performed at the Hospices Civils de Lyon on two patients (AD2 & AD3) with aortic dissection pathology. First, measurements in 2D PC-MRI with 3D velocity encoding were made on planes moved by the surgeon. The slice planes were selected to calculate flow rates at the ascending, supra-aortic, and descending thoracic aortas. The measurement accuracy at the level of the descending aorta is difficult to assess because the descending aorta is very long, and there are four branches on the descending aorta, which makes the measurement not very accurate. For this reason, flow values for the descending aorta were calculated as the subtract of the flow rates of the ascending aorta to supra-aortic trunks. These flow rates are shown in Figure 4.4.

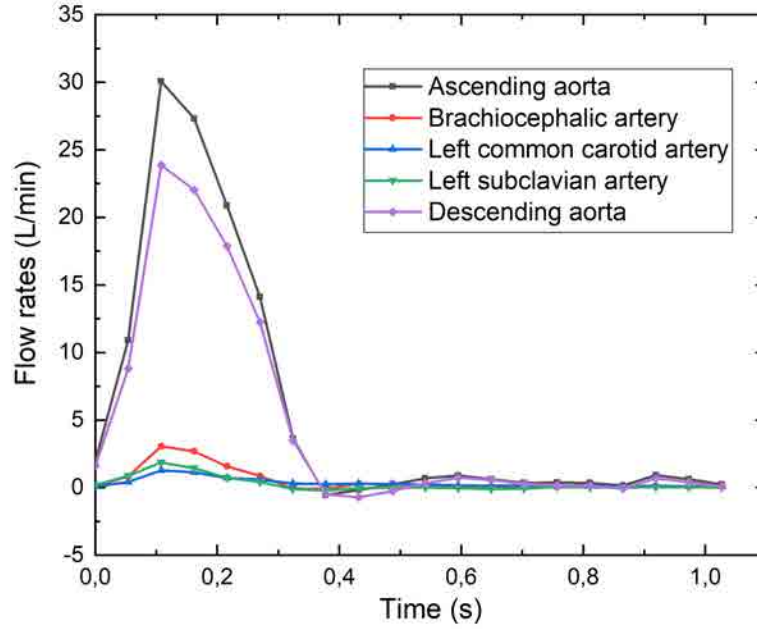


Figure 4.4: Flow rates measured by 2D PC-MRI on a patient with AD2 in 5 planes positioned by the operator at the level of the ascending and descending aorta and supra-aortic trunks.

As a result, the 4D flow MRI acquisition thus includes a dynamic sequence to cover the entire thoracic aorta with the aortic dissection over 20 cardiac phases. As described previously, a 2D PC-MRI is also performed perpendicular to the vessel axis to obtain a local measurement of velocities, and thus flow rates, at the inflow of the ascending thoracic aorta and outflow of the descending thoracic aorta and supra-aortic trunks (Figure 4.4). The images (DICOM) from MRI were exploited for the reconstruction of the 3D model that was used in our numerical simulations (Figure 4.2).

After constructing the model, as described in *Chapter 3.4.4 Mesh for fluid domain*, we create the grid for the AD2. Because we only need to simulate the fluid part in this section and reduce the computation time and ensure the convergence of the calculation, we use 1mm size of polyhedral element for meshing (Figure 4.5).

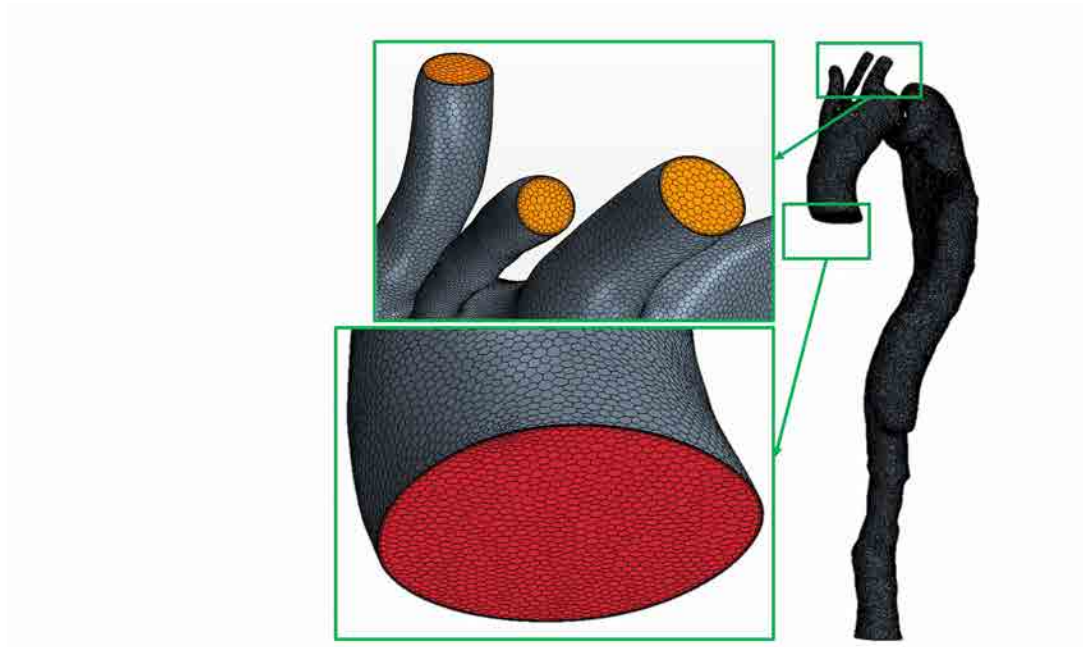


Figure 4.5: Polyhedral mesh generated with the commercial software Star-CCM+[©] (1043286 cells)

Following the collection of in-vivo data and the creation of the rheological bio-faithful model, the next step is to define the boundary conditions to solve the fluid flow simulation. This part describes the characteristics of these boundary conditions and how they are developed specifically for this model.

- Conditions of entry

For the ascending aorta (at the entrance), we followed the method described in *Chapter 3 Boundary conditions*, creating a velocity field consistent with the AD2 patient-specific entrance plane by combining Poiseuille's methods described in AppendixA with flow rates obtained from MRI data.

- Conditions of exit

For the four exits of the AD2 model, we use the same Windkessel module as described in *Chapter 3 Boundary conditions*. The parameters of the Windkessel model used are R_p , R_d , and C . The data from the work of [Menut \(2017\)](#) for the three supra-aortic trunks and the descending aorta of the numerical model were used to first fix the parameters of the Windkessel model which were then manually adjusted based on the dynamic imaging data. This recalibration of the parameters enables adaptation to the patient's personalities data, resulting in resistance and compliance levels unique to the individual patient.

The parameters of the three-element Windkessel model used for the numerical simulations are available in Table 4.2. R_p , R_d , and C are respectively the compliance of the ascending aorta hydraulic resistance of the vessel and the vessel's compliance.

Table 4.2: Windkessel model parameters applied to AD2 fluid model outputs and adjusted with MRI data

	R_p $\times 10^6 m^{-1} \cdot s^{-1}$	R_d $\times 10^6 m^{-1} \cdot s^{-1}$	C $\times 10^{-7} m \cdot s^2$
Brachiocephalic artery	0.166	0.83366	16
Left common carotid artery	0.46	2.23203	5.7
Left subclavian artery	0.24	1.2135	8.0
Descending aorta	0.056	0.2603	37.742

4.2.1.2 AD3

AD3 model is a rarely case. Due to the shape of its aortic dissection peculiarities and the circumstance of blood flow (helical flow) between the TL & FL *in vivo* (Figure 4.6), the surgeon places a stent inside FL when performing interventional procedures. The surgeon observed the helical flow in the stent *in vivo* with 4D-MRI. Therefore, it is interesting to perform both preoperative and postoperative numerical simulations for this case.

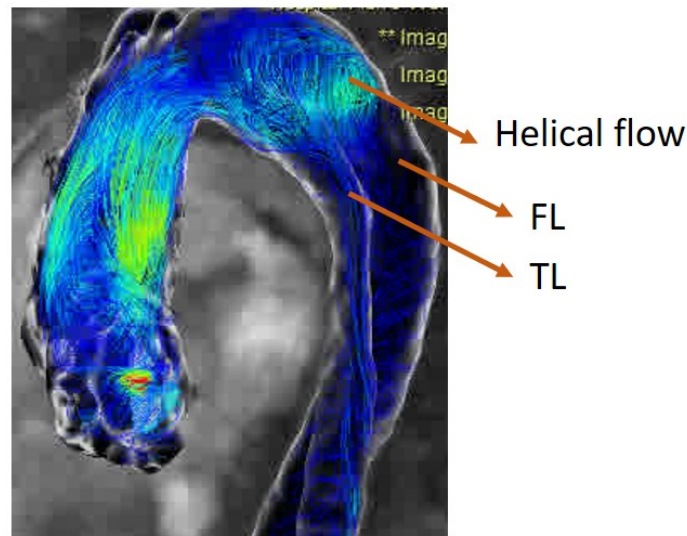


Figure 4.6: 4D-MRI flow data with helical flow

Previously published research has approximated helical flow qualitatively using 3D flow visualization and analysis of pathlines, streamlines, and flow vectors (Frydrychowicz et al., 2012, Clough et al., 2012). These techniques for analyzing and classifying helical flow may continue to be observation-dependent. A more quantitative assessment of flow helicity may be accomplished via the use of factors such as the vorticity magnitude threshold and local normalized helicity (LNH) (Garcia et al., 2013, Chiastra et al., 2013).

To determine helicity, vorticity must first be calculated using equation 4.1, the velocity vector's gradient. H_d is defined as the scalar product of velocity and vorticity in each voxel, computed in

three dimensions using equation 4.2.

$$\vec{\omega}(\vec{r}, t) = \nabla \times \vec{u}(\vec{r}, t) \quad (4.1)$$

$$H_d = \vec{u}(\vec{r}, t) \cdot \vec{\omega}(\vec{r}, t) \quad (4.2)$$

where $\vec{u}(\vec{r}, t)$ is the vector of local velocity, $\vec{\omega}(\vec{r}, t)$ is the vector of vorticity, \vec{r} is a three-dimensional vector and t represents time. H_d is computed for each three-dimensional voxel, and then for each area, the mean of all voxels is calculated. H_d can be defined as the kinetic helicity density and be normalized in accordance with the magnitude of the velocity and vorticity, resulting in a locally normalized helicity (LNH). And the angle α formed by the velocity and the vorticity may be computed and is denoted by the LNH, α :

$$LNH = \frac{\vec{u}(\vec{r}, t) \cdot \vec{\omega}(\vec{r}, t)}{|\vec{u}(\vec{r}, t)| |\vec{\omega}(\vec{r}, t)|} = \cos \alpha \quad (4.3)$$

As a result, the maximum value of LNH will be 1, and the minimum value will be -1. In earlier research with small populations, a visualization threshold of ± 0.8 for LNH was utilized to identify increased LNH areas (Morbiducci et al., 2013). Indeed, by definition, it is a measure of the alignment/misalignment of the local velocity and vorticity vectors, and its sign is a helpful indication of the helical structure's rotational direction. When observed in the forward flow direction, positive (negative) LNH values imply right(left)-handed spinning fluid formations.

For the simulation of the AD3 model in preoperative and postoperative conditions, we did the same procedures as above : reconstruction of the bio-faithful model with MRI data (Figure 4.7) and meshing the model by StarCCM+ (Figure 4.8, Figure 4.9). After, we constitute the patient-specific velocity field for ascending aorta (inlet) with the flow rate measured by MRI.

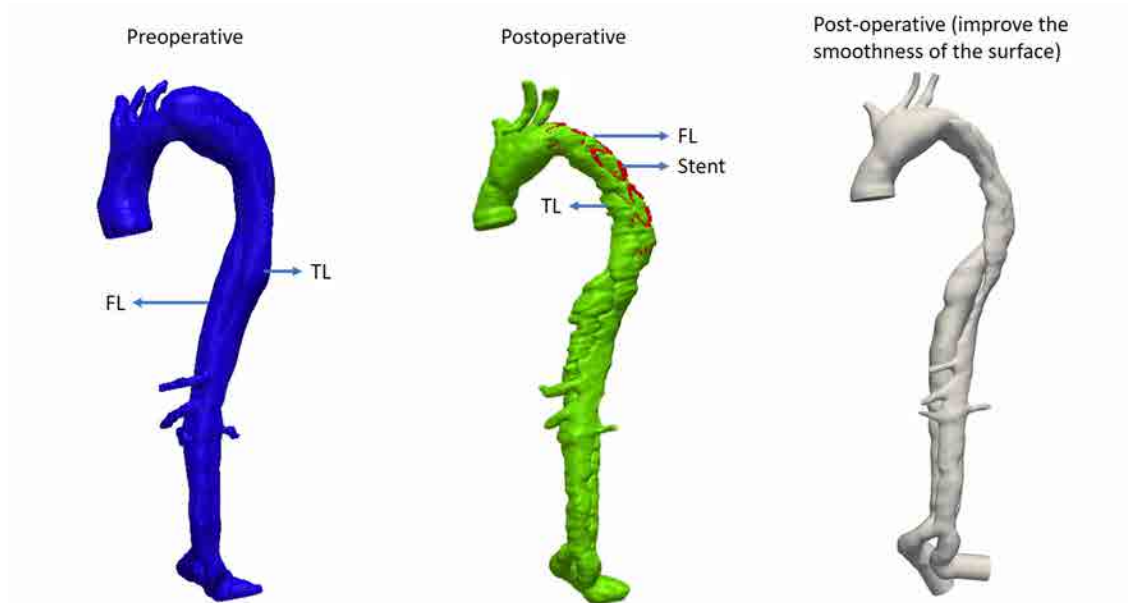


Figure 4.7: Reconstruction of the bio-faithful model with MRI data, AD3 preoperative & postoperative

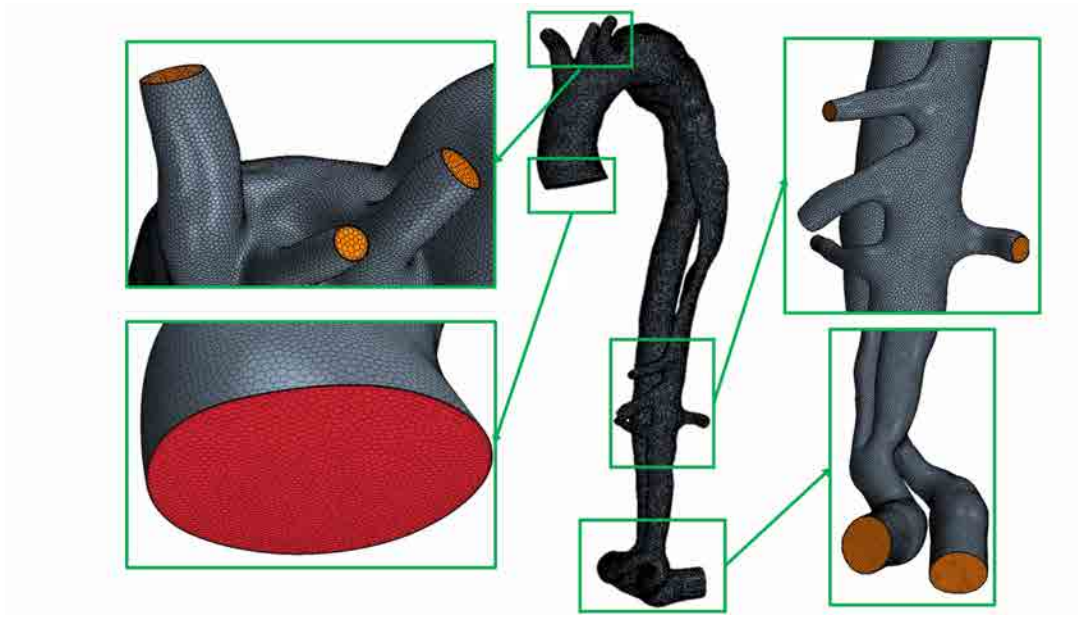


Figure 4.8: Polyhedral mesh generated with the commercial software Star-CCM+[©] (1438364 cells)

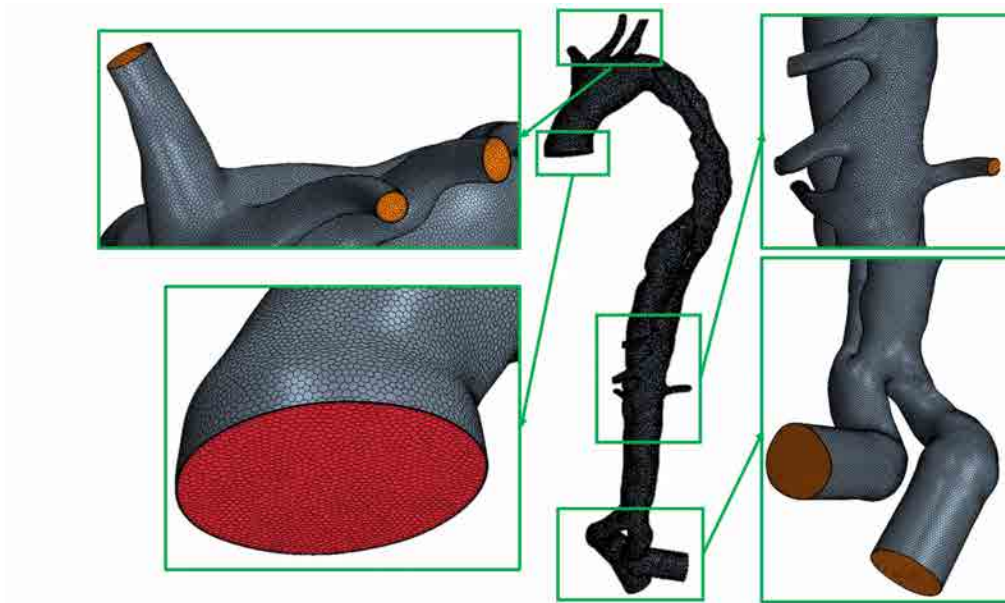


Figure 4.9: Polyhedral mesh generated with the commercial software Star-CCM+[©] (1642729 cells)

The Windkessel model parameters used, R_p , R_d , and C , first set based on data from [Bonfanti et al. \(2017\)](#), [Arthurs et al. \(2020\)](#) for the three supra-aortic trunks, the four artery on the descending aorta, and the two iliac arteries were used to fix the parameters of the Windkessel model, and then manually adjusted based on dynamic imaging data. This realignment of the parameters allows adaptation to the patient-specific data, providing patient-specific resistance and compliance values.

Table 4.3: Windkessel model parameters applied to AD3 fluid model outputs and adjusted with MRI data

	R_p $\times 10^6 m^{-1} \cdot s^{-1}$	R_d $\times 10^6 m^{-1} \cdot s^{-1}$	C $\times 10^{-7} m \cdot s^2$
Brachiocephalic artery	0.0525	0.834	8.63
Left common carotid artery	0.147	2.232	3.1
Left subclavian artery	0.072	1.2135	8.0
Hepatic artery	0.1387	0.78	5.15
Superior mesenteric artery	0.1387	0.78	5.15
Renal arteries (Right&Left)	0.314	0.692	5.725
Iliac arteries (Right&Left)	0.035	0.5	14.4

Table 4.4: The cardiac cycle of AD3 (preoperative & postoperative)

Case	peak systolic (s)	a cardiac cycle (s)
AD3(pre)	0.131	1.311
AD3(post)	0.124	0.823

4.3 Results & Comparison with MRI

4.3.1 AD2

Figure 4.10 shows the flow streamline at the beginning of systole (0.06s), peak systole (0.108s), systole deceleration (0.02s), and mid-diastole (0.4s).

Because of the strong narrowing of FL, flows are characterized by sharp contrasts between the top region (pre-narrowing area) and the lower region (post-narrowing area), where distinct patterns are seen depending on the cycle phase. A tremendous whirling shape is seen immediately before the narrowing area during the early-systole phase ($t=0.06s$). Around the systolic peak ($t=0.108s$), a narrowing pathway with a high velocity emerges and feeds the post-narrowing period. This unique channel flow shape is caused by the curvature of the left wall, which diverts the flow and pushes it into the smaller lumen. During this rising flow phase, the top area (aortic arch and three arteries branches) looks almost parallel streamlines, and all swirling patterns vanish. The flow of descending aorta features extremely crisp, ordered, and parallel streamlines in laminar flow.

As with normal divergent section pipe flow, the flow coils immediately below the constriction during systole deceleration ($t=0.2s$). Recirculation occurs in this post-reduction area, resulting in the formation of a vortex.

Finally, during diastole ($t=0.4s$), we witness the backflow phase at the re-entry, in which the flow ascends the TL from FL.

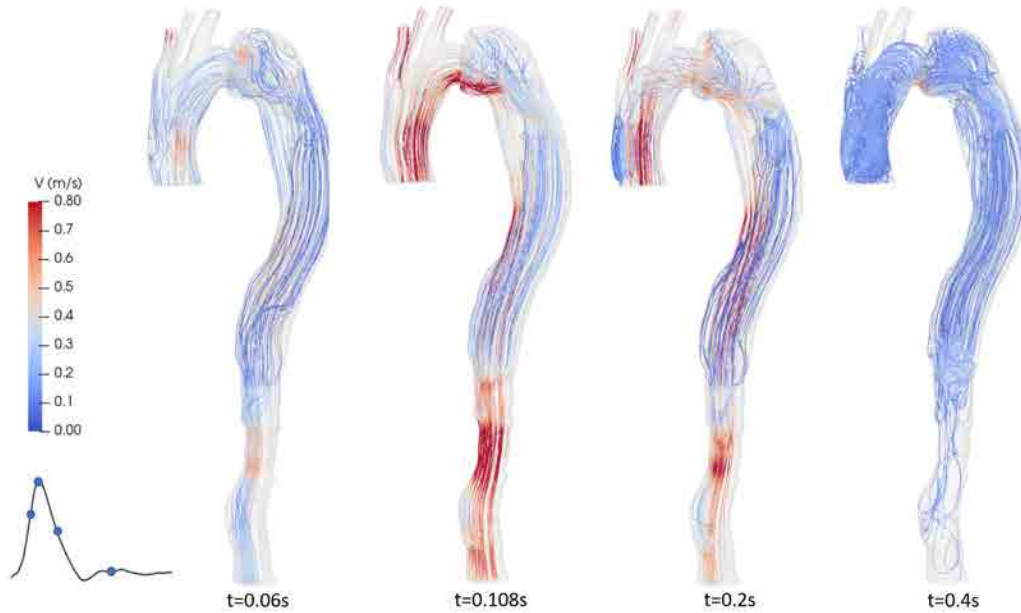


Figure 4.10: Streamline of the velocity profile at several periods during the cardiac cycle

Since the 4D-MRI images obtained from the AD2 are not of very high quality, we can only see from Figure 4.11 that the general velocity distribution in each section along the aorta has the same trend as that of the CFD model.

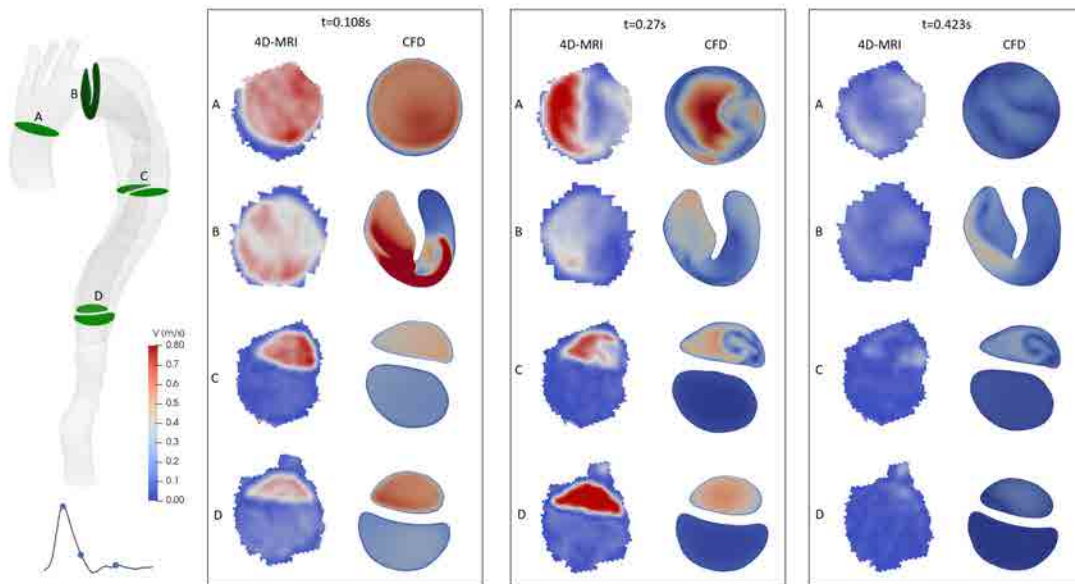


Figure 4.11: Velocity profiles on several sections along the aorta and compared with 4D-MRI

4.3.2 AD3

4.3.2.1 Preoperative

We first implement preoperative CFD Newtonian simulation. The following figure 4.12 shows a comparison between the blood flow rate recorded with PC-MRI and the blood flow rate produced with the CFD model at four distinct locations: ascending aorta(inlet), brachiocephalic artery, left common carotid artery and left subclavian artery. On the whole, the anticipated waveforms match with those seen in vivo, and there is excellent synchronization between the two waves in each of the four sites studied.

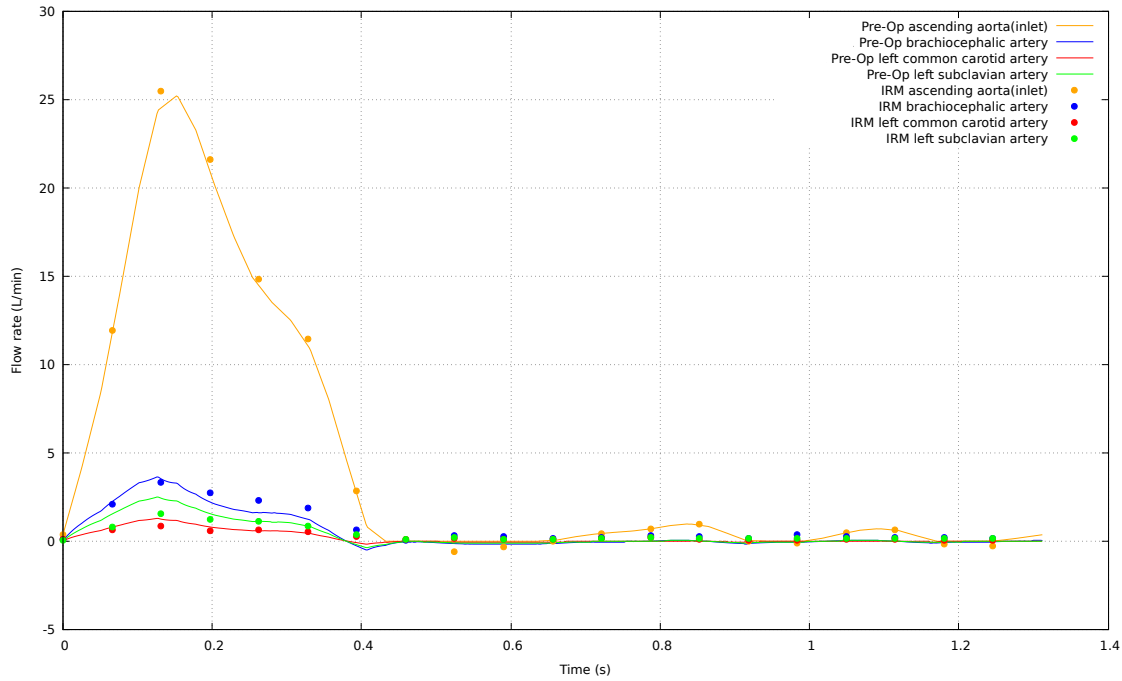


Figure 4.12: Comparison of MRI data and CFD simulation of preoperative for flow rates

The flow streamlines with preoperative 4D-MRI data and CFD simulations are compared (Figure 4.13). We could observe the same flow phenomena between in vivo and CFD simulation, even if at peak systole, the velocity in TL of CFD simulation is more significant than the MRI data.

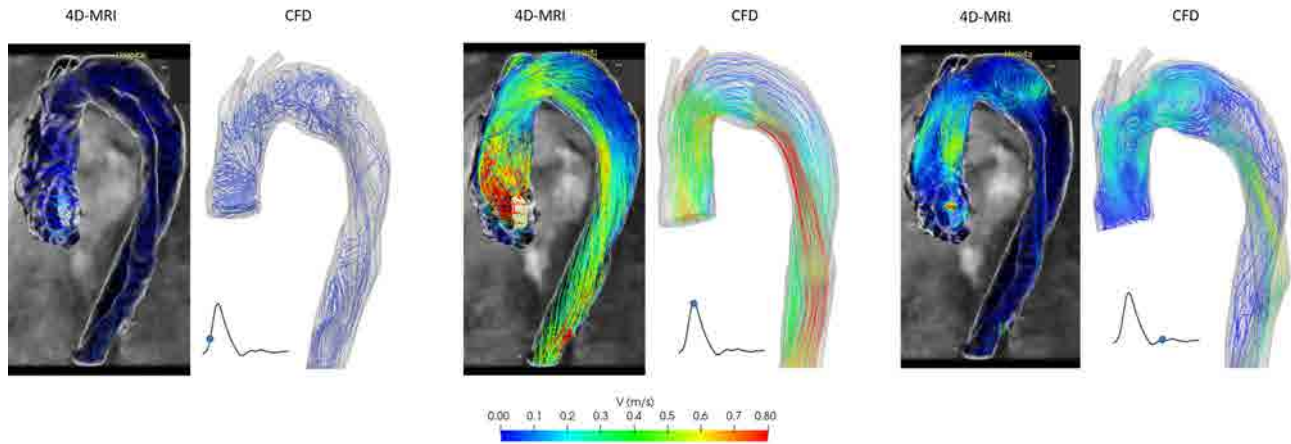


Figure 4.13: Comparison the flow streamline between 4D-MRI data and CFD simulation of preoperative

As shown in Figure 4.14, the velocity profiles on different sections of the aorta were measured at various times during the peak systole of the patient ($t=0.13s$), throughout the flow decay ($t=0.2s$), at the end of the systole ($t=0.3s$), and the beginning of diastole ($t=0.45s$). Compared with 4D-MRI, we could see that in the corresponding time, the velocity distribution has the same trend at each section, with an interesting agreement.

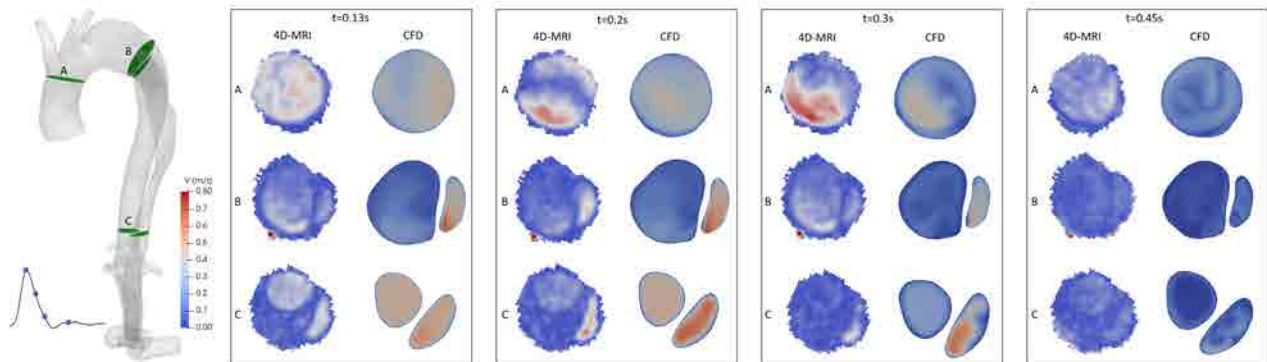


Figure 4.14: Velocity profiles on several sections along the aorta and compared with 4D-MRI

4.3.2.2 Postoperative

The comparison of the blood flow rate measured with PC-MRI and the blood flow rate obtained with the CFD simulation at three distinct locations (ascending aorta(inlet), brachiocephalic artery and left common carotid artery) is shown in Figure 4.15.

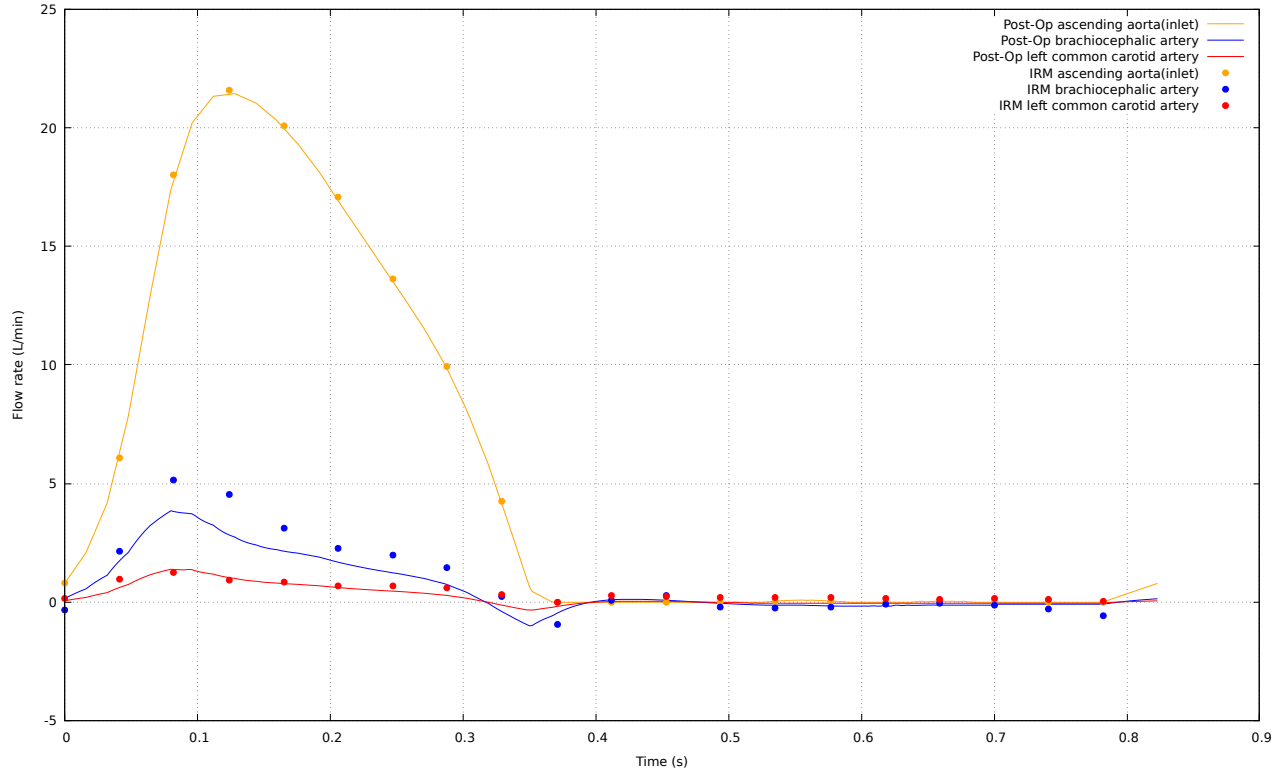


Figure 4.15: Comparison of MRI data and CFD simulation of postoperative for flow rates

The streamlining of flow is also compared with postoperative 4D-MRI data and CFD simulations (Figure 4.16). We can well observe a high agreement between MRI and numerical simulation results.

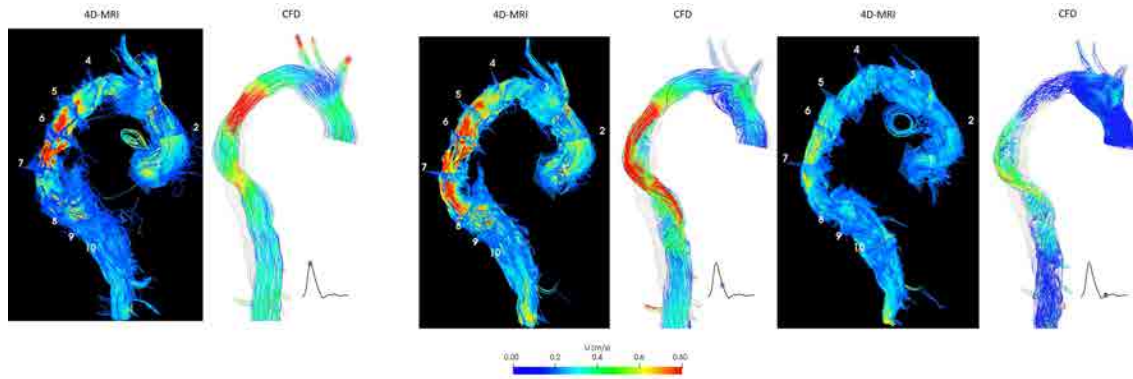


Figure 4.16: Flow streamline comparison between 4D-MRI data and postoperative CFD model

4.3.2.3 Preoperative & Postoperative

We also compared the preoperative and postoperative results for patients' flow rates and pressures. From Figure 4.18, Figure 4.19 and Figure 4.20, we can reasonably conclude that placing a stent in the FL for this patient during the interventional procedure is reasonable. We can also observe from Figure 4.20 that the four arteries (hepatic artery, superior mesenteric artery, and two renal arteries) connected to the true lumen are not affected by the blockage of the true lumen by the stent, because

of blood reflow from FL to the TL, where the four branches of the TL will be able to work and remain unaffected (Figure 4.17).

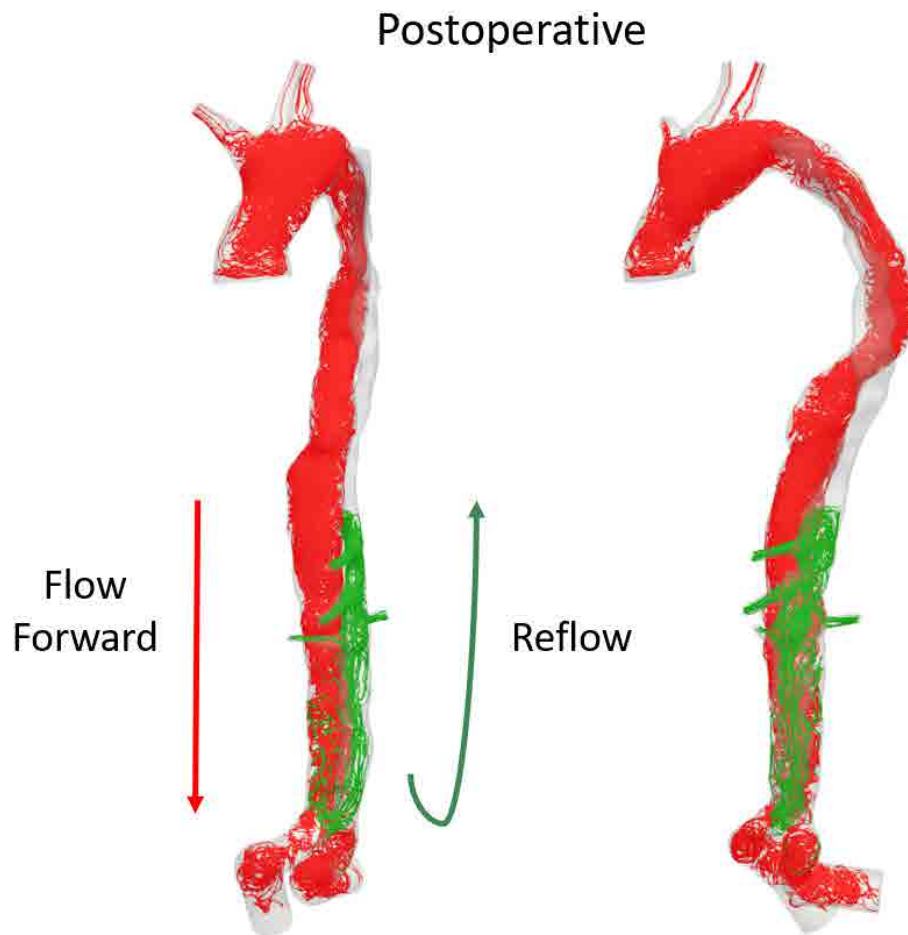


Figure 4.17: Fluid reflow from FL to TL for the postoperative

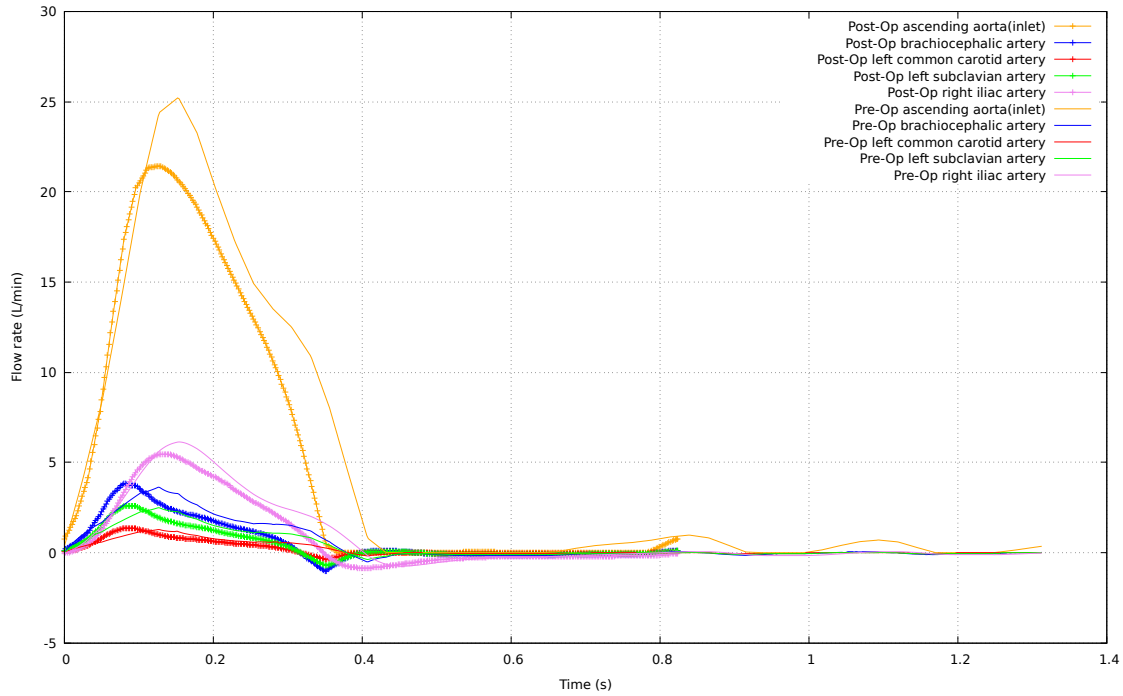


Figure 4.18: Flow rate compared between the preoperative and postoperative CFD model

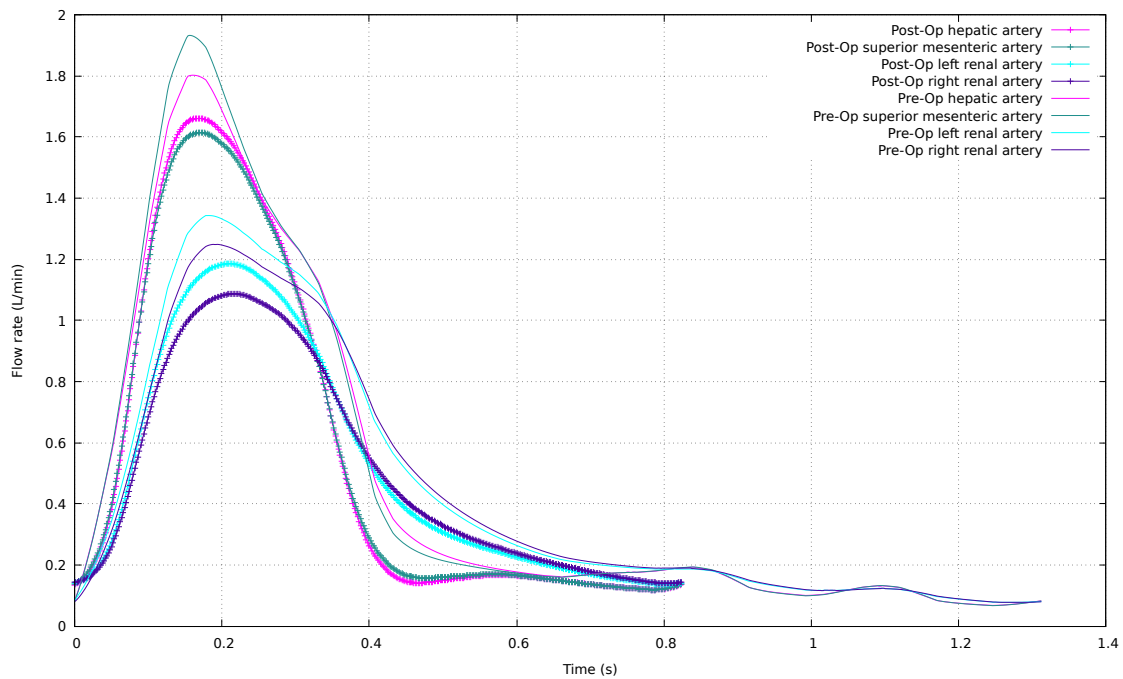


Figure 4.19: Comparison of flow rates in 4 branches arteries on descending thoracic in preoperative and postoperative CFD models

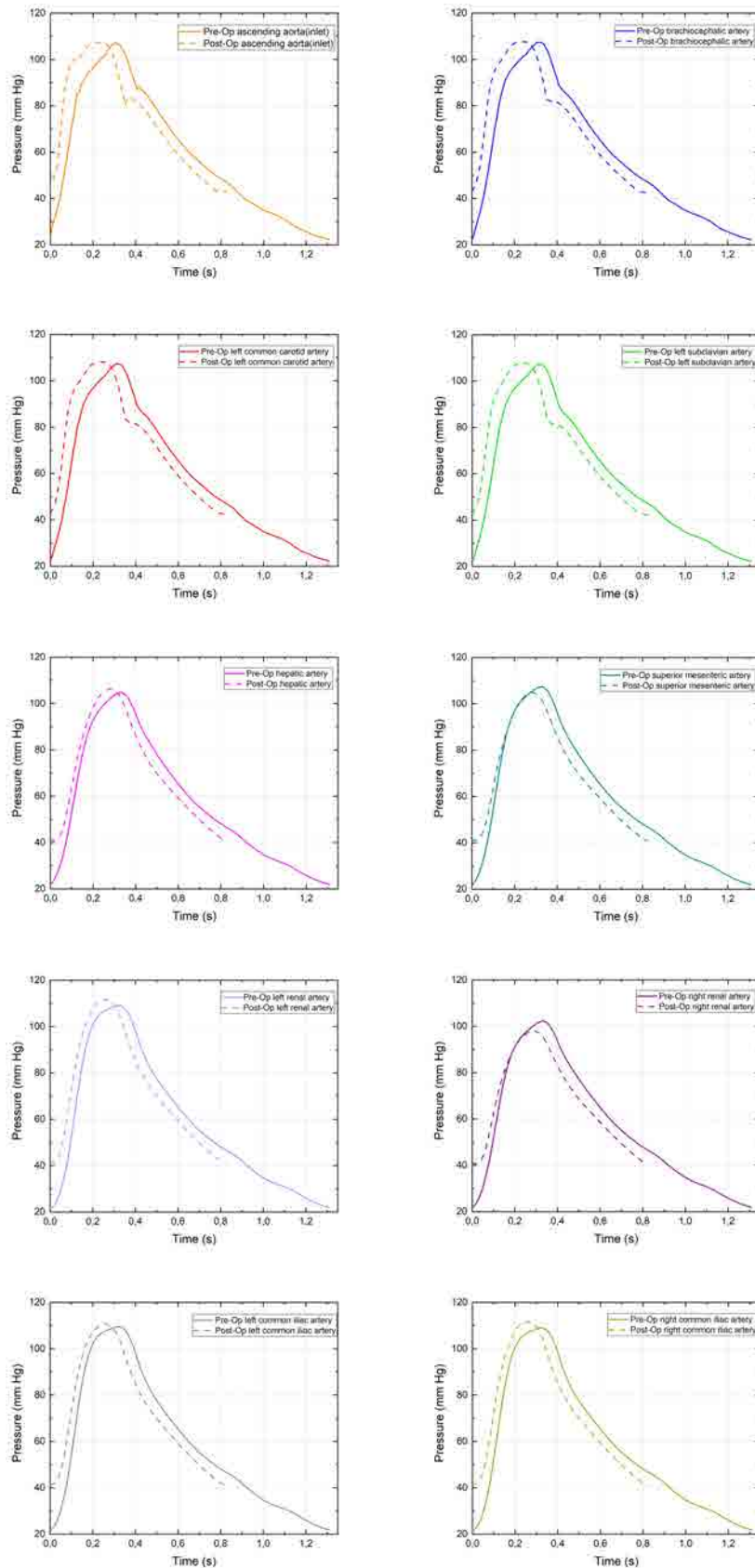


Figure 4.20: Pressure compared between the preoperative and postoperative CFD model on each boundary

Although rigid wall simulations cannot represent these intricate dynamics, the issue remains whether the extra simulation work required to achieve this level of detail is essential. One of the most important outcomes of these simulations is the prediction of wall shear stress, which is usually evaluated using a variety of indices, such as the time-averaged wall shear stress (TAWSS), oscillatory shear index (OSI), and relative residence time (RRT), which are already clearly explained in the chapter 3. The time-averaged wall shear stress is the average magnitude of the wall shear stress throughout the cardiac cycle. The distribution of the wall shear stress produced via CFD simulation is shown in Figure below.

In the aortic branches and the distal TL, elevated TAWSS values can be seen (Figure 4.21). Due to the pathological thoracic aorta's higher hydrodynamic resistance, there is more flow in the three branches than would usually be anticipated in a healthy aorta. As a consequence, the branches have higher TAWSS scores. Despite the decreased flow rate via the distal TL, its geometric constriction increases local velocities, resulting in higher TAWSS values. We also observed higher values of TAWSS greater than 5 Pa in postoperative analysis, not only because of the patient's advanced age (78 years old) but also because of the placement of the stent into the FL, which is narrow than the normal thoracic artery. The false lumen is subjected to the development of calcification plaque, therefore wall shear stress characteristics distribution and fluctuation throughout the cardiac cycle is essential evaluating of risky areas with preoperative and postoperative.

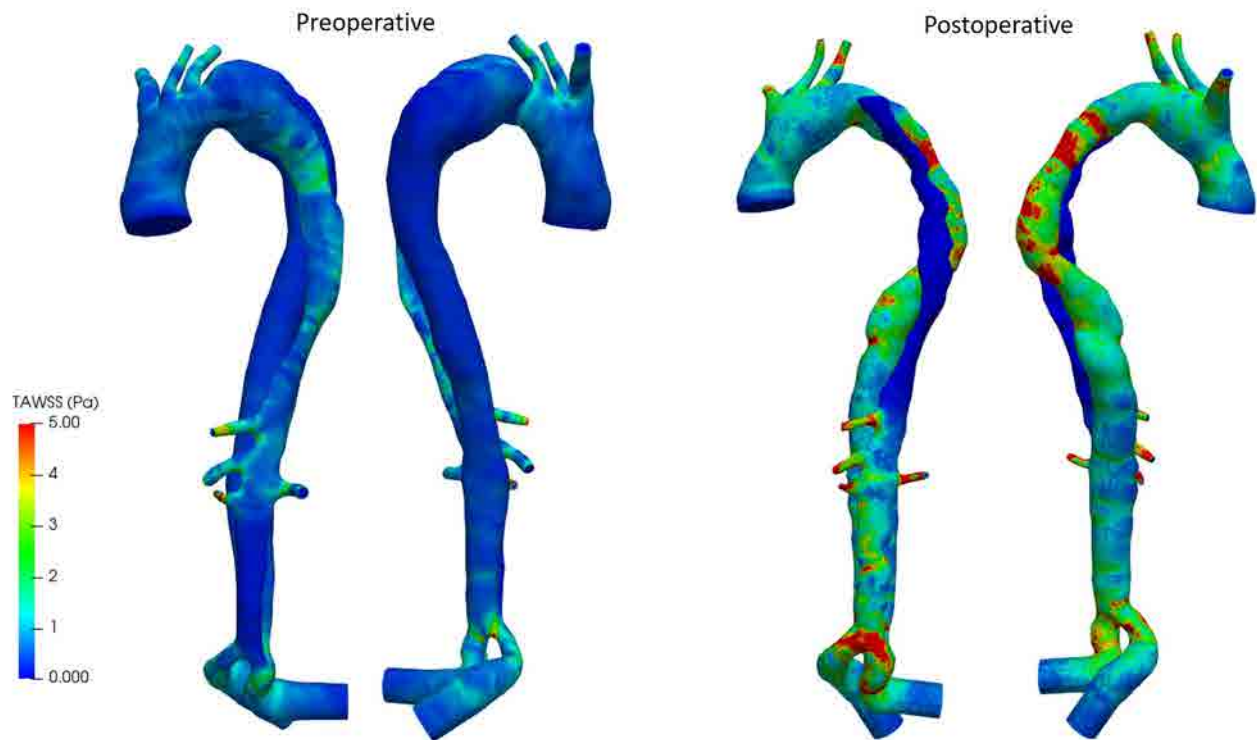


Figure 4.21: TAWSS distributions for preoperative and postoperative

The oscillatory shear index, shown in Figure 4.22, measures the flow's oscillatory character. This index fluctuates significantly throughout the domain, except in the distal and proximal TL. It continuously shows high values, indicating a significant variation in directionality compared to the

average flow. And we observe in the postoperative results a section upstream of the TL with extremely high OSI values, indicating that blood flows from the FL to the exit of dissection and backflows into the TL and generates oscillations in TL. Since WSS is one of the potential factors for atherosclerotic plaque formation, high WSS is linked with plaque rupture in atherosclerosis cases while low shear stress is associated with acceleration of plaque progression. Real-time postoperative monitoring of the patient is necessary.

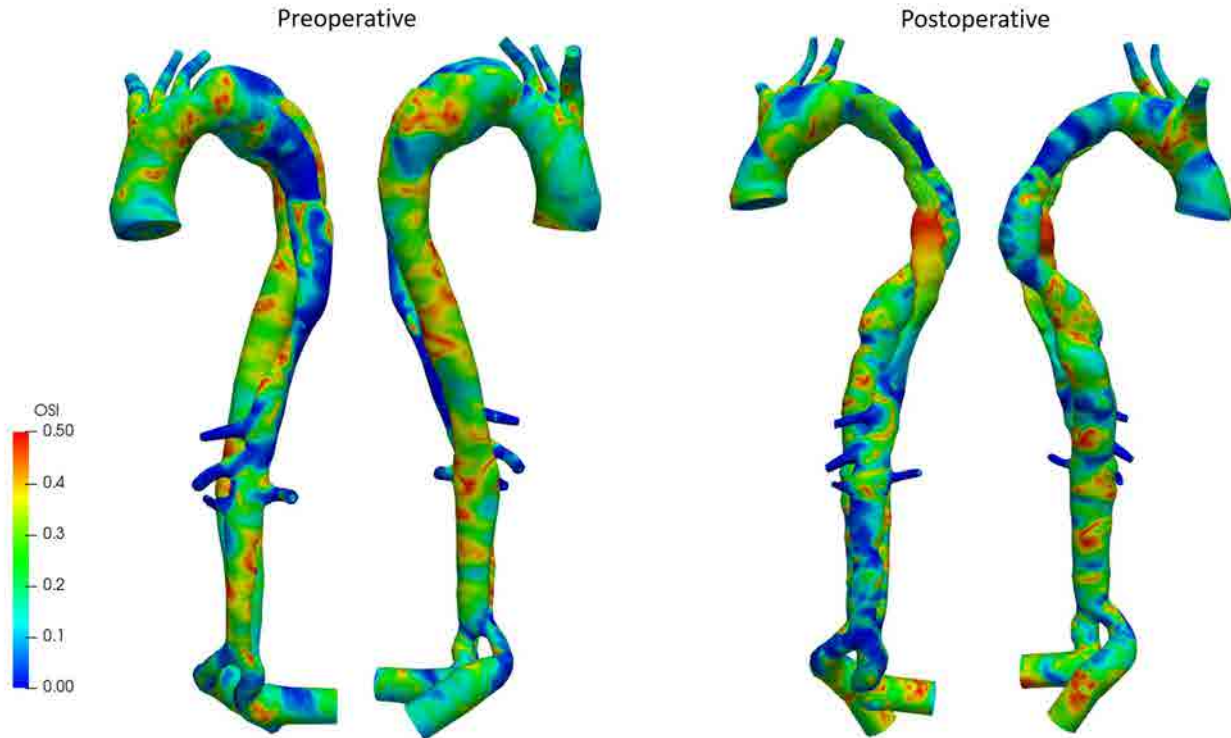


Figure 4.22: OSI distributions for preoperative and postoperative

The relative residence time (RRT) is a surrogate for disrupted blood flow, characterized by low magnitude and strong oscillatory wall shear stress. The RRT distribution (high values) is a useful tool for detecting potential atheromatic plaque localization areas. Figure 4.23 shows that RRT high values are significantly throughout the domain of FL in preoperative, leading to an aneurysm pathology if not treated quickly. And in postoperative, we observe the high RRT values domain is disappeared in FL. However, due to the small irregular amount of blood flow in the upstream region of the TL, the value was high.

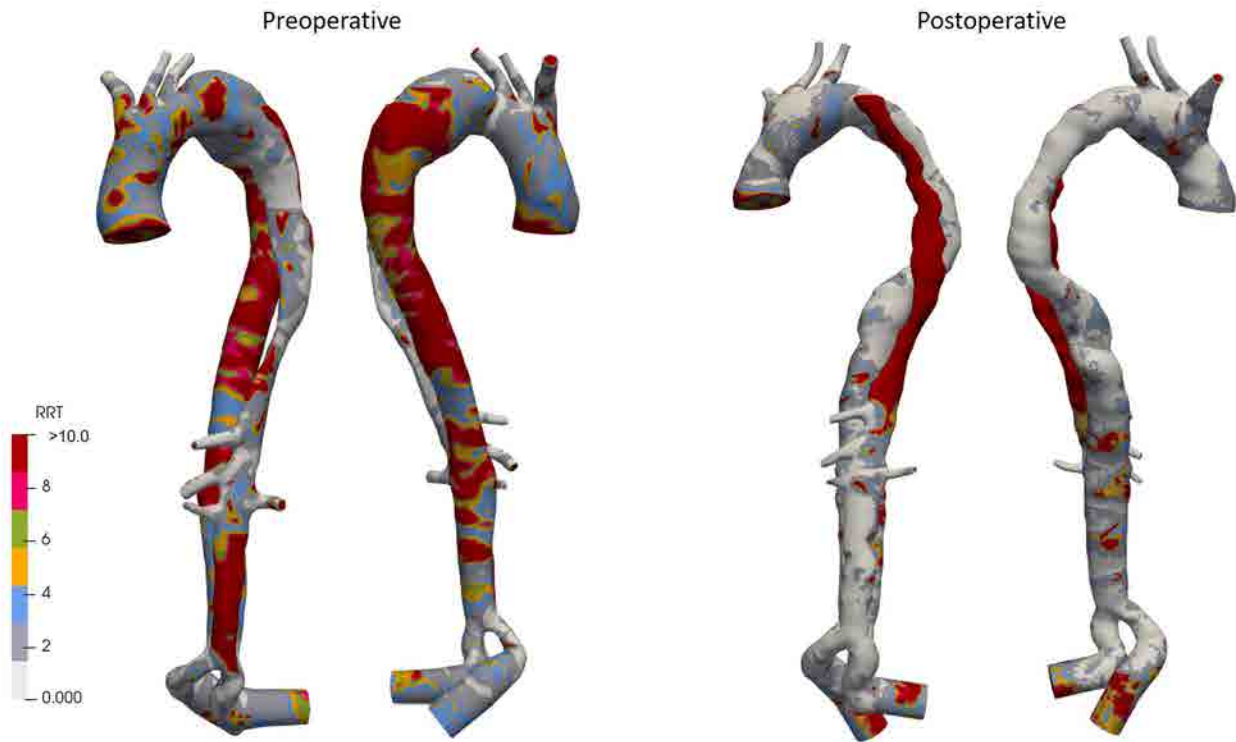


Figure 4.23: RRT distributions for preoperative and postoperative

And due to the presence of a helical flow observed in this patient both preoperatively and postoperatively from 4D MRI, it is necessary to use LNH (with a threshold of $LNH = \pm 0.8$) to identify if there were any elevated helical structures in the overall flow at onset of systole, at peak of systole, at deceleration of systole and at mid-diastole (Figure 4.24 left helical structure in blue, right in red). For preoperative, the presence of helical counter-rotating structures upstream of the ascending aorta, in the bulge area (the entry of dissection), and the region of two common iliac arteries are discovered over the cardiac cycle. And there are helical structures found along the descending thoracic aorta at systole deceleration and diastole.

For postoperative, LNH showed that helical structures distributed almost all the aorta during the cardiac cycle and distributed in approximately equal shares among clockwise (red) and counter-clockwise (blue) structures. This is because the postoperative patient has a narrower diameter than the preoperative patient's arterial size, indicating the existence of a more stable and helicoidal flow pattern as a consequence of vascular remodeling despite the higher blood flow.

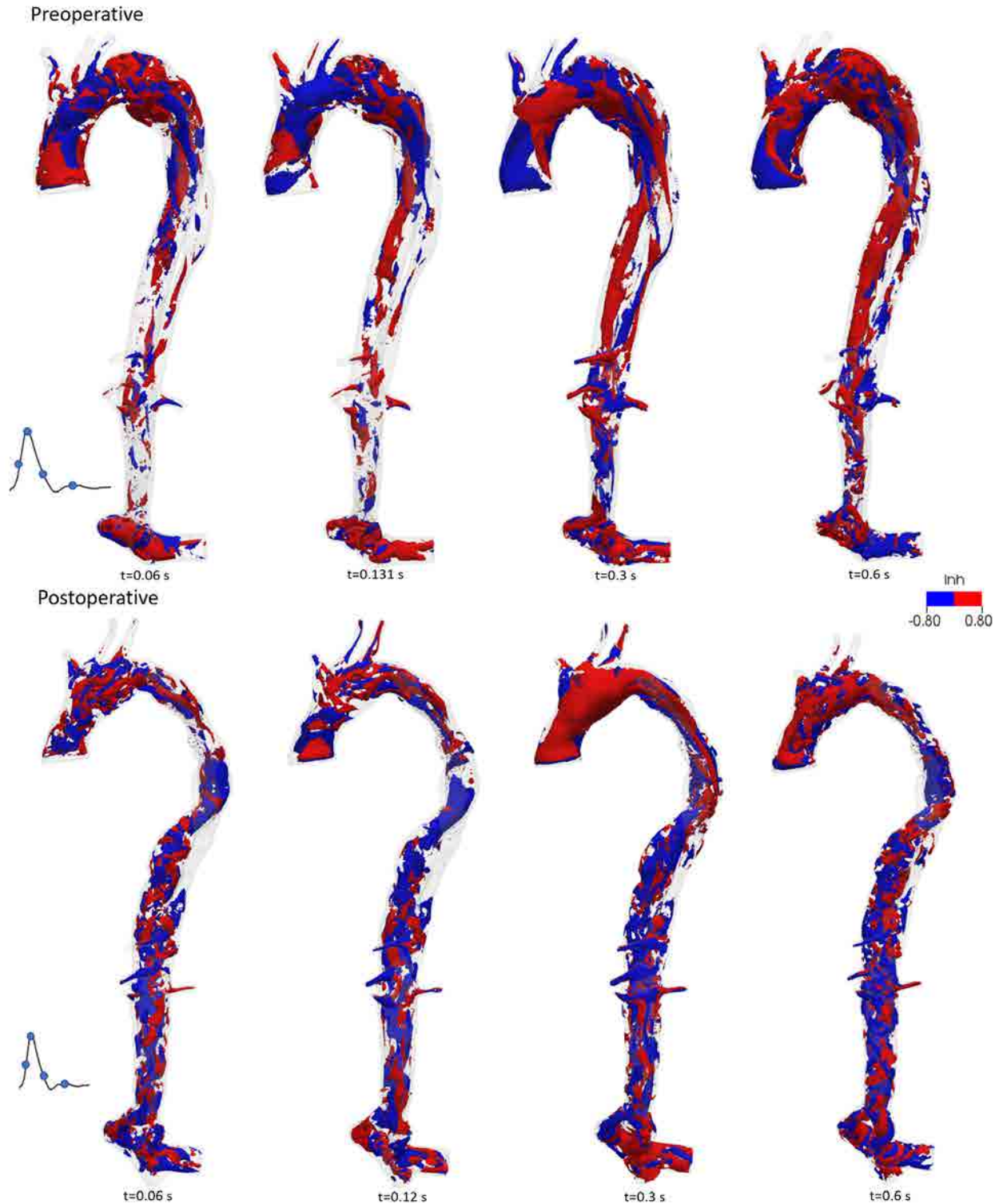


Figure 4.24: LNH distributions for preoperative and postoperative

4.3.3 Discussion

The purpose of this research was to assess and verify patient-specific preoperative and postoperative simulations of AD utilizing qualitative and quantitative comparisons to *in vivo* data obtained by 4D-MRI, not only the patient (AD2) with normal flow in aorta but also the patient (AD3) with strongly helical aortic flow. The findings of these simulations must be biologically correct to offer valuable insights. It means securing model parameters from patient-specific data, such as geometry and input and outflow boundary conditions. The use of 3D inlet velocity profiles and 3-element Windkessel outlet models has been shown to produce the most physiologically accurate CFD model results.

In addition, this project addressed the complex modeling of blood rheology and allowed the numerical results to be compared with new medical imaging data for a specific patient. Indeed, recent improvements in acquisition methods and resolution of medical imaging devices allow the acquisition of crucial quantitative information on the impact of vascular diseases and on aortic or pulmonary blood flow. In this project, the blood rheology model was validated on two patients due to the technical difficulty of the clinical examination. However, continued progress in this area will allow for clinical validation on a more significant number of patients in the future.

CFD models of AD have been created to investigate dissection's hemodynamics and obtain a mechanical knowledge of critical anatomical characteristics associated with different disease progressions (atherosclerosis, aneurysm, etc.). It can be concluded that numerical tools are a promising option for analysing hemodynamics in AD.

4.4 Comparison with *in vitro*

Until far, only a few researchers have tried to integrate *in vitro* and *in silico* methods to investigate AD. [Chen et al. \(2016\)](#) created a three-dimensional FSI model of an idealized AD and verified the findings using *in vitro* ultrasound measurements in a porcine AD model using a pulse duplicator device; however, clinical ultrasound data have limited resolution. A well-established method for flow diagnostics, particle image velocity (PIV), can generate high-resolution velocity fields for visualizing and quantifying vascular flows. Utilizing an experimental method such as PIV enables the validation of numerical models in a highly controlled setting with a degree of repeatability and precision not achievable *in vivo* ([Raffel et al., 2018](#)). Using calculations and tests, PIV was recently utilized to investigate the effect of tear size on the flow in an idealized AD model ([Zadrazil et al., 2020](#)). However, no patient-specific *in vitro* AD studies have been conducted so far using PIV with Carraeu-Yasuda model.

4.4.1 3D printed aorta model

In this section, we use the rigid and compliant 3D printed aortic dissections for *in vitro* experiment. These models are utilized for case studies based on *in vivo* data from patients and for comparisons between numerical and case studies. Compared to casting and silicone injection techniques, 3D printing provides quick prototyping (within 48 hours) at a cheap cost. It would be helpful for quickly manufacturing a human aorta and evaluating it in an *in vitro* setting for surgical training and stent-graft testing, among other applications. One of the advantages of 3D printing is the simplicity with which patient-specific geometry may be produced. However, in 3D printing, no

material is both flexible and transparent. The PIV must use the transparent model to function properly, so we sacrificed the soft one. We also tried to make soft prints, but the transparency was insufficient for the PIV (we could not see the particles). It was necessary to find a compromise between transparency and compliance while using 3D printing methods. Because PIV measures are dependent on transparency, it is a non-negotiable characteristic. With stiff walls, we have decided to create a less biomimetic model of AD, which is still useful for testing the validity of aortic flow measurements from CFD simulations. To produce a rigid, transparent model of the patient-specific AD, a 3D phantom was constructed using 3D printing technology from *3D MEDLAB Company* (Figure 4.25). Figure 4.26 shows the detail of AD1 and AD2 models that were printed using 3D printing.

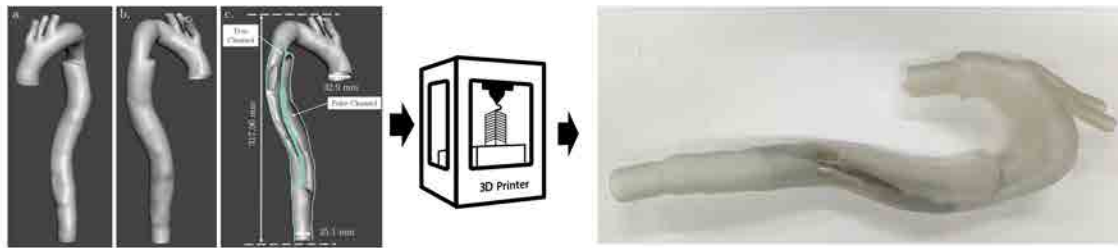


Figure 4.25: 3D printing to print a complete model of the aorta

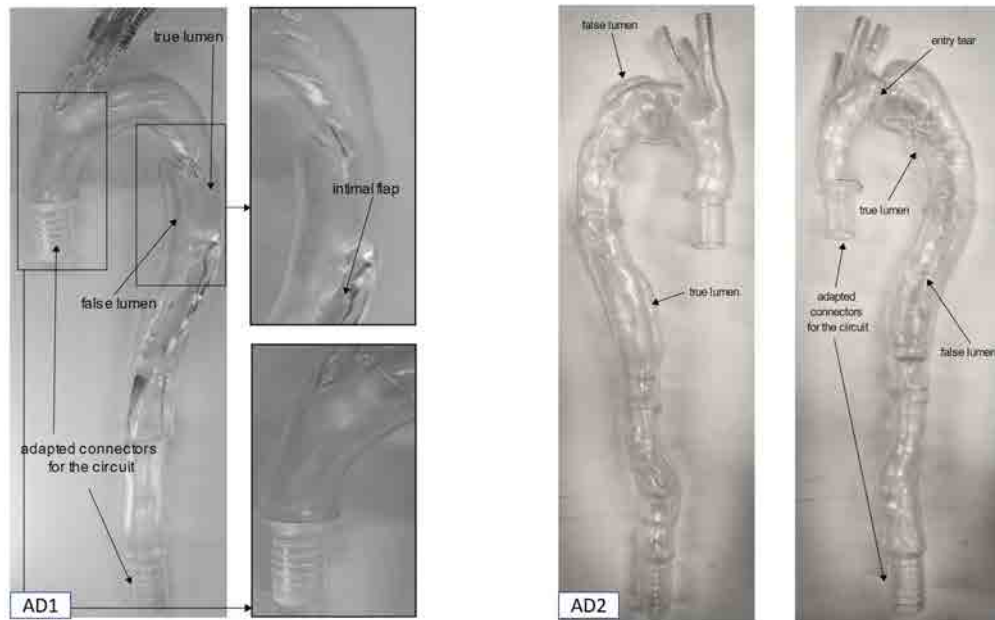


Figure 4.26: Detail of 3D printing model of AD1 & AD2

4.4.2 PIV

Figure 4.27 shows the circulatory mock loop setup ((Moravia, 2021)). With fast connections, each pipe and sensor may be relocated to accommodate different artery configurations. Flowmeters and pressure sensors are at the major aorta's entry and exit. The aortic arch has no sensors. It will

be determined using input and primary output data. Instead, the laser now lights the phantom from the tank's side while the camera feeds pictures from the tank's top. During the experiment, a plexiglas panel is positioned slightly above the tank fluid surface to prevent picture distortion. The aortic arch and dissection entrance rips are easier to see on all printed models.

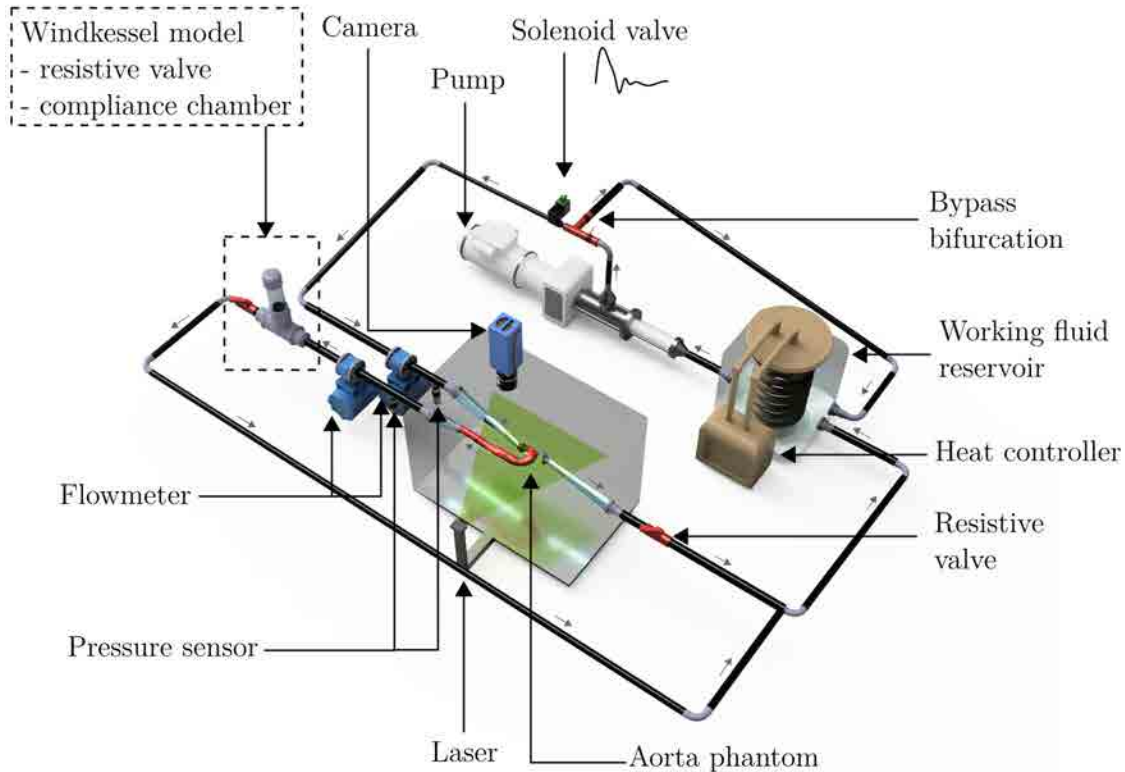


Figure 4.27: PIV experimental setup in AD configuration ((Moravia, 2021))

Additionally, in stiff AD models, extra components must be added to the mock loop to simulate the dampening effect. As a result, as illustrated in Figure 4.27, a compliance chamber is installed at the phantom's output. For this experiment, resistive valves are placed at each outlet (aorta, left common carotid, brachio-cephalic, and left subclavian arteries) to simulate capillary bed resistance. Because the "Solenoid valve" in PIV, which gives the pulse, cannot correspond to the flow rate from the MRI data. On the manipulator, the maximum flow rate limit from the experimental bench is less than three times that of the MRI image data. Therefore, The solenoid valve is used to impose a cardiac cycle with a period of $T=0.804$ s and a systolic peak flow rate of about 10 L/min on the patient. Due to the partial closure of resistive valves, 68 % of the entry flow rate is allowed to pass through the aorta and out via the primary exit valve. As a result, the three aortic arch branches evacuate 32% of the entry flow rate. These distribution values are consistent with clinical data from patients with AD1 and AD2 (for whom we have 4D-MRI data). They also match the *in vivo* distributions seen by Bonfanti et al. (2020) in a patient with Type-B aortic dissection. Temperature change throughout the course of an experiment within the range of $25 \pm 2^\circ\text{C}$. Carreau-Yasuda model is utilized for the whole set of data in AD. The working fluid was selected as blood mimicking fluid

(BMF), which must conform to both the rheological properties of blood and the requirements of the measurement instrument. So from the work of Moravia et al. (2019a), she designed the fluid with which refractive index(RI) is 1.399 to reduce optical distortion and render the phantom almost undetectable when submerged in the fluid.

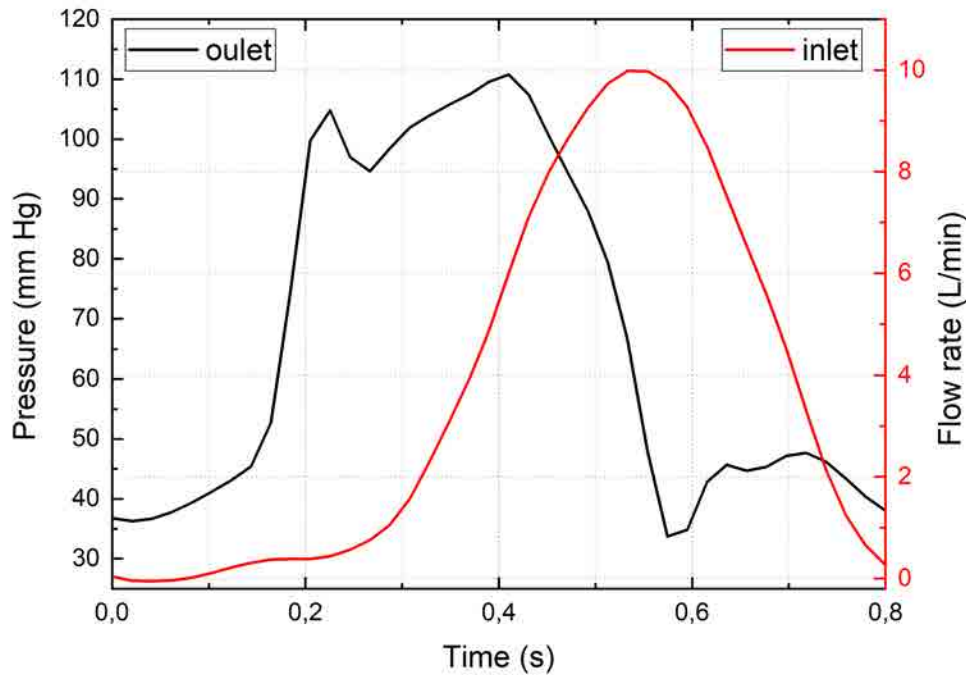


Figure 4.28: Boundary conditions at inlet (ascending thoracic aorta) and the major outlet (descending thoracic aorta)

Figure 4.29 illustrates the complete experimental conditions and the corresponding CFD numerical simulation boundary conditions and blood rheological model. A pulsatile 3D-Poiseuille velocity profile at the aorta's entrance is applied to mimic *in vitro* circumstances. The magnitude of the simulation velocity is adjusted following the flow rate (Figure 4.28) measured from the input flowmeter. A 3-element Windkessel model is implemented at each outlet (three aortic arch branches and descending aorta). Ensure that the *in vitro* and *in silico* setups were not adjusted to precisely match the boundary conditions of each other outlet. Setting such outlet boundary conditions properly would need further *in vitro* testing using various Windkessel configurations and lengthy simulation runs (almost a month for each configuration), which are not included in the scope of Moravia (2021)'s research. In *in vitro* experiments, it was challenging to implement 3-element Windkessel model at the outlet, so 2-element windkessel model (resistive value and compliance chamber) was used at the outlet (descending aorta), although it has been complicated. And the resistive valve applied on three aortic arch branches. It is anticipated that differences in boundary conditions would affect the amplitude of velocities throughout the cycle.

The characteristics of the model specified in the `transportProperties` file and whose numerical values of viscosities are divided by the density of the fluid are entered as follows in FOAM-Extend:

```
BirdCarreauCoeffs
{
nu0      nu0    [ 0 2 -1 0 0 0 0 ] 8.726e-5;
nuInf    nuInf  [ 0 2 -1 0 0 0 0 ] 5.2356e-5;
k        k      [ 0 0  1 0 0 0 0 ] 50;
n        n      [ 0 0  0 0 0 0 0 ] 0.22;
}
```

Both 2 case phantom experiments use the synchronization mode (solenoid valve/PIV synchronization) to implement the particles, PIV equipment, and process. The cardiac cycle is described using 12 cycle instants. Five hundred pairs of images are shot for each instant to compute velocities and reach an excellent statistical convergence. The time-lapse t is set for each cycle instant using this technique, as a wide range of flow velocities is observed throughout the cycle. Since each instant is treated independently, this t adaptation improves cross-correlation quality. The parameters of PIV imaging and their associated cycle instants are listed in Table 4.6.

Table 4.6: In all AD models, PIV synchronization parameters are used to photograph 12 cycle instants during the cardiac cycle

Cycle instant "k"	1	2	3	4	5	6	7	8	9	10	11	12
Cycle time (s)	0	0.04	0.08	0.12	0.16	0.2	0.24	0.3	0.4	0.5	0.6	0.7
Number of images captured	500	500	500	500	500	500	500	500	500	500	500	500

4.4.3 AD1

Indeed, optical access to regions in the phantom where limited. In AD1, PIV was focused on the entry tear region. The intimal flap's complicated shape and thickness resulted in light distortions and reflections in the region, resulting in blind areas for the camera to see through. The results were provided with a high degree of uncertainty, and there were several blind areas that prevented a thorough analysis of the tear region. In regions with non-straight geometries such as the entry tear, arch branches, and the intimal flap, it was expected that there would be some optical issues because the printed phantom surface quality was less smooth than expected. But when we compare it to the CFD results, the results are encouraging.

Figure 4.30 depicts the velocity fields in the entry site region of dissection as determined by numerical simulations and PIV data. The results describe the development of flow throughout a cardiac cycle. The comparison is presented for four distinct instants in the cycle: (a) beginning, (b) peak systole, (c) deceleration, and (d) diastole. The comparison is shown below:

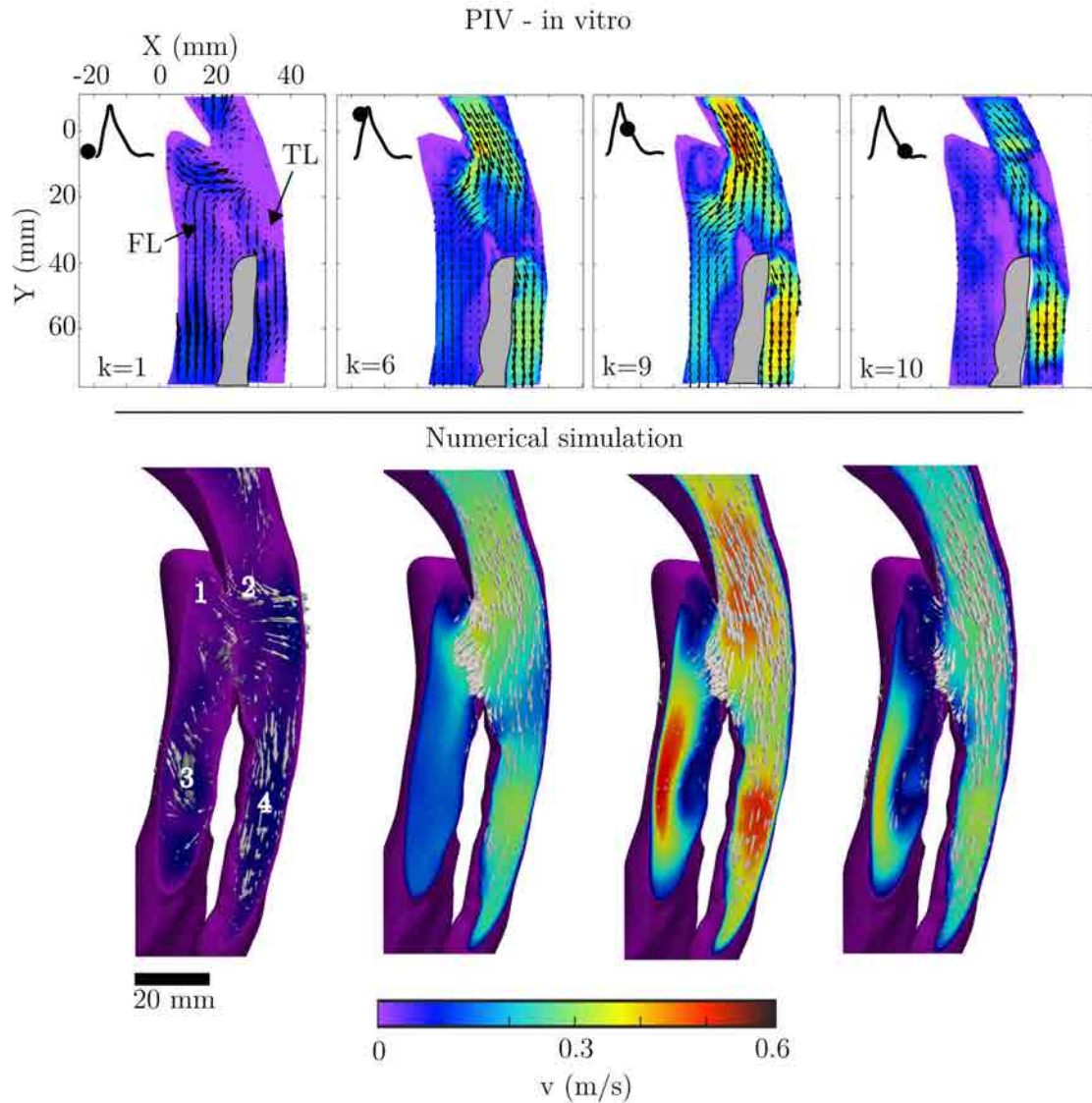


Figure 4.30: Comparison of PIV and numerical simulation velocity results for AD1 at four instants

Four areas 1, 2, 3 and 4 were singled out as particularly intriguing for discussing their similarities and contrasts. Regions 2, 3 and 4 are found as high-velocity areas in $k=6, 9$, and 10 , while region 1 is linked with a stagnation area. At the same instant, the in vitro experiment revealed a lower velocity in the FL than the numerical calculation. In terms of the TL, both methods exhibit similar trends.

Figure 4.31 depicts a three-dimensional representation of the velocity vectors with the CFD simulation results. The aorta's entrance and entry tear areas have the most significant velocity. Region 1 is once again recognized as a low-velocity stagnation zone. The preferred route is down once the flow has passed through the entrance tear and entered the FL. The 3D image confirms the trends seen in the 2D view for each area. According to these first findings, this aorta model is more straightforward than AD2, including an entrance rip and a false channel in the aortic arch's continuity. Thus, the flow is guided along a relatively smooth route with no significant direction

changes. 3-D analysis does not reveal anything significant about the flow structure.

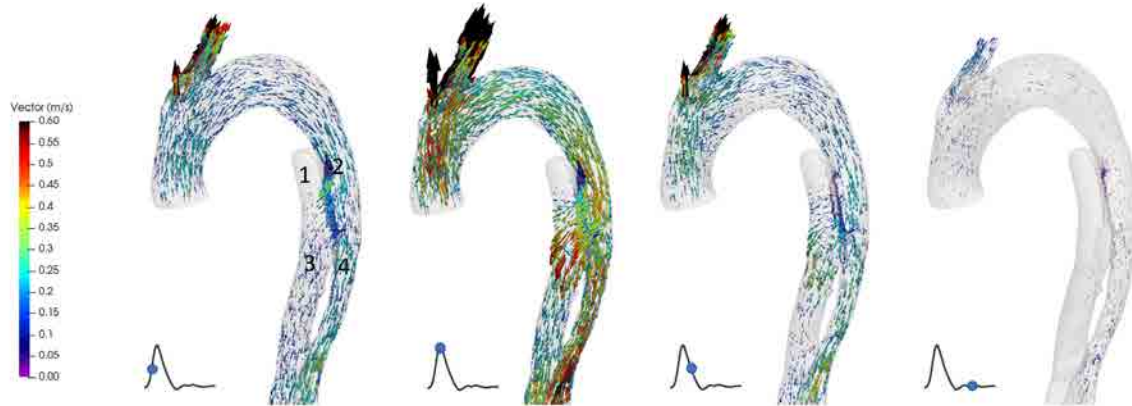


Figure 4.31: 3D observation on velocity vectors of CFD model for AD1 at four instants

These findings indicate the potential applications for *in silico* study combined *in vitro* bench, which is feasible in increasingly complicated phantom geometries.

4.4.4 AD2

The AD2 model has a more complex geometry with significant flow direction disturbances caused by the entrance tear's placement in the aortic arch and the FL's diameter shrinking. The three-dimensional perspective provided by the numerical simulation is anticipated to provide more information than in the AD1 scenario. And Due to the improved phantom surface quality and optical accessibility to areas of interest, AD2 produces much higher-quality findings.

This section compares AD2 flows between the PIV and CFD in the FL. In Figure 4.32, the first, PIV, and numerical simulations are compared in the same plane. The three recorded instants were selected to illustrate the two whirling formations designated regions 2 and 4 (upward and backward from the diameter narrowing, respectively) and the high-velocity route near the systolic peak in the narrowing (region 3). Region 1 is the entrance tear, which is situated behind the PIV plane from the camera's perspective. The dashed lines delimit the PIV ROI in the simulation results shown in the Figure 4.32. The CFD simulations results are shown with normalized magnitudes of velocity and vector projections to the PIV plane.

In the arrowing area, comparable velocity values are found in the PIV and numerical simulation for $k = 6$ and $k = 9$. At each moment, significantly greater velocities near the entrance tear are detected (region 1). They are less noticeable in the PIV data. At the systolic peak ($k = 6$), region 1 contains the simulation's most tremendous velocity. By comparison, there is no significant change in the magnitude of velocity in PIV findings for region 1 throughout the cycle. Note that, due to the entrance tear's position, the emerging fluid flows mostly in an orthogonal direction to the experimental plane. This strong out-of-plane flow cannot be detected adequately by the 2D-2C PIV system (Moravia et al., 2019b), resulting in an underestimate of velocity. PIV experiment's imaging method and selected plane are insufficient for quantifying velocities in this entrance tear

area.

In addition, the constricting areas where the flow is mostly contained inside the experimental plane. Lower velocities and whirling formations define Region 3. At $k=9$, this rotating flow is seen both *in vitro* and *in silico*. Additionally, at the systolic peak ($k=6$), the more excellent velocity route is seen in the narrowing for both approaches: near the wall, velocity is similarly close to zero in regions 2 and 4, with stagnation zones in these two bulges.

However, discrepancies between the PIV and numerical simulation results are also found. The upward constriction of the counterclockwise whirling structure is not seen in the numerical simulation at $k=1$. It never appears throughout the cycle. The reason is most likely due to variations in boundary conditions. The numerical simulation shows a less strong backward phase, and the upward velocity does not produce the whirling upward caused by the constriction.

In both methods, just the spiraling structure downhill into the constriction is visible. This last vortex remains longer throughout the cycle in the numerical simulation because the backward flow does not destroy it. This difference is most likely due to the *in vitro* experiment's Windkesel compliance chamber design. Indeed, excessive compliance would result in a more significant energy restoration in the system after systole, resulting in a more significant backward flow. The *in vitro* experiment over-represents reverse flow. The compliance system's inability to adjust in the *in vitro* simulator is a shortcoming that must be addressed further to cope with rigid wall models.

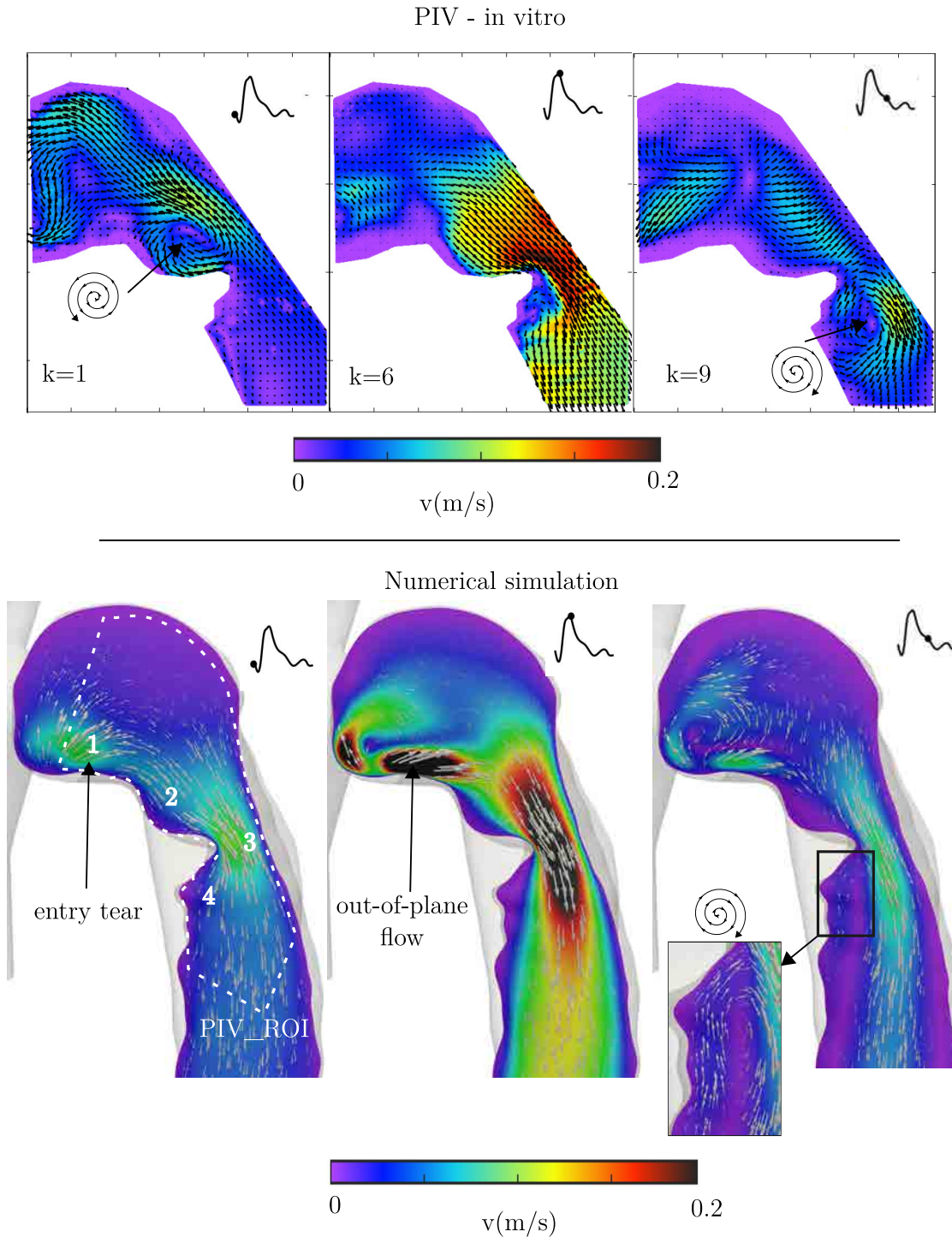


Figure 4.32: Comparison of PIV and numerical simulation velocity results for AD2 at three instants

Finally, the numerical simulation revealed a remarkable entrance tear flow. Due to the model's shape, the entrance rip could not be seen using PIV's 2-D plane. Figure 4.33 depicts a 3-D vector view in the FL. The entrance tear has the most incredible velocity and vectors pointing away from the PIV 2-D plane. Thus, the *in vitro* experiment with the selected plane could not evaluate

entrance tear velocities. The entrance tear area may be riskier for the patient than the diameter narrowing region.

Figure 4.33(b) shows the flow wrapping to form two clockwise whirling structures after the cycle deceleration phase. The upward vortex from the narrowing lasts just 40 ms before dissipating. The PIV experiment did not show this trend, where successive instants are spaced by 50-100 ms. This is because the numerical simulation succeeding cycle instants are separated by 10ms. AD2 model would need 3-D results to study flow. The 2-D perspective is insufficient for flow analysis, and the 3-D view with more excellent temporal resolution reveals a wealth of new information. Although the models' inflow and boundary conditions would need to be adjusted for a thorough analysis, this is an excellent illustration of how 2-D experimental and 3-D numerical simulation data may complement one another.

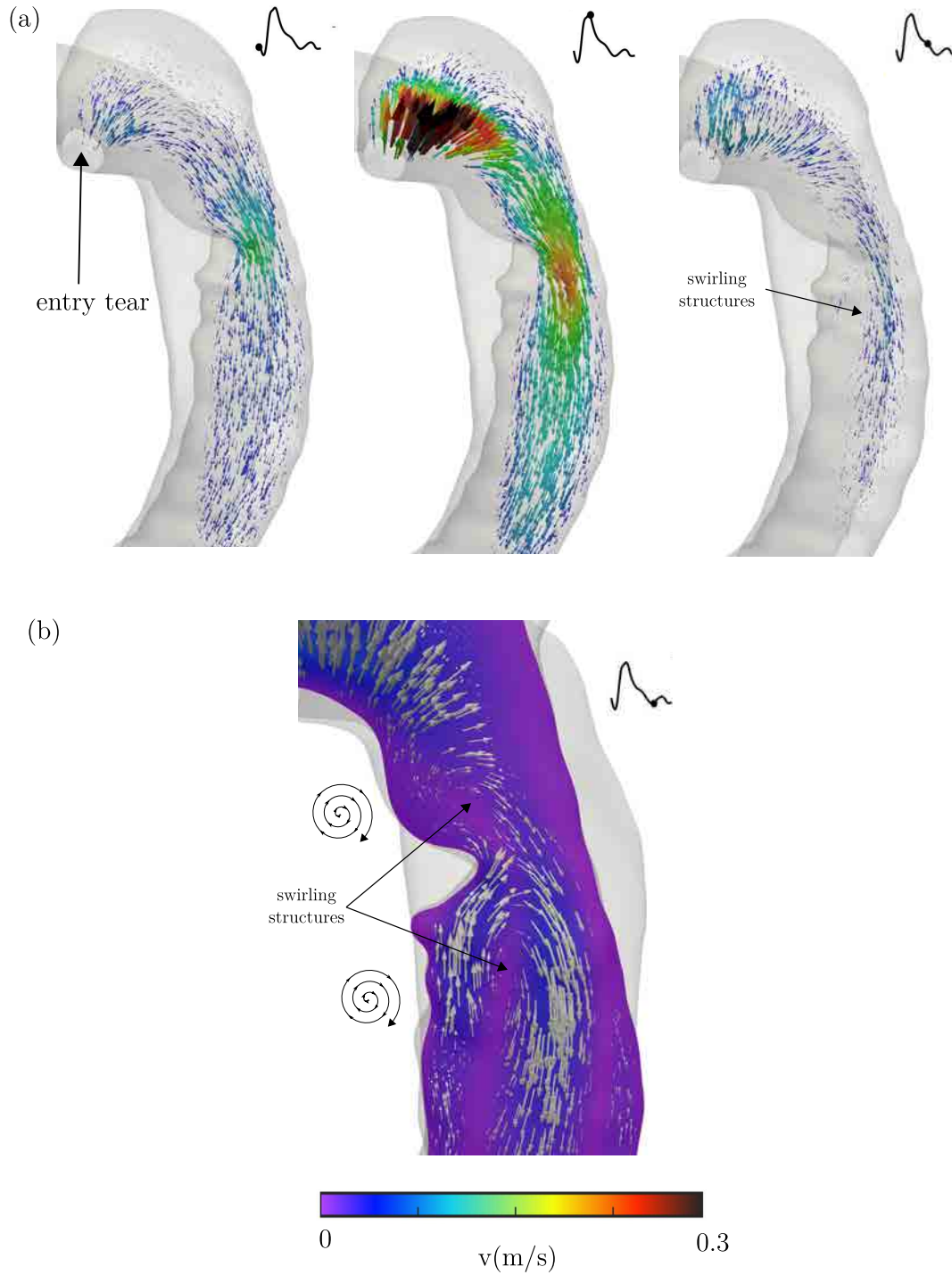


Figure 4.33: 3D observation on velocity vectors of CFD model for AD1 at four instants

4.4.5 Discussion

This is the first research to verify a patient-specific AD model with the dynamic BCs and the same pulsatile flow and Carreau-Yasuda rheological model, and to explore the hemodynamics of a personalized AD model using PIV and CFD model, and demonstrates the value of integrating

experimental and numerical techniques.

A thorough comparison of numerical simulations and experimental results established the consistency and accuracy of the aortic domain blood flow patterns. In the case of AD1, the numerical simulation's 3D visualization corroborated the trends seen in the 2D PIV plane. The third dimension provided no discernible information. In contrast, the 3D view added additional dimensions to the AD2 case by revealing which geometry had a 3D effect on the flow structure. These similarities prompted the notion of developing complementing flow visualization and analysis tools to understand aortic flow patterns better.

Additionally, differences were noticed, although, for the sake of this first comparison, the boundary conditions of each outlet were not tuned. The limitation of this experiment is that there is an absence of a way to achieve patient-specific dynamic BCs. In particular, the vessel input flow rate waveform and the afterload resistances and compliances are adjusted following available clinical datasets to achieve the desired systolic and diastolic pressures and cardiac output distribution.

4.5 Discussion and conclusion

This research describes a method to perform patient-specific AD simulations using the most significant anatomical and flows data available *in vivo*. In this section, the rigid wall model used for CFD simulations gives first flow estimates compared with dynamic imaging, imposing physiologically correct and individualized boundary conditions. Validations against *in vivo* measures reveal a high degree of concordance in general. The findings of this study should contribute to a better understanding of the flow patterns and hemodynamic conditions in type B aortic dissections, with the long-term goal of identifying biomechanical factors that can be used to predict the likelihood of subsequent aneurismal degeneration and rupture in these patients for preoperative and postoperative.

The cutting-edge models of PIV experiment [Moravia \(2021\)](#) featured computer-controlled pulsatile flow, a patient-specific AD model, and the corresponding blood flow characteristics (Carreau-Yasuda model). This study shows how *in vitro* and *in silico* techniques may be created in concert to precisely recreate the patient-specific hemodynamics of complicated AD cases, thus providing a new paradigm for treating AD or other vascular diseases. In addition, the PIV experiment aims to provide a robust framework for conducting accurate experimental and numerical hemodynamic investigations of AD pathology using non-invasive clinical data and investigation as a tool to improve clinical outcomes and are often validated against *in vitro* experimental data.

As recent researches ([Thubrikar et al., 1999](#), [Xiang et al., 2011](#), [Chiu and Chien, 2011](#), [Meng et al., 2014](#)) indicate, fluid dynamic markers such as WSS characteristics and FL & TL pressures significantly impact AD's long-term progression. Informed clinical planning cannot rely solely on geometric data. However, it must also consider the pathological and complicated hemodynamic environment that characterizes complex AD cases. It is impossible to overstate the importance of such a synergistic strategy to AD research and clinical translation. Assuring the validity and accuracy of simulations is a critical step in transferring such methods to the clinic. The experimental methods created in this study serve as a baseline for validating the findings generated *in silico*. Once validated, CFD models may be used to accurately predict hemodynamic indicators such as WSS that are difficult to measure experimentally and impossible to assess *in vivo*. Additionally, *in silico*

models may simulate various interventional situations (e.g., *Chapter 3.8 Modeling for the rise of surgical tools*).

General Conclusion

Currently, the growing popularity of endovascular surgery is characterized by a strong alternative to traditional open surgery for many AD patients. Endovascular repair of the thoracic aorta is characterized by reduced morbidity, shorter hospital stays, less invasive treatment, and thus faster recovery. The main criterion for the recommendation of endovascular surgery remains the prevention of rupture. In contrast, criteria concerning the medium- and long-term durability and performance of the stent graft are still secondary (Khanna, 2011). The main long-term complications are stent migration and endoleaks of various types, leading to dangerous pathology AD. These complications can result from several factors, and there are significant differences in clinical opinion regarding the best treatment procedure. In addition, these complications are more common in the thoracic aorta than in the abdominal aorta because of the curvature of the aortic arch. However, it is generally accepted that all of these complications are related to instability, poor sealing, or poor contact between the stent graft and the vessel wall at the fixation sites (Atkins et al., 2006). They result from several factors such as poor sizing or positioning of the stent-graft, material fatigue, or often a complex aortic morphology that is difficult to apprehend intraoperatively.

This thesis aimed to model the complete endovascular procedure (Figure 4.34) for AD to understand the origin of these complications and thus propose new criteria for a reliable operational solution for precise localization and control of stent-graft delivery. However, in clinical practice, the surgical tools' behavior and the stent delivery's success are affected by the blood flow and the periodic deformation of the vessel, in particular, the thoracic aorta subjected to displacements and deformations more critical than the rest of the arterial circuit. Therefore, the numerical simulation of hemodynamic in AD and the behavior of surgical instruments in a dynamic AD environment are the research that concerns both the rheology of arteries and blood.

To achieve this, we were first concerned with the mechanical behavior of the arterial wall because material characterization methods have demonstrated the nonlinear, anisotropic, and viscoelastic character of aortic tissue due to its layered structure. Uniaxial Menut et al. (2015) and biaxial (Deplano et al., 2019) traction tests and expansion experiments (Menut et al., 2015) on an aorta submerged in water were used to characterize the overall aortic tissue behavior. The mechanical behavior for all human thoracic aorta specimens is characteristic of hyperelastic behavior. Although the orthotropic characteristic of the aortic tissue is well-founded in the pieces of literature (Holzapfel et al., 2000, Gasser and Holzapfel, 2006, Fung, 2013) for healthy tissues, we decided to model the mechanical behavior using an isotropic hyperelastic Mooney-Rivlin type law. This choice for this study has its limitations but can be considered as giving good results for this research project.

The rheology of blood, which has a shear-thinning and thixotropic nature, is strongly influenced by the unsteadiness of shear stresses in the flow. In this study, we hypothesize that blood is a Newtonian fluid, which has been validated.

According to an increasing research, regions with a high OSI and a low TAWSS are more prone

to rupture(Xiang et al., 2011), calcification(Bassiouny et al., 1994), or wall thickening(Wen et al., 2010) in the presence of aneurysms. According to Meng et al. (2014), these regions show a range of endothelial dysfunction, including increased permeability and stickiness, and inflammatory responses (Chiu and Chien, 2011). Hence, for these critical, the role of blood flow and the parietal stresses it induces in developing these pathologies cannot be neglected.

A primary ambition in hemodynamic modeling is the representation of the rheological behavior of blood in the complex anatomical features of AD. For this reason, we chose to study hemodynamics in a specific patient AD model. For the solution of the Navier Stokes equations, we decided to use the open-source software OpenFOAM, which offers the possibility to develop new solvers that can be modified and compiled in an unlimited way, offering a straightforward implementation of complex mathematical models. The comparison of CFD numerical results between Newtonian and Carreau models shows no significant difference, demonstrating the possibility of fluid characteristic hypotheses. In the last chapter, we realize the two specific patient AD cases CFD simulation with the individual boundary conditions obtained from imaging data. The results showed highlight similarities with dynamic 4D MRI data during systolic and diastolic phases with the Newtonian model, confirming the use of such a simplified rheofluidic model.

The FSI simulation has also been addressed in this thesis using a partitioned approach and a strong coupling necessary for the coupling between blood and artery. A solver for fluid-structure interaction exists in the extended version of OpenFOAM, called FOAM-Extend. Hemodynamic simulation models must be employed to describe tissue behavior, and FSI numerical simulations must account for artery deformation. Because of the limitation in terms of the convergence and the computational time, we did not distinguish Young's modulus of the IF from other regions of the arterial wall. The FSI model outperforms rigid wall CFD simulations in recreating the thoracic aorta fluid hemodynamics when used to investigate the motion properties of arteries. It becomes clear that the absence of flap motion in rigid wall simulations has a substantial impact on the anticipated hemodynamic parameters, highlighting the critical role of FSI simulations in AD.

The work devoted to modeling the ascent of surgical tools, including the rigid guidewire and the catheter containing the stent graft, in the aorta with an AD pathology is also realized in this thesis. The Abaqus[®] software with an explicit scheme is used for the numerical simulation of this highly nonlinear problem, mainly due to numerous contacts between deformable, tortuous, and heterogeneous bodies and the large deformations and the complex materials involved. In the first step, the behavior of the arterial wall was modeled with an elastic law. The behavior of non-biological materials required for complete endovascular surgery models, such as surgical tools and stent-grafts are based on the results of Mouktadiri (2013) and Menut (2017). And The interest of this modeling is the possibility to model complex AD cases, considering the specificities related to each patient, simulating and evaluating the different steps of the endovascular procedure in the preoperative phase.

The last part of this thesis is the validation between *in vivo* and *in silico* and *in vitro* with in silico. For this study, we used qualitative and quantitative comparisons to *in vivo* data acquired by 4D-MRI

to evaluate and validate patient-specific preoperative and postoperative models of AD. To be valid, the results of these simulations must be physiologically accurate. Input and outflow boundary conditions, geometry, and patient-specific data correspond to MRI data. The most biologically realistic CFD models utilize 3D inlet velocity profiles and 3-element Windkessel exit models. Two AD bio-faithful CFD models were compared to MRI data for all patients and showed excellent qualitative agreement. Aortic dissection hemodynamics and key anatomical features linked with various disease progressions have been studied using CFD AD models (atherosclerosis, aneurysm, etc.). Numerical techniques are a potential alternative for AD hemodynamic analysis.

Additionally, there is a parallel thesis [Moravia \(2021\)](#) that focuses on aorta phantom flows PIV used in AD (similar geometry) allows the comparison and inter-validation of both model techniques throughout the research. A similar pulsatile flow and dynamic BCs were used in both *in vitro* and *in silico* models. Comparing hemodynamic results shows a high degree of qualitative agreement. The findings of this research establish the accuracy and reliability of numerical and experimental techniques for simulating the patient-specific models. This work demonstrates optimism that these models may be used further to investigate the hemodynamics of the patient-specific AD instance and evaluate surgical methods.

As well as supporting the creation of new or personalized in-vitro medical devices (PIV experiment), the proposed platform (Figure 4.34) can evaluate clinically significant hemodynamic indicators. Overall, the integrated method provided here is a valuable tool for investigating AD's hemodynamics in unprecedented depth. It, therefore, represents a breakthrough in patient-specific AD hemodynamic modeling and simulation and may be extended to other vascular diseases, altering the existing clinical paradigm.

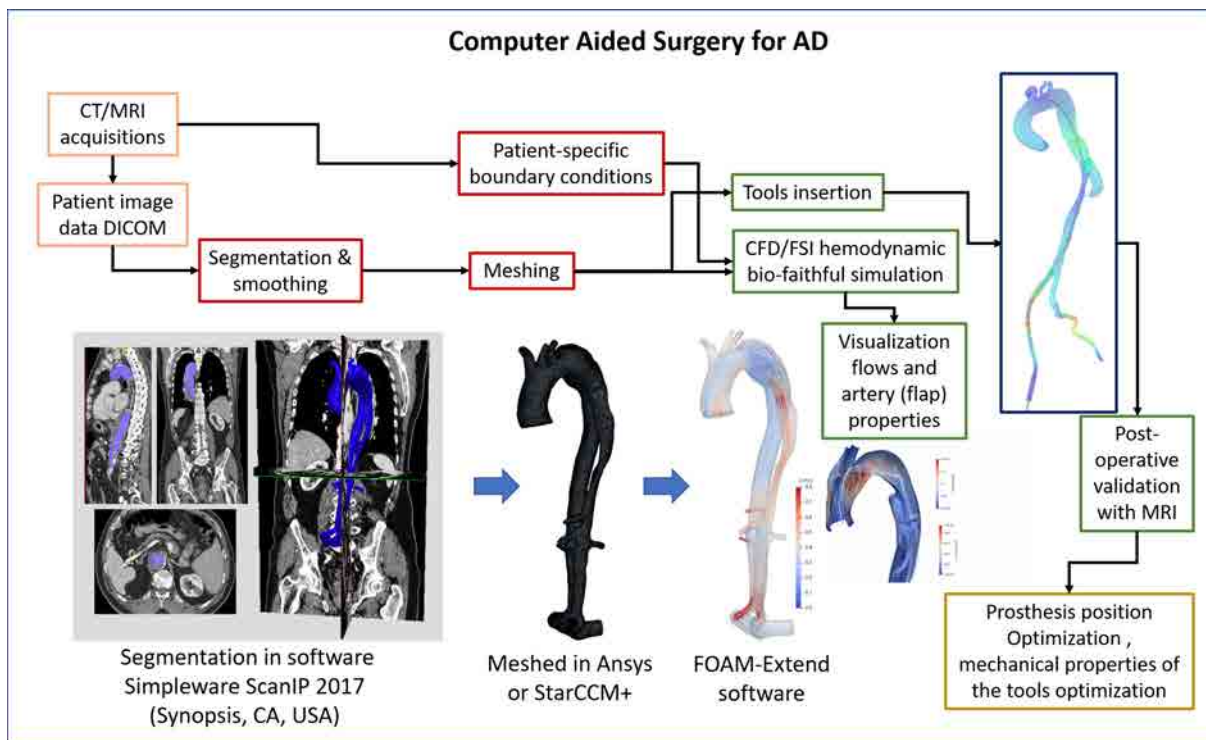


Figure 4.34: The procedure of computer aided surgery: application to AD

Perspectives

The final objective of our project is to perform a virtual surgical simulation of the whole endovascular stent graft procedure for the patient-specific AD model. This procedure has a high rate of short-term success, and its indication compared to open surgery is increasing. Despite many benefits (reduced blood loss, reduced recovery time), hindsight is insufficient and has limitations related to complex anatomical configurations. This procedure, therefore, needs to be more reliable and secure. In this context, it is essential to identify the mechanical behavior of the aorta for further numerical simulations. This approach is part of a computer-aided design project for surgical procedures. It needs accurate tools/tissue interaction, including blood behavior simulations (CFD & FSI), to suggest a realistic customized solution for a proper deployment system and a suitable stent recommendation.

This research effort explored simplifying the numerical modeling of the whole endovascular process for treating the AD pathology model. These simplifications first concern the global mechanical characterization of the artery with a hyperelastic and isotropic law. However, there exists research that has led to many anisotropic hyperelastic models (Gültekin et al., 2019). Also, numerical models do not account for the thrombus behavior (Yazdani et al., 2018) and also the motion of RBCs. The porous-hyperelastic and viscoelastic behavior of thrombus requires further investigation on the effect of vascular disease.

In addition, for the complete modeling of the endovascular treatment, it is necessary to address the stent graft deployment in a thoracic aorta with AD pathology, for which numerical simulations have not been performed in this thesis work. However, the work performed at LaMCoS (Altnji et al., 2015) has allowed us to advance in this field by considering the hyperelastic mechanical behavior of the aortic wall and the stent-graft assembly. This assembly includes modeling the fabric performing the sealing of the stent and the metal part with superelastic and shape mechanical memory behavior, allowing the stent to recover its initial shape and adapt to the shape of the vessel. These simulations are illustrated in Figure 4.35 and show the gradual and realistic deployment of the stent when the surgeon removes the catheter. Our aim is to perform the same process for the aortic dissection and validate with MRI.

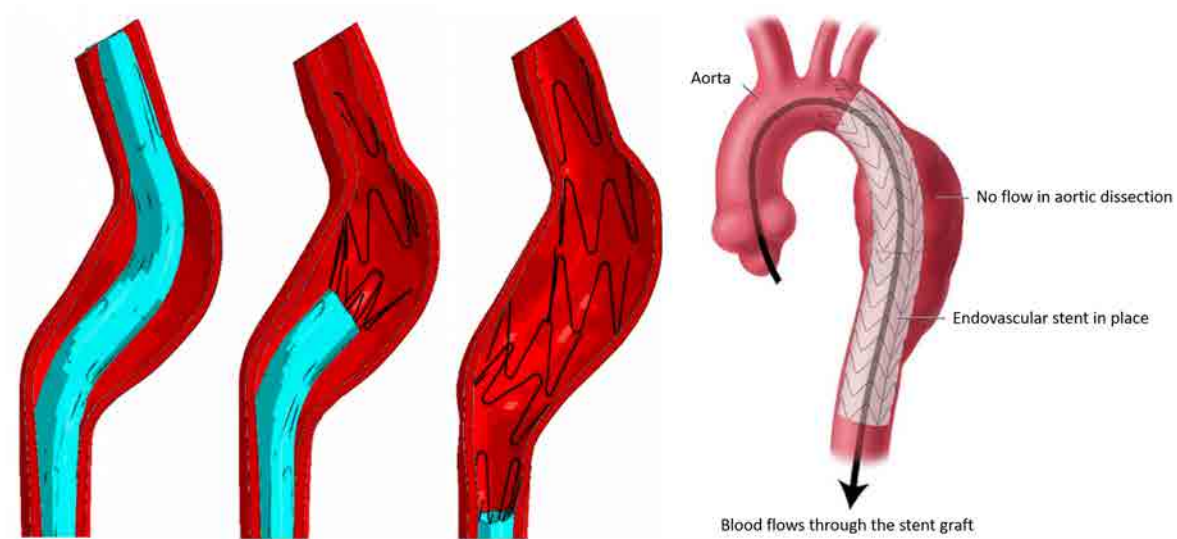


Figure 4.35: Progressive and realistic deployment of a stent (adapted from [Altınji et al. \(2015\)](#))

In the future, simulations of AD pathology, with the most appropriate conditions as possible, could be used to analyze patient-specific AD model and assess whether they should be treated or not. In this sense, we opted to develop all the numerical steps with free and open-source software. This choice has several positive consequences:

1. If needed – since the source code of the applications used is publicly available –improvements and their implementation within the software can be made by any user with the ability to do it;
2. If someone wishes to follow the same approach, it only needs to download and use it, accelerating the process of improving the results and repeatability;
3. The whole methodology can be performed without commercial complications (interoperability).

Poiseuille flow adapted to a non-circular face

A.1 Methodology

To apply a Poiseuille flow profile to a non-circular surface, the method described in the work of [Mynard and Nithiarasu \(2008\)](#) was applied to the geometric data of the model. The 3D velocity profile is plotted on the 2D inlet surface of the aorta. If the inlet were perfectly circular, then each mesh center could be assigned a velocity for each time step as a function of the radial distance r where it is located (equation 3.6). However, the input surface is generally not circular, and the velocities assigned to each mesh center are more complex. Figure A.1 illustrates the method applied to the entry surface of the aorta.

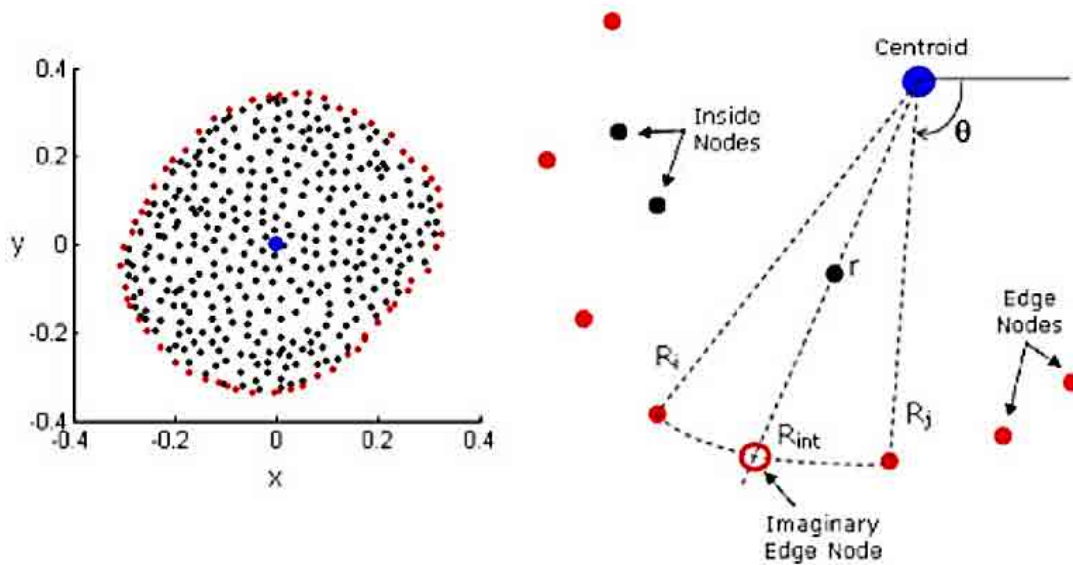


Figure A.1: A diagram illustrating how to transfer a radial velocity profile onto the nodes of a 2D boundary surface ([Mynard and Nithiarasu, 2008](#))

The method applied to the aortic entry surface to plot velocities involves five steps:

1. First, the centers of the meshes on the surface contour must be identified and isolated from the other surrounding elements. The center of these meshes has a velocity value assigned to 0 to respect the condition of no-slip at the walls, meaning that the fluid velocity at the walls is the same as that of the wall.
2. It is a matter of determining the center of the surface, computed as the average of values in

x and y , and moving all the points (which are the centers of meshes) so that this center is located at coordinates $(0, 0)$.

3. Then it is necessary to express the positions of all the points in 2D polar coordinates (r, θ) . The third coordinate is supposed to be constant on the whole input surface.
4. Next, we need to compute a normalized radius for each interior point. This radius is calculated by first identifying the two points on the contour with the closest θ values. From the radii of these two points on the outline (R_i and R_j), an interpolated radius R_{int} of an imaginary point of the contour is computed. This fictitious point is on the same line that connects the interior point to the center of the surface.
5. Based on the radius of the imaginary point of the contour, the normalized radius (r_n) of the interior point can be calculated as $r_n = r/R_{int}$ and the appropriate velocity can be associated with this point.

A.2 Matlab[®] Code

The Matlab[®] code below allows adapting a Poiseuille profile to a non-circular surface for OpenFOAM or FOAM-Extend (The function for calculation the ratio is from the work of [Menut \(2017\)](#)).

```

1 clear all
2 close all
3 clc
4 addpath donnees
5 addpath fonctions
6
7 %%%%%%%%%%%%%%%%%%%%%%%%%%%%%%%%%%%%%%%%%%%%%%%%%%%%%%%%%%%%%%%%%%%%%%%%%
8 %      DATA IMPORT      %
9 %%%%%%%%%%%%%%%%%%%%%%%%%%%%%%%%%%%%%%%%%%%%%%%%%%%%%%%%%%%%%%%%%%%%%%%%%
10
11 faceCentres=importdata('faceCentres_AD_poly');
12 faceCentres(:,3)=0;
13 cycle=load('7cycles_AD1.txt');
14 cycle(:,2)=cycle(:,2)*0.01*2; % Conversion of speeds in m/s
15 cycle(:,1)=cycle(:,1)*0.001; % Conversion of time in s
16
17
18 %%%%%%%%%%%%%%%%%%%%%%%%%%%%%%%%%%%%%%%%%%%%%%%%%%%%%%%%%%%%%%%%%%%%%%%%%
19 % RATIO CALCULATION Rn = R / Rint %
20 %%%%%%%%%%%%%%%%%%%%%%%%%%%%%%%%%%%%%%%%%%%%%%%%%%%%%%%%%%%%%%%%%%%%%%%%%
21 %Function for calculating the ratio Rn
22 [Rn,faceCentres,centroid,EN,Rint,coord]=extraction_wenyang(faceCentres);
23
24 % verification trace

```

```

25 figure(1)
26 plot3(faceCentres(:,1),faceCentres(:,2), Rn(:,1), '.b','MarkerSize',3)
27 hold on
28 plot3(centroid(:,1),centroid(:,2), centroid(:,3), 'or')
29 hold on
30 plot3(EN(:,1),EN(:,2),EN(:,3),'.g')
31 axis equal
32 view([0 0 1])
33
34 load('MyColormaps','mycmap')
35 mkdir('constant/boundaryData/velocity_inlet/')
36 cd('constant/boundaryData/velocity_inlet/')
37
38
39 for i=1:length(cycle)
40 Vit=cycle(i,2)*(1-(coord(:,2).^2./Rint(:,1).^2)); %parabolique
41
42 VectVit(:,1)=-Vit*vecteur(1,1);
43 VectVit(:,2)=-Vit*vecteur(1,2);
44 VectVit(:,3)=-Vit*vecteur(1,3);
45
46 x=faceCentres(:,1);
47 y=faceCentres(:,2);
48 z=Vit;
49
50 % 3D trace
51 figure(4)
52 tri = delaunay(x,y);
53 % trisurf(tri,x,y,z,'LineStyle','none');
54 trisurf(tri,x,y,z);
55 axis([-0.02 0.02 -0.02 0.02 -0.3 1])
56 % view([1 0 0])
57
58 colormap(mycmap)
59
60 %%%%%%%%%%%%%%%%%%%%%%%%%%%%%%%%%%%%%%%%%%%%%%%%%%%%%%%%%%%%%%%%%%%%%%%%%
61
62 %%% ECRITURE
63
64 if i==1
65     mkdir(sprintf('%i',cycle(i,1))); % create the file
66 else
67     mkdir(sprintf('%1.3f',cycle(i,1))); % create the file

```

Cette thèse est accessible à l'adresse : <http://theses.insa-lyon.fr/publication/2021LYSEI075/these.pdf>
© [W. Pan], [2021], INSA Lyon, tous droits réservés

Implementation of the model with rigid walls in OpenFOAM

U

```

1  /*-----*-- C++ --*-----*\
2  | ===== |
3  | \ \      / F ield      | OpenFOAM: The Open Source CFD Toolbox |
4  | \ \      / O peration  | Version: 2.3.0                        |
5  | \ \ /    A nd          | Web:      www.OpenFOAM.org            |
6  |  \ \ /    M anipulation |                                     |
7  \*-----*--*/
8  FoamFile
9  {
10     version      2.0;
11     format        ascii;
12     class         volVectorField;
13     object        U;
14 }
15 // *****
16
17 dimensions      [0 1 -1 0 0 0 0];
18
19 internalField    uniform (0 0 0);
20
21 boundaryField
22 {
23     velocity_inlet
24     {
25         type      timeVaryingMappedFixedValue;
26         offset     (0 0 0);
27         setAverage  off;
28     }
29
30     arterialwall

```

```

31     {
32         type          fixedValue;
33         value          uniform (0 0 0);
34     }
35
36     outlet_thoracic
37     {
38         type          pressureInletOutletVelocity;
39         value          uniform (0 0 0);
40
41     }
42
43     outlet_brachio
44     {
45         type          pressureInletOutletVelocity;
46         value          uniform (0 0 0);
47     }
48
49     outlet_carotid
50     {
51         type          pressureInletOutletVelocity;
52         value          uniform (0 0 0);
53     }
54
55     outlet_subclavian
56     {
57         type          pressureInletOutletVelocity;
58         value          uniform (0 0 0);
59     }
60 }
61
62 // ***** //

```

p

```

1  /*-----*- C++ -*-----*\
2  | ===== | |
3  | \ \ / F i e l d | OpenFOAM: The Open Source CFD Toolbox |
4  | \ \ / O p e r a t i o n | Version: 2.3.1 |
5  | \ \ / A n d | Web: www.OpenFOAM.org |
6  | \ \ / M a n i p u l a t i o n | |
7  /*-----*- */
8  FoamFile
9  {

```

```

10     version    2.0;
11     format      ascii;
12     class       volScalarField;
13     object      p;
14 }
15 // * * * * *
16
17 dimensions     [0 2 -2 0 0 0 0];
18
19 internalField   uniform 0;
20
21 boundaryField
22 {
23     velocity_inlet
24     {
25         type      zeroGradient;
26     }
27
28     arterialWall
29     {
30         type      zeroGradient;
31     }
32
33     outlet_thoracic
34     {
35         type      ImpedanceBC;
36         R1        1.5443e+4;
37         R2        2.6032e+5;
38         C         2.7742e-6;
39         p0        0;
40     }
41
42     outlet_brachio
43     {
44         type      ImpedanceBC;
45         R1        5.2500e+4;
46         R2        8.3366e+5;
47         C         8.6334e-7;
48         p0        0;
49     }
50
51     outlet_carotid
52     {

```

```

53         type            ImpedanceBC;
54         R1               1.4700e+5;
55         R2               2.3203e+6;
56         C                3.1003e-7;
57         p0               0;
58     }
59     outlet_subclavian
60     {
61         type            ImpedanceBC;
62         R1               7.1985e+4;
63         R2               1.2135e+6;
64         C                5.9511e-7;
65         p0               0;
66     }
67
68
69 }
70
71 // *****

```

transportProperties

```

1  /*-----*- C++ -*-----*\
2  | ===== |
3  | \ \      / F i e l d      | OpenFOAM: The Open Source CFD Toolbox |
4  | \ \      / O p e r a t i o n | Version: 2.3.0 |
5  |  \ \ /   A n d              | Web:      www.OpenFOAM.org |
6  |   \ \ /   M a n i p u l a t i o n | |
7  \*-----*-
8  FoamFile
9  {
10     version    2.0;
11     format      ascii;
12     class       dictionary;
13     location     "constant";
14     object       transportProperties;
15 }
16 // *****
17
18 transportModel Newtonian;
19
20 nu              nu [0 2 -1 0 0 0 0] 3.30189e-6;
21
22

```

23

24 `// ***** //`

RASProperties

```

1  /*-----* C++ *-----*\
2  | ===== |
3  | \ \ / F i e l d | OpenFOAM: The Open Source CFD Toolbox |
4  | \ \ / O p e r a t i o n | Version: 2.3.0 |
5  | \ \ / A n d | Web: www.OpenFOAM.org |
6  | \ \ / M a n i p u l a t i o n | |
7  \*-----*\
8  FoamFile
9  {
10     version    2.0;
11     format      ascii;
12     class       dictionary;
13     location     "constant";
14     object       RASProperties;
15 }
16 // ***** //
17
18 RASModel        laminar;
19
20 turbulence       off;
21
22 printCoeffs      off;
23
24
25 // ***** //

```

turbulenceProperties

```

1  /*-----* C++ *-----*\
2  | ===== |
3  | \ \ / F i e l d | OpenFOAM: The Open Source CFD Toolbox |
4  | \ \ / O p e r a t i o n | Version: 2.3.0 |
5  | \ \ / A n d | Web: www.OpenFOAM.org |
6  | \ \ / M a n i p u l a t i o n | |
7  \*-----*\
8  FoamFile
9  {
10     version    2.0;
11     format      ascii;

```

```

12     class      dictionary;
13     location   "constant";
14     object     turbulenceProperties;
15 }
16 // * * * * *
17
18 simulationType RASModel;
19
20 // *****

controlDict

1 /*-----*- C++ -*-----*\
2 | ===== |
3 | \ \      / F i e l d      | OpenFOAM: The Open Source CFD Toolbox |
4 | \ \      / O p e r a t i o n | Version: 2.3.0 |
5 | \ \      / A n d      | Web: www.OpenFOAM.org |
6 | \ \      / M a n i p u l a t i o n | |
7 \*-----*-*/
8 FoamFile
9 {
10     version     2.0;
11     format       ascii;
12     class        dictionary;
13     location     "system";
14     object        controlDict;
15 }
16 // * * * * *
17
18 application     pimpleFoam;
19
20 startFrom        startTime;
21
22 startTime        0;
23
24 stopAt           endTime;
25
26 endTime          6.5;
27
28 deltaT           0.0001;
29
30 writeControl     adjustableRunTime;
31
32 writeInterval    0.01;

```

```

33
34 purgeWrite      0;
35
36 writeFormat      ascii;
37
38 writePrecision 6;
39
40 writeCompression off;
41
42 timeFormat        general;
43
44 timePrecision 6;
45
46 runTimeModifiable yes;
47
48 adjustTimeStep no;
49
50 libs ("libImpedanceBC.so");
51
52 // ***** //
53 functions
54 {
55     probes
56     {
57         type          probes;
58         functionObjectLibs ("libsampling.so");
59         enabled        true;
60         outputControl  timeStep; //outputTime;
61         outputInterval 1;
62
63         fields
64         (
65             p
66             U
67         );
68
69         probeLocations
70         (
71             (-0.0127 -0.0602 -0.953) //velocity_inlet
72             (-0.000849 -0.0399 -0.878) // outlet_carotide
73             (-0.0117 -0.039 -0.885) //outlet_brachio
74             (0.0132 -0.0347 -0.878) //outlet_subclavian
75             (0.0304 -0.0339 -1.20) //outlet_thoracic

```

```

76         );
77
78     }
79 }
80
81 functions
82 {
83     massFlow
84     {
85         type patchMassFlow;
86         functionObjectLibs
87         (
88             "libsimpleFunctionObjects.so"
89         );
90         verbose true;
91         outputControl timeStep;
92         outputControlMode timeStep;
93         outputInterval 1;
94         patches
95         (
96             velocity_inlet
97             outlet_carotide2
98             outlet_carotide
99             outlet_claviere
100            outlet_thoracic
101        );
102        factor 1.0;
103    }
104 };

```

fvSchemes

```

1  /*-----*-- C++ --*-----*\
2  | ===== |
3  | \ \      / F i e l d      | OpenFOAM: The Open Source CFD Toolbox |
4  | \ \      / O p e r a t i o n | Version: 2.3.0 |
5  | \ \ /    A n d              | Web:      www.OpenFOAM.org |
6  |  \ \ /    M a n i p u l a t i o n | |
7  /*-----*-----*/
8  FoamFile
9  {
10     version    2.0;
11     format      ascii;
12     class       dictionary;

```

```

13     location    "system";
14     object      fvSchemes;
15 }
16 // * * * * *
17
18 ddtSchemes
19 {
20     default      Euler;
21 }
22
23 gradSchemes
24 {
25     default      Gauss linear;
26 }
27
28 divSchemes
29 {
30     default      none;
31     div(phi,U)    bounded Gauss upwind;
32     div(phi,k)    bounded Gauss upwind;
33     div(phi,epsilon) bounded Gauss upwind;
34     div(phi,R)    bounded Gauss upwind;
35     div(R)        Gauss linear;
36     div(phi,nuTilda) bounded Gauss upwind;
37     div((nuEff*dev(T(grad(U)))) Gauss linear;
38 }
39
40 laplacianSchemes
41 {
42     default      Gauss linear corrected;
43 }
44
45 interpolationSchemes
46 {
47     default      linear;
48 }
49
50 snGradSchemes
51 {
52     default      corrected;
53 }
54
55 fluxRequired

```

```

56 {
57     default      no;
58     p            ;
59 }
60
61
62 // ***** //

fvSolution

1 /*----- C++ -----*\
2 | ===== |
3 | \\      / F i e l d | OpenFOAM: The Open Source CFD Toolbox |
4 | \\      / O p e r a t i o n | Version: 2.3.0 |
5 | \\      / A n d | Web: www.OpenFOAM.org |
6 | \\      / M a n i p u l a t i o n | |
7 /*-----*/
8 FoamFile
9 {
10     version      2.0;
11     format        ascii;
12     class         dictionary;
13     location      "system";
14     object        fvSolution;
15 }
16 // ***** //
17
18 solvers{
19     p
20     {
21         solver      GAMG;
22         tolerance    1e-06;
23         relTol       0.01;
24         smoother     GaussSeidel;
25         cacheAgglomeration true;
26         nCellsInCoarsestLevel 10;
27         agglomerator  faceAreaPair;
28         mergeLevels   1;
29     }
30
31     pFinal
32     {
33         solver      GAMG;
34         tolerance    1e-06;

```

```

35     relTol      0;
36     smoother    GaussSeidel;
37     cacheAgglomeration true;
38     nCellsInCoarsestLevel 10;
39     agglomerator  faceAreaPair;
40     mergeLevels   1;
41 }
42
43 U
44 {
45     solver        PBiCG;
46     preconditioner DILU;
47     tolerance      1e-05;
48     relTol         0.1;
49 }
50
51 UFinal
52 {
53     $U;
54     tolerance      1e-05;
55     relTol         0;
56 }
57 tau
58 {
59     solver          PBiCG;
60     preconditioner   DILU;
61     tolerance        1e-06;
62     relTol           0.0;
63     maxIter          1000;
64 }
65 }
66
67 SIMPLE
68 {
69     nNonOrthogonalCorrectors 2;
70
71     residualControl
72     {
73         p          1e-4;
74         U          1e-4;
75         tau        1e-4;
76     }
77 }

```

```

78
79 PIMPLE
80 {
81     nOuterCorrectors 100;
82     nCorrectors 2;
83     nNonOrthogonalCorrectors 4;
84     pRefCell 0;
85     pRefValue 0;
86
87 residualControl
88     {
89         U
90         {
91             tolerance 1e-3;
92             relTol 0;
93         }
94
95         p
96         {
97             tolerance 1e-3;
98             relTol 0;
99         }
100        tau
101        {
102            tolerance 1e-3;
103            relTol 0;
104        }
105    }
106
107 }
108
109 PISO
110 {
111     nCorrectors 2;
112     nNonOrthogonalCorrectors 3;//2
113     pRefCell 0;
114     pRefValue 0;
115 }
116
117 relaxationFactors
118 {
119     fields
120     {

```

```
121     }
122     equations
123     {
124         "U.*"          1;
125     }
126     tau                0.3;
127 }
128
129
130 // ***** //
```

Implementation of the model with FSI in FOAM-Extend

C.1 Fluid domain

The principal fluid files are identical to those in Appendix B. The addition files below provide definitions for fluid-structure interaction in FOAM-Extend.

createZones

```

1  #!/bin/sh
2
3  # Source tutorial run functions
4
5  . $WM_PROJECT_DIR/bin/tools/RunFunctions
6
7  runApplication setSet -batch setBatch
8  runApplication setsToZones -noFlipMap

```

setBatch

```

1  faceSet wall-zone new patchToFace fluid.wall
2  quit

```

decomposePar

```

1  /*-----* C++ -*-----*\
2  | ===== |
3  | \ \ / F i e l d | foam-extend: Open Source CFD |
4  | \ \ / O p e r a t i o n | Version: 4.0 |
5  | \ \ / A n d | Web: http://www.foam-extend.org |
6  | \ \ / M a n i p u l a t i o n | |
7  /*-----*/
8  FoamFile
9  {

```

```

10     version    2.0;
11     format      ascii;
12     class       dictionary;
13     object      fvSchemes;
14 }
15 // * * * * *
16
17 numberOfSubdomains 20;
18
19 method          hierarchical;
20
21 simpleCoeffs
22 {
23     n              (1 1 20);
24     delta          0.001;
25 }
26
27 hierarchicalCoeffs
28 {
29     n              (1 1 20);
30     delta          0.001;
31     order          xyz;
32 }
33
34 manualCoeffs
35 {
36     dataFile       "";
37 }
38
39 distributed      no;
40
41 roots            ( );
42
43
44 // *****

```

p

```

1  /*----- C++ -----*\
2  | ===== |
3  |  \ \      /  F i e l d      | foam-extend: Open Source CFD |
4  |  \ \      /  O p e r a t i o n  | Version: 4.0 |
5  |   \ \ /    A n d      | Web: http://www.foam-extend.org |
6  |    \ \ /    M a n i p u l a t i o n  |

```

```

7  \*-----*/
8  FoamFile
9  {
10     version      2.0;
11     format        ascii;
12     class         dictionary;
13     object        fvSchemes;
14 }
15 // *****
16
17 dimensions      [0 2 -2 0 0 0 0];
18
19 internalField uniform 0;
20
21 boundaryField
22 {
23     fluid.wall
24     {
25         type      zeroGradient;
26     }
27     fluid.inlet
28     {
29         type      zeroGradient;
30     }
31     fluid.brachio
32     {
33         type      ImpedanceBC;
34         Rp        5.2500e+4;
35         Rd        8.3366e+5;
36         C         8.6334e-7;
37         Pout      0;
38         value     uniform 12.2744;
39     }
40     fluid.carotid
41     {
42         type      ImpedanceBC;
43         Rp        1.4700e+5;
44         Rd        2.3203e+6;
45         C         3.1003e-7;
46         Pout      0;
47         value     uniform 12.2625;
48     }
49     fluid.sub

```

```

50     {
51         type            ImpedanceBC;
52         Rp              7.1985e+4;
53         Rd              1.2135e+6;
54         C               5.9511e-7;
55         Pout            0;
56         value           uniform 12.2625;
57     }
58     fluid.outlet
59     {
60         type            ImpedanceBC;
61         Rp              1.5443e+4;
62         Rd              2.6032e+5;
63         C               2.7742e-6;
64         Pout            0;
65         value           uniform 12.3642;
66     }
67 }
68
69
70 // *****

```

transportProperties

```

1  /*-----* C++ -*-----*\
2  | ===== | |
3  | \ \      / F ield      | foam-extend: Open Source CFD |
4  | \ \      / O peration  | Version:      4.0             |
5  | \ \      / A nd        | Web:          http://www.foam-extend.org |
6  |  \ \     \/ M anipulation | |
7  \*-----*/
8  FoamFile
9  {
10     version    2.0;
11     format     ascii;
12     class      dictionary;
13     object     transportProperties;
14
15 }
16 // *****
17 transportModel Newtonian;
18 nu              nu [0 2 -1 0 0 0 0] 3.30189e-6;
19
20 rho            rho [1 -3 0 0 0 0 0] 1060;

```

```

21
22 // *****

fsiProperties

1  /*-----*-- C++ --*-----*\
2  | ===== |
3  | \\ / F i e l d | foam-extend: Open Source CFD |
4  | \\ / O p e r a t i o n | Version: 4.0 |
5  | \\ / A n d | Web: http://www.foam-extend.org |
6  | \\ / M a n i p u l a t i o n | |
7  \*-----*--*/
8  FoamFile
9  {
10     version 2.0;
11     format ascii;
12     class dictionary;
13     object flowProperties;
14 }
15 // *****

16
17 solidPatch solid.in;
18 solidZone inner-wall-zone;
19
20 fluidPatch fluid.wall;
21 fluidZone wall-zone;
22
23 relaxationFactor 0.01;
24
25 interfaceDeformationLimit 0;
26
27 outerCorrTolerance 1e-5;
28 nOuterCorr 200;
29
30 interpolatorUpdateFrequency 0;
31
32
33 couplingScheme Aitken;
34
35 couplingReuse 0;
36
37 coupled yes;
38 predictor yes;
39

```

```

40 // *****

fluidProperties

1 /*-----*- C++ -*-----*\
2 | ===== |
3 | \ \ / F i e l d | foam-extend: Open Source CFD |
4 | \ \ / O p e r a t i o n | Version: 3.0 |
5 | \ \ / A n d | Web: http://www.extend-project.de |
6 | \ \ / M a n i p u l a t i o n | |
7 /*-----*-
8 FoamFile
9 {
10     version 2.0;
11     format ascii;
12     class dictionary;
13     object flowProperties;
14 }
15 // *****
16
17 fluidSolver pisoFluid;
18
19 pisoFluidCoeffs
20 {
21     nCorrectors 20;
22     nNonOrthogonalCorrectors 4;
23 }
24
25
26
27 // *****

dynamicMeshDict

1 /*-----*- C++ -*-----*\
2 | ===== |
3 | \ \ / F i e l d | foam-extend: Open Source CFD |
4 | \ \ / O p e r a t i o n | Version: 4.0 |
5 | \ \ / A n d | Web: http://www.foam-extend.org |
6 | \ \ / M a n i p u l a t i o n | |
7 /*-----*-
8 FoamFile
9 {
10     version 2.0;

```

```

11     format      ascii;
12     class       dictionary;
13     object      dynamicMeshDict;
14 }
15 // * * * * *
16
17 dynamicFvMesh dynamicMotionSolverFvMesh;
18
19 solver velocityLaplacian;
20 diffusivity quadratic inverseDistance 1(fluid.wall);
21
22 nNonOrthogonalCorrectors 2;
23 leastSquaresVolPoint yes;
24
25
26 // *****

fvSchemes

1 /*----- C++ -----*\
2 | ===== |
3 | \ \ / F i e l d | foam-extend: Open Source CFD |
4 | \ \ / O p e r a t i o n | Version: 4.0 |
5 | \ \ / A n d | Web: http://www.foam-extend.org |
6 | \ \ / M a n i p u l a t i o n | |
7 /*-----*/
8 FoamFile
9 {
10     version      2.0;
11     format      ascii;
12     class       dictionary;
13     object      fvSchemes;
14 }
15 // * * * * *
16
17 ddtSchemes
18 {
19     default      Euler;
20 }
21
22 gradSchemes
23 {
24     default      Gauss linear;
25     grad(p)      Gauss linear;

```

```

26     grad(U)          cellLimited Gauss linear 0.333;
27 }
28
29 divSchemes
30 {
31     default          none;
32     div(phi,U)       Gauss Upwind grad(U);
33     div(phi,omega)   Gauss linear;
34     div(phi,nuTilda) Gauss limitedLinear 1;
35     div(phi,k)       Gauss linear;
36     div((nuEff*dev(T(grad(U))))) Gauss linear;
37 }
38
39 laplacianSchemes
40 {
41     default          Gauss linear corrected;
42 }
43
44 interpolationSchemes
45 {
46     default          linear;
47 }
48
49 snGradSchemes
50 {
51     default          corrected;
52 }
53
54 fluxRequired
55 {
56     default          no;
57     p                ;
58 }
59
60
61 // ***** //

fvSolution

1  /*-----* C++ *-----*\
2  | ===== |
3  | \ \      / F ield      | foam-extend: Open Source CFD |
4  | \ \      / O peration  | Version:      4.0           |
5  | \ \      / A nd         | Web:          http://www.foam-extend.org |

```

```

6 |  \ \ /      M anipulation |
7 \*-----*/
8 FoamFile
9 {
10     version      2.0;
11     format        ascii;
12     class         dictionary;
13     object        fvSolution;
14 }
15 // * * * * *
16
17 solvers
18 {
19     p
20     {
21         solver      GAMG;
22         tolerance    1e-10;
23         relTol       0.0000001;
24         minIter      1;
25         maxIter      300;
26         smoother     GaussSeidel;
27         nPreSweeps    0;
28         nPostSweeps   2;
29         nFinestSweeps 2;
30         scaleCorrection true;
31         directSolveCoarsest false;
32         cacheAgglomeration true;
33         nCellsInCoarsestLevel 20;
34         agglomerator  faceAreaPair;
35         mergeLevels   1;
36     }
37
38     pFinal
39     {
40         solver      GAMG;
41         tolerance    1e-10;
42         minIter      1;
43         maxIter      300;
44         smoother     GaussSeidel;
45         nPreSweeps    0;
46         nPostSweeps   2;
47         nFinestSweeps 2;
48         scaleCorrection true;

```

```

49     directSolveCoarsest false;
50     cacheAgglomeration true;
51     nCellsInCoarsestLevel 20;
52     agglomerator faceAreaPair;
53     mergeLevels 1;
54 }
55
56 cellMotionU
57 {
58     solver GAMG;
59     tolerance 1e-06;
60     relTol 0.0001;
61     minIter 1;
62     maxIter 100;
63     smoother GaussSeidel;
64     nPreSweeps 0;
65     nPostSweeps 2;
66     nFinestSweeps 2;
67     scaleCorrection true;
68     directSolveCoarsest false;
69     cacheAgglomeration true;
70     nCellsInCoarsestLevel 20;
71     agglomerator faceAreaPair;
72     mergeLevels 1;
73 }
74
75 U
76 {
77     solver PBiCG;
78     preconditioner DILU;
79     tolerance 1e-12;
80     relTol 0.0001;
81     minIter 1;
82 }
83 UFinal
84 {
85     solver PBiCG;
86     preconditioner DILU;
87     tolerance 1e-12;
88     relTol 0;
89     minIter 1;
90 }
91 }

```

92

93 `// ***** //`

C.2 Solid domain

setBatch

```
1 faceSet inner-wall-zone new patchToFace solid.in
2 quit
```

createZones

```
1 #!/bin/sh
2
3 # Source tutorial run functions
4
5 . $WM_PROJECT_DIR/bin/tools/RunFunctions
6
7 runApplication setSet -batch setBatch
8 runApplication setsToZones -noFlipMap
```

controlDict

```
1 /*-----* C++ *-----*\
2 | ===== |
3 | \ \ / F i e l d | foam-extend: Open Source CFD |
4 | \ \ / O p e r a t i o n | Version: 4.0 |
5 | \ \ / A n d | Web: http://www.foam-extend.org |
6 | \ \ / M a n i p u l a t i o n | |
7 /*-----*/
8 FoamFile
9 {
10     version    2.0;
11     format      ascii;
12     class       dictionary;
13     object       controlDict;
14 }
15 // ***** //
16
17 application    stressFoam;
18
19 startFrom       latestTime;
20
21 startTime       0;
```

```

22
23 stopAt      endTime;
24
25 endTime     6;
26
27 deltaT      1e-5;
28
29 writeControl  timeStep;
30
31 writeInterval 100;
32
33 purgeWrite   0;
34
35 writeFormat  ascii;
36
37 writePrecision 6;
38
39 writeCompression uncompressed;
40
41 timeFormat   general;
42
43 timePrecision 6;
44
45 runTimeModifiable yes;
46
47 adjustTimeStep no;
48
49 maxCo        0.2;
50
51
52 // ***** //

decomposePar

1  /*-----*-- C++ --*-----*\
2  | ===== |
3  |  \ \      /  F ield      | foam-extend: Open Source CFD |
4  |  \ \      /  O peration  | Version:      4.0             |
5  |   \ \ /    A nd          | Web:          http://www.foam-extend.org |
6  |    \ \ /    M anipulation | |
7  \*-----*-----*/
8  FoamFile
9  {
10     version      2.0;

```

```

11     format      ascii;
12     class       dictionary;
13     object      decomposeParDict;
14 }
15 // * * * * *
16
17 numberOfSubdomains 20;
18
19
20 method          hierarchical;
21
22 globalFaceZones ( inner-wall-zone );
23
24 simpleCoeffs
25 {
26     n              (1 1 20);
27     delta          0.001;
28 }
29
30 hierarchicalCoeffs
31 {
32     n              (1 1 20);
33     delta          0.001;
34     order          xyz;
35 }
36
37
38 manualCoeffs
39 {
40     dataFile       "";
41 }
42
43 distributed      no;
44
45 roots
46 (
47 );
48
49
50 // * * * * *

```

D

```

1  /*-----*-- C++ --*-----*\

```

```

2 | ===== |
3 | \\ / F i e l d | foam-extend: Open Source CFD |
4 | \\ / O p e r a t i o n | Version: 4.0 |
5 | \\ / A n d | Web: http://www.foam-extend.org |
6 | \\ / M a n i p u l a t i o n | |
7 |*-----*/
8 FoamFile
9 {
10     version 2.0;
11     format ascii;
12     class volVectorField;
13     location "0";
14     object D;
15 }
16 // ***** //
17
18 dimensions [0 1 0 0 0 0 0];
19
20 internalField uniform (0 0 0);
21
22 boundaryField
23 {
24     solid.inlet
25     {
26         type fixedValue;
27         value uniform (0 0 0);
28     }
29     solid.brachio
30     {
31         type fixedValue;
32         value uniform (0 0 0);
33     }
34     solid.carotid
35     {
36         type fixedValue;
37         value uniform (0 0 0);
38     }
39     solid.sub
40     {
41         type fixedValue;
42         value uniform (0 0 0);
43     }
44     solid.outlet

```

```

45     {
46         type          fixedValue;
47         value          uniform (0 0 0);
48     }
49     solid.out
50     {
51         type          tractionDisplacement;
52         traction      uniform ( 0 0 0 );
53         pressure      uniform 7.44;
54         value         uniform (0 0 0);
55     }
56     solid.in
57     {
58         type          tractionDisplacement;
59         traction      uniform ( 0 0 0 );
60         pressure      uniform 0;
61         value         uniform (0 0 0);
62     }
63 }
64
65
66 // ***** //

```

DD

```

1  /*-----*- C++ -*-----*\
2  | ===== |
3  | \\      / F i e l d      | foam-extend: Open Source CFD |
4  | \\      / O p e r a t i o n | Version: 4.0 |
5  | \\      / A n d      | Web: http://www.foam-extend.org |
6  |  \\     / M a n i p u l a t i o n | |
7  \*-----*/
8  FoamFile
9  {
10     version 2.0;
11     format  ascii;
12     class   volVectorField;
13     location "0";
14     object  DD;
15 }
16 // * * * * * //
17
18 dimensions [0 1 0 0 0 0 0];
19

```

```

20  internalField uniform (0 0 0);
21
22  boundaryField
23  {
24      solid.inlet
25      {
26          type          fixedValue;
27          value          uniform (0 0 0);
28      }
29      solid.brachio
30      {
31          type          fixedValue;
32          value          uniform (0 0 0);
33      }
34      solid.carotid
35      {
36          type          fixedValue;
37          value          uniform (0 0 0);
38      }
39      solid.sub
40      {
41          type          fixedValue;
42          value          uniform (0 0 0);
43      }
44      solid.outlet
45      {
46          type          fixedValue;
47          value          uniform (0 0 0);
48      }
49      solid.out
50      {
51          type          tractionDisplacementIncrement;
52          traction       uniform ( 0 0 0 );
53          pressure       uniform 7.44;
54          value          uniform (0 0 0);
55      }
56      solid.in
57      {
58          type          tractionDisplacementIncrement;
59          traction       uniform ( 0 0 0 );
60          pressure       uniform 0;
61          value          uniform (0 0 0);
62      }

```

```

63 }
64
65
66 // *****
pointD

1 /*-----* C++ -*-----*\
2 | ===== |
3 | \ \ / F i e l d | foam-extend: Open Source CFD |
4 | \ \ / O p e r a t i o n | Version: 4.0 |
5 | \ \ / A n d | Web: http://www.foam-extend.org |
6 | \ \ / M a n i p u l a t i o n | |
7 /*-----*\
8 FoamFile
9 {
10     version    2.0;
11     format      ascii;
12     class       pointVectorField;
13     object      pointD;
14 }
15 // *****
16
17 dimensions      [0 1 0 0 0 0 0];
18
19 internalField    uniform (0 0 0);
20
21 boundaryField
22 {
23     solid.inlet
24     {
25         type      fixedValue;
26         value      uniform (0 0 0);
27     }
28
29     solid.outlet
30     {
31         type      fixedValue;
32         value      uniform (0 0 0);
33     }
34
35     solid.carotid

```

```

38     {
39         type          fixedValue;
40         value          uniform (0 0 0);
41
42     }
43
44     solid.sub
45     {
46         type          fixedValue;
47         value          uniform (0 0 0);
48
49     }
50
51     solid.brachio
52     {
53         type          fixedValue;
54         value          uniform (0 0 0);
55
56     }
57
58     solid.in
59     {
60         type          calculated;
61         value          uniform (0 0 0);
62     }
63
64     solid.out
65     {
66         type          calculated;
67         value          uniform (0 0 0);
68
69     }
70
71 }
72
73 // *****

```

fvSchemes

```

1  /*-----* C++ *-----*\
2  | ===== |
3  | \ \      / F i e l d      | foam-extend: Open Source CFD |
4  | \ \      / O p e r a t i o n | Version: 4.0 |
5  | \ \      / A n d              | Web: http://www.foam-extend.org |

```

```

6 |  \ \ /   M anipulation |
7 | *-----* /
8 FoamFile
9 {
10     version    2.0;
11     format      ascii;
12     class       dictionary;
13     object      fvSchemes;
14 }
15 // * * * * *
16
17 d2dt2Schemes
18 {
19     default none;
20     d2dt2(D) Euler;
21     d2dt2(DD) Euler;
22 }
23
24 ddtSchemes
25 {
26     default none;
27     ddt(D) Euler;
28     ddt(DD) Euler;
29 }
30 }
31
32
33 gradSchemes
34 {
35     default none;
36 }
37
38 divSchemes
39 {
40     default none;
41 }
42
43 laplacianSchemes
44 {
45     default none;
46     laplacian(DD,D) Gauss linear skewCorrected 1;
47     laplacian(DDD,DD) Gauss linear skewCorrected 1;
48 }

```

```

49
50 snGradSchemes
51 {
52     default none;
53     snGrad(D) skewCorrected 1;
54     snGrad(DD) skewCorrected 1;
55 }
56
57 interpolationSchemes
58 {
59     default none;
60     interpolate(mu) linear;
61     interpolate(lambda) linear;
62 }
63
64 // ***** //

fvSolution

1  /*----- C++ -----*\
2  | ===== |
3  | \ \ / F i e l d | foam-extend: Open Source CFD |
4  | \ \ / O p e r a t i o n | Version: 4.0 |
5  | \ \ / A n d | Web: http://www.foam-extend.org |
6  | \ \ / M a n i p u l a t i o n | |
7  \*-----*/
8  FoamFile
9  {
10     version 2.0;
11     format ascii;
12     class dictionary;
13     object fvSolution;
14 }
15 // ***** //
16
17 solvers
18 {
19     D
20     {
21         solver GAMG;
22         tolerance 1e-12;
23         relTol 0;
24         minIter 1;
25         maxIter 1000;

```

```

26
27     smoother      GaussSeidel;
28     nPreSweeps     0;
29     nPostSweeps    2;
30     nFinestSweeps  2;
31
32     scaleCorrection true;
33     directSolveCoarsest false;
34
35     cacheAgglomeration true;
36
37     nCellsInCoarsestLevel 20;
38     agglomerator    faceAreaPair;
39     mergeLevels     1;
40 };
41
42 DD
43 {
44     solver          PCG;
45     preconditioner   DIC;
46     tolerance        1e-06;
47     relTol           0.01;
48 }
49 }
50
51
52
53 // ***** //

```

rheologyProperties

```

1  /*-----*- C++ -*-----*\
2  | ===== |
3  | \ \      / F i e l d      | foam-extend: Open Source CFD |
4  | \ \      / O p e r a t i o n | Version: 4.0 |
5  | \ \      / A n d             | Web: http://www.foam-extend.org |
6  | \ \      / M a n i p u l a t i o n | |
7  /*-----*- C++ -*-----*\
8  FoamFile
9  {
10     version      2.0;
11     format        ascii;
12     class         dictionary;
13     object        rheologyProperties;

```

```

14 }
15 // * * * * *
16
17 planeStress no;
18
19 rheology
20 {
21     type          linearElastic;
22     rho           rho [1 -3 0 0 0 0 0] 1200;
23     E             E   [1 -1 -2 0 0 0 0] 3e8;
24     nu           nu  [0 0 0 0 0 0 0] 0.3;
25 }
26
27 // * * * * *

```

solidProperties

```

1 /*-----* C++ *-----*\
2 | ===== |
3 | \ \      / F i e l d      | foam-extend: Open Source CFD |
4 | \ \      / O p e r a t i o n | Version: 4.0 |
5 | \ \      / A n d             | Web: http://www.foam-extend.org |
6 | \ \      / M a n i p u l a t i o n | |
7 \*-----*
8 FoamFile
9 {
10     version      2.0;
11     format        ascii;
12     class         dictionary;
13     object        solidProperties;
14 }
15 // * * * * *
16
17 solidSolver unsTotalLagrangianSolid;
18
19 unsTotalLagrangianSolidCoeffs
20 {
21     nCorrectors 500;
22
23     convergenceTolerance 1e-7;
24     relConvergenceTolerance 1e-3;
25
26     nonLinear off;
27     debug no;

```

```
28 }
29
30 unsIncrTotalLagrangianSolidCoeffs
31 {
32     nCorrectors 500;
33
34     convergenceTolerance 1e-7;
35     relConvergenceTolerance 1e-3;
36
37     nonLinear off;
38     debug no;
39 }
40
41 // ***** //
```

Bibliography

- (2021). Aortic dissection - Wikipedia. https://en.wikipedia.org/wiki/Aortic_dissectionCauses.39
- Abraham, F., Behr, M., and Heinkenschloss, M. (2005). Shape optimization in steady blood flow: a numerical study of non-newtonian effects. *Computer methods in biomechanics and biomedical engineering*, 8(2):127–137. 65
- Al Akhras, H., Elguedj, T., Gravouil, A., and Rochette, M. (2017). Towards an automatic isogeometric analysis suitable trivariate models generation—application to geometric parametric analysis. *Computer Methods in Applied Mechanics and Engineering*, 316:623–645. 104
- Alimohammadi, M., Sherwood, J. M., Karimpour, M., Agu, O., Balabani, S., and Díaz-Zuccarini, V. (2015). Aortic dissection simulation models for clinical support: fluid-structure interaction vs. rigid wall models. *Biomedical engineering online*, 14(1):1–16. 123, 142, 154
- Allen, B. D., Aouad, P. J., Burris, N. S., Rahsepar, A. A., Jarvis, K. B., François, C. J., Barker, A. J., Malaisrie, S. C., Carr, J. C., Collins, J. D., et al. (2019). Detection and hemodynamic evaluation of flap fenestrations in type b aortic dissection with 4d flow mri: comparison with conventional mri and ct angiography. *Radiology: Cardiothoracic Imaging*, 1(1):e180009. 61
- Altnji, H.-E., Bou-Saïd, B., and Walter-Le Berre, H. (2015). Morphological and stent design risk factors to prevent migration phenomena for a thoracic aneurysm: a numerical analysis. *Medical engineering & physics*, 37(1):23–33. 13, 28, 92, 192, 193
- Arthurs, C. J., Xiao, N., Moireau, P., Schaeffter, T., and Figueroa, C. A. (2020). A flexible framework for sequential estimation of model parameters in computational hemodynamics. *Advanced modeling and simulation in engineering sciences*, 7(1):1–37. 162
- Atkins, M. D., Black, J. H., and Cambria, R. P. (2006). Aortic dissection: perspectives in the era of stent-graft repair. *Journal of vascular surgery*, 43(2):A30–A43. 48, 189
- Avril, S., Badel, P., and Duprey, A. (2010). Anisotropic and hyperelastic identification of in vitro human arteries from full-field optical measurements. *Journal of biomechanics*, 43(15):2978–2985. 24, 80, 82
- Avril, S., Huntley, J. M., and Cusack, R. (2009). In vivo measurements of blood viscosity and wall stiffness in the carotid using pc-mri. *European Journal of Computational Mechanics/Revue Européenne de Mécanique Numérique*, 18(1):9–20. 53
- Azadani, A. N., Chitsaz, S., Matthews, P. B., Jaussaud, N., Leung, J., Tsinman, T., Ge, L., and Tseng, E. E. (2012). Comparison of mechanical properties of human ascending aorta and aortic sinuses. *The Annals of thoracic surgery*, 93(1):87–94. 82
- Baaijens, J., Van Steenhoven, A., and Janssen, J. (1993). Numerical analysis of steady generalized newtonian blood flow in a 2d model of the carotid artery bifurcation. *Biorheology*, 30(1):63–74. 66

- Babu, A. R., Byju, A. G., and Gundiah, N. (2015). Biomechanical properties of human ascending thoracic aortic dissections. *Journal of biomechanical engineering*, 137(8). 77, 79
- Balafas, G. (2014). Polyhedral mesh generation for cfd-analysis of complex structures. *Diplomityö. Münchenin teknillinen yliopisto*. 25, 105, 106
- Bank, A. J., Wang, H., Holte, J. E., Mullen, K., Shammass, R., and Kubo, S. H. (1996). Contribution of collagen, elastin, and smooth muscle to in vivo human brachial artery wall stress and elastic modulus. *Circulation*, 94(12):3263–3270. 68
- Bao, K., Lavrov, A., and Nilsen, H. M. (2017). Numerical modelling of non-newtonian fluid flow in fractures and porous media. In *ECMOR XV-15th European Conference on the Mathematics of Oil Recovery*, volume 21, pages 1313–1324. European Association of Geoscientists & Engineers. 23, 56
- Barton, I. E. (1998). Comparison of simple-and piso-type algorithms for transient flows. *International Journal for numerical methods in fluids*, 26(4):459–483. 99
- Basciano, C. and Kleinstreuer, C. (2009). Invariant-based anisotropic constitutive models of the healthy and aneurysmal abdominal aortic wall. *Journal of Biomechanical Engineering*, 131(2). 77, 79
- Baskurt, O. K., Hardeman, M. R., and Rampling, M. W. (2007). *Handbook of hemorheology and hemodynamics*, volume 69. IOS press. 57
- Baskurt, O. K. and Meiselman, H. J. (2003). Blood rheology and hemodynamics. In *Seminars in thrombosis and hemostasis*, volume 29, pages 435–450. Copyright© 2003 by Thieme Medical Publishers, Inc., 333 Seventh Avenue, New 57
- Bassiouny, H. S., Zarins, C. K., Kadowaki, M. H., Glagov, S., et al. (1994). Hemodynamic stress and experimental aortoiliac atherosclerosis. *Journal of vascular surgery*, 19(3):426–434. 117, 143, 190
- Bäumler, K., Vedula, V., Sailer, A. M., Seo, J., Chiu, P., Mistelbauer, G., Chan, F. P., Fischbein, M. P., Marsden, A. L., and Fleischmann, D. (2020). Fluid–structure interaction simulations of patient-specific aortic dissection. *Biomechanics and modeling in mechanobiology*, 19(5):1607–1628. 129, 142
- BECQUEMIN, J., KIRSCH, M., Canaud, L., and Kobeiter, H. (2010). Chirurgie de la crosse de l’aorte: conventionnelle, endoluminale ou hybride? une stratégie à la carte. *L’histoire*, 9(1/105):28. 49
- Bergel, D. (1961). The static elastic properties of the arterial wall. *The Journal of physiology*, 156(3):445–457. 76, 79, 82
- Biagini, E., Lofiego, C., Ferlito, M., Fattori, R., Rocchi, G., Graziosi, M., Lovato, L., di Diodoro, L., Cooke, R. M., Petracci, E., et al. (2007). Frequency, determinants, and clinical relevance of acute coronary syndrome-like electrocardiographic findings in patients with acute aortic syndrome. *The American journal of cardiology*, 100(6):1013–1019. 46
- Birjiniuk, J., Ruddy, J. M., Iffrig, E., Henry, T. S., Leshnower, B. G., Oshinski, J. N., Ku, D. N., and Veeraswamy, R. K. (2015). Development and testing of a silicone in vitro model of descending aortic dissection. *Journal of Surgical Research*, 198(2):502–507. 154

- Bonfanti, M., Balabani, S., Greenwood, J. P., Puppala, S., Homer-Vanniasinkam, S., and Díaz-Zuccarini, V. (2017). Computational tools for clinical support: a multi-scale compliant model for haemodynamic simulations in an aortic dissection based on multi-modal imaging data. *Journal of The Royal Society Interface*, 14(136):20170632. 62, 154, 162
- Bonfanti, M., Franzetti, G., Homer-Vanniasinkam, S., Díaz-Zuccarini, V., and Balabani, S. (2020). A combined in vivo, in vitro, in silico approach for patient-specific haemodynamic studies of aortic dissection. *Annals of Biomedical Engineering*, 48(12):2950–2964. 154, 177
- Boussel, L., Rayz, V., Martin, A., Acevedo-Bolton, G., Lawton, M. T., Higashida, R., Smith, W. S., Young, W. L., and Saloner, D. (2009). Phase-contrast magnetic resonance imaging measurements in intracranial aneurysms in vivo of flow patterns, velocity fields, and wall shear stress: comparison with computational fluid dynamics. *Magnetic Resonance in Medicine: An Official Journal of the International Society for Magnetic Resonance in Medicine*, 61(2):409–417. 102
- Box, F. M., van der Geest, R. J., Rutten, M. C., and Reiber, J. H. (2005). The influence of flow, vessel diameter, and non-newtonian blood viscosity on the wall shear stress in a carotid bifurcation model for unsteady flow. *Investigative radiology*, 40(5):277–294. 66
- Burattini, R. and Gnudi, G. (1982). Computer identification of models for the arterial tree input impedance: comparison between two new simple models and first experimental results. *Medical and Biological Engineering and Computing*, 20(2):134–144. 113
- Carew, T. E., Vaishnav, R. N., and Patel, D. J. (1968). Compressibility of the arterial wall. *Circulation research*, 23(1):61–68. 73
- Chen, C.-W., Tseng, Y.-H., Lin, C.-C., Kao, C.-C., Wong, M. Y., Ting, H., and Huang, Y.-K. (2021). Aortic dissection assessment by 4d phase-contrast mri with hemodynamic parameters: the impact of stent type. *Quantitative Imaging in Medicine and Surgery*, 11(2):490. 154
- Chen, H., Peelukhana, S., Berwick, Z., Kratzberg, J., Krieger, J., Roeder, B., Chambers, S., and Kassab, G. (2016). Editor’s choice—fluid–structure interaction simulations of aortic dissection with bench validation. *European Journal of Vascular and Endovascular Surgery*, 52(5):589–595. 175
- Cheng, D., Martin, J., Shennib, H., Dunning, J., Muneretto, C., Schueler, S., Von Segesser, L., Sergeant, P., and Turina, M. (2010). Endovascular aortic repair versus open surgical repair for descending thoracic aortic disease: a systematic review and meta-analysis of comparative studies. *Journal of the American College of Cardiology*, 55(10):986–1001. 44
- Chiastra, C., Morlacchi, S., Gallo, D., Morbiducci, U., Cárdenes, R., Larrabide, I., and Migliavacca, F. (2013). Computational fluid dynamic simulations of image-based stented coronary bifurcation models. *Journal of The Royal Society Interface*, 10(84):20130193. 160
- Chien, S. (1970). Shear dependence of effective cell volume as a determinant of blood viscosity. *Science*, 168(3934):977–979. 23, 59
- Chien, S. (1975). Biophysical behavior of red cells in suspensions. *The red blood cell*, 2:1031–1133. 57

- Chien, S., Dormandy, J. A., Ernst, E., and Matrai, A. (2012). *Clinical hemorheology: applications in cardiovascular and hematological disease, diabetes, surgery and gynecology*, volume 74. Springer Science & Business Media. 9–71. 55, 56
- Chien, S., Sung, K. L., Skalak, R., Usami, S., and Tözeren, A. (1978). Theoretical and experimental studies on viscoelastic properties of erythrocyte membrane. *Biophysical Journal*, 24(2):463–487. 58
- Chien, S. and Sung, L. A. (1987). Physicochemical basis and clinical implications of red cell aggregation. *Clinical Hemorheology and Microcirculation*, 7(1):71–91. 58
- Chien, S., Usami, S., Taylor, H. M., Lundberg, J. L., and Gregersen, M. I. (1966). Effects of hematocrit and plasma proteins on human blood rheology at low shear rates. *Journal of applied physiology*, 21(1):81–87. 23, 58, 60
- Chiu, J.-J. and Chien, S. (2011). Effects of disturbed flow on vascular endothelium: pathophysiological basis and clinical perspectives. *Physiological reviews*, 91(1):327–387. 15, 117, 143, 187, 190
- Chiu, P. and Miller, D. C. (2016). Evolution of surgical therapy for stanford acute type a aortic dissection. *Annals of cardiothoracic surgery*, 5(4):275. 22, 44
- Cho, Y. I. and Kensey, K. R. (1991). Effects of the non-newtonian viscosity of blood on flows in a diseased arterial vessel. part 1: Steady flows. *Biorheology*, 28(3-4):241–262. 65
- Claude, V. (2021). Anévrisme de l’aorte abdominale. <http://drclaudevaislic.com/anevrisme-de-laorte-abdominale/>. 37
- Clough, R. E., Waltham, M., Giese, D., Taylor, P. R., and Schaeffter, T. (2012). A new imaging method for assessment of aortic dissection using four-dimensional phase contrast magnetic resonance imaging. *Journal of vascular surgery*, 55(4):914–923. 160
- Clouse, W. D., Hallett, J. W., Schaff, H. V., Spittell, P. C., Rowland, C. M., Ilstrup, D. M., and Melton III, L. J. (2004). Acute aortic dissection: population-based incidence compared with degenerative aortic aneurysm rupture. In *Mayo Clinic Proceedings*, volume 79, pages 176–180. Elsevier. 39
- Criado, F. J. (2011). Aortic dissection: a 250-year perspective. *Texas Heart Institute Journal*, 38(6):694. 40
- Cross, M. M. (1965). Rheology of non-newtonian fluids: a new flow equation for pseudoplastic systems. *Journal of colloid science*, 20(5):417–437. 65
- Daily, P. O. (1970). Management of acute aortic dissections. *Ann Thorac Surg*, 10:237–247. 42
- Dake, M. D., Kato, N., Mitchell, R. S., Semba, C. P., Razavi, M. K., Shiono, T., Hirano, T., Takeda, K., Yada, I., and Miller, D. C. (1999). Endovascular stent-graft placement for the treatment of acute aortic dissection. *New England Journal of Medicine*, 340(20):1546–1552. 45
- De Bakey, M. E., Henly, W. S., Cooley, D. A., Morris Jr, G. C., Crawford, E. S., and Beall Jr, A. C. (1965). Surgical management of dissecting aneurysms of the aorta. *The Journal of thoracic and cardiovascular surgery*, 49(1):130–149. 42

- de Jong, P. A., Hellings, W. E., Takx, R. A., Išgum, I., van Herwaarden, J. A., and Mali, W. P. T. M. (2014). Computed tomography of aortic wall calcifications in aortic dissection patients. *PloS one*, 9(7):e102036. 24, 72, 142
- De Santis, G., De Beule, M., Van Canneyt, K., Segers, P., Verdonck, P., and Verhegghe, B. (2011). Full-hexahedral structured meshing for image-based computational vascular modeling. *Medical engineering & physics*, 33(10):1318–1325. 104
- Degroote, J., Bathe, K.-J., and Vierendeels, J. (2009). Performance of a new partitioned procedure versus a monolithic procedure in fluid–structure interaction. *Computers & Structures*, 87(11-12):793–801. 26, 132, 133, 134
- Demiray, H. (1972). A note on the elasticity of soft biological tissues. *Journal of biomechanics*, 5(3):309–311. 76, 77
- Deplano, V., Boufi, M., Gariboldi, V., Loundou, A. D., D'journo, X. B., Cautela, J., Djemli, A., and Alimi, Y. S. (2019). Mechanical characterisation of human ascending aorta dissection. *Journal of biomechanics*, 94:138–146. 82, 154, 189
- Dillon-Murphy, D., Noorani, A., Nordsletten, D., and Figueroa, C. A. (2016). Multi-modality image-based computational analysis of haemodynamics in aortic dissection. *Biomechanics and modeling in mechanobiology*, 15(4):857–876. 23, 53, 62, 63
- Donner, M., Siadat, M., and Stoltz, J. (1988). Erythrocyte aggregation: approach by light scattering determination. *Biorheology*, 25(1-2):367–376. 58
- Eckmann, D. M., Bowers, S., Stecker, M., and Cheung, A. T. (2000). Hematocrit, volume expander, temperature, and shear rate effects on blood viscosity. *Anesthesia & Analgesia*, 91(3):539–545. 60
- Erbel, R., Alfonso, F., Boileau, C., Dirsch, O., Eber, B., Haverich, A., Rakowski, H., Struyven, J., Radegran, K., Sechtem, U., et al. (2001). Diagnosis and management of aortic dissection: task force on aortic dissection, european society of cardiology. *European heart journal*, 22(18):1642–1681. 29, 41, 143
- Errill, E. (1969). Rheology of blood. *Physiological reviews*, 49(4):863–888. 55, 56
- Fann, J. I., Smith, J. A., Miller, D. C., Mitchell, R. S., Moore, K. A., Grunkemeier, G., Stinson, E. B., Oyer, P. E., Reitz, B. A., and Shumway, N. E. (1995). Surgical management of aortic dissection during a 30-year period. *Circulation*, 92(9):113–121. 44
- Figueroa, C. A., Taylor, C. A., Chiou, A. J., Yeh, V., and Zarins, C. K. (2009a). Magnitude and direction of pulsatile displacement forces acting on thoracic aortic endografts. *Journal of Endovascular Therapy*, 16(3):350–358. 96
- Figueroa, C. A., Taylor, C. A., Yeh, V., Chiou, A. J., and Zarins, C. K. (2009b). Effect of curvature on displacement forces acting on aortic endografts: a 3-dimensional computational analysis. *Journal of Endovascular Therapy*, 16(3):284–294. 95
- Figueroa, C. A., Vignon-Clementel, I. E., Jansen, K. E., Hughes, T. J., and Taylor, C. A. (2006). A coupled momentum method for modeling blood flow in three-dimensional deformable arteries. *Computer methods in applied mechanics and engineering*, 195(41-43):5685–5706. 95

- Formaggia, L., Gerbeau, J.-F., Nobile, F., and Quarteroni, A. (2001). On the coupling of 3d and 1d navier–stokes equations for flow problems in compliant vessels. *Computer methods in applied mechanics and engineering*, 191(6-7):561–582. 110, 130
- Formaggia, L., Lamponi, D., and Quarteroni, A. (2003). One-dimensional models for blood flow in arteries. *Journal of engineering mathematics*, 47(3):251–276. 97
- Formaggia, L., Moura, A., and Nobile, F. (2007). On the stability of the coupling of 3d and 1d fluid-structure interaction models for blood flow simulations. *ESAIM: Mathematical Modelling and Numerical Analysis*, 41(4):743–769. 130
- Förster, C., Wall, W. A., and Ramm, E. (2007). Artificial added mass instabilities in sequential staggered coupling of nonlinear structures and incompressible viscous flows. *Computer methods in applied mechanics and engineering*, 196(7):1278–1293. 133
- Foucault, E., Huberson, S., Braud, P., and Coisne, D. (2017). On the pulsatile flow through a coronary bifurcation with stent. *European Journal of Mechanics-B/Fluids*, 61:177–186. 97
- François, C. J., Markl, M., Schiebler, M. L., Niespodzany, E., Landgraf, B. R., Schlensak, C., and Frydrychowicz, A. (2013). Four-dimensional, flow-sensitive magnetic resonance imaging of blood flow patterns in thoracic aortic dissections. *The Journal of thoracic and cardiovascular surgery*, 145(5):1359–1366. 61
- Frydrychowicz, A., Berger, A., Del Rio, A. M., Russe, M. F., Bock, J., Harloff, A., and Markl, M. (2012). Interdependencies of aortic arch secondary flow patterns, geometry, and age analysed by 4-dimensional phase contrast magnetic resonance imaging at 3 tesla. *European radiology*, 22(5):1122–1130. 160
- Fung, Y., Fronek, K., and Patitucci, P. (1979). Pseudoelasticity of arteries and the choice of its mathematical expression. *American Journal of Physiology-Heart and Circulatory Physiology*, 237(5):H620–H631. 13, 77, 79, 81, 92
- Fung, Y. and Liu, S. (1989). Change of residual strains in arteries due to hypertrophy caused by aortic constriction. *Circulation research*, 65(5):1340–1349. 74
- Fung, Y.-C. (2013). *Biomechanics: circulation*. Springer Science & Business Media. 35, 54, 64, 122, 189
- Gallo, D., Lefieux, A., Morganti, S., Veneziani, A., Reali, A., Auricchio, F., Conti, M., and Morbiducci, U. (2016). A patient-specific follow up study of the impact of thoracic endovascular repair (tevar) on aortic anatomy and on post-operative hemodynamics. *Computers & Fluids*, 141:54–61. 95
- Garcia, J., Capoulade, R., Le Ven, F., Gaillard, E., Kadem, L., Pibarot, P., and Larose, É. (2013). Discrepancies between cardiovascular magnetic resonance and doppler echocardiography in the measurement of transvalvular gradient in aortic stenosis: the effect of flow vorticity. *Journal of Cardiovascular Magnetic Resonance*, 15(1):1–9. 160
- Gasser, T. C. and Holzapfel, G. A. (2006). Modeling the propagation of arterial dissection. *European Journal of Mechanics-A/Solids*, 25(4):617–633. 13, 77, 92, 189

- Gawinecka, J., Schönrath, F., and von Eckardstein, A. (2017). Acute aortic dissection: pathogenesis, risk factors and diagnosis. *Swiss medical weekly*, 147:14489. 22, 42
- Gijssen, F., Allanic, E., Van de Vosse, F., and Janssen, J. (1999). The influence of the non-newtonian properties of blood on the flow in large arteries: unsteady flow in a 90 curved tube. *Journal of biomechanics*, 32(7):705–713. 66
- Gindre, J., Bel-Brunon, A., Rochette, M., Lucas, A., Kaladji, A., Haigron, P., and Combescure, A. (2016). Patient-specific finite-element simulation of the insertion of guidewire during an evar procedure: guidewire position prediction validation on 28 cases. *IEEE Transactions on Biomedical Engineering*, 64(5):1057–1066. 144, 151
- Golledge, J. and Eagle, K. A. (2008). Acute aortic dissection. *The Lancet*, 372(9632):55–66. 40
- Guivier-Curien, C., Deplano, V., and Bertrand, E. (2009). Validation of a numerical 3-d fluid–structure interaction model for a prosthetic valve based on experimental piv measurements. *Medical engineering & physics*, 31(8):986–993. 97
- Gültekin, O., Hager, S. P., Dal, H., and Holzapfel, G. A. (2019). Computational modeling of progressive damage and rupture in fibrous biological tissues: application to aortic dissection. *Biomechanics and modeling in mechanobiology*, 18(6):1607–1628. 192
- Ha, S. T., Ngo, L. C., Saeed, M., Jeon, B. J., and Choi, H. (2017). A comparative study between partitioned and monolithic methods for the problems with 3d fluid-structure interaction of blood vessels. *Journal of Mechanical Science and Technology*, 31(1):281–287. 131
- Hachiya, J., Nitatori, T., Yoshino, A., Okada, M., and Furuya, Y. (1993). Ct of calcified chronic aortic dissection simulating atherosclerotic aneurysm. *Journal of computer assisted tomography*, 17(3):374–378. 72
- Haider, L., Snabre, P., and Boynard, M. (2004). Rheology and ultrasound scattering from aggregated red cell suspensions in shear flow. *Biophysical journal*, 87(4):2322–2334. 58
- Hanna, J. M., Andersen, N. D., Ganapathi, A. M., McCann, R. L., and Hughes, G. C. (2014). Five-year results for endovascular repair of acute complicated type b aortic dissection. *Journal of vascular surgery*, 59(1):96–106. 45
- Hardy, C. J., Bolster, B. D., McVeigh, E. R., Adams, W. J., and Zerhouni, E. A. (1994). A one-dimensional velocity technique for nmr measurement of aortic distensibility. *Magnetic resonance in medicine*, 31(5):513–520. 53
- Hellmuth, R. (2017). Scaled velocity profiles of pulsatile flow are compared according to Womersley number. https://commons.wikimedia.org/wiki/File:Comparison_of_velocity_profile_of_Womersley_flow.svg. 23, 64
- Himburg, H. A., Grzybowski, D. M., Hazel, A. L., LaMack, J. A., Li, X.-M., and Friedman, M. H. (2004). Spatial comparison between wall shear stress measures and porcine arterial endothelial permeability. *American Journal of Physiology-Heart and Circulatory Physiology*, 286(5):H1916–H1922. 118

- Hoi, Y., Zhou, Y.-Q., Zhang, X., Henkelman, R. M., and Steinman, D. A. (2011). Correlation between local hemodynamics and lesion distribution in a novel aortic regurgitation murine model of atherosclerosis. *Annals of biomedical engineering*, 39(5):1414–1422. 118
- Holzapfel, G. A. (2000). *Nonlinear solid mechanics: a continuum approach for engineering*. Wiley. 29, 77
- Holzapfel, G. A., Gasser, T. C., and Ogden, R. W. (2000). A new constitutive framework for arterial wall mechanics and a comparative study of material models. *Journal of elasticity and the physical science of solids*, 61(1):1–48. 13, 23, 70, 92, 189
- Holzapfel, G. A. and Ogden, R. W. (2003). *Biomechanics of soft tissue in cardiovascular systems*, volume 441. Springer. 24, 77, 78
- Holzapfel, G. A., Sommer, G., Auer, M., Regitnig, P., and Ogden, R. W. (2007). Layer-specific 3d residual deformations of human aortas with non-atherosclerotic intimal thickening. *Annals of biomedical engineering*, 35(4):530–545. 24, 74, 75
- Hope, M. D., Hope, T. A., Meadows, A. K., Ordovas, K. G., Urbania, T. H., Alley, M. T., and Higgins, C. B. (2010). Bicuspid aortic valve: four-dimensional mr evaluation of ascending aortic systolic flow patterns. *Radiology*, 255(1):53–61. 61
- Humphrey, J. D. (1995). Mechanics of the arterial wall: review and directions. *Critical Reviews™ in Biomedical Engineering*, 23(1-2). 13, 77, 79, 81, 92
- Imura, T., Yamamoto, K., Satoh, T., Kanamori, K., Mikami, T., and Yasuda, H. (1990). In vivo viscoelastic behavior in the human aorta. *Circulation research*, 66(5):1413–1419. 79, 80
- Issa, R. I. (1986). Solution of the implicitly discretised fluid flow equations by operator-splitting. *Journal of computational physics*, 62(1):40–65. 99
- Jaffrin, M.-Y. and Goubel, F. (1998). *Biomécanique des fluides et des tissus*. Masson. 59, 67, 68, 73
- Jang, H., Kim, M.-D., Kim, G. M., Won, J. Y., Ko, Y.-G., Choi, D., Joo, H.-C., and Lee, D. Y. (2017). Risk factors for stent graft-induced new entry after thoracic endovascular aortic repair for stanford type b aortic dissection. *Journal of vascular surgery*, 65(3):676–685. 49
- Jasak, H. (1996). *Error analysis and estimation for the finite volume method with applications to fluid flows*. PhD thesis, Imperial College London (University of London). 100
- Kamenskiy, A. V., Dzenis, Y. A., Kazmi, S. A. J., Pemberton, M. A., Pipinos, I. I., Phillips, N. Y., Herber, K., Woodford, T., Bowen, R. E., Lomneth, C. S., et al. (2014). Biaxial mechanical properties of the human thoracic and abdominal aorta, common carotid, subclavian, renal and common iliac arteries. *Biomechanics and modeling in mechanobiology*, 13(6):1341–1359. 82
- Karmonik, C., Bismuth, J., Shah, D., Davies, M., Purdy, D., and Lumsden, A. B. (2011). Computational study of haemodynamic effects of entry-and exit-tear coverage in a debakey type iii aortic dissection: technical report. *European journal of vascular and endovascular surgery*, 42(2):172–177. 62

- Khanna, N. (2011). Endovascular repair of thoracic and abdominal aortic aneurysms/dissections. *Apollo Medicine*, 8(3):217–227. 48, 189
- Kim, B., Lee, S. B., Lee, J., Cho, S., Park, H., Yeom, S., and Park, S. H. (2012). A comparison among neo-hookean model, mooney-rivlin model, and ogden model for chloroprene rubber. *International Journal of Precision Engineering and Manufacturing*, 13(5):759–764. 76, 77
- Kim, S., Cho, Y. I., Jeon, A. H., Hogenauer, B., and Kensey, K. R. (2000). A new method for blood viscosity measurement. *Journal of non-newtonian fluid mechanics*, 94(1):47–56. 65
- Kojić, M., Filipović, N., Stojanović, B., and Kojić, N. (2008). *Computer Modeling in Bioengineering: Theoretical background, examples and software*. John Wiley & Sons. 35
- Ku, D. N., Giddens, D. P., Zarins, C. K., and Glagov, S. (1985). Pulsatile flow and atherosclerosis in the human carotid bifurcation. positive correlation between plaque location and low oscillating shear stress. *Arteriosclerosis: An Official Journal of the American Heart Association, Inc.*, 5(3):293–302. 117
- Küttler, U. and Wall, W. A. (2008). Fixed-point fluid–structure interaction solvers with dynamic relaxation. *Computational mechanics*, 43(1):61–72. 133
- Lacombe, C., Bucherer, C., Ladjouzi, J., and Lelievre, J. (1988). Competitive role between fibrinogen and albumin on thixotropy of red cell suspensions. *Biorheology*, 25(1-2):349–354. 57, 59
- Latson, T. W., Yin, F. C., and Hunter, W. C. (1987). The effects of finite wave velocity and discrete reflections on ventricular loading. In *Ventricular/vascular coupling*, pages 334–383. Springer. 113
- Learoyd, B. M. and Taylor, M. G. (1966). Alterations with age in the viscoelastic properties of human arterial walls. *Circulation research*, 18(3):278–292. 69
- Lehmann, E., Hopkins, K., and Gosling, R. (1993). Aortic compliance measurements using doppler ultrasound: in vivo biochemical correlates. *Ultrasound in medicine & biology*, 19(9):683–710. 53
- Leshnower, B. G. and Chen, E. P. (2018). Tevar for acute complicated type b aortic dissection. *Operative Techniques in Thoracic and Cardiovascular Surgery*, 23(1):21–33. 22, 47
- Linck, V. (2005). *Modélisation numérique temporelle d’un contact frottant: mise en évidence d’instabilités locales de contact: conséquences tribologiques*. PhD thesis, Lyon, INSA. 148
- Liu, D., Fan, Z., Li, Y., Zhang, N., Sun, Z., An, J., Stalder, A. F., Greiser, A., and Liu, J. (2018). Quantitative study of abdominal blood flow patterns in patients with aortic dissection by 4-dimensional flow mri. *Scientific reports*, 8(1):1–8. 46
- Liu, L., Zhang, S., Lu, Q., Jing, Z., Zhang, S., and Xu, B. (2016). Impact of oversizing on the risk of retrograde dissection after tevar for acute and chronic type b dissection. *Journal of Endovascular Therapy*, 23(4):620–625. 48
- Liu, M., Liang, L., Sulejmani, F., Lou, X., Iannucci, G., Chen, E., Leshnower, B., and Sun, W. (2019). Identification of in vivo nonlinear anisotropic mechanical properties of ascending thoracic aortic aneurysm from patient-specific ct scans. *Scientific reports*, 9(1):1–13. 86

- Liu, X., Pu, F., Fan, Y., Deng, X., Li, D., and Li, S. (2009). A numerical study on the flow of blood and the transport of ldl in the human aorta: the physiological significance of the helical flow in the aortic arch. *American Journal of Physiology-Heart and Circulatory Physiology*, 297(1):H163–H170. 96
- Löhner, R., Cezbral, J., Soto, O., Yim, P., and Burgess, J. E. (2003). Applications of patient-specific cfd in medicine and life sciences. *International journal for numerical methods in fluids*, 43(6-7):637–650. 95
- Lombardi, J. V., Hughes, G. C., Appoo, J. J., Bavaria, J. E., Beck, A. W., Cambria, R. P., Charlton-Ouw, K., Eslami, M. H., Kim, K. M., Leshnower, B. G., et al. (2020). Society for vascular surgery (svs) and society of thoracic surgeons (sts) reporting standards for type b aortic dissections. *The Annals of thoracic surgery*, 109(3):959–981. 45
- Lou, Z. and Yang, W.-J. (1993). A computer simulation of the non-newtonian blood flow at the aortic bifurcation. *Journal of biomechanics*, 26(1):37–49. 66
- Lowe, G. and Barbenel, J. (2019). Plasma and blood viscosity. In *Clinical blood rheology*, volume 1, pages 11–44. CRC Press. 56, 57
- Lowe, G. D. (2019). Rheology of paraproteinemias and leukemias. In *Clinical Blood Rheology*, volume 2, pages 67–88. CRC Press. 57
- Marchandise, E., Willemet, M., and Lacroix, V. (2009). A numerical hemodynamic tool for predictive vascular surgery. *Medical engineering & physics*, 31(1):131–144. 110
- Markl, M., Chan, F. P., Alley, M. T., Wedding, K. L., Draney, M. T., Elkins, C. J., Parker, D. W., Wicker, R., Taylor, C. A., Herfkens, R. J., et al. (2003). Time-resolved three-dimensional phase-contrast mri. *Journal of Magnetic Resonance Imaging: An Official Journal of the International Society for Magnetic Resonance in Medicine*, 17(4):499–506. 101
- Markl, M., Schnell, S., Wu, C., Bollache, E., Jarvis, K., Barker, A., Robinson, J., and Rigsby, C. (2016). Advanced flow mri: emerging techniques and applications. *Clinical radiology*, 71(8):779–795. 24, 95, 101
- Markl, M., Wallis, W., Bredecke, S., Simon, J., Frydrychowicz, A., and Harloff, A. (2010). Estimation of global aortic pulse wave velocity by flow-sensitive 4d mri. *Magnetic Resonance in Medicine: An Official Journal of the International Society for Magnetic Resonance in Medicine*, 63(6):1575–1582. 23, 61, 62
- Marsden, A. L., Bernstein, A. J., Reddy, V. M., Shadden, S. C., Spilker, R. L., Chan, F. P., Taylor, C. A., and Feinstein, J. A. (2009). Evaluation of a novel y-shaped extracardiac fontan baffle using computational fluid dynamics. *The Journal of thoracic and cardiovascular surgery*, 137(2):394–403. 95
- Mbodj, C., Altnji, H., Bou-Said, B., and Walter-Le Berre, H. (2016). Analysis of the phenomenon of endoleak of type i a. influence of the mechanical characterization of the aorta. *Journal of Hypertension and Management*, 2(1):1510014. 96

- Meng, H., Tutino, V., Xiang, J., and Siddiqui, A. (2014). High wss or low wss? complex interactions of hemodynamics with intracranial aneurysm initiation, growth, and rupture: toward a unifying hypothesis. *American Journal of Neuroradiology*, 35(7):1254–1262. 15, 143, 187, 190
- Menut, M. (2017). *Chirurgie endovasculaire virtuelle pour patient-spécifique: Application au traitement de l'anévrisme de l'aorte thoracique*. PhD thesis, Université de Lyon. 13, 15, 23, 24, 25, 26, 29, 60, 79, 81, 82, 83, 84, 85, 87, 88, 90, 92, 102, 108, 116, 117, 142, 144, 145, 148, 151, 152, 156, 159, 190, 195
- Menut, M., Bou-Said, B., Walter-Le Berre, H., Vezin, P., and Boubaker, L. B. (2015). Characterization of the mechanical properties of the human aortic arch using an expansion method. *Journal of Vascular Medicine & Surgery*, 3(2):4–p. 24, 83, 189
- Merrill, E., Gilliland, E., Cokelet, G., Shin, H., Britten, A., and Wells Jr, R. (1963a). Rheology of human blood, near and at zero flow: effects of temperature and hematocrit level. *Biophysical Journal*, 3(3):199–213. 59, 60
- Merrill, E. W., Cokelet, G. C., Britten, A., and WELLS Jr, R. E. (1963b). Non-newtonian rheology of human blood-effect of fibrinogen deduced by” subtraction”. *Circulation research*, 13(1):48–55. 57
- Mescher, A. L. (2013). *Junqueira’s basic histology: text and atlas*, volume 12. McGraw-Hill Medical 13th ed. New York. 22, 23, 55, 71
- Meszaros, I., Morocz, J., Szlavi, J., Schmidt, J., Tornoci, L., Nagy, L., and Szép, L. (2000). Epidemiology and clinicopathology of aortic dissection. *Chest*, 117(5):1271–1278. 39
- Metz, R., Hendriks, J., Rouwet, E., Muhs, B., Poldermans, D., Verhagen, H., et al. (2010). Decision-making in type-b dissection: current evidence and future perspectives. *The Journal of cardiovascular surgery*, 51(5):657–667. 129
- Meyers, M. A. and Chawla, K. K. (2008). *Mechanical behavior of materials*. Cambridge university press. 24, 74
- Michler, C., Hulshoff, S., Van Brummelen, E., and De Borst, R. (2004). A monolithic approach to fluid–structure interaction. *Computers & fluids*, 33(5-6):839–848. 132
- Millon, A., Bros, S., Boussel, L., Robson, P., Fayad, Z., Sigovan, M., and Douek, P. (2014). A new carotid 3d mri sequence for stenosis measurement and plaque characterization at the same time. *European Journal of Vascular and Endovascular Surgery*, 48(3):342. 61, 86, 91, 103
- Moghadam, M. E., Vignon-Clementel, I. E., Figliola, R., Marsden, A. L., of Congenital Hearts Alliance (MOCHA) Investigators, M., et al. (2013). A modular numerical method for implicit 0d/3d coupling in cardiovascular finite element simulations. *Journal of Computational Physics*, 244:63–79. 110
- Moireau, P., Xiao, N., Astorino, M., Figueroa, C. A., Chapelle, D., Taylor, C., and Gerbeau, J.-F. (2012). External tissue support and fluid–structure simulation in blood flows. *Biomechanics and modeling in mechanobiology*, 11(1):1–18. 151

- Mooney, M. (1940). A theory of large elastic deformation. *Journal of applied physics*, 11(9):582–592. 76, 77, 84
- Moore, J., Steinman, D., Holdsworth, D., and Ethier, C. (1999). Accuracy of computational hemodynamics in complex arterial geometries reconstructed from magnetic resonance imaging. *Annals of biomedical engineering*, 27(1):32–41. 95
- Moravia, A. (2021). *Design of an in vitro circulatory mock loop to study non-Newtonian hemodynamical flows in aorta phantoms: application to aortic dissection*. PhD thesis, Université de Lyon. 8, 9, 16, 27, 32, 176, 177, 178, 187, 191
- Moravia, A., Pan, W., Le Berre, H., Menut, M., Bou-Said, B., Elhajem, M., Escriva, X., Kulisa, P., Simoëns, S., Lermusiaux, P., et al. (2019a). In vitro assessment of abdominal aortic dissection hemodynamics based on particle image velocimetry. In *24^{ème} Congrès Français de Mécanique CFM 2019*. 178
- Moravia, A., Pan, W., Walter-Le Berre, H., Menut, M., Said, B. B., El Hajem, M., Escriva, X., Kulisa, P., Simoens, S., and Lermusiaux, P. (2019b). In vitro assessment of abdominal aorta non-newtonian hemodynamics based on particle image velocimetry. In *European Symposium of Biomechanics*. 182
- Morbiducci, U., Ponzini, R., Gallo, D., Bignardi, C., and Rizzo, G. (2013). Inflow boundary conditions for image-based computational hemodynamics: impact of idealized versus measured velocity profiles in the human aorta. *Journal of biomechanics*, 46(1):102–109. 161
- Morris, L., Delassus, P., Callanan, A., Walsh, M., Wallis, F., Grace, P., and McGloughlin, T. (2005). 3-d numerical simulation of blood flow through models of the human aorta. *Journal of biomechanical engineering*, 127(5):767–775. 96
- Mouktadiri, G. (2013). *Angiovision-Pose d’endoprothèse aortique par angionavigation augmentée*. PhD thesis, Lyon, INSA. 13, 15, 24, 26, 85, 86, 90, 91, 92, 143, 144, 145, 146, 147, 151, 152, 190
- Munshi, B., Parker, L. P., Norman, P. E., and Doyle, B. J. (2020). The application of computational modeling for risk prediction in type b aortic dissection. *Journal of vascular surgery*, 71(5):1789–1801. 62
- Mynard, J. and Nithiarasu, P. (2008). A 1d arterial blood flow model incorporating ventricular pressure, aortic valve and regional coronary flow using the locally conservative galerkin (lcg) method. *Communications in numerical methods in engineering*, 24(5):367–417. 28, 109, 194
- Nayak, K. S., Nielsen, J.-F., Bernstein, M. A., Markl, M., Gatehouse, P. D., Botnar, R. M., Saloner, D., Lorenz, C., Wen, H., Hu, B. S., et al. (2015). Cardiovascular magnetic resonance phase contrast imaging. *Journal of Cardiovascular Magnetic Resonance*, 17(1):1–26. 100
- Nienaber, C. A., Kische, S., Rousseau, H., Eggebrecht, H., Rehders, T. C., Kundt, G., Glass, A., Scheinert, D., Czerny, M., Kleinfeldt, T., et al. (2013). Endovascular repair of type b aortic dissection: long-term results of the randomized investigation of stent grafts in aortic dissection trial. *Circulation: Cardiovascular Interventions*, 6(4):407–416. 45

- Nordon, I. M., Hinchliffe, R. J., Loftus, I. M., Morgan, R. A., and Thompson, M. M. (2011). Management of acute aortic syndrome and chronic aortic dissection. *Cardiovascular and interventional radiology*, 34(5):890–902. 143
- O’Callaghan, S., Walsh, M., and McGloughlin, T. (2006). Numerical modelling of newtonian and non-newtonian representation of blood in a distal end-to-side vascular bypass graft anastomosis. *Medical engineering & physics*, 28(1):70–74. 123
- Ogden, R. W. (1972). Large deformation isotropic elasticity—on the correlation of theory and experiment for incompressible rubberlike solids. *Proceedings of the Royal Society of London. A. Mathematical and Physical Sciences*, 326(1567):565–584. 13, 76, 77, 81, 92
- Oliveira, I. L. (2017). *Using foam-extend to assess the influence of fluid-structure interaction on the rupture of intracranial aneurysms*. PhD thesis, Universidade Estadual Paulista (UNESP). 133
- Olsson, C., Thelin, S., Stahle, E., Ekbom, A., and Granath, F. (2006). Thoracic aortic aneurysm and dissection: increasing prevalence and improved outcomes reported in a nationwide population-based study of more than 14 000 cases from 1987 to 2002. *Circulation*, 114(24):2611–2618. 39
- O’Rourke, M. F., Hartley, C., and McDonald, D. A. (1998). *McDonald’s blood flow in arteries: theoretic, experimental, and clinical principles*. Arnold. 23, 29, 66, 68, 72
- Osswald, A., Karmonik, C., Anderson, J., Rengier, F., Karck, M., Engelke, J., Kallenbach, K., Kotelis, D., Partovi, S., Böckler, D., et al. (2017). Elevated wall shear stress in aortic type b dissection may relate to retrograde aortic type a dissection: a computational fluid dynamics pilot study. *European Journal of Vascular and Endovascular Surgery*, 54(3):324–330. 60
- Ouattara, A. (2013). Pathologie de l’isthme aortique. page 11. Le Congrès SFAR 2013. Urgences vitales. 39
- Pan, W., Kulisa, P., Escriva, X., BenyebkaBou, Saïd, Menut, M., Lermusiaux, P., and Millon, A. (2020). Computer aided surgery: Application to aortic dissection. *Annals of Vascular Medicine & Research*, 7(5):1120. 8, 9
- Patil, T. and Nierich, A. (2016). Transesophageal echocardiography evaluation of the thoracic aorta. *Annals of cardiac anaesthesia*, 19(Suppl 1):44–55. 46
- Pedersen, E. M., Oyre, S., Agerbaek, M., Kristensen, I., Ringgaard, S., Boesiger, P., and Paaske, W. (1999). Distribution of early atherosclerotic lesions in the human abdominal aorta correlates with wall shear stresses measured in vivo. *European journal of vascular and endovascular surgery*, 18(4):328–333. 23, 61, 95
- Perić, M. and Ferguson, A. (2005). The advantage of polyhedral meshes. 106
- Perktold, K., Karner, G., Leuprecht, A., and Hofer, M. (1999). Influence of non-newtonian flow behavior on local hemodynamics. *ZAMM-Journal of Applied Mathematics and Mechanics/Zeitschrift Für Angewandte Mathematik Und Mechanik*, 79(S1):187–190. 66
- Peterson, L. H., Jensen, R. E., and Parnell, J. (1960). Mechanical properties of arteries in vivo. *Circulation Research*, 8(3):622–639. 73, 79, 80

- Prendergast, P., Lally, C., Daly, S., Reid, A., Lee, T., Quinn, D., and Dolan, F. (2003). Analysis of prolapse in cardiovascular stents: a constitutive equation for vascular tissue and finite-element modelling. *J. Biomech. Eng.*, 125(5):692–699. 24, 82, 84, 85
- Pries, A. R., Neuhaus, D., and Gaetgens, P. (1992). Blood viscosity in tube flow: dependence on diameter and hematocrit. *American Journal of Physiology-Heart and Circulatory Physiology*, 263(6):H1770–H1778. 60
- Qiao, Y., Zeng, Y., Ding, Y., Fan, J., Luo, K., and Zhu, T. (2019). Numerical simulation of two-phase non-newtonian blood flow with fluid-structure interaction in aortic dissection. *Computer methods in biomechanics and biomedical engineering*, 22(6):620–630. 129, 142, 154
- Raffel, M., Willert, C. E., Scarano, F., Kähler, C. J., Wereley, S. T., and Kompenhans, J. (2018). *Particle image velocimetry: a practical guide*. Springer. 175
- Raghavan, M. and Vorp, D. A. (2000). Toward a biomechanical tool to evaluate rupture potential of abdominal aortic aneurysm: identification of a finite strain constitutive model and evaluation of its applicability. *Journal of biomechanics*, 33(4):475–482. 76, 77
- Raghavan, M. L., Webster, M. W., and Vorp, D. A. (1996). Ex vivo biomechanical behavior of abdominal aortic aneurysm: assessment using a new mathematical model. *Annals of biomedical engineering*, 24(5):573–582. 24, 77, 80, 81, 82
- Ramplung, M. (2019). Red cell aggregation and yield stress. In *Clinical blood rheology*, pages 45–64. CRC Press. 56
- Razavi, A., Shirani, E., and Sadeghi, M. (2011). Numerical simulation of blood pulsatile flow in a stenosed carotid artery using different rheological models. *Journal of biomechanics*, 44(11):2021–2030. 29, 124
- Ríos-Ruiz, I., Cilla, M., Martínez, M. A., and Peña, E. (2021). Methodology to calibrate the dissection properties of aorta layers from two sets of experimental measurements. *Mathematics*, 9(14):1593. 81
- Rivlin, R. (1948). Large elastic deformations of isotropic materials iv. further developments of the general theory. *Philosophical Transactions of the Royal Society of London. Series A, Mathematical and Physical Sciences*, 241(835):379–397. 76
- Rivlin, R. S. and Saunders, D. (1951). Large elastic deformations of isotropic materials vii. experiments on the deformation of rubber. *Philosophical Transactions of the Royal Society of London. Series A, Mathematical and Physical Sciences*, 243(865):251–288. 76, 81
- Rizzoli, G., Scalia, D., Casarotto, D., and Tiso, E. (1997). Aortic dissection type a versus type b: a different post-surgical death hazard? *European journal of cardio-thoracic surgery*, 12(2):202–208. 29, 43
- Robicsek, F. and Thubrikar, M. J. (1994). Hemodynamic considerations regarding the mechanism and prevention of aortic dissection. *The Annals of thoracic surgery*, 58(4):1247–1253. 53, 60

- Rodríguez, J. F., Martufi, G., Doblaré, M., and Finol, E. A. (2009). The effect of material model formulation in the stress analysis of abdominal aortic aneurysms. *Annals of biomedical engineering*, 37(11):2218–2221. 77, 78, 79
- Roy, C. S. (1881). The elastic properties of the arterial wall. *The Journal of physiology*, 3(2):125–159. 79
- Sagawa, K., Lie, R., and Schaefer, J. (1990). Translation of otto frank’s paper ”die grundform des arteriellen pulses” zeitschrift für biologie 37: 483-526 (1899). *Journal of molecular and cellular cardiology*, 22(3):253–254. 111
- Schriebl, A. J., Zeindlinger, G., Pierce, D. M., Regitnig, P., and Holzapfel, G. A. (2012). Determination of the layer-specific distributed collagen fibre orientations in human thoracic and abdominal aortas and common iliac arteries. *Journal of the Royal Society Interface*, 9(71):1275–1286. 23, 68, 69
- Sequeira, A. and Janela, J. (2007). An overview of some mathematical models of blood rheology. *A Portrait of State-of-the-Art Research at the Technical University of Lisbon*, pages 65–87. 65
- Seta, F. and Cohen, R. A. (2014). The endothelium: paracrine mediator of aortic dissection. *Circulation*, 129(25):2629–2632. 60
- Shahcheraghi, N., Dwyer, H., Cheer, A., Barakat, A., and Rutaganira, T. (2002). Unsteady and three-dimensional simulation of blood flow in the human aortic arch. *J. Biomech. Eng.*, 124(4):378–387. 96
- Sherrah, A. G., Grieve, S. M., Jeremy, R. W., Bannon, P. G., Vallely, M. P., and Puranik, R. (2015). Mri in chronic aortic dissection: a systematic review and future directions. *Frontiers in cardiovascular medicine*, 2:5. 61
- Sherwin, S., Franke, V., Peiró, J., and Parker, K. (2003). One-dimensional modelling of a vascular network in space-time variables. *Journal of engineering mathematics*, 47(3):217–250. 97
- Shi, Y., Lawford, P., and Hose, R. (2011). Review of zero-d and 1-d models of blood flow in the cardiovascular system. *Biomedical engineering online*, 10(1):1–38. 95
- Shibeshi, S. S. and Collins, W. E. (2005). The rheology of blood flow in a branched arterial system. *Applied Rheology*, 15(6):398–405. 65
- Siasos, G., Sara, J. D., Zaromytidou, M., Park, K. H., Coskun, A. U., Lerman, L. O., Oikonomou, E., Maynard, C. C., Fotiadis, D., Stefanou, K., et al. (2018). Local low shear stress and endothelial dysfunction in patients with nonobstructive coronary atherosclerosis. *Journal of the American College of Cardiology*, 71(19):2092–2102. 95
- Sigovan, M., Dyverfeldt, P., Wrenn, J., Tseng, E. E., Saloner, D., and Hope, M. D. (2015). Extended 3d approach for quantification of abnormal ascending aortic flow. *Magnetic resonance imaging*, 33(5):695–700. 23, 61, 62, 91
- Somer, T. and Meiselman, H. J. (1993). Disorders of blood viscosity. *Annals of medicine*, 25(1):31–39. 57

- Sommer, G., Gasser, T. C., Regitnig, P., Auer, M., and Holzapfel, G. A. (2008). Dissection properties of the human aortic media: an experimental study. *Journal of biomechanical engineering*, 130(2). 81
- Soudah, E., Rudenick, P., Bordone, M., Bijmens, B., García-Dorado, D., Evangelista, A., and Oñate, E. (2015). Validation of numerical flow simulations against in vitro phantom measurements in different type b aortic dissection scenarios. *Computer methods in biomechanics and biomedical engineering*, 18(8):805–815. 154
- Stalder, A. F., Russe, M., Frydrychowicz, A., Bock, J., Hennig, J., and Markl, M. (2008). Quantitative 2d and 3d phase contrast mri: optimized analysis of blood flow and vessel wall parameters. *Magnetic Resonance in Medicine: An Official Journal of the International Society for Magnetic Resonance in Medicine*, 60(5):1218–1231. 101, 154
- Stergiopulos, N., Meister, J., and Westerhof, N. (1995). Evaluation of methods for estimation of total arterial compliance. *American Journal of Physiology-Heart and Circulatory Physiology*, 268(4):H1540–H1548. 112, 114
- Stergiopulos, N., Meister, J.-J., and Westerhof, N. (1994). Simple and accurate way for estimating total and segmental arterial compliance: the pulse pressure method. *Annals of biomedical engineering*, 22(4):392–397. 114
- Stergiopulos, N., Segers, P., and Westerhof, N. (1999a). Use of pulse pressure method for estimating total arterial compliance in vivo. *American Journal of Physiology-Heart and Circulatory Physiology*, 276(2):H424–H428. 114
- Stergiopulos, N., Westerhof, B. E., and Westerhof, N. (1999b). Total arterial inertance as the fourth element of the windkessel model. *American Journal of Physiology-Heart and Circulatory Physiology*, 276(1):H81–H88. 113
- Stergiopulos, N., Young, D., and Rogge, T. (1992). Computer simulation of arterial flow with applications to arterial and aortic stenoses. *Journal of biomechanics*, 25(12):1477–1488. 108
- Strumia, M. M., Phillips, M., Sample, A. B., Burns, M. E., and Mariano, P. (1963). Effect of red cell factors on the relative viscosity of whole blood. *American journal of clinical pathology*, 39(5):464–474. 60
- Takamizawa, K. and Hayashi, K. (1987). Strain energy density function and uniform strain hypothesis for arterial mechanics. *Journal of biomechanics*, 20(1):7–17. 77, 79
- Taylor, C. A., Hughes, T. J., and Zarins, C. K. (1998). Finite element modeling of blood flow in arteries. *Computer methods in applied mechanics and engineering*, 158(1-2):155–196. 95
- Ten Bosch, J. A., Rouwet, E. V., Peters, C. T., Jansen, L., Verhagen, H. J., Prins, M. H., and Teijink, J. A. (2010). Contrast-enhanced Ultrasound versus Computed Tomographic Angiography for Surveillance of Endovascular Abdominal Aortic Aneurysm Repair. *Journal of Vascular and Interventional Radiology*, 21(5):638–643. 48
- Tennekes, H. and Lumley, J. L. (2018). *A first course in turbulence*. MIT press. 56

- Themes, U. F. O. (2016). The Heart as a Pump. Chapter 21. 22, 36
- Thubrikar, M., Agali, P., and Robicsek, F. (1999). Wall stress as a possible mechanism for the development of transverse intimal tears in aortic dissections. *Journal of medical engineering & technology*, 23(4):127–134. 15, 143, 187
- Timmis, A., Townsend, N., Gale, C. P., Torbica, A., Lettino, M., Petersen, S. E., Mossialos, E. A., Maggioni, A. P., Kazakiewicz, D., May, H. T., et al. (2020). European society of cardiology: cardiovascular disease statistics 2019. *European heart journal*, 41(1):12–85. 8, 9
- Tolenaar, J. L., Jonker, F. H., Moll, F. L., Van Herwaarden, J., Morasch, M. D., Makaroun, M. S., and Trimarchi, S. (2013). Influence of oversizing on outcome in thoracic endovascular aortic repair. *Journal of Endovascular Therapy*, 20(6):738–745. 48
- Trimarchi, S., Jonker, F. H., Hutchison, S., Isselbacher, E. M., Pape, L. A., Patel, H. J., Froehlich, J. B., Muhs, B. E., Rampoldi, V., Grassi, V., et al. (2011). Descending aortic diameter of 5.5 cm or greater is not an accurate predictor of acute type b aortic dissection. *The Journal of thoracic and cardiovascular surgery*, 142(3):101–107. 66
- Uchida, S. (1956). The pulsating viscous flow superposed on the steady laminar motion of incompressible fluid in a circular pipe. *Zeitschrift für angewandte Mathematik und Physik ZAMP*, 7(5):403–422. 63
- Uchida, T. and Sadahiro, M. (2018). Thoracic endovascular aortic repair for acute aortic dissection. *Annals of vascular diseases*, 11(4):464–472. 22, 45
- Vaishnav, R. N. and Vossoughi, J. (1987). Residual stress and strain in aortic segments. *Journal of biomechanics*, 20(3):235–239. 74
- Vajravelu, K., Sreenadh, S., Devaki, P., and Prasad, K. (2011). Mathematical model for a herschel-bulkley fluid flow in an elastic tube. *Open Physics*, 9(5):1357–1365. 67
- Vignon-Clementel, I. E., Figueroa, C., Jansen, K., and Taylor, C. (2010). Outflow boundary conditions for 3d simulations of non-periodic blood flow and pressure fields in deformable arteries. *Computer methods in biomechanics and biomedical engineering*, 13(5):625–640. 130
- Vito, R. P. and Hickey, J. (1980). The mechanical properties of soft tissues—ii: The elastic response of arterial segments. *Journal of biomechanics*, 13(11):951–957. 76, 81
- Vorp, D. A., Schiro, B. J., Ehrlich, M. P., Juvonen, T. S., Ergin, M. A., and Griffith, B. P. (2003). Effect of aneurysm on the tensile strength and biomechanical behavior of the ascending thoracic aorta. *The Annals of thoracic surgery*, 75(4):1210–1214. 48
- Walraevens, J., Willaert, B., De Win, G., Ranftl, A., De Schutter, J., and Vander Sloten, J. (2008). Correlation between compression, tensile and tearing tests on healthy and calcified aortic tissues. *Medical engineering & physics*, 30(9):1098–1104. 48
- Wang, H., Wu, J., Wei, M., and Ma, X. (2015). A robust and fast approach to simulating the behavior of guidewire in vascular interventional radiology. *Computerized Medical Imaging and Graphics*, 40:160–169. 13, 92

- Watanabe, M. and Matsuzawa, T. (2006). Unsteady and three-dimensional simulation of blood flow in aortic dissection reconstructed from ct images. *Journal of Biomechanics*, 39:S294. 96
- Wells Jr, R. E. and EW, M. (1961). The variability of blood viscosity. *The American journal of medicine*, 31:505–509. 60
- Wen, C.-Y., Yang, A.-S., Tseng, L.-Y., and Chai, J.-W. (2010). Investigation of pulsatile flowfield in healthy thoracic aorta models. *Annals of biomedical engineering*, 38(2):391–402. 143, 190
- Westerhof, N., Lankhaar, J.-W., and Westerhof, B. E. (2009). The arterial windkessel. *Medical & biological engineering & computing*, 47(2):131–141. 25, 112, 113, 114
- White, R. A., Miller, D. C., Criado, F. J., Dake, M. D., Diethrich, E. B., Greenberg, R. K., Piccolo, R. S., Siami, F. S., for Vascular Surgery Outcomes Committee, M. S., et al. (2011). Report on the results of thoracic endovascular aortic repair for acute, complicated, type b aortic dissection at 30 days and 1 year from a multidisciplinary subcommittee of the society for vascular surgery outcomes committee. *Journal of vascular surgery*, 53(4):1082–1090. 48
- Wolinsky, H. and Glagov, S. (1964). Structural basis for the static mechanical properties of the aortic media. *Circulation research*, 14(5):400–413. 79, 82
- Womersley, J. R. (1955). Method for the calculation of velocity, rate of flow and viscous drag in arteries when the pressure gradient is known. *The Journal of physiology*, 127(3):553–563. 63
- Xiang, J., Natarajan, S. K., Tremmel, M., Ma, D., Mocco, J., Hopkins, L. N., Siddiqui, A. H., Levy, E. I., and Meng, H. (2011). Hemodynamic–morphologic discriminants for intracranial aneurysm rupture. *Stroke*, 42(1):144–152. 15, 143, 187, 190
- Xiao, N., Humphrey, J. D., and Figueroa, C. A. (2013). Multi-scale computational model of three-dimensional hemodynamics within a deformable full-body arterial network. *Journal of computational physics*, 244:22–40. 130
- Yang, S., Li, X., Chao, B., Wu, L., Cheng, Z., Duan, Y., Wu, D., Zhan, Y., Chen, J., Liu, B., et al. (2014a). Abdominal aortic intimal flap motion characterization in acute aortic dissection: assessed with retrospective ecg-gated thoracoabdominal aorta dual-source ct angiography. *PLoS One*, 9(2):87664. 46
- Yang, S., Li, X., Chao, B., Wu, L., Cheng, Z., Duan, Y., Wu, D., Zhan, Y., Chen, J., Liu, B., et al. (2014b). Abdominal aortic intimal flap motion characterization in acute aortic dissection: assessed with retrospective ecg-gated thoracoabdominal aorta dual-source ct angiography. *PLoS One*, 9(2):e87664. 142
- Yazdani, A., Li, H., Bersi, M. R., Di Achille, P., Insley, J., Humphrey, J. D., and Karniadakis, G. E. (2018). Data-driven modeling of hemodynamics and its role on thrombus size and shape in aortic dissections. *Scientific reports*, 8(1):1–18. 192
- Yeoh, O. H. (1990). Characterization of elastic properties of carbon-black-filled rubber vulcanizates. *Rubber chemistry and technology*, 63(5):792–805. 76, 77

Zadrazil, I., Corzo, C., Voulgaropoulos, V., Markides, C. N., and Xu, X. Y. (2020). A combined experimental and computational study of the flow characteristics in a type b aortic dissection: effect of primary and secondary tear size. *Chemical Engineering Research and Design*, 160:240–253. 175

FOLIO ADMINISTRATIF

THÈSE DE L'UNIVERSITÉ DE LYON OPÉRÉE AU SEIN DE L'INSA LYON

NOM : PAN

Date de soutenance : 26 Novembre 2021

Prénom : Wenyang

Titre : Computer Aided Surgery : application to aortic dissection

Nature : Doctorat

Numéro d'ordre : 2021LYSEI075

École doctorale : Mécanique, Énergétique, Génie Civil et Acoustique (MEGA)

Spécialité : Biomécanique

Résumé : Les maladies cardiovasculaires sont la principale cause de mortalité dans le monde. Parmi ces maladies, la dissection aortique constitue une pathologie méconnue et difficile à traiter, avec un taux de survie, pour les cas les plus graves ne dépassant pas les 10%. Cette pathologie survient dans l'aorte et se caractérise par l'irruption de sang à l'intérieur de la paroi de l'aorte. Elle correspond à une déchirure localisée des couches internes de la paroi aortique, appelée porte d'entrée, par laquelle le sang sous pression pénètre et décolle les différentes couches qui constituent la paroi de l'aorte. Le traitement endovasculaire vise à obturer la fausse lumière à l'aide d'un stent. Les outils actuels de la chirurgie endovasculaire reposent uniquement sur les techniques d'imagerie médicale. Comme les images sont prises avant l'intervention, elles ne tiennent pas compte de la déformation de la structure vasculaire par la prothèse. Les phénomènes de flux sanguin postopératoire dans le traitement endovasculaire des dissections aortiques sont rares. L'hémodynamique du sang dans l'aorte après une intervention est critique car le déploiement du stent modifie le flux sanguin. Cette thèse a pour but de présenter un outil numérique, issu du logiciel open-source FOAM-Extend®, permettant des simulations numériques multiphysiques réalisant le couplage fluide-structure entre l'hémodynamique et la déformation artérielle pour aider au processus de planification. En outre, à l'aide du logiciel Abaqus, nous réalisons le placement des outils chirurgicaux dans un AD "bio-fidèle" modèle. Cela permettra de prédire la déformation du lambeau et de la paroi de l'artère lors de la mise en place des outils. Et aussi, avec la simulation numérique, nous pourrions réaliser l'hémodynamique dans l'aorte du postopératoire pour prédire la modification du flux. Enfin, les résultats de la simulation numérique sont comparés aux données de l'IRM pour avoir une validation des modèles numériques.

Mots-clés : Biomécanique, Maladies Cardiovasculaires, Chirurgie Virtuelle, Aorte, La dissection aortique, Endovasculaire. Simulation numérique, Hémodynamique, Interaction fluide-structure, IRM-4D, OpenFOAM, FOAM-Extend

Laboratoire de recherche : Laboratoire de Mécanique des Contacts et des Structures (LaMCoS)

Directeur de thèse: Benyebka BOU-SAÏD

Président de jury : Michel FILLON

Composition du jury : Corneliu BALAN, Francesco MASSI, Pascale KULISA, Loïc BOUSSEL, Michel FILLON